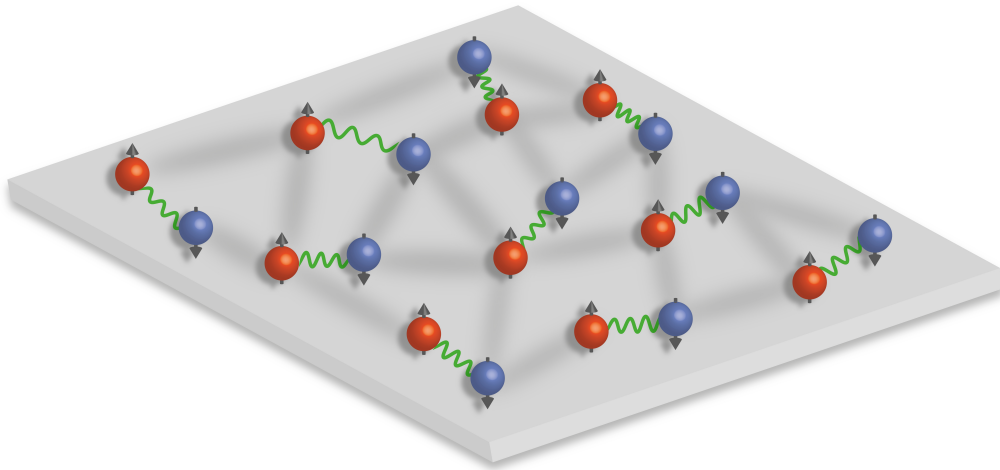


Dissertation
submitted to the
Combined Faculties of the Natural Sciences and Mathematics
of the Ruperto-Carola University of Heidelberg, Germany
for the degree of
Doctor of Natural Sciences

Put forward by
Puneet Anantha Murthy
Born in Bangalore, India
Oral examination: June 12, 2018

Emergent phenomena in two-dimensional Fermi systems



Referees:

Prof. Dr. Selim Jochim
Prof. Dr. Markus K. Oberthaler

*To my parents, Uma and Anantha Murthy,
and my grandparents, Lalithamma and Venkatasubba Jois.*

Abstract

In this thesis, I present the experimental exploration of emergent effects in a two-dimensional gas of ultracold atoms. First, I describe a novel method to measure the momentum distribution of a strongly interacting gas. Using this technique, we map out the phase diagram of the 2D BEC-BCS crossover and measure the critical temperature for superfluidity. We observe, for the first time, the Berezinskii–Kosterlitz–Thouless phase transition in a Fermi gas that is characterized by algebraic decay of phase correlations. In a second experiment, we investigate fermion pairing in the normal phase using radio-frequency spectroscopy. We observe a crossover from two-body to many-body pairing at remarkably high temperatures, thus answering a long-standing question concerning the existence of a pseudogap in this system. In the next experiment, we address the question of scale-invariance breaking, also known as a quantum anomaly, in the dynamics of a 2D Fermi superfluid. We observe a striking manifestation of this quantum anomaly in the momentum-space dynamics of the system, which demonstrates that short-range fermionic interactions have a strong influence on long-range coherence in the system. By revealing the intriguing effects emerging from the interplay between fermionic statistics, strong interactions and reduced dimensionality, this thesis advances our general understanding of many-body quantum systems.

Zusammenfassung:

In dieser Arbeit präsentiere ich die experimentelle Erforschung emergenter Effekte in einem zweidimensionalen Gas ultrakalter Atome. Zuerst beschreibe ich eine neuartige Methode zum Messen der Impulsverteilung eines stark wechselwirkenden Gases. Wir verwenden diese Technik um das Phasendiagramm des 2D BEC-BCS Crossovers abzubilden und messen die kritische Temperatur für Superfluidität. Zum ersten Mal beobachten wir den Berezinskii–Kosterlitz–Thouless Phasenübergang in einem Fermigas, welcher durch einen algebraischen Zerfall der Phasenkorrelation charakterisiert ist. In einem zweiten Experiment verwenden wir Radiofrequenzspektroskopie um das Paaren von Fermionen in der normalen Phase zu untersuchen. Wir beobachten einen Übergang von Zweiteilchen- zu Vielteilchenpaaren bei bemerkenswert hohen Temperaturen und beantworten dadurch die seit langem bestehende Frage nach der Existenz einer Pseudogap in diesem System. Im nächsten Experiment behandeln wir die Frage nach der Skaleninvarianzbrechung, welche auch als Quantenanomalie bekannt ist, in der Dynamik eines 2D Fermi-Superfluids. Wir beobachten eine eindrucksvolle Manifestation dieser Quantenanomalie in der Impulsraumdynamik dieses Systems. Dies demonstriert, dass kurzreichweitige fermionische Wechselwirkungen starken Einfluss auf die langreichweitige räumliche Kohärenz eines Superfluids haben können. Diese Arbeit legt die faszinierenden Effekte des Wechselspiels von fermionischer Statistik, starken Wechselwirkungen und verringerter Dimensionalität offen und entwickelt dadurch unser generelles Verständnis von Quantenvielteilchensystemen weiter.

Contents

1	Introduction	15
1.0.1	Content of this thesis	18
2	Superfluidity: an emergent quantum phenomenon	23
2.0.1	A brief history	23
2.0.2	Bogoliubov’s Approach	26
2.0.3	Off-diagonal long-range order	29
2.1	Fermionic superfluidity	30
2.1.1	Cooper pairing	32
2.1.2	Bardeen–Cooper–Schrieffer theory	34
2.1.3	Unconventional superfluidity beyond the BCS paradigm	38
2.1.4	The BEC-BCS crossover	41
2.2	The role of dimensionality	45
2.2.1	Crystalline ordering in lower dimensions: Peierls theory	45
2.2.2	Mermin–Wagner–Hohenberg Theorem	47
2.2.3	Superfluidity in 2D	48
2.2.4	The Berezinskii–Kosterlitz–Thouless phase transition	50
2.3	Fermions in 2D	54
2.3.1	The bound state in 2D	54
2.3.2	Scale invariance	55
2.3.3	The 2D BEC-BCS crossover	57
3	Ultracold Fermi gases in reduced dimensions	59
3.0.1	Creating a cold atomic gas	60
3.0.2	Optical dipole traps	60
3.0.3	Entering the 2D regime in a 3D world	63
3.0.4	Tuning interactions using Feshbach resonances	63
3.0.5	Probing the many-body system	70
3.0.6	The 2D Fermi gas	70
4	Synopsis of the thesis	73
4.1	Measuring the momentum distribution of a 2D Fermi gas	74
4.2	The phase diagram of the 2D BEC-BCS crossover	75

4.3	BKT Superfluidity in a 2D Fermi gas	78
4.4	Fermion pairing in the normal phase	79
4.5	Breaking of scale invariance in the dynamics of a 2D superfluid	82
4.6	How to take a snapshot of the superfluid order parameter?	86
5	Measuring the momentum distribution of a 2D Fermi gas	87
5.1	Introduction	88
5.2	Working principle	89
5.3	Experimental realization	91
5.3.1	Focusing	92
5.3.2	Collimation	93
5.3.3	Magnification	95
5.4	Conclusions	97
5.5	Appendix	97
5.5.1	Time-evolution of quantum field operators in a harmonic potential	97
5.5.2	Collisions in an expanding 2D gas	101
6	The phase diagram of the BEC-BCS crossover	103
6.1	Introduction	103
6.2	Experimental system	105
6.3	Condensation of pairs at low momenta	108
6.4	The phase diagram	111
6.5	Appendix	113
6.5.1	Preparation of the sample	113
6.5.2	Distribution of particles in the standing-wave trap	114
6.5.3	Influence of the finite aspect ratio	116
6.5.4	The rapid ramp of the magnetic field	119
6.5.5	Absorption imaging parameters and calibrations	120
6.5.6	Temperature determination	122
7	Superfluidity in a 2D Fermi gas	125
7.1	Introduction	126
7.2	Experimental System	127
7.3	The First-order Correlation Function $g_1(r)$	128
7.3.1	Algebraic decay in $g_1(r)$	130
7.3.2	Scaling exponents	130
7.4	Local properties of the superfluid	133
7.5	Appendix	136
7.5.1	Extracting the first-order correlation function	136
7.5.2	Extracting critical temperature and critical scaling exponent	137
7.5.3	Systematic Effects	138

7.5.4	Local density approximation	142
8	Fermion pairing in the normal phase	145
8.1	Introduction	146
8.2	Experimental System	147
8.2.1	Quasi-particle spectroscopy	149
8.3	Pairing in the 2D BEC-BCS Crossover	151
8.4	Crossover from two- to many-body pairing in the normal phase . . .	153
8.5	Appendix	156
8.5.1	Creating a Spin-Imbalanced Mixture	156
8.5.2	Radio-Frequency Spectroscopy	156
8.5.3	Theoretical Background on BEC and BCS Limits in 2D . . .	159
8.5.4	Axial Excitations	163
9	Scale-invariance breaking in a 2D superfluid	165
9.1	Introduction	166
9.2	Experimental protocol	167
9.3	Scale-invariance breaking in momentum space	170
9.4	Quantum anomaly and phase correlations	174
9.5	Appendix	176
9.5.1	Preparing the sample	176
9.5.2	Kinetic energy scaling	177
9.5.3	Frequency doubling in k -space	178
10	How to take a snapshot of the superfluid order parameter?	183
10.1	Introduction	183
10.2	Superfluid Density	188
10.3	Local Phase	189
10.4	Velocity and vorticity	192
10.5	Experimental Issues	195
11	Discussion and Outlook	197
11.1	Methodological progress	197
11.2	Physical insights	199
11.3	A new direction: quantum state assembly	204
12	Bibliography	209

Publications and Preprints

This thesis is based on the following publications:

1. **Matterwave Fourier optics with a strongly interacting two-dimensional Fermi gas.** P. A. Murthy, D. Kedar, T. Lompe, M. Neidig, M. G. Ries, A. N. Wenz, G. Zürn and S. Jochim;
[Physical Review A 90, 043611 \(2014\)](#).
2. **Observation of pair-condensation in the quasi-2D BEC-BCS crossover.** M. G. Ries, A. N. Wenz, G. Zürn, L. Bayha, I. Boettcher, D. Kedar, P. A. Murthy, M. Neidig, T. Lompe and S. Jochim;
[Physical Review Letters 114, 230401 \(2015\)](#).
3. **Observation of the Berezinskii–Kosterlitz–Thouless phase transition in an ultracold Fermi gas.** P. A. Murthy, I. Boettcher, L. Bayha, M. Holzmann, D. Kedar, M. Neidig, M. G. Ries, A. N. Wenz, G. Zürn and S. Jochim;
[Physical Review Letters 115, 010401 \(2015\)](#).
4. **High-temperature pairing in a strongly interacting two-dimensional Fermi gas.** P. A. Murthy, M. Neidig, R. Klemt, L. Bayha, I. Boettcher, T. Enss, M. Holten, G. Zürn, P. M. Preiss and S. Jochim;
[Science 359, 452-455 \(2018\)](#).

5. **Quantum scale anomaly and spatial coherence in a 2D Fermi superfluid.** P. A. Murthy, N. Defenu, L. Bayha, M. Holten, P. M. Preiss, T. Enss and S. Jochim;
Preprint (2018)

6. **Directly imaging the order parameter of an atomic superfluid using matterwave optics.**
P. A. Murthy and S. Jochim;
Preprint (2018)

Additional publications not included in this thesis:

1. **Equation of State of ultracold Fermions in the 2D BEC-BCS crossover region.** I. Boettcher, L. Bayha, D. Kedar, P. A. Murthy, M. G. Ries, A. N. Wenz, G. Zürn and S. Jochim;
Physical Review Letters 116, 045303 (2016).

2. **Anomalous breaking of scale invariance in a 2D Fermi gas.** M. Holten, L. Bayha, A. C. Klein P. A. Murthy, P. M. Preiss and S. Jochim;
Preprint: [arXiv:1803.08879](https://arxiv.org/abs/1803.08879)

Introduction

The ability to reduce everything to simple fundamental laws does not imply the ability to start from those laws and reconstruct the universe.

– P. W. Anderson (1972)

The world around us is truly complex. At every scale - from cosmological to cellular to atomic - we encounter systems that organize into larger scale structures which exhibit fascinating collective behavior that do not exist in their individual components. These are generally classified as emergent phenomena. Our own existence as humans is a prime example of emergence. Understanding the organizing principles underlying these emergent effect is the central scientific question of our age.

At the microscopic level of every physics system, of course, we do know that the quantum mechanical wavefunction of every particle is governed by the elegant Schrödinger equation

$$i\hbar\frac{\partial}{\partial t}\psi(\mathbf{r}, t) = \left[\frac{-\hbar^2}{2m}\nabla^2 + V(\mathbf{r}, t) \right] \psi(\mathbf{r}, t), \quad (1.1)$$

The validity of the equation has been established beyond reasonable doubt with number of experiments on isolated quantum systems. However, is this knowledge sufficient to predict or explain the collective properties of many-body systems, even the most obvious ones? For example, can we understand from first principles how atoms organize into different states of matter or how a system abruptly transforms from one state to another? Is it possible to understand how systems thermalize with their surroundings? Can we predict the existence of sound or pressure in materials?

It turns out that in most situations involving many particles, it is not possible to anticipate a priori the emergent properties of systems starting from the Schrödinger equation [1]. The reason for the failure of the reductionist approach is that the size of the Hilbert space of quantum systems grows exponentially with number of particles.

Already for multi-electron atoms, solving the Schrödinger equation proves to be a difficult task which necessitates the use of several approximations. In condensed matter systems where we deal with 10^{23} particles, the complexity is immense which calls for a qualitatively different approach to understanding the physics in these regimes. This is the state of affairs that P. W. Anderson refers to in his famous article "More is different" [2].

Naturally, experiments play a central part in our quest to understand collective behavior of systems. For instance, if not for the discovery of superconductivity and superfluidity, we could not have predicted the existence of systems that exhibit collective quantum effects. The same goes for a large number of phenomena, including the more recent and serendipitous ones such as Fractional quantum Hall effect and high- T_c superconductivity. Experiments such as these not only reveal the existence of new phenomena but provide crucial clues towards finding their theoretical descriptions.

Emergent phenomena can of course occur in various forms and systems, which can complicate their understanding. However, this is not always the case. A remarkable attribute of some emergent effects is their insensitivity to microscopic details of systems. These are sometimes referred to as quantum protectorates[3]. The robustness of many-body phases is spectacularly demonstrated by the fact that several fundamental constants are defined in terms of them. For example, the value of h/e^2 can be measured to unprecedented accuracy in quantum Hall systems, even in the presence of impurities [4]. The quantum of magnetic flux $hc/2e$ is determined accurately in Josephson junctions, irrespective of the microscopic structure of the system [5]. Intriguingly, neither of these facts can be predicted from first principles, which motivates the question, what are the higher organizing principles behind these protected phases?

One of the key organizing principles, as realized by Lev Landau, is the symmetry of a system. Typically, we discuss symmetries in the context of conservation laws, but they also play a central role in many-body physics. When an abrupt transition occurs from one phase to another, there is a dramatic shift in how the constituents are ordered. Landau realized that the shift from disorder to order can be viewed in terms a symmetry being spontaneously broken. For e.g. a transition from water to crystalline ice corresponds to the violation of the translation symmetry since the

system goes from a disordered configuration in the liquid phase to a particular well-defined lattice configuration in the solid phase. Similarly, the superfluid transition is associated with the violation of the $U(1)$ gauge symmetry. Therefore, changes in symmetry can be used to characterize emergent phases in systems. In fact, the accurate determination of $hc/2e$ is a direct consequence of spontaneous symmetry breaking and is independent of microscopic details.

The symmetry breaking argument, however, does not always hold, and this brings us to another important organizing principle - the topology of a system. By topology, we refer to those properties which remain invariant when a system is continuously deformed. The well-known example is the continuous transformation between a coffee cup and a doughnut which puts them in the same topological class. The topological properties of many-body systems are directly linked to dimensionality. Already in the 1960s, the Mermin-Wagner-Hohenberg theorem had shown that spontaneous symmetry breaking is impossible in 1D and 2D systems [6]. This was the precursor to the work of Berezinskii, Kosterlitz and Thouless that brought the idea of topology to the realm of many-body physics. BKT theory showed the existence of a phase transition in two dimensions that is driven by topological changes rather than symmetry breaking [7, 8, 9, 10] (see Sec.2.2.4). This work began the new field of topological phases in physics, which resulted in the Nobel Prize in Physics being awarded to Michael Kosterlitz and David Thouless in 2016, along with Duncan Haldane. Indeed several systems which exhibit these topological phases are two-dimensional such as quantum Hall materials, topological insulators [11], spin Hall systems [12], and superfluid and superconducting films [13].

The development of these ideas has been fundamental to our understanding of many-body physics. However, most of these theories rely on approximations that limit their applicability to the perturbative regime of weak interactions. This usually means that a many-body quantum state can be effectively described in terms of the one or two particle correlations. The Bogoliubov theory for Bose liquids and the BCS theory for Fermi liquids are two paradigmatic examples which rely on mean-field approximations as we will see later in this chapter. In the past few decades, however, several new systems have been discovered, such as high- T_c superconductors, fractional quantum Hall systems and graphene, which depart from this category. These systems often exhibit a complex interplay of reduced dimensionality and strong

interactions which leads to emergent effects that are fascinating, and perhaps also technologically relevant, but at the same time also extremely difficult to describe theoretically. The fact that almost three decades after the discovery of high- T_c cuprate superconductivity, we do not yet have an explanation for its underlying mechanism is a testament to the hardness of the problem. Therefore, understanding the macroscopic behavior of strongly interacting systems in lower dimensions can be stated as an extremely important question in the field.

Indeed, there are several experimental systems to study emergent phenomena in the strongly correlated regime. We began our research program in 2013 to investigate the many-body physics of interacting fermions in two dimensions. Our experimental system is a gas of fermionic ${}^6\text{Li}$ atoms that has been cooled to extremely low temperatures of the order of 50 – 100 nK. Ultracold atomic systems have been shown to be an excellent platform for exploring quantum many-body physics because of the high degree of tunability and observability that they enable [14]. Most importantly, we can tune the interactions between particles using Feshbach resonances and tune the dimensionality using optical dipole potentials. Using these methods, several remarkable observations have been made such as vortex lattices in superfluids, the BEC-BCS crossover in degenerate Fermi gases, the superfluid to Mott-insulator quantum phase transition in optical lattices and many more.

1.0.1 Content of this thesis

In our work, we are interested in exploring the phenomena of fermionic superfluidity and pairing in the two-dimensional Fermi gas. We create an ultracold 2D Fermi gas in a highly anisotropic optical potential which restricts the kinematics of the system to a 2D plane. By tuning the scattering length, we can reach the strongly correlated regime. When we started our research on this topic, there had already been a substantial amount of theoretical work and also some experiments at higher temperature. However, the low-temperature phenomenology with regard to superfluidity and pairing had not been understood. The 2D Fermi gas in fact turned out to be a remarkable system with several exotic properties. In the course of our research on the subject, we studied different aspects of this system –from phases to correlations to thermodynamics - and found new emergent effects. In addition, we developed novel tools that allowed us access to key observables in the system. This

thesis reports on our progress in understanding strongly correlation two-dimensional Fermi systems over the past four years.

The goal of Chapter 2 is to establish a conceptual framework for the experiments presented in the thesis. I provide an introduction to the phenomenon of superfluidity, both in bosonic and fermionic systems. Here, I explain the landmark concepts such as the Bogoliubov approximation, Off-diagonal long-range order and Cooper pairing. All these concepts are directly relevant to our study. I present a review of unconventional superfluidity in strongly correlated systems which departs from the mean-field description and serves as the motivation for our experimental work. Subsequently, I introduce the paradigmatic model of the BEC-BCS crossover which is a versatile theoretical platform to study pairing and superfluidity in fermionic systems. In the next part of the introduction, I explain the effects of reduced dimensionality on the emergent properties of many-body systems with particular focus on 2D superfluidity that is described by the Berezinskii–Kosterlitz–Thouless mechanism. Studying 2D superfluidity in a strongly fermionic systems raises several interesting questions such as the existence of a quantum anomaly, and the pairing of fermions in the normal phase.

In the Chapter 3, I introduce ultracold atomic systems as a platform to study superfluidity in strongly correlated fermionic systems. In particular, I describe our experimental apparatus that allows us to trap and cool ultracold atomic gases. I focus on the preparation of a 2D Fermi gas in highly anisotropic potentials and on the tunability of interactions using Feshbach resonances. I also describe the subtleties of inter-particle scattering in trapped 2D systems and the intriguing consequences of the reduced dimensionality on many-body properties.

In Chapter 4, I provide a brief synopsis of the publications in this thesis, with contextual information that includes previous theoretical and experimental works.

In Chapter 5, I describe a novel method to measure the exact in-situ momentum distribution of a strongly interacting 2D Fermi gas. The method is directly inspired by Fourier optics, wherein a lens performs a Fourier transform of a complex field. Here, we extend these techniques to the classical field of a strongly correlated superfluid. The momentum distribution is a key quantity to study phase transitions, especially in 2D where superfluidity is driven by fluctuations of the phase of the superfluid order parameter.

In Chapter 6, I report on the measurement of the phase diagram of a 2D Fermi gas as a function of temperature and interaction strength. In the momentum distribution of the sample, we observed a dramatic enhancement in the occupation of low-momentum modes, which signals long-range coherence in the system. Using this as a proxy for superfluidity, we measured the critical temperature for various interaction strengths. This provides a benchmark for various theories on strongly correlated 2D Fermi gases.

In Chapter 7, I report on the observation of the Berezinskii–Kosterlitz–Thouless phase transition to superfluidity. We measured the first-order correlation function of the gas as a function of temperature. Here, we observed a sharp transition from exponential to power-law decay which is one of the main predictions of BKT theory. We made a rather surprising finding that even in an inhomogeneous sample, the phase correlations decay algebraically. Remarkably, our measurements were in very good agreement with Quantum Monte Carlo computations. We were able to show that the behavior of correlations is universal for a wide range of interaction strengths suggesting that through out the BEC-BCS crossover, the phase transition is described by BKT theory.

In Chapter 8, we address the question of fermion pairing in the 2D Fermi gas. Specifically, we investigate the evolution of pairing for different interaction strengths in the normal phase of the system, i.e. above the critical temperature. We discovered that, in the strongly interacting regime, pairing is no longer driven by the two-body bound state but is significantly modified by many-body correlations. Even more surprising was the finding that these many-body correlations persist to remarkably high temperatures almost up to the Fermi temperature.

In all the chapters until now, we studied systems in equilibrium. In Chapter 9, I report on the investigation into the dynamical properties of the system. In particular, we measured the violation of scale invariance in a 2D Fermi gas in the strongly interacting regime. We found that the density-dependent pairing actually has a key role to play in the long-range properties of the system.

In Chapter 10, I describe a new method to directly image the superfluid order parameter in space. For this method, we draw close analogies with well-known optical techniques and show that the essential components of the superfluid, including superfluid density, complex phase, velocity and vorticity, can be directly obtained by

using certain momentum-space operations.

Finally, I conclude the thesis in Chapter 11 with a discussion of our experiments and their implications on the understanding of 2D Fermi gases. In the outlook, I briefly present our recent experimental upgrades that will allow for greater control of the system at a single-particle level.

Superfluidity: an emergent quantum phenomenon

2

The discovery of superconductivity and superfluidity are among the most important milestones in physics as they opened the door to a new class of phenomena where quantum mechanical effects emerge at macroscopic scales. The structure of this chapter is the following. I start with some historical remarks on superfluidity and subsequently move on to a general discussion on some of the milestones in our understanding of superfluidity.

In the first part, I discuss concepts related to Bose systems which include Bogoliubov theory and long-range coherence . In Section 2.1, I explore the problem of fermionic superfluidity, where I introduce the ideas of Cooper and Bardeen–Cooper–Schrieffer theory . I end this section with a brief review of unconventional superfluidity and the paradigmatic model of BEC-BCS crossover . In Section 2.2, I consider the role of dimensionality in the organization of particles in many-body systems. After a discussion of crystal ordering in different dimensions, I explain the occurrence of superfluidity and the Berezinskii–Kosterlitz–Thouless phase transition in 2D systems. I end this chapter by considering the problem of fermions in 2D and the intriguing effects that arise out of interactions.

2.0.1 A brief history

In the late 19th and early 20th century, physicists had begun to realize that many-body systems have dramatically different properties at low temperatures. The research in this direction was driven by substantial progress in the understanding of thermodynamic principles as well as the development of efficient cooling techniques. Heike Kammerlingh Onnes, one of the pioneers of experimental low-temperature physics, was the first to succeed in cooling and liquifying Helium and in the process made an intriguing discovery that unlike conventional fluids, ^4He does not freeze under

its own vapor pressure down to the lowest attainable temperatures! Subsequently, he began using liquid Helium as a coolant and was able to bring different materials to temperatures as low as 1 K which were the lowest temperatures on Earth at the time. In 1911, while measuring the conductance of mercury, Onnes made the remarkable discovery that the electrical resistance of mercury vanishes abruptly at a critical temperature of 4.2 K. This peculiar effect was termed superconductivity.

Almost three decades following this discovery, the groups of Kapitza in Moscow, and Allen and Misener in Cambridge set about exploring the flow properties of liquid Helium through capillary tubes. Prior to these experiments, it was already known that liquid Helium behaves in an anomalous manner around a characteristic temperature of 2.17 K - for instance the thermal conductance showed a non-linear dependence on the temperature gradient unlike normal fluids and the liquid could pass through small pores [15]. Both groups discovered that at and below 2.17 K (also known as the lambda temperature), the flow viscosity suddenly dropped by three orders of magnitude and no longer showed any dependence on the capillary tube size [16, 17]. In analogy to superconductors, this frictionless flow phenomenon was termed superfluidity.

In the past years, several new and exotic experimental systems have been found which exhibit some variant of superconductivity or superfluidity. These include layered superconductors such as cuprates, superfluid ^3He , exciton-polariton condensates and notably ultracold atomic gases. The concepts of superfluidity have been extended to systems at vastly different scales such as neutron stars and quark gluon plasmas. Several fundamental effects related to superfluidity continue to puzzle physicists almost a century after its first observation.

What are the origins of these fascinating effects? A tremendous amount of theoretical effort has been devoted to uncovering the mechanisms underlying these phenomena. The early breakthrough in describing superfluids came from Fritz London [19], who realized that the peculiar effects in Helium were fundamentally connected to the fact that ^4He atoms have integer spin and therefore follow Bose-Einstein distribution that had only been postulated a decade earlier. Therefore, the many-body wave function of this system must be symmetric under particle exchange much like an electromagnetic field. Satyendranath Bose and Albert Einstein had predicted that a non-interacting gas of bosonic particles will, at a critical temperature,

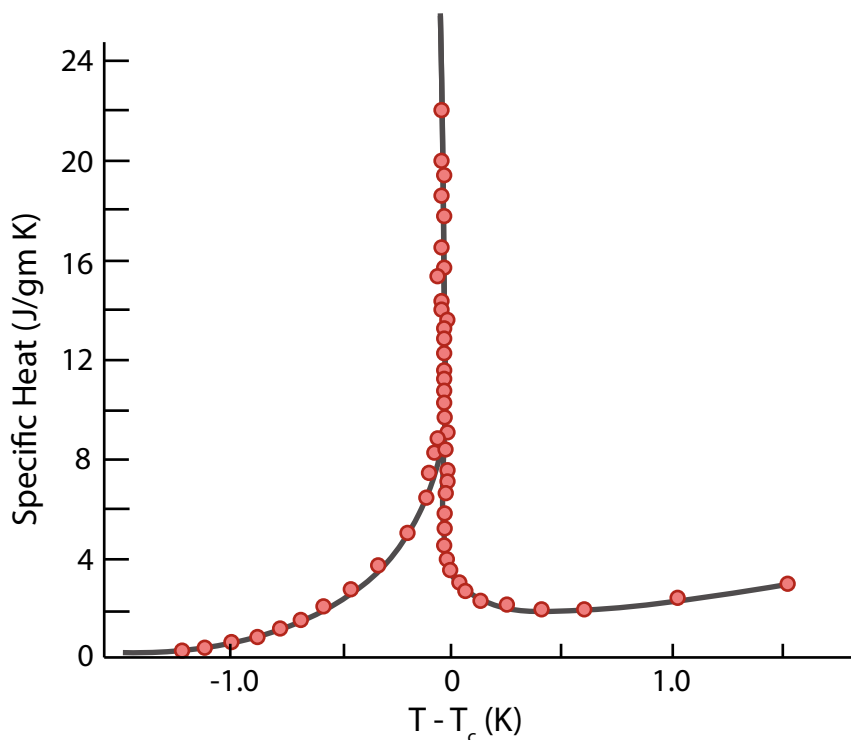


Figure 2.1: **λ -transition in Helium.** At the critical temperature, $T_c = 2.17$ K, where the normal fluid undergoes a transition to superfluid, the specific heat diverges. This occurs due to the dispersion relation becoming abruptly "gapped" at T_c . The characteristic shape of the curve in the critical region resembles the Greek letter λ , hence the term λ -point. The *lambda*-point is in fact a generic effect that has also been observed in superconductors and ultracold Fermi gases. Figure adapted from [18].

macroscopically occupy a single motional state - an effect known as Bose-Einstein condensation. London extended these arguments to interacting systems and was the first to suggest that superfluidity had a fundamental connection to Bose-Einstein condensation.

The description of superfluids received a major push with the groundbreaking work of Lev Landau [20]. Landau developed the two-fluid model for superfluids and introduced the seminal idea of quasiparticles that has subsequently revolutionized not only the field of superfluidity but of the wider field of many-body physics. Quasiparticles can be seen as collective excitations of the system with well-defined energy

E and momentum p . For instance, an electron moving in a Fermi sea is perturbed by its interactions with the surrounding electrons and nuclei which complicates its description. However, in the quasiparticle picture, it can be approximated as an electron with a different effective mass travelling through a free medium. The concept of quasiparticles greatly simplifies the description of several many-body systems.

Applying this idea to the superfluid Helium, Landau theorized that a general description of superfluidity could be attained in terms of two types of collective excitations in the system: (a) low energy sound waves or phonons which have a linear dispersion $E = cp$, where c is the sound velocity; and (b) so-called rotonic excitations corresponding to rotation motion. These have a dispersion $E \propto \Delta + p^2/2\mu$, where Δ is an excitation gap and μ is the chemical potential. Such a dispersion relation suggests that at low energies, all excitations in the system are collective (phonons) and a critical perturbation has to be provided to excite single particle modes in the system. This gave rise to the well-known criterion of Landau critical velocity. Using such a dispersion relation, Landau was able to construct a hydrodynamic description of superfluid flow which explained the mechanisms for energy dissipation in terms of the spontaneous creation of these collective excitations in the system. A crucial aspect of the description is the two fluid model wherein the superfluid component carries zero entropy and flows irrotationally whereas the normal component carries the excitations and is therefore responsible for the net viscosity.

2.0.2 Bogoliubov's Approach

The phenomenological theory of Landau was further solidified by N.N Bogoliubov [21] for the case of a dilute gas of bosonic atoms interacting weakly via a short-range potential. Assuming that such a system would undergo Bose-Einstein condensation, Bogoliubov developed a series of approximations that allowed computation of the state of the system. Here, it is worth taking a deeper look at the Bogoliubov approach, particularly as it applies to ultracold atomic systems that are the subject of this thesis. Using the formalism of second quantization, the field $\hat{\Psi}(\mathbf{r})$ of the Bose gas can be written in terms of single particle states in the form:

$$\hat{\Psi}(\mathbf{r}) = \sum_i \varphi_i \hat{a}_i, \quad (2.1)$$

where \hat{a}_i is the annihilation operator for a particle in state φ_i . Separating the lowest energy (condensate) component from the other excited components, we get:

$$\hat{\Psi}(\mathbf{r}) = \varphi_0 \hat{a}_0 + \sum_{i \neq 0} \varphi_i(\mathbf{r}) \hat{a}_i. \quad (2.2)$$

The first key idea of Bogoliubov concerns the low energy state of the system. He realized that in the BEC scenario where the lowest state is macroscopically occupied by N_0 particles, the operator \hat{a}_0 can be replaced with the c -number $\sqrt{N_0} = \sqrt{\hat{a}_0^\dagger \hat{a}_0}$. In this setting, the field operator can be reduced to:

$$\hat{\Psi}(\mathbf{r}) = \Psi_0(\mathbf{r}) + \delta\hat{\Psi}(\mathbf{r}), \quad (2.3)$$

where $\Psi_0 = \sqrt{N_0} \varphi_0$ and $\delta\hat{\Psi}(\mathbf{r}) = \sum_{i \neq 0} \varphi_i \hat{a}_i$. This description boils down to describing the condensed component as a complex field in a manner analogous to electrodynamics where the microscopic picture of photons is replaced by a classical electromagnetic field. It is instructive to rewrite the classical BEC field in an amplitude-phase representation according to:

$$\Psi_0(\mathbf{r}) = |\Psi_0(\mathbf{r})| e^{i\phi(\mathbf{r})}. \quad (2.4)$$

This complex field is known as the order parameter of a condensate. Even though the absolute value of the phase $\phi(\mathbf{r})$ has no physical relevance, the fact that the whole system "picks" a single phase corresponds to the breaking of the $U(1)$ gauge symmetry of the Hamiltonian. Later in the thesis, we will see that the complex phase $\phi(\mathbf{r})$ plays the central role in determining the peculiar properties not only of weakly interacting dilute Bose gases but of superfluids in general.

The second crucial consequence of the Bogoliubov approach concerns the higher energy excitations in the system. Bogoliubov considered the following Hamiltonian to describe a dilute Bose gas confined, with interaction strength V_0 , confined in volume Ω :

$$\hat{H} = \frac{V_0}{2\Omega} \hat{H}_0 + \sum_{\mathbf{k}} \xi_{\mathbf{k}} \hat{a}_{\mathbf{k}}^\dagger \hat{a}_{\mathbf{k}} + \frac{V_0}{2\Omega} \sum_{\mathbf{k} \neq 0} (4\hat{a}_0^\dagger \hat{a}_{\mathbf{k}}^\dagger \hat{a}_0 \hat{a}_{\mathbf{k}} + \hat{a}_{\mathbf{k}}^\dagger \hat{a}_{-\mathbf{k}}^\dagger \hat{a}_0 \hat{a}_0 + \hat{a}_0^\dagger \hat{a}_0^\dagger \hat{a}_{\mathbf{k}} \hat{a}_{-\mathbf{k}}). \quad (2.5)$$

Here, $\xi_{\mathbf{k}} = \frac{\hbar^2 k^2}{2m}$ is the free boson dispersion, $\hat{a}_{\mathbf{k}}$ ($\hat{a}_{\mathbf{k}}^\dagger$) is the annihilation (creation)

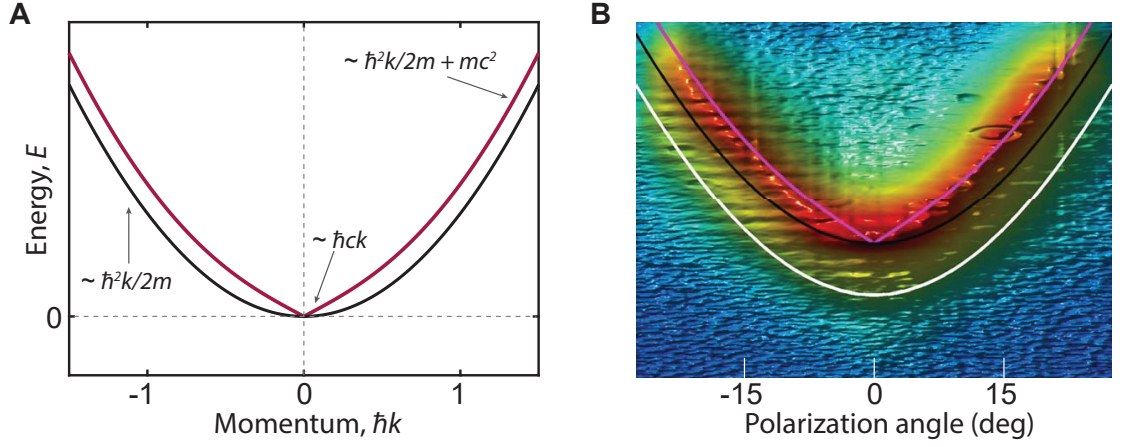


Figure 2.2: **Bogoliubov dispersion relation for weakly interacting Bose gas.** The dispersion is phonon-like at low momenta ($E \sim c\hbar k$) and has the free particle form at large momenta (pink curve). The transition between the two occurs approximately at the inverse healing length $k \sim 1/\xi$. The black line is the reference free-particle dispersion for a non-interacting gas. **B** The experimental observation of the Bogoliubov dispersion in an exciton-polariton condensate. Figure has been adapted with permission from [22]. The dispersion relation is measured spectroscopically by tuning the polarization angle of a pump beam and measuring the system response.

operator for a boson in a momentum state \mathbf{k} , and $\hat{H}_0 = \hat{a}_0^\dagger \hat{a}_0^\dagger \hat{a}_0 \hat{a}_0$ is the Hamiltonian for the particles in the ground state ($\mathbf{k} = 0$). Bogoliubov demonstrated that the Hamiltonian for interacting particles can be diagonalized using the canonical transformation

$$\hat{a}_{\mathbf{p}} = u_{\mathbf{p}} \hat{b}_{\mathbf{p}} + v_{-\mathbf{p}}^* \hat{b}_{-\mathbf{p}}^\dagger, \quad \hat{a}_{\mathbf{p}}^\dagger = u_{\mathbf{p}} \hat{b}_{\mathbf{p}}^\dagger + v_{-\mathbf{p}}^* \hat{b}_{-\mathbf{p}}, \quad (2.6)$$

where $\hat{b}_{\mathbf{p}}$ ($\hat{b}_{\mathbf{p}}^\dagger$) is the annihilation (creation) operator Bogoliubov quasiparticle in momentum state \mathbf{p} . The transformed Hamiltonian has the form:

$$\hat{H} = \frac{1}{2} \sum_{\mathbf{k}} E_{\mathbf{k}} (\hat{b}_{\mathbf{k}}^\dagger \hat{b}_{\mathbf{k}} + \hat{b}_{-\mathbf{k}}^\dagger \hat{b}_{-\mathbf{k}}) \quad (2.7)$$

This procedure essentially reduces the problem of interacting particles to one of

non-interacting quasiparticles. Here, a Bogoliubov quasiparticle can be described as being in a superposition of a particle with momentum \mathbf{k} and a hole with momentum $-\mathbf{k}$ respectively. The Bogoliubov quasiparticle operators follow the same commutation relations as those for particle operators and hence they are bosonic. The central outcome of this treatment is the famous Bogoliubov dispersion law for these quasiparticles which reads

$$E(k) = \left[\left(\frac{\hbar^2 k^2}{2m} \right)^2 + \frac{gn}{m} \hbar^2 k^2 \right]^{1/2}, \quad (2.8)$$

where g is the coupling parameter determined by the interaction potential and n is the density which determines the speed of sound $c = gn/m$. From this it follows that at low momenta $\hbar k \ll mc$, the quasiparticle dispersion has the phonon form $E = \hbar ck$ whereas in the high momentum limit $\hbar k \gg mc$ it approaches the free particle dispersion $E \propto k^2$. Qualitatively this is somewhat similar to the Landau dispersion except for the absence of the roton minimum. The Landau criterion for critical velocity still holds in the Bogoliubov dispersion. Using this dispersion law, several key properties of weakly interacting Bose gases, such as equation of state, sound propagation etc., can be computed.

2.0.3 Off-diagonal long-range order

From the Bogoliubov approach, we conclude that the Bose-Einstein condensates can be described as classical fields with a complex phase that is uniform across the whole system! O. Penrose and L. Onsager [23] were the first to suggest a criterion for the existence of condensation in a system in terms of the single particle density matrix

$$\rho(\mathbf{r}, \mathbf{r}') = \langle \hat{\Psi}^\dagger(\mathbf{r}) \hat{\Psi}(\mathbf{r}') \rangle. \quad (2.9)$$

This quantity itself is physically applicable to any system independent of its statistics and whether it is interacting. The diagonal elements of the density matrix correspond to the local density of particles $n(\mathbf{r}) = \langle \hat{\Psi}^\dagger(\mathbf{r}) \hat{\Psi}(\mathbf{r}) \rangle = \rho(\mathbf{r}, \mathbf{r})$. The momentum distribution of particles can also be obtained from the density matrix $n(\mathbf{p}) = \langle \hat{\Psi}^\dagger(\mathbf{p}) \hat{\Psi}(\mathbf{p}) \rangle$, where $\hat{\Psi}(\mathbf{p})$ is simply the Fourier transform of its real space counterpart $\hat{\Psi}(\mathbf{r})$. Penrose and Onsager noted that Bose-Einstein Condensation can be confirmed

2.1. Fermionic superfluidity

from the measurement of a large eigenvalue of $\rho(\mathbf{r}, \mathbf{r}')$. C. N. Yang extended these arguments and showed that the interesting features of condensates are in general encoded in the off-diagonal elements of the density matrix in real space [24].

For this, it is convenient to consider the so-called first-order correlation function $g_1(s) = \langle \hat{\Psi}^\dagger(\mathbf{r}) \hat{\Psi}(\mathbf{r} + \mathbf{s}) \rangle \sim \langle e^{i(\phi(\mathbf{r}) - \phi(\mathbf{r} + \mathbf{s}))} \rangle$, which quantifies the phase correlations between two spatially separated points¹. It is straightforward to show that for free bosons at high temperatures, the off-diagonal correlations decay quickly with short decay lengths set either by the thermal de-Broglie wavelength.

$$g_1(s) \rightarrow 0, \quad \text{as } s \rightarrow \infty \quad \text{thermal.} \quad (2.10)$$

On the other hand, when the system is in the condensed state, the phase correlation does not vanish even at very large distances, i.e.

$$g_1(s) \rightarrow \alpha, \quad \text{as } s \rightarrow \infty \quad \text{BEC,} \quad (2.11)$$

where α is the condensate fraction. This is also referred to as Off-diagonal-long-range-order (ODLRO).

Having described the Bogoliubov theory and the concept of off-diagonal long-range order criterion for Bose-Einstein condensation, the natural question that arises is, how are the phenomena of BEC and superfluidity connected? It turns out that the simple notion of a macroscopically occupied state (as in a BEC) fails to provide a complete description of superfluids beyond the weakly interacting regime considered by Bogoliubov. However, the notion of a local order parameter $\hat{\psi}(\mathbf{r})$ that encompasses the low-energy excitations in the symmetry broken phase always remains valid.

2.1 Fermionic superfluidity

In the previous sections, we considered how a bosonic system such as liquid Helium or a weakly interacting Bose gas could become superfluid. Can these ideas be carried over to fermionic systems? At a fundamental level, we know that fermions are anti-symmetric under particle exchange. Equivalently, from Pauli exclusion principle, two

¹Here we assume a translation invariant system, wherein only the absolute distance between two points $|\mathbf{r} - \mathbf{r}'| = s$ is relevant and not their positions.

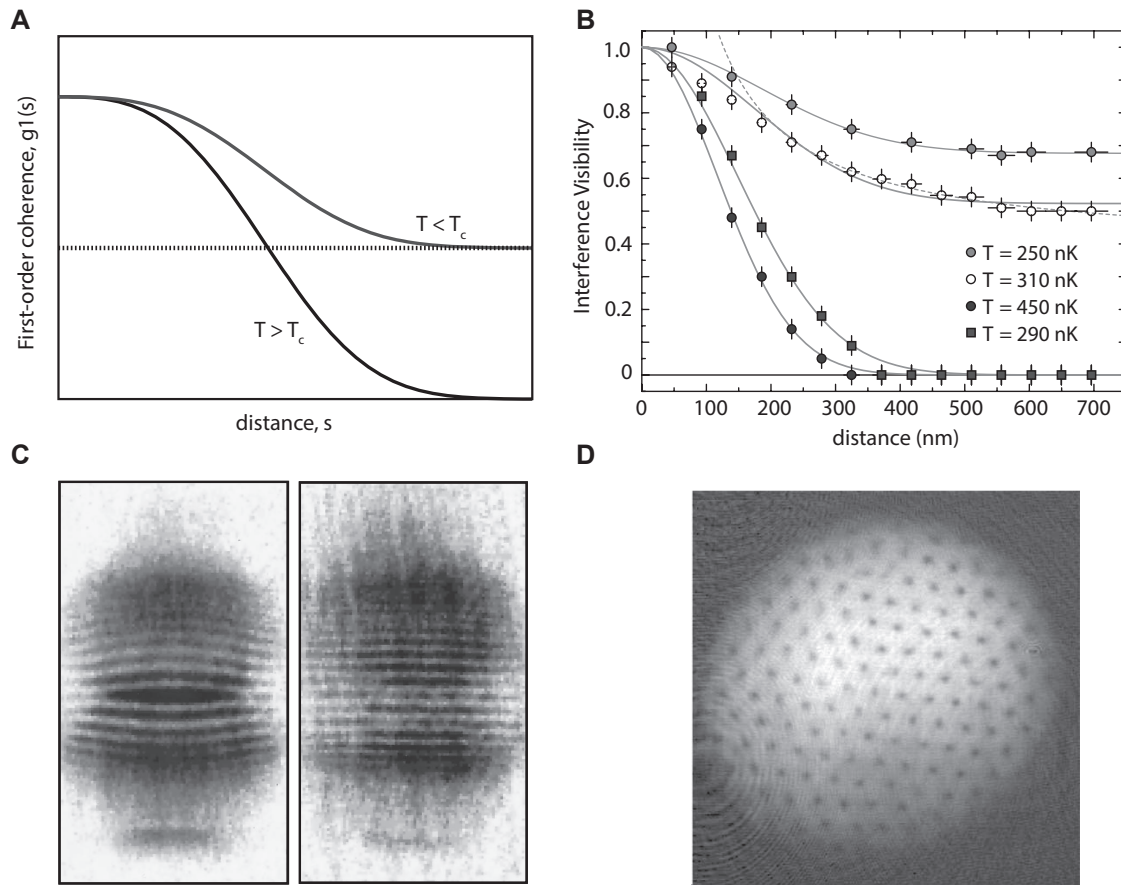


Figure 2.3: **Off-diagonal long range order in superfluids.** **A** The Penrose-Onsager criterion for superfluidity and Bose-Einstein condensation in terms of the first order correlation function $g_1(r)$. For a thermal gas, $g_1(r)$ decays exponentially with the characteristic length scale determined by the thermal de Broglie wavelength. On the other hand, in the superfluid phase, $g_1(r)$ approaches a finite value that corresponds to the fraction of atoms in the ground state. **B-C** Various manifestations of ODLRO in ultracold Bose gases. **B** The measurement of spatial coherence using a double-slit analogue technique in a BEC [25]. **C** Fringes in density observed after interference between two independent BECs [26]. This shows the validity of the description in terms of classical fields. **D** The observation of a vortex lattice in a rotated BEC [27]. The appearance of such features is a direct consequence of ODLRO. Figures **B-D** have been adapted with permission from the respective publications.

2.1. Fermionic superfluidity

identical fermions cannot occupy the same quantum state. Therefore a gas of identical fermions will never satisfy the Penrose-Onsager criterion or the requirement for off-diagonal long-range order (Eq. 2.11) thus precluding the possibility of superfluidity in such systems. On the other hand, the observation of superconductivity in metals, superfluidity in fermionic ^3He , heavy nuclei, excitonic systems etc. tells us that superfluidity is a general phenomenon that does indeed occur also in fermionic systems. How does this happen?

One rather simple mechanism for fermionic superfluidity, first suggested by Ogg [28] and Schafroth [29], is the formation of fermion pairs (spin-singlets) from two opposite spin fermions that have a strong attraction between them. If the attraction is very strong, such pair have some bosonic properties and may consequently satisfy the conditions for superfluidity that we put forth earlier. However, for pairing to occur in an electron gas in metals, there needs to be some sort of mechanism that induces attractive interaction between them. The presence of such an attractive interaction or a physical mechanism that produces it was completely unknown for several decades following the experiments of Kammerlingh Onnes. In 1950, the isotope effect was observed which revealed for the first time that there was indeed an effective attraction between electrons which was mediated by lattice vibrations or phonons [30, 31]. In these experiments, the superconducting transition temperature T_c was measured for materials that contained different isotopes and it was demonstrated that $T_c \propto 1/\sqrt{m}$, where m is the isotope mass. Since the mass is given by the nuclei forming the lattice, it could be concluded that vibrations of the lattice were playing an important role in the superconducting phase.

2.1.1 Cooper pairing

The presence of a weak phonon-mediated attraction between electrons, although a crucial clue to the superconductivity puzzle, does not readily provide a mechanism for pair formation. A breakthrough in this direction came in 1956, when Leon Cooper demonstrated that fermions interacting via a weak attractive potential occupying states close to the Fermi surface can form pairs for arbitrarily weak attraction [32].

To better understand this crucial point, we consider the question of two fermions interacting via an attractive potential V . We are interested in finding the conditions which support the existence of a bound state, say with energy $E_B = \frac{2\hbar^2 k^2}{m}$, for

arbitrary strength of V [33]¹. The Schrödinger equation for the relative wavefunction in momentum space reads

$$\psi_{\mathbf{k}}(\mathbf{q}) = -\frac{m}{\hbar^2} \frac{1}{q^2 + k^2} \int \frac{d^n q'}{(2\pi)^n} V(\mathbf{q} - \mathbf{q}') \psi_{\mathbf{k}}(\mathbf{q}'), \quad (2.12)$$

where, n is the dimensionality. Assuming a short-range potential well $V_0 \sim VR^n$, with range R , it can be shown that the final bound state energy depends on the (n -dimensional) density of states $\rho_n(\varepsilon)$ according to:

$$\int_{\varepsilon < E_R} d\varepsilon \frac{\rho_n(\varepsilon)}{2\varepsilon + |E_B|} = -\frac{\Omega}{V_0}, \quad (2.13)$$

where Ω is the volume and $E_R = \hbar^2/mR^2$ is the energy cut-off corresponding to the finite-range potential. From this, the existence of a bound state can be shown for different density of states. The main condition is that for vanishing attraction ($V_0 \rightarrow 0$), the integral should diverge for a vanishing binding energy $|E_B| \rightarrow 0$. The question then boils down to whether the integral of $\rho_n(\varepsilon)$ diverges, the answer to which crucially depends on the form of $\rho_n(\varepsilon)$ for different dimensions. In 1D, $\rho_1(\varepsilon) \propto 1/\sqrt{\varepsilon}$ and hence the system always supports a bound state. In the case of 2D - which is particularly important for this thesis - $\rho_2(\varepsilon)$ is a constant, which leads to a logarithmically diverging integral and hence a finite binding energy for arbitrarily small attraction. For 3D systems however, $\rho_3(\varepsilon) \propto \sqrt{\varepsilon}$, therefore the integral does not diverge leading to the conclusion that a finite threshold interaction strength has to be provided for a bound state to exist.

However, we have only considered the interaction of individual fermions in free-space and overlooked an important feature: that the fermions in a superconductor are surrounded by a Fermi sea. In this scenario, only the states slightly above the Fermi surface (with momentum k_F) are available for scattering and the ones below are blocked by the Pauli principle. When the Fermi surface is well-defined which is the case at weak interactions, scattering can only occur between fermions in a thin shell of energy states $E_F < \varepsilon < E_F + \delta$ 2.4. This turns out to be an effectively 2D situation, where the density of states, $\rho_3(\varepsilon) \approx \rho_3(E_F) = \frac{\Omega k_F}{2\pi^2 \hbar^2}$, is constant. In this

¹We follow the pedagogical description given in the Varenna Lecture notes by Wolfgang Ketterle and Martin Zwierlein [33]

2.1. Fermionic superfluidity

picture, Eq. 2.13 for the binding energy including the new density of states becomes

$$\int_{E_F < \varepsilon < E_F + \delta} d\varepsilon \frac{\rho_3(\varepsilon)}{2(\varepsilon - E_F) + |E_B|} = -\frac{\Omega}{V_0}. \quad (2.14)$$

The density of states at the Fermi surface is simply $\rho_3(E_F) = \frac{\Omega k_F}{2\pi^2 \hbar^2}$ where $k_F = \sqrt{2mE_F/\hbar^2}$. Therefore the effective binding energy E_B can be shown to be

$$E_B = -\frac{8}{e^2} E_F e^{-\pi/k_F |V_0|}. \quad (2.15)$$

The remarkable consequence is that even though free fermions in 3D require a threshold attraction to pair up, the presence of a surrounding sea of interacting fermions leads to the existence of a bound state for arbitrarily weak interaction strength! This is the seminal idea of Cooper pairing.

2.1.2 Bardeen–Cooper–Schrieffer theory

In the previous sections, we discussed the occurrence of Cooper pairing in fermionic systems. How does this relate to the occurrence of superfluidity? Although pairing is absolutely necessary for fermionic superfluidity, it may not be sufficient. The conceptual and mathematical foundation for the relation between Cooper pairing and superfluidity was provided by Bardeen–Cooper–Schrieffer theory (BCS) in 1957 [34].

Assuming that superfluidity arises due to the formation of Cooper pairs, John Bardeen, Leon Cooper and John Schrieffer set about trying to find the conditions which would support both the effects simultaneously. Specifically, the BCS approach consists of finding the wavefunction

$$|\Psi_{\text{BCS}}\rangle = \sum_{\mathbf{k}} \varphi_{\mathbf{k}} e^{i\mathbf{k}(\mathbf{r}_1 - \mathbf{r}_2)} (|\uparrow\downarrow\rangle - |\downarrow\uparrow\rangle), \quad (2.16)$$

that corresponds to finding the Cooper pairs at rest, a situation that would automatically exhibit ODLRO in the center-of-mass frame of the pairs. To do so, we start by constructing an effective Hamiltonian:

$$H = \sum_{\mathbf{k}\sigma} \xi_{\mathbf{k}} \hat{c}_{\mathbf{k}\sigma}^\dagger \hat{c}_{\mathbf{k}\sigma} + \frac{1}{N} \sum_{\mathbf{k}\mathbf{k}'} V_{\mathbf{k}\mathbf{k}'} \hat{c}_{\mathbf{k}\uparrow}^\dagger \hat{c}_{-\mathbf{k}\downarrow}^\dagger \hat{c}_{-\mathbf{k}'\downarrow} \hat{c}_{\mathbf{k}'\uparrow}. \quad (2.17)$$

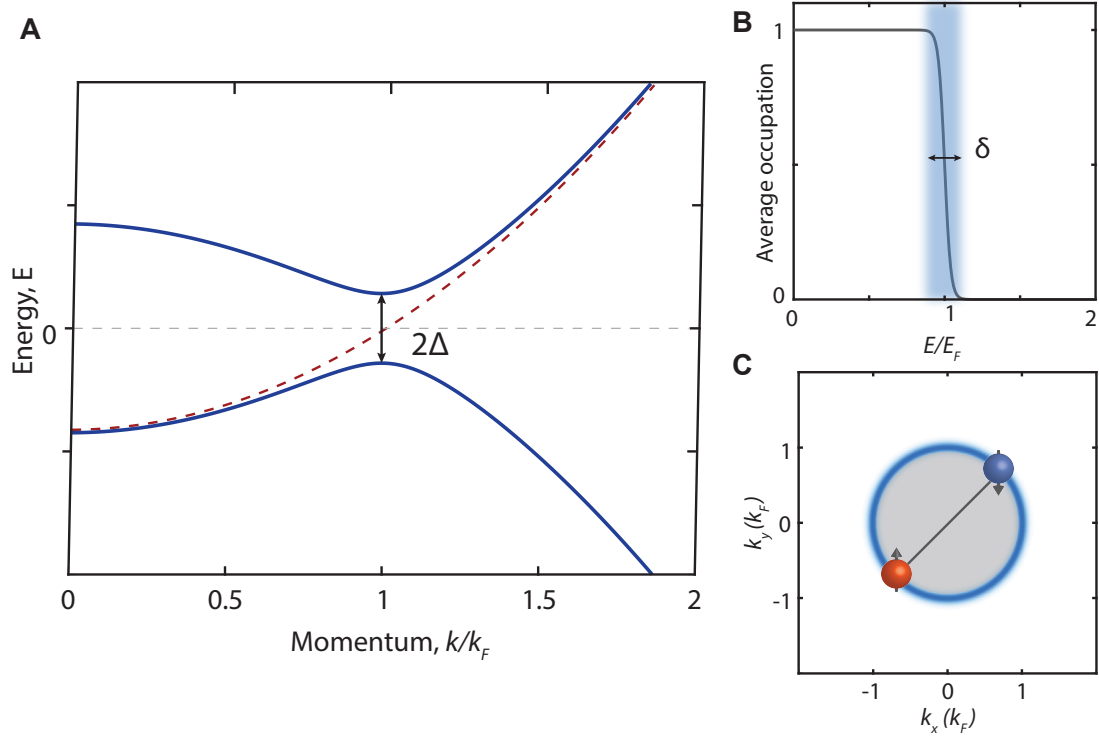


Figure 2.4: **Bardeen–Cooper–Schrieffer theory.** **A:** The BCS dispersion relation for a weakly attractive gas of fermions. The main feature of this relation is the development of an energy gap at the Fermi momentum at $T \leq T_c$. This is the minimum energy required to remove a fermion from the system. The dashed red line corresponds to the free-particle dispersion. The pairing gap can be treated as the order parameter in the system. **B:** The fermions occupy different energy states according to the Fermi–Dirac distribution. Due to this, only the energy states in a thin shell near the Fermi surface are available for scattering. This is responsible for Cooper pairing at arbitrarily small attraction. **C** The BCS mechanism predicts the formation of Cooper pairs at the Fermi surface. They have the peculiar property that they are correlated in momentum space instead of position space as is the case of ordinary molecules. Most importantly, Cooper pairing is a many-body effect since the formation of pairs necessarily depends on the existence of a surrounding Fermi sea.

2.1. Fermionic superfluidity

Here, $\hat{c}_{\mathbf{k}\sigma}^\dagger$ ($\hat{c}_{\mathbf{k}\sigma}$) creates (annihilates) a fermion with momentum \mathbf{k} and spin $\sigma \equiv \uparrow, \downarrow$, and hence the first term denotes the kinetic energy of electrons. The chemical potential is included through $\xi_{\mathbf{k}} = \varepsilon_{\mathbf{k}} - \mu$. The second term represents the annihilation of a Cooper pair, and the creation of another Cooper pair. We define a mean field potential, also known as the gap function,

$$\hat{\Delta}_{\mathbf{k}} = - \sum_{\mathbf{k}'} V_{\mathbf{k}\mathbf{k}'} \langle \hat{c}_{\mathbf{k}\uparrow} \hat{c}_{-\mathbf{k}\downarrow} \rangle, \quad (2.18)$$

that denotes the energy required to remove a fermion from the many-body state. Note that, since we are now in the interacting system, the quantity Δ is not necessarily the same as the binding energy obtained in the previous section. Now, similar to the case of a weakly interacting Bose gas, we employ the Bogoliubov transformation that describes the fermion operators (\hat{c}, \hat{c}^\dagger) in terms of quasi-particle operators ($\hat{\gamma}, \hat{\gamma}^\dagger$), and allows to diagonalize the Hamiltonian:

$$\hat{c}_{\mathbf{k}\uparrow} = u_{\mathbf{k}}^* \hat{\gamma}_{\mathbf{k}0} + v_{\mathbf{k}} \hat{\gamma}_{\mathbf{k}1}^\dagger; \quad \hat{c}_{\mathbf{k}\downarrow}^\dagger = -v_{\mathbf{k}}^* \hat{\gamma}_{\mathbf{k}0} + u_{\mathbf{k}} \hat{\gamma}_{\mathbf{k}1}^\dagger, \quad (2.19)$$

where $|u_{\mathbf{k}}|^2 + |v_{\mathbf{k}}|^2 = 1$. However, in contrast to the Bose gas, these quasiparticles are fermionic and satisfy the anticommutation relations for fermions. From this procedure, we obtain two important results. The first one concerns the dispersion relation, which turns out to be

$$E_{\mathbf{k}} = \sqrt{\xi_{\mathbf{k}}^2 + |\Delta_{\mathbf{k}}|^2}. \quad (2.20)$$

This illustrates that in order to excite free fermions in the system, a finite pairing energy gap $\Delta_{\mathbf{k}}$ has to be surpassed. The second crucial result concerns the wavefunction $|\Psi_{\text{BCS}}\rangle$ in terms of the original fermion operators:

$$|\Psi_{\text{BCS}}\rangle = \prod_{\mathbf{k}} (u_{\mathbf{k}} + v_{\mathbf{k}} \hat{c}_{\mathbf{k}\uparrow}^\dagger \hat{c}_{-\mathbf{k}\downarrow}^\dagger) |0\rangle. \quad (2.21)$$

This shows the existence of pairs that are correlated in momentum space, unlike deeply bound molecules which are characterized by a large wave-function overlap in real space.

As elegant as this theory is, the main reason for its fame is its success in predicting

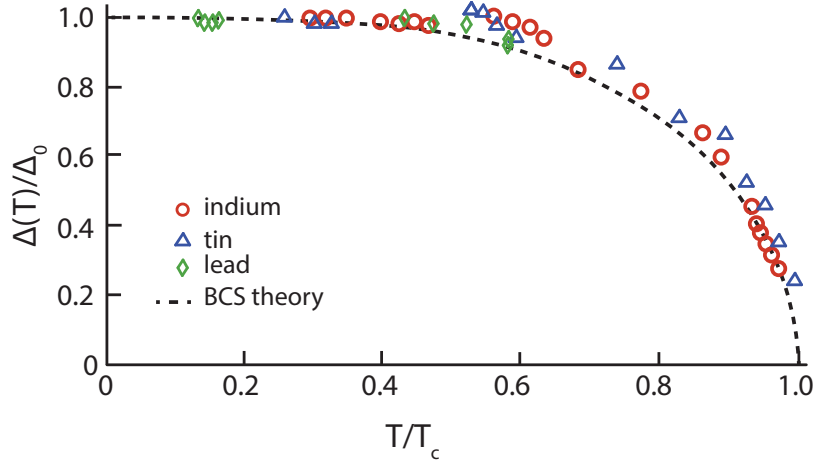


Figure 2.5: **Experimental verification of BCS theory.** The success of BCS theory lies in its ability to predict the properties of superconductors accurately, which can be experimentally confirmed. In this example, the pairing gap was measured as a function of temperature for different materials: Indium, Tin and Lead. After rescaling with the zero temperature gap Δ_0 , all the measured data are reasonably consistent with the BCS expectation. In the next section, we will discuss where BCS theory fails. Figure adapted with permission from [35].

quantities that could be experimentally measured in real systems! Among the most important are the predictions of critical temperature, pairing gap and specific heat. Without going into their detailed derivations, we present the final expressions for these quantities. The pairing gap at zero temperature is given by

$$\Delta_0 = 2\delta e^{-\pi/k_F|V_0|}. \quad (2.22)$$

For superconductors, the width of the energy shell corresponds to the Debye energy $\delta = \hbar\omega_D$. From the zero temperature gap, one can compute the critical superfluid temperature T_c , which is the temperature at which the thermal fluctuations break Cooper pairs. We obtain a universal relation

$$k_B T_c = \frac{e^{\gamma_E}}{\pi} \Delta_0, \quad (2.23)$$

where $\gamma_E = 0.577$ is the Euler constant. The specific heat at T_c is given in terms of

2.1. Fermionic superfluidity

the pairing gap according to

$$\Delta C = \rho_3(E_F) \left(\frac{\partial \Delta^2}{\partial T} \right)_{T_c}. \quad (2.24)$$

Since the gap has a discontinuity at T_c , the specific heat diverges giving rise to the λ -transition. All these predictions have been extensively verified in experiments in a wide array of materials. In addition, the BCS theory successfully explains the mechanisms of other fascinating effects related to superconductors, most notably the Meissner effect wherein a superconducting material excludes externally applied magnetic fields leading to diamagnetic behavior.

2.1.3 Unconventional superfluidity beyond the BCS paradigm

In the previous sections, we discussed how momentum-space fermion pairs can form due to the presence of an interacting Fermi sea and how this connects to fermionic superfluidity. This mechanism crucially relies on the existence of a well-defined Fermi surface, a condition only satisfied in the limit of weak interactions i.e. when $k_F|V_0| \ll 1$. Several systems fall in this regime, which contributed to the phenomenal success of BCS theory. However, in the decades following these developments, a growing number of systems were found to exhibit superfluid behavior that departed significantly from BCS predictions. Since a microscopic description of these phenomena doesn't yet exist, they are known as *unconventional* superfluids (UcS), whereas the systems described by BCS theory have been relegated to the rather unfortunate category of *conventional* superfluids.

The first material to be identified in the UcS category was superfluid ^3He , discovered by David Lee, Douglas Osheroff and Robert Richardson in 1972 [37]. ^3He atoms are fermionic, neutral and behave as hard-core objects, which suppresses s -wave pairing required by BCS theory. It is now known the ^3He atoms in fact form higher orbital p -wave pairs, leading to a rather complicated phase diagram with different types of superfluid phases. In electron systems, unconventional superconductivity was first observed in so-called heavy-fermion materials (CeCu_2Si_2 , UPt_3 etc.) in 1979 by Steglich [38]. These materials contain magnetic ions which were previously thought to inhibit pair formation, but in fact lead to antiferromagnetic ordering. One hypothesis is that antiferromagnetic spin fluctuations are the source of superconductivity in

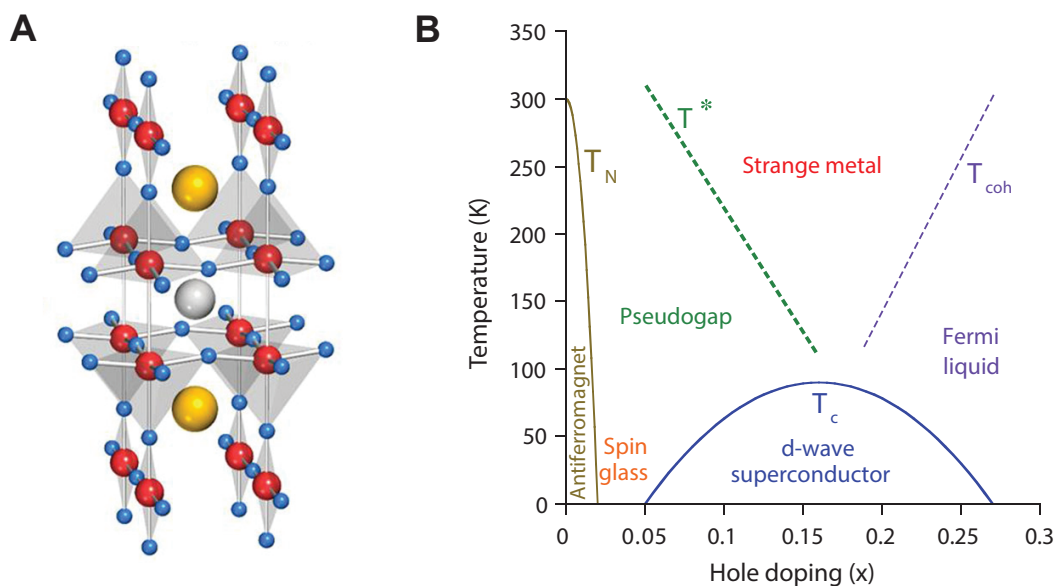


Figure 2.6: **Unconventional superconductivity in cuprates.** Several systems which exhibit high- T_c superconductivity, for e.g. copper oxide compounds as shown in **A**, are composed of two-dimensional layers with weak interactions between them. The reduced dimensionality is believed to play an important role in the properties of these systems. **B** A schematic phase diagram of cuprates as a function of hole doping and temperature. These systems exhibit d-wave pairing, as opposed to conventional BCS superconductors which are s-wave paired. Intriguingly, the normal phase of cuprates ($T > T_c$) features a pairing pseudogap, whose mechanism is not yet understood. Figure adapted with permission from [36]

these systems. Perhaps the most famous of the unconventional systems are a class of compounds known as Cuprates. In 1986, while exploring superconductivity in ceramic materials, Georg Bednorz and K. Alex Müller discovered that certain layered compounds, eg. $\text{La}_{2-x}\text{Ba}_x\text{Cu}_4$, have a superconducting transition at 40 K, almost an order of magnitude larger than any previously known material [39]. Obviously, this falls in a new class of many-body phenomena with profound technological implications, leading to Bednorz and Müller being awarded the Nobel Prize in Physics in 1987. These materials exhibit both spin-ordering and pairing instabilities that lead to a rich phase diagram with closely existing AFM and superconducting phases. In recent

years, unconventional superconductivity has been observed in several new systems such as Iron-based Pnictides [40], graphene [41] etc. The origin of these emergent phases and the fermion pairing mechanisms in these materials are some of the most outstanding questions in physics today.

It is now understood that the departure from the BCS prescription may occur in a number of ways, and consequently several definitions exist for unconventional superconductors. One commonly used definition of UcS is a state wherein the pairing mechanism is driven not by phonon-exchange like in BCS theory but by a different effect such as exchange of spin fluctuations [42]. Consequently, the pair wavefunction may no longer contain BCS-type spin singlets but higher orbital effects (eg. p -wave pairs). An alternative definition is based on the symmetries of the Hamiltonian. It is generally accepted that ODLRO in superconductors implies the breaking of the global $U(1)$ symmetry [24]. A material may be classified as UcS if, in addition to the $U(1)$ symmetry, another symmetry such as time-reversal or inversion symmetry is simultaneously broken [43]. For example, p -, d -, or f - orbital pairing all break the inversion symmetry.

In terms of many-body properties there are some strongly suggestive features common to many of the UcS systems mentioned above.

1. **Characteristic Fermi energy (E_F) is smaller than the Debye energy $\hbar\omega_D$:** In BCS-type systems, E_F is much larger than $\hbar\omega_D$ leading to a well-defined Fermi surface, which is essential for Cooper pairs. On the other hand, in UcS materials, E_F is usually much smaller than $\hbar\omega_D$, which intuitively suggests much stronger interactions. In terms of lengthscales, these systems are often referred to as short-coherence-length superconductors, meaning the correlation length of the pairs (average pair size) is of the same order as the inter-particle spacing ($1/k_F$). In contrast to BCS pairs which are much larger than average spacing almost by a factor of about 10^3 [42].
2. **Superconductivity develops out of a non-Fermi liquid normal phase with a pseudogap:** To understand superconductivity, it is crucial to understand the normal phase out of which it is formed. In BCS superconductors, Cooper pairing instability occurs exactly at T_c . The normal phase $T > T_c$ is a gapless Fermi liquid of unpaired interacting fermions. However, in most UcS materials, strong pairing correlations are known to develop already in the

normal phase, an effect known as a pseudogap. The mechanism which leads to a pseudogap is not yet understood [36, 43].

- 3. Two-dimensional layered structure:** Several UcS materials, cuprates in particular, are known to have quasi-two-dimensional structures with weak coupling between layers. Consequently, electron transport and pair correlations predominantly occur in 2D planes. This is believed to play a fundamental role in these systems as fluctuation effects are known to be much stronger in lower dimensions [44].

The general problem of unconventional superfluidity is extremely difficult to solve. However, the problem can be simplified by studying model Hamiltonians that only contain the essential features of these systems. The Hubbard model is one of the prominent models for strongly correlated systems in lattices. In the next section, we will discuss another paradigmatic model for fermionic pairing and superfluidity in a strongly interacting bulk system- the BEC-BCS crossover.

2.1.4 The BEC-BCS crossover

One of the early proposals to explain fermionic superfluidity was in terms of diatomic molecules made up of strongly attractive fermions. These dimers behave essentially as bosonic particles which undergo Bose-Einstein condensation and hence become superfluid. The idea however did not gain much traction at the time since the predicted critical temperatures were several times larger than the measured ones. The subsequent BCS theory solved this problem through the mechanism of Cooper pairing which occurs at very weak attraction and indeed predicts the correct critical temperatures in conventional superfluids.

With the discovery of unconventional superfluidity, the tight dimer approach began to receive more attention because of the short pair correlation lengths and high critical temperatures observed in these systems. This led to the paradigmatic model of the BEC-BCS crossover which conjectures the existence of a continuous crossover between the two regimes. It turns out that ultracold Fermi gases in the vicinity of a Feshbach resonance reproduce the BEC-BCS crossover beautifully and hence they are ideal platforms to study the associated physics as we will show in the later parts of this thesis. Historically, the idea of the BEC-BCS crossover predates ultracold

2.1. Fermionic superfluidity

atoms by several decades. The existence of such a crossover was first pointed out by Keldysh in the context of exciton condensation in 1968 [45]. Subsequently, Eagles [46] and Leggett [47] built upon these ideas while working on superconductivity and superfluidity in systems where the attraction between fermions was no longer small compared to the Fermi energy.

It was realized that in the ground state ($T=0$), the BCS theory in fact successfully provides a qualitatively accurate description of fermion pairs for any value of attraction. The only difference being that the chemical potential μ decreases monotonically for increasing attraction and is no longer simply the Fermi energy E_F as expected from BCS theory. In fact in the BEC limit, μ takes negative values equal to half the pair binding energy.

It is quite remarkable that a smooth crossover exists between these two distinct pairing regimes! On the one hand, we have a BEC of tightly bound dimers which form solely due to the existence of two-body bound states and on the other we have Cooper pairs which form only in the presence of a surrounding Fermi sea. In some sense, we can view the dimers as position space pairs as they form due to a wavefunction overlap in space. In contrast, the Cooper pairs are correlated in momentum space. This is illustrated in Fig. 2.7A,B. To get a deeper understanding of the BEC-BCS crossover, we first consider the features of key observables in the BEC and BCS limits.

First, let us consider the form of the pair wave function in the two regimes starting from the BCS ansatz $\langle \Psi_{\text{BCS}} | \hat{c}_{k\uparrow}^\dagger \hat{c}_{-k\downarrow}^\dagger \rangle = u_k v_k$. The pairs can be characterized by the two-point pair correlation function in position space

$$\begin{aligned} \phi(\mathbf{r}_1 - \mathbf{r}_2) &= \langle \Psi_{\text{BCS}} | \Psi_\uparrow^\dagger(\mathbf{r}_1) \Psi_\downarrow^\dagger(\mathbf{r}_2) | \text{BCS} \rangle = \int \frac{d^3k}{(2\pi)^3} u_k v_k e^{i\mathbf{k} \cdot (\mathbf{r}_1 - \mathbf{r}_2)} \\ &= \frac{1}{2} \int \frac{d^3k}{(2\pi)^3} \frac{\Delta}{\sqrt{\xi_k^2 + \Delta^2}} e^{i\mathbf{k} \cdot (\mathbf{r}_1 - \mathbf{r}_2)}. \end{aligned} \quad (2.25)$$

In the BCS regime, we get

$$\phi(\mathbf{r}_1 - \mathbf{r}_2) \sim \frac{\Delta}{r v_F} \sin(k_F r) K_0\left(\frac{r}{\pi \xi_{\text{BCS}}}\right), \quad (2.26)$$

where v_F is the velocity of particles at the Fermi surface, ξ_{BCS} is the pair correlation length and K_0 is the Bessel function. Qualitatively, this shows that only the fermions

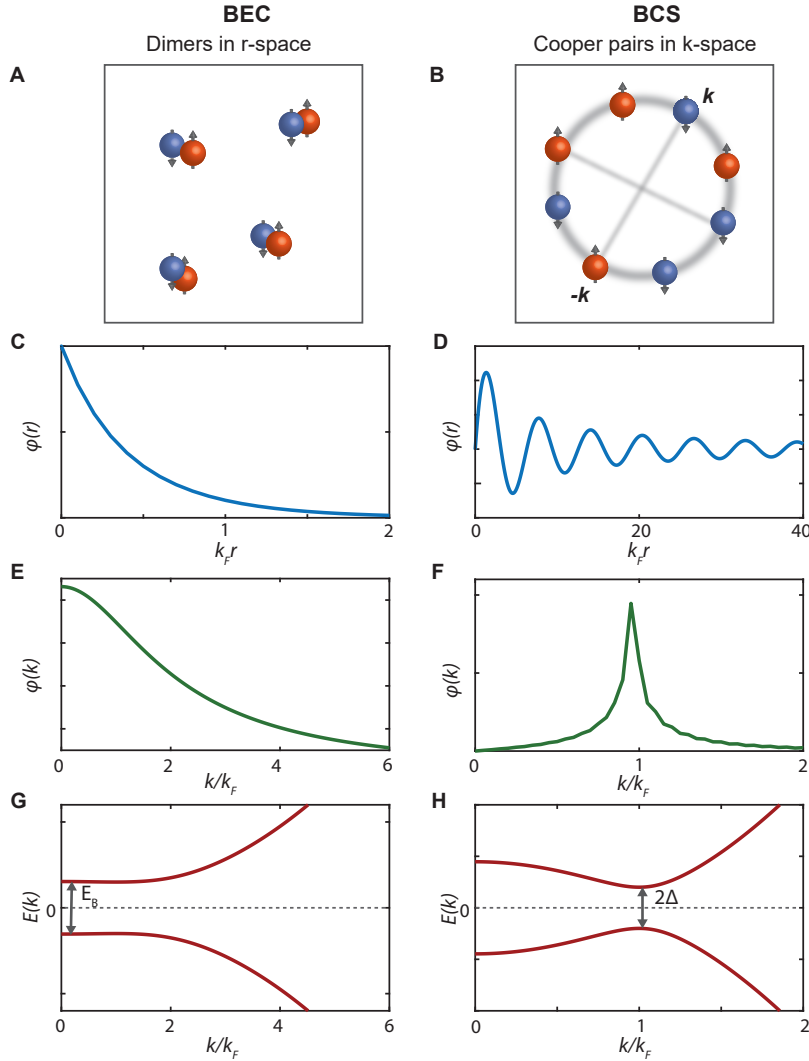


Figure 2.7: **Pairing in the BEC and BCS limits.** Here, we show the difference in pairing and related properties in the BEC (left row) and BCS limits (right row) **A, B:** Illustration of position space and momentum space pairs. **C** The exponentially decaying pair correlation function of a molecular dimer, leading to a broad momentum space distribution in relative coordinates (**E**). **D** The spatial correlation function in the BCS limit has strong modulations at a spatial frequency $1/k_F$, leading to a sharp well-defined momentum space distribution peaked at k_F (**F**). **G, H** The single particle dispersion relation on the BEC and BCS limits. The BEC regime has the energy minimum at $k = 0$ whereas in the BCS dispersion it occurs at $k = k_F$. This shows the crossover from a two-body pairing effect (BEC) to a many-body pairing effect which depends on the presence of the surrounding medium.

2.1. Fermionic superfluidity

pair in a thin shell near the Fermi surface form pairs with well defined momenta k_F . Then the position space pair wavefunction must have spatial oscillations at a wavelength $\sim 1/k_F$. The BEC regime, on the other hand, has molecular dimers with a well-defined position distribution given by

$$\phi_{\text{BEC}}(\mathbf{r}_1 - \mathbf{r}_2) \sim \frac{e^{-b|\mathbf{r}_1 - \mathbf{r}_2|}}{|\mathbf{r}_1 - \mathbf{r}_2|}. \quad (2.27)$$

This corresponds to a broad momentum space correlation function. This is qualitative illustrated in Figs. 2.7 **C - F**.

The single particle dispersion relations in the BEC and BCS limits are shown in Fig. 2.7 **G, H**. We see that while the BCS dispersion relation has its energy minimum at $k = k_F$ owing to Cooper pairing, the energy minimum for the BEC regime occurs at $k = 0$. This implies that the energy gap on the BEC side arises out of intrinsic two-body bound state and hence it is independent of the surrounding Fermi sea. On the contrary, the gap on the BCS side depends on k_F which in turn is a function of the local density. Hence Cooper pairing can be understood as a true many-body effect.

While the $T = 0$ behavior provides a versatile platform to explore pairing, the physics of the BEC-BCS crossover becomes even more rich at finite temperatures. The problem is subtle at many fronts. In the BCS limit of weak attraction, it is clear that Cooper pairing and superfluidity occur simultaneously at T_c . The normal phase $T > T_c$ is a Fermi liquid of unpaired fermions. Due to the exponentially small pairing gap, the critical temperature is much smaller than the Fermi temperature. In the BEC limit, the two-body binding energy (E_B) is stronger than the Fermi energy, and therefore the dimers naturally form at high temperatures $E_B \gg k_B T_c$. One point worth emphasizing here is that even though the BEC regime corresponds to strong attraction between fermions, it is in fact a weakly interacting system. This is because, for strong enough attraction $E_B \gg E_F$, the fermionic degree of freedom is no longer resolvable. Still, the dimers have a weak residual repulsion arising out of Pauli exclusion of the constituent fermions. Therefore, a strongly attractive regime of fermions can be described as a weakly repulsive regime of bosons and therefore the critical temperatures in this regime can be computed from mean-field bosonic theory.

In the interaction regime between these limits, the problem becomes considerably more difficult and at the same time more interesting. Here, the pair size approaches the average spacing between fermions which leads to a breakdown of both bosonic and fermionic mean-field descriptions. In other words, both the bosonic and fermionic degrees of freedom start to play a comparable role. Much of our interest is in understanding the phenomenology in this region. Here it is worth noting that ultracold Fermi gases are particularly suited to study this problem due to the tunability of interaction strength near a Feshbach resonance. In fact, the demonstration of superfluidity in the unitary Fermi gas has been one of the big successes in cold atom physics.

2.2 The role of dimensionality

So far, we have discussed how long-range coherence develops in bosonic and fermionic systems and its relation to the phenomena of superfluidity. Long-range coherence can be viewed as a form of ordering in the system. In the normal phase, the system is disordered due to thermal fluctuations. The spontaneous breaking of the $U(1)$ symmetry leads to the entire system being described by a single order parameter. However, most of the preceding discussions focused on superfluidity in three-dimensional systems. One of the most fundamental questions in many-body physics is: how does the order in the system depend on its dimensionality? Here, we will review the role of dimensionality in many-body physics and demonstrate that in lower dimensions (2D and 1D), the picture is fundamentally different than in 3D. We will follow the explanation presented in Jean Dalibard's Collège de France lectures [48].

2.2.1 Crystalline ordering in lower dimensions: Peierls theory

Studying the role of dimensionality has a long tradition in physics. The impact of dimensionality on ordering phenomena in many-body systems was first discussed by Rudolf Peierls in 1934 [49, 50]. In particular, Peierls was mainly interested in crystalline order in solids and made the crucial observation that perfect crystals could not form in 2D and 1D.

Consider an array of atoms which only have nearest neighbour interactions $V(x_j) =$

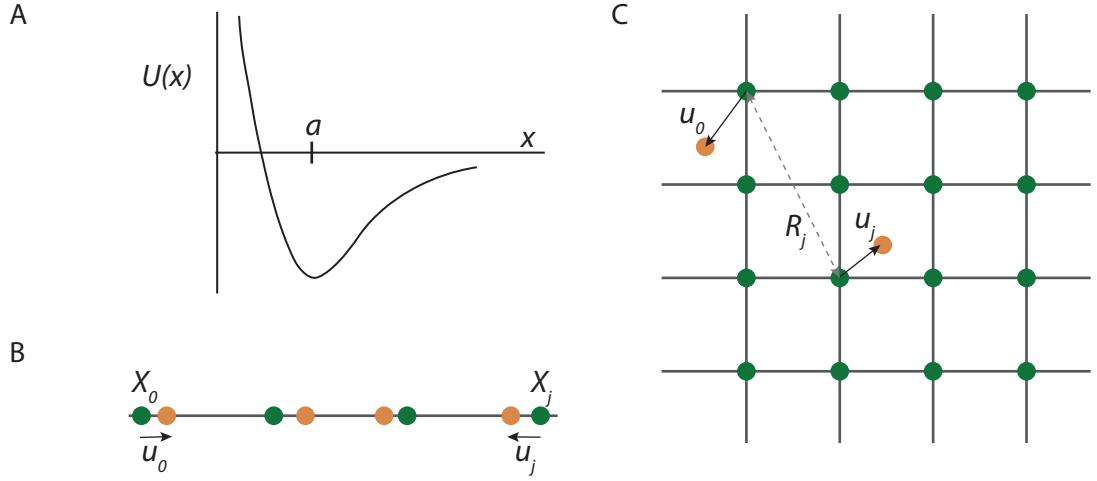


Figure 2.8: **Peierls theory of crystal ordering in different dimensions. A:** The short-ranged interaction potential which has an energy minimum at the lattice distance. **B:** A 1D chain of atoms with the green circles representing the perfectly ordered configuration. The orange circles denote the displacement of atoms from the crystal configuration caused either by thermal or quantum fluctuations. **C:** The similar situation in 2D. Peierls was the first to show that the ability of a system to form a crystal depends fundamentally on the dimensionality.

$\sum_j U(x_{j+1} - x_j)$. We assume the existence of a local potential minimum at $x = a$ which favours the formation of a regular array of particles in the absence of thermal or quantum fluctuations, i.e. at $T = 0$. The question is, how does the configuration of the system deviate from the perfect crystal at finite temperature? At finite temperature, each atom jitters around its original position with average displacement

$$u_j = x_j - X_j, \quad X_j = ja, \quad (2.28)$$

averaging to zero. Peierls demonstrated that the correlation between the position uncertainties at two points, $\langle (u_j - u_0)^2 \rangle$ depends crucially on the dimensionality of the system. The quantity is a direct measure of long-range order in crystals: a larger uncertainty corresponds to a smaller possibility for particles to form an ordered

structure. For a classical 1D chain of atoms at finite temperature, the function has the form:

$$\mathbf{1D\ thermal:} \quad \langle (u_j - u_0)^2 \rangle = \frac{k_B T}{\kappa a} X_j, \quad (2.29)$$

where $\kappa = d^2U/dx^2$ is the rigidity of the crystal. The above equation shows that the uncertainty in predicting the position of an atom at X_j relative to an initial atom (at X_0) grows with linearly with the distance between them as well as with the temperature. In the quantum case $T = 0$, we get:

$$\mathbf{1D\ quantum\ (T=0):} \quad \langle (u_j - u_0)^2 \rangle \sim \frac{\hbar}{\pi \sqrt{m\kappa}} \ln(X_j/a). \quad (2.30)$$

The logarithmic divergence with distance shows that in 1D, even at $T = 0$, quantum fluctuations destroy long-range order. For a 2D array at finite temperature, we get

$$\mathbf{2D\ thermal:} \quad \langle (u_j - u_0)^2 \rangle \sim \frac{2k_B T}{\pi^2 \kappa} \ln(R_j/a). \quad (2.31)$$

Like in the previous 1D quantum case, we see that the uncertainty in relative positions grows logarithmically with distance and hence perfect crystalline order in 2D is possible only at zero temperature. For 3D systems, however, the uncertainty:

$$\mathbf{3D\ thermal:} \quad \langle (u_j - u_0)^2 \rangle = \frac{k_B T}{\kappa}, \quad (2.32)$$

does not depend at all on the distance between the two points but only on the temperature, which leads to true crystalline order. A crystal forms when the thermal fluctuations are small enough, i.e. $k_B T \ll a^2$. In fact the condition for crystal formation is, as shown by Lindeman, is:

$$[\langle (u_j - u_0)^2 \rangle]^{1/2} \sim 0.15 - 0.3a. \quad (2.33)$$

2.2.2 Mermin–Wagner–Hohenberg Theorem

The approach of Peierls was seminal as it showed for the first time the influence of dimensionality in the ordering behavior of many-body systems. This was the precursor to a more general and rigorous statement on dimensionality - the Mermin–Wagner–Hohenberg theorem. David Mermin and Herbert Wagner published a groundbreaking

article in 1966 on magnetism in solids [6], which was followed by an article by Pierre Hohenberg on Bose gases in 1967 [51]. The subject of both these works was whether spontaneous symmetry breaking - which leads to ordering phenomena in 3D - was possible in lower dimensions. Mermin, Wagner and Hohenberg considered a general category of systems which (i) have short range interactions, (ii) possess some continuous symmetry such as translational, rotational, $U(1)$ etc., and (iii) are in the thermodynamic limit. The theorem is the following:

A continuous symmetry of a $d \leq 2$ dimensional system cannot be spontaneously broken at non-zero temperature.

The fundamental reason behind this constraint is that any thermal system with a continuous symmetry has a massless fields of low-energy excitations called Goldstone bosons. There are several examples of Goldstone modes: phonons in superfluids, spin waves in the XY model etc. The form of the density of states in 1D and 2D leads to a divergent contribution of these modes at low momenta, which always destroys long-range order and restores the symmetry of the Hamiltonian. In the context of superfluidity, the Mermin–Wagner theorem directly precludes the spontaneous breaking of the $U(1)$ symmetry. Consequently, the first-order correlation function has to vanish at infinite distance unlike 3D systems where it asymptotically approaches a finite value. This motivates the question: can there be superfluidity in 2D and 1D? If so, what is the mechanism that drives the transition to superfluidity?

2.2.3 Superfluidity in 2D

The Mermin-Wagner-Hohenberg theorem explicitly precludes spontaneous symmetry breaking in 2D. Formally, this means that the first-order correlation function must vanish at large enough distances unlike in 3D systems where it asymptotically approaches a finite value. Therefore, the Penrose-Onsager-Yang criterion for superfluidity can never be satisfied in 2D. However, this does not prohibit the possibility of superfluidity altogether. Here, we will follow the treatment presented in the review by Z. Hadzibabic and J. Dalibard [52], and demonstrate that superfluidity exists in 2D at finite temperature while satisfying the Mermin-Wagner theorem.

Let us consider a homogeneous 2D gas of bosons confined in an area A and

interacting via a repulsive contact potential.

$$V(\mathbf{r}_1 - \mathbf{r}_2) = \frac{\hbar^2}{m} g \delta^2(\mathbf{r}_1 - \mathbf{r}_2), \quad (2.34)$$

where g is a coupling constant. There are some fundamental aspects of interactions in 2D - for instance the existence of a two-body bound state - which makes the problem quite complicated. For now, let us assume g is small enough that we can operate in the *classical* limit where the bound state can be ignored².

At $T = 0$, a 2D gas is completely condensed and can be described as a classical field $\Psi_0 = \sqrt{\langle n \rangle} e^{i\phi(r)}$. At any finite temperature, there exist excitations in the system which, in this simple case, may occur either due to fluctuations of the density n or the phase ϕ . In 2D repulsive gases, density fluctuations are strongly suppressed at low temperatures and therefore the main contribution to the kinetic energy comes only from the fluctuations in the phase. The Hamiltonian can then be described as

$$H = \frac{\hbar^2}{2m} \int [n_s (\nabla \phi)^2]. \quad (2.35)$$

The first term incorporates the phase fluctuations in the system and also encodes the information of transport properties. In particular, the superfluid velocity is defined by $v_s = |\nabla \phi(r)|$.

To determine the existence of superfluidity, we must investigate the behavior of $g_1(r)$ at large distances which depends on the occupation of phonon modes with small momenta. For a homogeneous system at finite temperature the phonon occupation can be obtained by using the equipartition theorem and has the form:

$$n_s A \frac{\hbar^2 k^2}{2m} \langle |c_k|^2 \rangle = \frac{k_B T}{2}. \quad (2.36)$$

Here, c_k are the complex Fourier coefficients of the phase: $\phi(\mathbf{r}) = \int c_{\mathbf{k}} e^{i\mathbf{k}\cdot\mathbf{r}} d^2k$. Therefore the coefficients have the form

$$\langle |c_{\mathbf{k}}|^2 \rangle = \frac{\pi}{D_s A} \frac{1}{k^2}, \quad (2.37)$$

²We will see that in the last part of the thesis that this assumption in fact breaks down in the regime of strong interactions.

2.2. The role of dimensionality

where $D_s = n_s \lambda_T^2$ is the superfluid phase space density. From this, we can compute the first-order correlation function $g_1(r) = \langle \Psi^*(\mathbf{r}) \Psi(0) \rangle = n_s \langle \exp[i(\phi(\mathbf{r}) - \phi(0))] \rangle$. For an independent gaussian variable u , $\langle e^{iu} \rangle = e^{-\langle u^2 \rangle / 2}$ and therefore we obtain the function

$$g_1(r) = n_s \exp \left(-\frac{1}{2\pi D_s} \int \frac{1 - \cos(\mathbf{k} \cdot \mathbf{r})}{k^2} d^2 k \right). \quad (2.38)$$

Since we are only interested in the small momentum/large distance limit, the numerator $1 - \cos(\mathbf{k} \cdot \mathbf{r}) \sim 1$ and hence the integral simplifies to $\int dk/k$ resulting in the logarithmic expression:

$$g_1(r) = n_s \exp \left(-\frac{1}{D_s} \ln \frac{r}{\xi} \right), \quad (2.39)$$

where ξ is the healing length which serves as a short-range cutoff for the integration. Therefore, we obtain the final form of the first-order correlation function:

$$g_1(r) = n_s \left(\frac{\xi}{r} \right)^{1/D_s}. \quad (2.40)$$

The correlation function therefore decays algebraically at large distances, which is often referred to as quasi-long-range order! The first crucial implication is that since $g_1(\infty) = 0$, the Mermin-Wagner theorem is satisfied. The rate of decay of $g_1(r)$ depends inversely on the superfluid phase space density and can be arbitrarily small. In other words, the power law decay can be made "slow" enough such that at any finite distance $r \gg \lambda_T$, the system has finite phase correlations. This implies that at low enough temperatures, the system exhibits *some* global stiffness to external perturbations and hence this can be regarded as a superfluid.

2.2.4 The Berezinskii–Kosterlitz–Thouless phase transition

The analysis presented above elucidates the existence of superfluidity at low temperatures. At high enough temperatures, we approach the classical regime of a Boltzmann gas, where the correlations decay exponentially with a short decay constant set by thermal fluctuations, i.e. $g_1(r) \sim e^{-r/\lambda_T}$. Therefore, there must be a transition point where the form of the correlations shift from an exponential to a power-law decay. What is the mechanism that drives this transition?

This question was answered by Berezinskii [7, 8], Kosterlitz and Thouless [9, 10] in 1973. The key problem they considered is that of a phase transition that does

not require spontaneous symmetry breaking as it is forbidden in 2D. The transition must still be driven by phase fluctuations as the density fluctuations are suppressed. However, the low-energy phonons have a monotonous dependence on temperature and do not show non-analytic behavior that would be required for an abrupt transition. Instead BKT theory proposed that the transition is a topological one that involves vortex excitations.

A vortex is a topological object wherein the phase winds in multiples of 2π around a singular point known as the vortex core. The phase can be described as

$$\phi_v(r) = \pm \ell \theta, \quad (2.41)$$

where $\pm \ell$ is the winding number of the vortex. At the core, the superfluid density must vanish so that the kinetic energy $n_s v_s^2 = n_s (\nabla \phi)^2$ is non-divergent. The size of the vortex core is determined by the healing length ξ . Then, a vortex carries a quantum of angular momentum with the velocity field around the vortex core varying as $v_s(r) = \hbar \nabla \theta / m = \hbar \ell / m r$. The presence of a vortex disturbs the local phase by inducing a circulation and several free vortices can have the effect of destroying long-range correlations in a superfluid. The main property of vortices relevant for 2D superfluidity is their intrinsic topological character: they cannot be unwound using continuous deformations of the field. In 2D, they can annihilate by combining with a vortex of opposite charge. Since a pair has no net angular momentum, it no longer has a significant effect on the phase $\phi(r)$ at large distances $R \gg \xi$ and hence quasi-long-range correlations can persist. This was precisely the mechanism proposed by BKT theory.

They demonstrated that the transition to superfluidity was intimately linked to the binding of vortices (of opposite charge) at a critical temperature. As the formation of bound pairs affects the topology of the system, this phenomenon is also classified as a topological phase transition. To find out the conditions for such a transition, we note that the kinetic energy cost of a free vortex can be written as:

$$E = \int_{\xi}^R \frac{1}{2} n_s (\nabla \phi)^2 d^2 r = \int_{\xi}^R \frac{1}{2} n_s \left(\frac{\hbar^2}{m r} \right)^2 d^2 r = \frac{\hbar^2 \pi}{m} n_s \ln(R/\xi), \quad (2.42)$$

where R is the radial distance from the vortex core. The entropy of a single vortex is the number of possibilities to place the vortex in a disc of radius R , which is

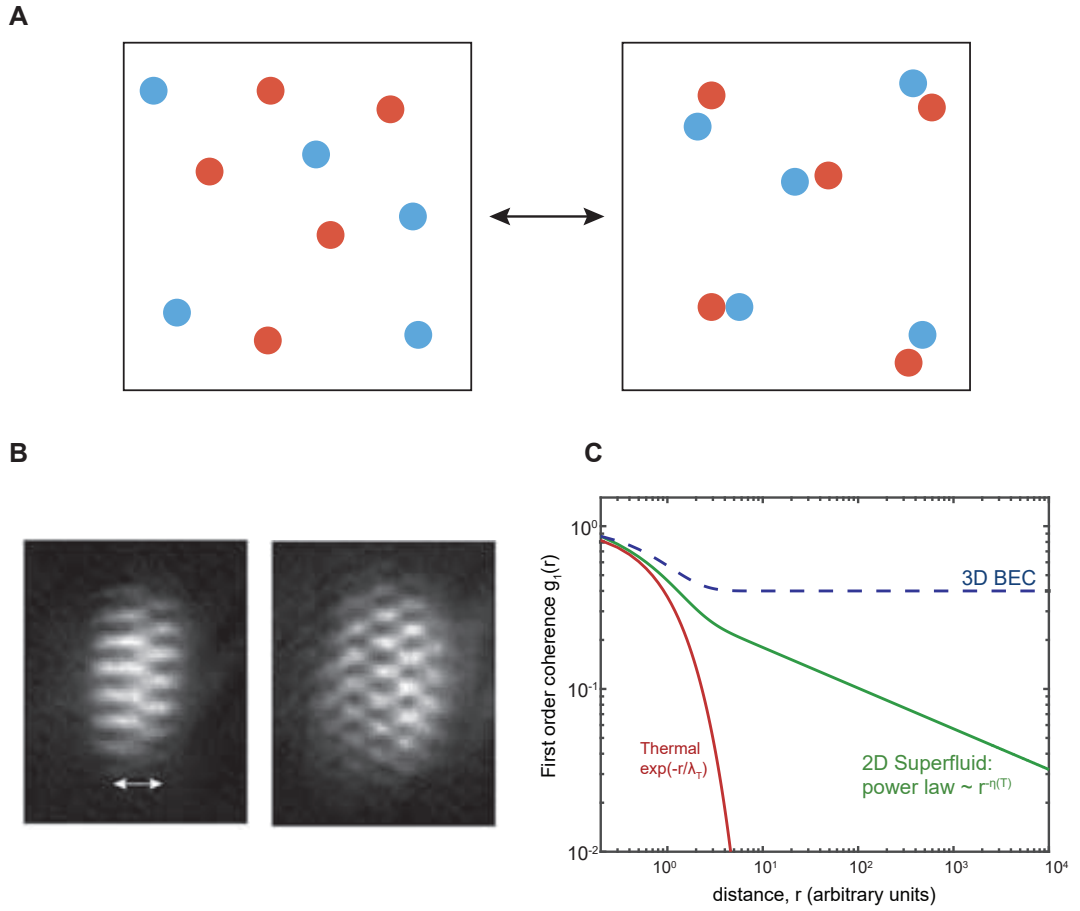


Figure 2.9: **Berezinskii–Kosterlitz–Thouless transition.** **A:** Illustration of the BKT mechanism. The blue and red circles represent topological vortices with opposite charge. At high temperatures, the vortices proliferate freely which prevents phase order. At a critical temperature (and below), the opposite charge vortices pair up and cancel each other. Then their effect on the phase at large differences is negligible and hence superfluidity can occur. **B** The observation of vortex proliferation by interfering two independent 2D Bose gases. Figure adapted with permission from [53]. **C** The predicted first-order correlation function $g_1(r)$ in a 2D gas. In contrast to 3D, $g_1(r)$ of a 2D gas decays algebraically at large distances. The transition can then be seen in the change in behavior from exponential to algebraic decay. The power-law exponent η depends on temperature and has a universal value $\eta(T_c) = 1/4$ at the critical point.

$S = 2k_B \ln(R/\xi)$. The free energy $F = E - TS$ is therefore

$$\frac{F}{k_B T} = \frac{1}{2}(n_s \lambda_T^2 - 4) \ln\left(\frac{R}{\xi}\right). \quad (2.43)$$

This equation shows that the free energy has a zero crossing at $D_s = 4$. In the thermodynamic limit $R \gg \xi$, $\ln(R/\xi)$ takes a large value and therefore the free energy is suddenly large and negative for $D_s > 4$. This means that the system become unstable against the proliferation of vortices at the point $D_s = 4$. Therefore, the logarithmic diverging terms results in a sudden universal jump in the superfluid phase space density from 0 to 4. Hence, the condition for the transition to superfluidity can be simply written as:

$$n_s \lambda_T^2 = 4. \quad (2.44)$$

Since the exponent of the power-law decay $g_1(r) \sim r^{-\eta}$ is inversely proportional to the superfluid phase space density, the critical exponent at the transition is give by:

$$\textbf{Critical Exponent: } \eta(T_c) = 1/(n_s \lambda_T^2)_c = 1/4. \quad (2.45)$$

The above results are universal in the sense that they apply to any 2D system with short range interactions. The universal jump in superfluid density was confirmed in experiments on thin Helium films by Bishop and Reppy in 1978 [13]. Furthermore, the transition was observed more recently in 2D Bose gases. In this work, we present the first observation of algebraic correlations in a fermionic system (see Chapter 6.5.6 and [54]).

The BKT transition and the corresponding superfluid phase at $T < T_c$ have some special features. First, it is worthwhile noting that the correlation function decays algebraically and is therefore "scale-free" at any temperature below T_c . This is in contrast to second-order phase transitions that are typical in 3D systems where such behavior, also known as divergence of correlation length, occurs only in a small temperature window around T_c known as the critical region. In some sense, the 2D superfluid is always critical. In addition, this transition is sometimes termed an infinite order transition. In second order phase transitions, the second derivative of thermodynamic quantities shows a discontinuity at T_c . This is not the case in 2D: the thermodynamic properties are continuous in any order of differentiation and hence the term infinite order.

2.3 Fermions in 2D

So far we discussed the phenomenology of ordering, particularly superfluidity, in two dimensions. In the analysis presented in the preceding section, we considered the case of a weakly interacting bosonic gas in 2D which provides a conceptual basis for superfluidity in lower dimensions. What we are actually interested in is the many-body physics of a strongly interacting 2D gas of Fermions.

To dive deeper into this topics, it is helpful to consider the basic aspects of quantum mechanical scattering. Earlier, the assumption of weak interactions allowed us to make a classical approximation. It turns out that at the quantum mechanical level, the scattering in 2D is fundamentally different compared to 3D. In fact most of the results presented in this thesis are closely connected to these effects and hence it is useful to describe them in some detail.

2.3.1 The bound state in 2D

Let us consider the scattering of two fermions via a short-range potential $V_{\text{int}}(\mathbf{r}_1 - \mathbf{r}_2)$, which is described by the Schrödinger equation

$$\left[\frac{\hbar^2}{2m_r} \nabla^2 + V_{\text{int}}(\mathbf{r}) \right] \Psi(\mathbf{r}) = E \Psi(\mathbf{r}), \quad (2.46)$$

where $\mathbf{r} = \mathbf{r}_1 - \mathbf{r}_2$ represents the relative coordinates between the particles and $m_r = m_1 m_2 / (m_1 + m_2) = m/2$ is their effective mass. We assume that the potential depends only on $r \equiv |\mathbf{r}|$ such that the Schrödinger equation is separable into radial and azimuthal components: $\Psi(\mathbf{r}) = \chi(r)P(\theta)$. The radial wavefunction has the form:

$$-\frac{\hbar^2}{2m_r} \left[\frac{1}{r} \frac{d}{dr} \left(r \frac{d}{dr} \right) + \frac{\ell(\ell+1)}{r^2} \right] \chi + V(r)\chi = E\chi. \quad (2.47)$$

The asymptotic form of the wavefunction can be described in terms of an incoming plane wave and an outgoing spherical wave:

$$\Psi(\mathbf{r}) \xrightarrow{r \rightarrow \infty} e^{ik_0 z} + \frac{e^{i\mathbf{k} \cdot \mathbf{r}}}{r} f(\mathbf{k}, \theta), \quad (2.48)$$

where k_0 and k are the respective wavenumbers, and $f(\mathbf{k}, \theta)$ is the scattering amplitude. At low energies, the centrifugal barrier prevents higher angular momenta

from playing a role and the scattering amplitude is dominated by the cylindrically symmetric s-wave term ($l = 0$).

$$f(k) = \frac{-4}{\cot \delta_0(k) - i}, \quad (2.49)$$

where $\delta_0(k)$ is the scattering phase shift between the incoming and outgoing waves. The scattering properties in 2D are quite subtle. For instance, the solution of Eq. (2.46) for short-range potentials contains divergent terms at large momenta, which results in an unphysical situation of diverging interaction energy. To overcome this problem, a hard cutoff must be introduced at some large momentum [55]. This procedure is known as *regularization* of the Hamiltonian. The new cutoff scale naturally corresponds to an equivalent length and energy scale. In fact, the scattering phase shift in 2D takes the form:

$$\cot \delta_0(k) = -\frac{2}{\pi} \ln(ka_{2D}), \quad (2.50)$$

where a_{2D} is the effective 2D scattering length that results from the regularization procedure. The crucial point here is that, since the cutoff momentum is always positive, so is a_{2D} . In other words, for arbitrarily small values of the interaction strength between fermions, the 2D system always supports a two-body bound state with energy

$$E_B = \frac{\hbar^2}{2ma_{2D}^2}. \quad (2.51)$$

2.3.2 Scale invariance

Here it is worth making some remarks on the scale invariance of 2D systems. Scale invariance is usually an emergent property which is usually observed in systems close to critical transitions. The basic premise of scale-invariance is that a rescaling of parameters, such as coordinates, temperature etc, does not change the fundamental properties of systems. Mathematically, this translates to a function $f(x)$ remaining unchanged under a scaling transformation, i.e $f(\lambda x) = \lambda^d f(x)$, where λ is a real scaling factor.

In the 2D system we just considered, the Hamiltonian in Eq. (2.46) is obviously scale invariant in the absence of a scattering potential. Introducing a general short-range

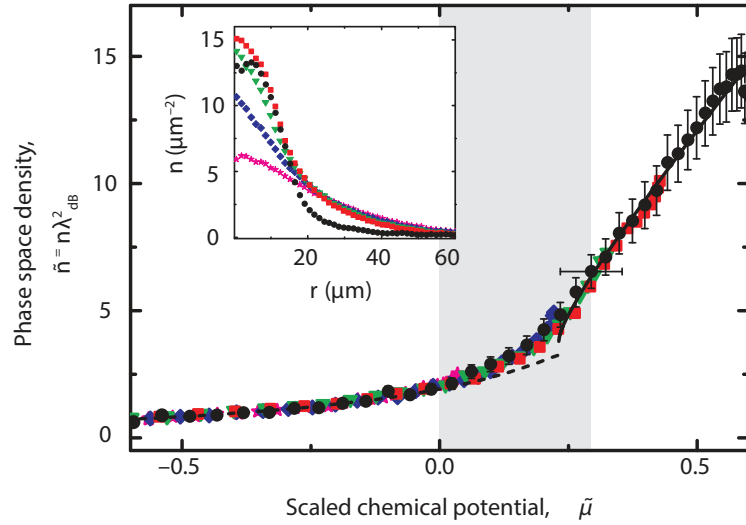


Figure 2.10: **Scale invariance in a 2D Bose gas.** In a weakly interacting 2D gas, the 2D scattering length does not play a significant role and the interactions are only defined in terms of a dimensionless parameter \tilde{g} . In this scenario, the gas is said to be scale-invariant. One of the consequences of scale-invariance is that the thermodynamic equations of state at different temperatures and interaction strengths can be scaled on to each other. This was observed in 2D Bose gas experiment shown above. Figure adapted with permission from [56]

scattering potential breaks this scale invariance due to the existence of a two-body bound state. However, the case of a contact interactions ($V = g\delta^2(\mathbf{r} - \mathbf{r}')$) presents an interesting and subtle situation. The δ^2 -potential is intrinsically scale-invariant at the classical level as a transformation $\mathbf{r} \rightarrow \lambda\mathbf{r}$ scales the interaction energy in the same way as the kinetic energy. However, at the quantum mechanical level, there exists the bound state which breaks this scaling relation. Such a violation of a scaling symmetry which exists in a classical system but is broken by quantum fluctuations is known as a quantum anomaly.

The δ^2 -potential is immediately relevant to cold atomic systems. This is because in the low-energy scattering regime where the de Broglie wavelength of particles dominates over the effective range of the Van der Waals interaction potential, the potential can be regarded as a δ -potential to a very good approximation. The

existence of the two-body bound state in cold fermionic systems is beyond debate and has been confirmed in several experiments. The question is how does the bound state affect the many-body properties of the system. In which regime is the concept of scale-invariance relevant and where is it violated.

For instance, in Section 2.2.4, we approximated a weakly interacting Bose gas as being described by a dimensionless coupling parameter \tilde{g} . In doing so, we implicitly ignored the contribution of the ground state. It turns out that in the weakly interacting limit, this is a reasonable approximation. In fact, experiments on the thermodynamic properties of the 2D Bose gases confirm that these systems are essentially scale-invariant. One particularly important quantity which reveals scale-invariance is the equation of state. In [56], it was shown that the equations of state for various different parameters such as temperature, chemical potential and interaction strength can be simply rescaled on top of each other (see Fig. 2.10).

However, when we increase the interaction strength between particles away from the perturbative regime, we can no longer make the approximation. Here, the bound state may play an enhanced role in determining the state of the many-body system. The fundamental question for us is, how does the bound state influence the macroscopic properties such as the thermodynamic equation of state, the collective modes and even the quasi-long-range coherence which characterizes the 2D superfluid.

2.3.3 The 2D BEC-BCS crossover

To explore these questions, it is instructive to revisit the BEC-BCS crossover. Similar to the 3D case, we can characterize different interaction regimes in the many-body system by comparing the inherent Fermi energy E_F to the binding energy E_B which results in a dimensionless interaction parameter $\ln(E_F/E_B)/2 = \ln(k_F a_{2D})$. When $E_F \gg E_B$ or when $\ln(k_F a_{2D}) \gg 1$, we are in the weakly attractive BCS regime. On the other hand, $E_F \ll E_B$ ($\ln(k_F a_{2D}) \ll -1$) corresponds to the strongly attractive (but weak repulsive between pairs) BEC regime. In between these limits, we have the strongly correlated crossover regime $\ln(k_F a_{2D}) \sim 0$, where the binding energy and Fermi energy are of the same order of magnitude. Several fundamental questions arise in this scenario.

First, how does pairing occur in this regime? Indeed, due to the smooth crossover between the BEC and BCS limits, even the pairing at finite temperatures should

smoothly evolve from Cooper pairing at T_c to two-body dimer formation at $T \gg T_c$. Several proposals have been put forth that suggest the existence of a "pre-formed" pairing region known as a pseudogap, which is driven by a suppression of density of states at the Fermi surface already at temperatures above T_c . The existence of a pseudogap is one of the most debated and outstanding problems in the physics of strongly interacting fermions. Shedding light on the nature of pairing in the normal phase may be crucial to understanding unconventional superfluidity.

Second, what determines the critical temperature? In this regime, the condition for superfluidity is not directly related to the formation of Cooper pairs if the pairing gap already opens at $T > T_c$. Then the critical temperature is determined by the superfluid stiffness rather than pair breaking. However, the mechanism for the critical transition is not understood.

Third, what are the collective excitations in the system. Of course, the simple bosonic or fermionic quasiparticles discussed in preceding sections are not sufficient to capture the collective excitations in this regime. A more involved description is needed.

Ultracold Fermi gases in reduced dimensions

3

The experimental realization of Bose–Einstein condensation and degenerate Fermi gases has ushered a new era to explore the physics of quantum many-body systems. With these systems, it is possible to selectively study the essential aspects of complex systems, particularly the interplay of particle statistics, interactions and dimensionality, without undesirable effects of impurities. In the initial years, the research was focused on studying the exotic properties of BECs such as vortex states and long-range coherence. However the recent decade has seen explosive growth in the application of ultracold gases to a wide variety of problems. Some notable examples include optical lattice systems, strongly interacting Fermi gases, matterwave interferometry with cold atoms, lower-dimensional systems, spin-orbit coupled systems, non-equilibrium phenomena etc.

The central features that make quantum gases so versatile are (i) **Tunability**. Cold atomic systems are among the most tunable experimental systems currently. We can tune various fundamentally relevant parameters: Quantum statistics (use either fermionic or bosonic atomic species or a mixture of both), interactions, external confining potentials using optical dipole traps and thermodynamic parameters (particle number, temperature and chemical potential). ii. **Observability**. Quantum gases are stable and have long lifetimes which allow reliable measurement of different observables. In addition, several observables are directly accessible in these systems such as local density distributions and momentum distributions, spin populations etc. This has enabled several key innovations and breakthroughs in the field.

In this work, we are primarily interested in the preparation and study of two-dimensional Fermi gases with strong interactions. We perform all our experiments with a gas of fermionic ${}^6\text{Li}$ atoms. Therefore, I will discuss some of the concepts and tools used to create such systems, with particular focus on the experimental

apparatus used in this thesis.

3.0.1 Creating a cold atomic gas

To study the physics described above, we need to create extremely cold samples which are in the degenerate regime where the fermionic nature of atoms plays a dominant role. This requires achieving large phase space densities $n\lambda_T^2 > 1$. We also need to create samples with long enough lifetimes which enable reliable measurements. Therefore all cold atom experiments are performed in an ultrahigh vacuum chamber with typical pressures of 10^{-11} mbar.

In our experiment, ${}^6\text{Li}$ atoms are evaporated in an oven ($T \sim 620$ K) and collimated through a narrow aperture. The atoms in this beam have an average velocity of approximately 1500 ms^{-1} and need to be slowed down by several orders of magnitude. This is done by a series of dissipative laser cooling schemes which include a Zeeman slower and a magneto-optical trap both of which employ resonant light beams to slow down the atoms. These steps bring the temperatures down to about $400 \mu\text{K}$ with typical phase-space densities of about 10^{-6} . Therefore much more cooling is needed. However, the lowest temperatures from the laser cooling techniques are limited by the photon recoil energy.

3.0.2 Optical dipole traps

To prepare a degenerate Fermi gas and perform any sort of measurement on the atoms, it is first necessary to confine them in a finite volume. This is typically achieved using magnetic and optical potentials. To create magnetic traps, an external magnetic field $B(x)$ is used, acting on the magnetic dipole moment of atoms to create a restoring potential $V = \mu B(x)$. By suitably aligning B-field coils, a potential minimum is created at some point in space.

In a similar manner, optical dipole traps rely on the electric dipole moment induced on an atom due to the oscillating electric field of a light beam. The interactions of neutral atoms with an electromagnetic field can be either dissipative or conservative. For laser cooling, the absorption and spontaneous emission of resonant photons leads to an effective dissipative force. However, for large detunings of the light frequency with respect to resonance, spontaneous emission becomes negligible and only the energy shift due to the induced electric dipole moment remains relevant. This energy

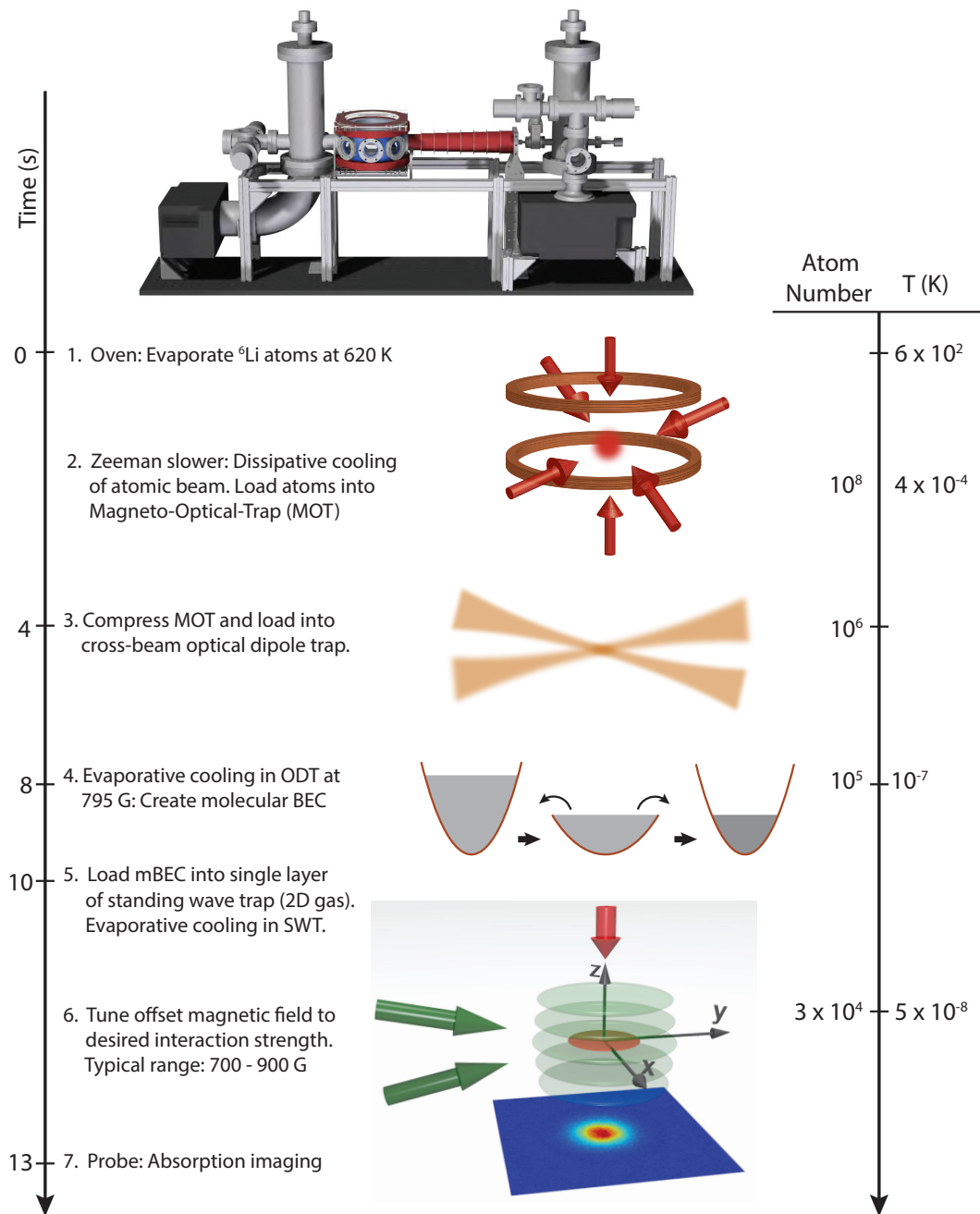


Figure 3.1: Preparing an ultracold 2D Fermi gas

shift can be used to create tailor-made trapping conservative potentials for atoms. The dipole potential experienced by an atom in an electric field \mathbf{E} depends on its polarizability $\alpha(\omega)$ and can be written as:

$$V_{\text{dip}}(\mathbf{r}) = -\frac{\text{Re}(\alpha(\omega))}{2\epsilon_0 c} \langle |E|^2 \rangle \sim \frac{3\pi c^2}{2\omega_0^3} \left(\frac{\Gamma}{\omega_0 - \omega} + \frac{\Gamma}{\omega_0 + \omega} \right) I(\mathbf{r}). \quad (3.1)$$

Here, Γ is the damping rate determined by the line width of the spontaneous transition, ω_0 the resonance frequency and $I(r)$ the spatial intensity distribution. The key point is that for large detunings, it is possible to create optical potentials that depend linearly on the local intensity of the light beam. In addition, by choosing red or blue detuning, it is possible to obtain confining or anti-confining potentials. In our experiments, since ${}^6\text{Li}$ atoms are resonant at 671 nm, we use a far red detuned laser beam with wavelength 1064 nm to create the optical dipole potentials.

It is clear from Eq. 3.1, that arbitrary potentials can be created by shaping the light field spatially. The simplest and most commonly used potential is created using a Gaussian laser beam $I(r) \propto e^{-r^2/2\sigma^2}$. Close to the center, the trap can be approximated as a harmonic potential using the parabolic approximation. In addition, by suitably shaping the laser beams, several different types of potentials can be engineered which include optical lattices, homogeneous box traps, annular traps etc.

In our experiments, we transfer the atoms from the Magneto-Optical-Trap (MOT) to an optical dipole trap (ODT) which is formed by two orthogonally polarized gaussian beams that intersect at a small angle. The high power of the laser (200 W) results in cigar-shaped trap a large trap depth of approximately 1.5 mK in the intersecting region of the focused beams.

To cool down to degeneracy, we employ the evaporative cooling scheme. This consists of lowering the trapping potential to the point that the atoms in the higher energy (and entropy) levels are ejected and in the process carry out a significant amount of thermal energy. The remaining atoms are allowed to interact with each other which leads to a new thermalized distribution with a much lower temperature. Indeed, the evaporative cooling procedure leads to a reduction in the atom number, but still a big gain in phase-space density. At the end of the evaporation, we finally reach degeneracy with temperatures of the order of 100 nK, which is approximately

10% of the Fermi temperature T_F .

3.0.3 Entering the 2D regime in a 3D world

To explore 2D physics, we need to reach a regime where the kinematics along one direction (z -axis) is essentially frozen out. For cold atoms, this can be achieved by ensuring a much stronger confinement in the axial direction compared to the radial $x - y$ directions. Therefore we need a strongly anisotropic trapping potential, where $\omega_{x,y} \ll \omega_z$. We create this optical potential by interfering two elliptically shaped far detuned (1064 nm) laser beams at a shallow angle of approximately 14° . Due to the small angle, this results in an interference pattern with fringe spacing of about $4 \mu\text{m}$.

By compressing the molecular BEC in the ODT, we load about 5×10^4 atoms in a single interference fringe, which is confirmed by means of a tomographic scheme. The final trapping frequencies in the new potential are $\omega_r \approx 21 \text{ Hz}$ in the radial plane and $\omega_z \approx 7 \text{ kHz}$ in the axial direction. This gives us a sufficiently large aspect ratio of the sample of approximately $\omega_z : \omega_r \sim 300$. The large ratio by itself is not sufficient to attain 2D kinematics. We need to ensure that excitations in the axial direction are negligible. For a non-interacting gas at $T = 0$, the critical number of particles we can add before axially higher states start becoming populated is set by the aspect ratio: $N_{\text{crit}} = \omega_z^2 / 2\omega_r^2 \approx 5 \times 10^4$. Intuitively, this happens when $E_F \sim \hbar\omega_z$. In our system, we keep the particle number well below this critical value and in addition the thermodynamic energy scales such as chemical potential μ and temperature $k_B T$ are kept smaller than $\hbar\omega_z$. Hence, the kinematics of the system is predominantly in the radial plane and axial excitations can be neglected.

3.0.4 Tuning interactions using Feshbach resonances

One of the most crucial tools in cold atom physics is the ability to tune the effective interactions between atoms. To understand how this works, we recall the previous discussion on scattering between fermions in Sec. 2.3.1. We can describe two particle scattering in terms of an incoming plane wave and outgoing spherical wave. The scattering amplitude and the associated scattering length (in 3D) a_s is directly related to the phase shift between these two waves δ_0 . When $0 < \delta_0 < \pi/2$, we obtain a negative scattering length $a_s < 0$; for $\delta_0 > \pi/2$, the scattering length is positive and finally when $\delta_0 \sim \pi/2$, the scattering length diverges. Is it possible to tune

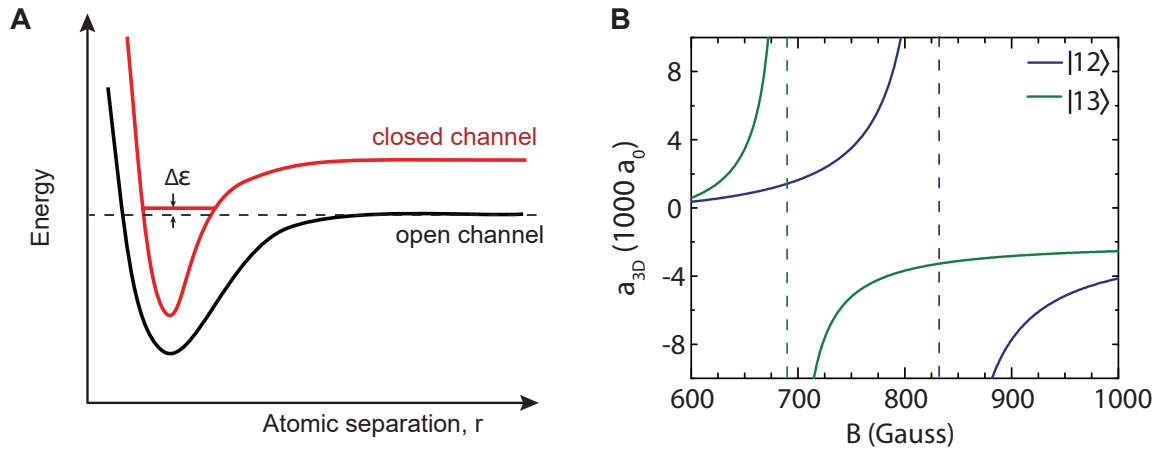


Figure 3.2: **Feshbach resonance.** **A:** The scattering of atoms occurs due to an interatomic interaction potential. Two particles enter in a particular spin configuration, known as an open channel (black). There exists a configuration, known as a closed channel (red), that supports a bound state. If the energy of the incoming particles is close to the closed channel, a resonant coupling to the bound state results. In ultracold atomic systems, the energy difference $\Delta\varepsilon$, and hence the scattering length, can be tuned using an external magnetic field. **B** s-wave scattering length as a function of magnetic field for two different hyperfine spin mixtures $|12\rangle$ (blue) and $|13\rangle$ (green). The Feshbach resonance positions are $|12\rangle$: 832.2 G, and $|13\rangle$: 690 G.

the scattering length in an experimental system? This brings us to the concept of Feshbach resonances.

Cold atoms interact with each other via a Van-der-Waals potential whose shape is determined by natural atomic properties. Consider two atoms scattering via this potential in some spin configuration. In principle there may exist other higher lying states for the particles to scatter into. However, if their initial energy is too low, the coupling to any higher states is negligible and consequently they leave in the same channel they arrived in. The energetically allowed states are known as open channels whereas the forbidden ones are known as closed channels.

For cold ${}^6\text{Li}$ atoms for instance, the open and closed channels correspond to different spin configurations - singlet and triplet - which intrinsically have different magnetic

moments. Hence the two channels are energetically separated in the presence of an external magnetic field by an amount $\delta E = \delta\mu B$. Now, simply by tuning the external magnetic field the energy difference can be tuned. When the energy difference between the incoming particles and the bound state of the closed channel becomes small enough, the free atoms in the open channel can couple to the bound state leading to a resonant enhancement of the scattering length! In other words, the scattering length can be tuned using an external magnetic field. The dependence on B has the form:

$$a_{3D}(B) = a_{\text{bg}} \left(1 - \frac{\Delta}{B - B_0} \right), \quad (3.2)$$

where a_{bg} is the background scattering length, B_0 is the Feshbach resonance field and Δ is the width of the resonance.

Since ${}^6\text{Li}$ is fermionic, we need two spin states to obtain an interacting system. We perform our experiments with a mixture of atoms in two of the three lowest hyperfine states labeled by $|1\rangle$, $|2\rangle$ and $|3\rangle$. The Feshbach resonances depend on the choice of the mixture: $|12\rangle : B_0 = 832.2 \text{ G}$, $|13\rangle : 690 \text{ G}$, which is illustrated in Fig. 3.2. In 3D, the regime $B < B_0$ supports the formation of two-body dimers. In our experiments, we can create any of the three mixtures by starting with the lowest two hyperfine states $|12\rangle$ and subsequently transferring atoms in one state to another using Landau-Zeener sweeps.

The strongly interacting regime

In the 3D scenario, the scattering amplitude between fermions has the form:

$$f(k) = \frac{1}{-\frac{1}{a_{3D}} + \frac{k^2}{2} r_{\text{eff}} - ik}, \quad (3.3)$$

where a_{3D} is the scattering length. Here, an interesting situation occurs. At the Feshbach resonance, the a_{3D} diverges. Therefore, the scattering amplitude no longer contains a lengthscale and only depends on momentum. In the low-energy approximation $r_{\text{eff}} \ll 1/k$, this simplifies to :

$$f(k) = \begin{cases} -a_{3D}, & \text{for } k|a_{3D}| \ll 1 \text{ (weakly interacting regime)} \\ \frac{i}{k}, & \text{for } k|a_{3D}| \gg 1 \text{ (strongly interacting regime)}. \end{cases} \quad (3.4)$$

In the weakly interacting regime, the scattering amplitude is only determined by the scattering length. This occurs for small values of a_{3D} , on both sides of the Feshbach resonance (see Fig. 3.2). The interactions in the many-body system are characterized by a dimensionless parameter $1/k_F a_{3D}$. For small positive values of $1/k_F a_{3D}$, we obtain a gas of dimers with binding energy $E_{B, 3D} = \hbar/m a_{3D}^2$, which is referred to as the BEC regime. The system is effectively a weakly repulsive Bose gas with the scattering length between molecules being $a_{3D, \text{mol}} = 0.6 a_{3D}$. For small negative values of $1/k_F a_{3D}$, we obtain a weakly attractive Fermi gas which does not have an underlying bound state. In between these two regions exists the unitary regime, where $1/k_F a_{3D} \rightarrow \infty$ in the vicinity of the Feshbach resonance. Here, the scattering amplitude is described only by the momenta of particles. Since the scattering lengthscale is removed from the problem, this system is effectively scale-invariant.

Scattering in a trapped quasi-2D system

In Sec. 2.3.1, we introduced the concept of the 2D scattering length and two-body bound state for a purely 2D system, where third dimension is assumed to be absent. Of course, this is an unrealistic situation. In the experiment, the axial dimension always plays a role and we only work in the approximate 2D regime. The effective dimensionality is reduced by means of a tight confinement in the z -direction and intuitively, the quasi-2D regime is reached when the z -confinement is much stronger than all other energy scales in the system. The question then is, what are the scattering properties in the quasi-2D system and how can it be mapped to the theoretical 2D case.

First, we must keep in mind that the axial confinement length scale in experiments is always larger than the effective range of the Van der Waals potential which is of the order of a few nanometers. Therefore, at short distances between fermions, the problem is always three-dimensional. To obtain the exact scattering wavefunction, we have to solve the two-body Schrödinger equation in the full trapping potential and the Van der Waals interaction potential in three-dimensional space. However, in the limit of low-energy scattering [57, 58], the problem is simpler and the scattering amplitude $f(k)$ can be written in terms of the axial confinement length $\ell_z = \sqrt{\hbar/m\omega_z}$

and the 3D scattering length a_{3D} according to:

$$f(k) = \frac{4\pi}{\sqrt{2\pi}\ell_z/a_{3D} - 2\ln(ka_{2D}) + i\pi}, \quad (3.5)$$

where a_{2D} is the effective 2D scattering length in the quasi-2D system give by

$$a_{2D} = \ell_z \sqrt{\frac{\pi}{B}} \exp\left(-\sqrt{\frac{\pi}{2}} \frac{\ell_z}{a_{3D}}\right). \quad (3.6)$$

Here, $B = 0.905$ is a constant [58]. This has some interesting consequences. First, we note that a_{2D} is always positive and finite, therefore we always have a finite binding energy between fermions. Second, even when at the 3D unitary point where a_{3D} diverges, the a_{2D} is still finite. In the limit of strong attraction, i.e. when $a_{3D} \ll \ell_z$, the fermions form very deeply bound dimers, with $E_B \gg \hbar\omega_z$. In this regime, the pairs are essential three-dimensional and are no longer influenced by the axial confinement. More importantly, the relevant interactions at the many-body level are the ones between pairs. Therefore, even though the pairs are three-dimensional, the scattering between pairs is still in the 2D regime and is described by the dimensionless bosonic coupling parameter:

$$\tilde{g} = \sqrt{8\pi} \frac{\ell_z}{a_{3D, \text{mol}}}, \quad (3.7)$$

where $a_{3D, \text{mol}} = 0.6.a_{3D}$ is the 3D scattering length between dimers [59, 60]. From this, we can see how the strong attraction limit between fermions in fact connects smoothly to the weakly repulsion regime between bosonic pairs, where the coupling is energy-independent. Therefore, we can easily relate our experiments with the 2D Fermi gas with the 2D Bose gas experiments in the weakly interacting regime. In fact, when the interactions of the gas are described by this dimensionless coupling parameter, the interaction energy then has the form

$$E_{\text{int}} = \frac{\hbar^2}{2m} \tilde{g} \int n^2(\mathbf{r}) d^2r. \quad (3.8)$$

In this situation, the system becomes completely scale invariant since rescaling the coordinates rescales the interaction energy in the same way as the kinetic energy. As we increase the interaction strength (decrease ℓ_z/a_{3D}), the momentum dependence of the scattering amplitude becomes appreciable and the interactions are no longer only

described by \tilde{g} . In other words, the bound state starts to play a role and this can potentially lead to the violation of scale-invariance in the Fermi gas. We observed such a violation in two different experiments, as I will discuss later in the thesis.

It is important to note that from Eq. 3.6, we obtain the effective scattering length in the system. From this, we cannot directly derive the two-body bound state between fermions. The binding energy \tilde{E}_B in the quasi-2D system is determined from the equation:

$$\frac{\ell_z}{a_{3D}} = \int_0^\infty \frac{du}{\sqrt{4\pi u^3}} \left(1 - \frac{e^{-\tilde{E}_B u / \hbar \omega_z}}{\sqrt{(1 - e^{-2u})/2u}} \right). \quad (3.9)$$

The corresponding scattering length from this description, $\tilde{E}_B = \hbar^2 / m \tilde{a}_{2D}^2$ can also be used to quantify the interactions only in the regime where $\tilde{a}_{2D} \gg \ell_z$, i.e. where the internal structure of dimers is two-dimensional.

Interaction regimes

The interactions in the many-body system are characterized by a dimensionless parameter $\ln(k_F a_{2D})$, which represents the competition between the two-body binding energy and the Fermi energy. The BEC-BCS crossover can then be explored by tuning (a) the Fermi momentum $k_F = \sqrt{4\pi n}$, which is a function of density or (b) the 2D scattering length which is a function of the 3D scattering length and hence the magnetic field. Due to the logarithmic dependence of the interaction strength on these parameters, we need to be able to tune either of them by orders of magnitude in order to explore a wide enough region of the BEC-BCS crossover. Tuning the density by orders of magnitude is unfeasible but tuning the scattering length is easily achieved near the Feshbach resonance. Therefore, in our experiments, the density is typically of the order of $1 - 2 \text{ atoms}/\mu\text{m}^2$ and the magnetic field is tuned from 690 G which corresponds to the deeply bound dimer regime (BEC) to 900 G which corresponds to the weakly attractive BCS regime. The parameter $\ln(k_F a_{2D})$ varies from -7 far on the BEC side to $+3$ on the BCS side.

How do the interactions in our system relate to other 2D systems? The logarithmic dependence of the scattering phase shift on the momentum and scattering length is a direct consequence of the strong confinement, and has a significant influence on interaction regimes. In weakly repulsive Bose gas experiments, the typical densities are approximately $10 \mu\text{m}^{-2}$ and the 2D scattering lengths are of the order of

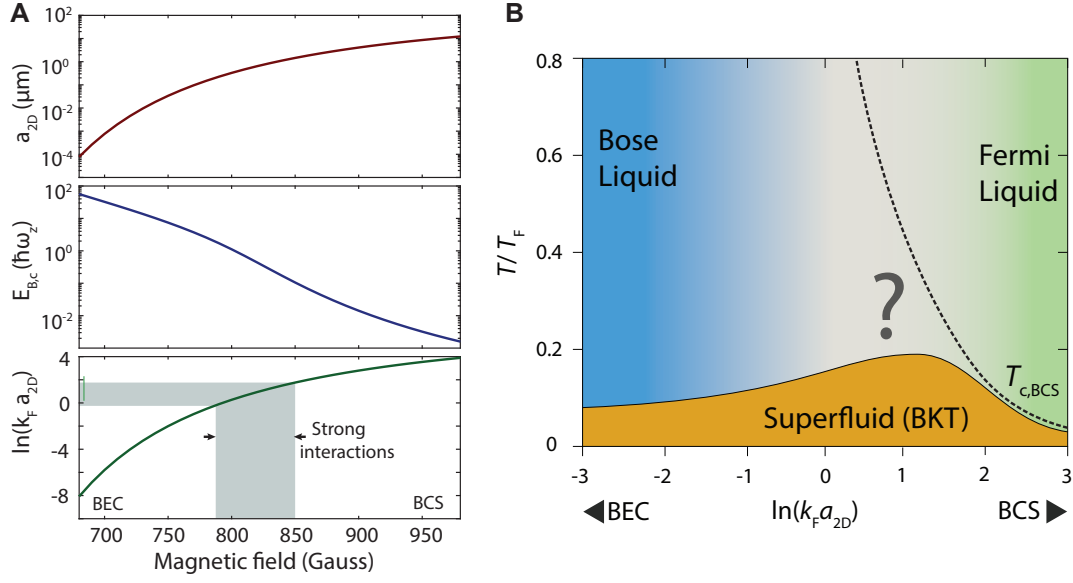


Figure 3.3: **Experimentally exploring the 2D BEC-BCS crossover.** **A:** The dependence of the 2D scattering length a_{2D} (top panel), confinement-induced bound state energy E_B^c (middle panel), and the dimensionless interaction parameter $\ln(k_F a_{2D})$ (bottom panel) as a function of the magnetic field. The parameters have been calculated for our experimental parameters: $\ell_z = 0.55 \mu\text{m}$, $k_F = 3.9 \mu\text{m}^{-1}$. The scattering length and the binding energy vary by several orders of magnitude as we span the region near the Feshbach resonance (832 G). The strongly interacting regime corresponds to $-0.5 \lesssim \ln(k_F a_{2D}) \lesssim 2$ where the 2D scattering length is the same order of magnitude as the interparticle spacing. **B:** A schematic phase diagram that illustrates the different interaction regimes and expected phases.

$10^{-29} \mu\text{m}^{-1}$, which leads to the bosonic coupling parameter having values of $\tilde{g} \sim 0.1$ and crossover parameter $\ln(k_F a_{2D}) \sim -22$ [61]. In the other limit, a conventional 2D superconductor has pair sizes that are approximately a 10^3 times the interparticle spacing leading to $\ln(k_F a_{2D}) \sim 13$. However, several unconventional materials, such as graphene [41] and Iron pnictides [62] lie in the intermediate regime where $a_{2D} \sim 1/k_F$.

3.0.5 Probing the many-body system

Preparing the sample in just one part of the process. The next question is, how do we probe various observables of the system? One of the most essential tools of cold atom experiments is the ability to detect the spatial distribution of atoms. In the past decade, several key innovations have been made in this direction. Among the notable examples is the Quantum gas microscope which allows to measure the occupation number of every site of an optical lattice with almost single-atom resolution. In our group, a method to measure the position of atoms also in free space has been demonstrated. This will be crucial for future steps towards quantum gas assemblers which are discussed in the outlook.

Absorption imaging

For our experiments on 2D Fermi gases, we utilize a standard technique known as absorption imaging to measure the density distribution of atoms in space. This is done by shining a resonant laser beam on the atomic cloud, part of which is absorbed by the atoms. The transmitted intensity distribution ($I_t(\mathbf{r})$) is imaged on a camera. The final density distribution is extracted by comparing this image with a reference intensity ($I_0(\mathbf{r})$) without any atoms. Since the atoms lie in a plane, we directly obtain the two-dimensional density distribution given by:

$$n_{2D}(\mathbf{r})\sigma_0^* = -\ln \frac{I_t(\mathbf{r})}{I_0(\mathbf{r})} + \frac{I_0(\mathbf{r}) - I_t(\mathbf{r})}{I_{\text{sat}}^*}. \quad (3.10)$$

Here, σ_0^* is the absorption cross-section of the atoms and I_{sat}^* is the effective saturation intensity of the atoms. In our experiments, the spatial density distribution is the main observable and all the other quantities that characterize the system such as temperature, particle number and momentum distribution are extracted from density images. An interesting possibility, as I will show in Chapter 10, is that even the phase fluctuations of the superfluid can be mapped to the spatial density.

3.0.6 The 2D Fermi gas

Finally, we successfully prepare the sample, which will be our experimental playground for the rest of the thesis. We can tune various properties of the sample such as

inter-particle interactions, number of particles and the temperature of the gas. In addition, we can image the density distribution using absorption imaging. Typically, we work with 20 - 40 thousand atoms in each spin state. Since the atoms are trapped in a harmonic potential, they have a spatially inhomogeneous distribution with an approximately gaussian shape.

Here, I provide a brief recap of the various energy and length scales involved in the experiment which can serve as a reference for subsequent chapters.

Energy scales	Hz	nK
Axial confinement ($\hbar\omega_z$)	7×10^3	370
Radial confinement ($\hbar\omega_r$)	22	1
Lowest temperatures	10^3	50
Typical Fermi temperature	10^4	470

Length scales	μm
Thomas–Fermi radius	~ 60
Axial width	~ 0.5
Typical inter-particle distance	$\sim 0.5 - 1$
Imaging resolution	~ 5

Synopsis of the thesis

4

In this chapter, I will provide a contextual introduction to the experiments and concepts reported in this thesis.

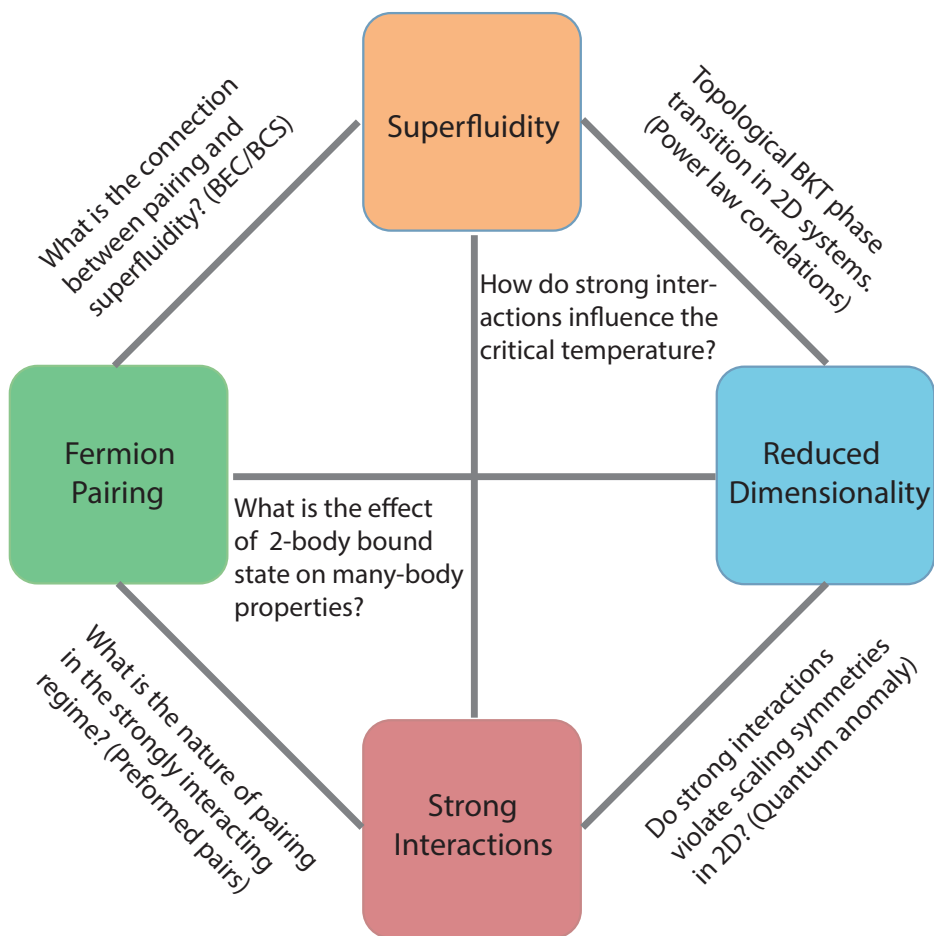


Figure 4.1: Themes explored in this thesis

4.1 Measuring the momentum distribution of a 2D Fermi gas

To start with, we are interested in exploring superfluidity in the strongly interacting regime. In the previous sections, we discussed the BKT phase transition that occurs due to phase fluctuations in the system. Importantly, the transition is characterized by a change in the decay of the first-order correlation function from exponential to power law decay. How do we observe these signatures?

A superfluid can be described as a classical field $\Psi(\mathbf{r}) = \sqrt{n(\mathbf{r})}e^{i\phi(\mathbf{r})}$. An important issue is that the phase information is lost when we measure the in-situ density distribution $n(r) = |\Psi^*(r)\Psi(r)|$. To investigate the phase distribution, we require some sort of interferometric method.

A conceptually simple way is to interfere two identical samples and analyze the resulting pattern. In fact, this method was used to observe the BKT transition in a 2D Bose gas in the group of Jean Dalibard [53]. However, preparing two identical samples is a technically challenging task. In addition, for strongly interacting systems, the interference procedure may not be straightforward as the interactions may distort the fringe patterns, which complicates the interpretation of experiments.

Another method to investigate is the so-called time-of-flight method which consists of switching off the trapping potential and allowing the cloud to evolve ballistically in free space for some duration of time t_{TOF} . This leads to different regions of the system interfering with each other and thus mapping some phase information on the density. Our initial attempts focused on measuring the density after a short t_{TOF} , following the proposals of [63]. Coherent phase domains in the initial sample are expected to lead to density clustering, which we were able to observe qualitatively at low temperatures. However, obtaining quantitative information from this method, particularly about the transition, proved to be elusive.

Following along similar lines, we developed a method to access the far-field distribution. When the system propagates in free-space for a long duration of time, the different momentum components separate spatially. The field in the far-field limit corresponds to a Fourier transform of the initial field. However the exact mapping (between momentum and position) occurs only at infinite time and moreover in typical experiments, interactions between atoms during the expansion can distort

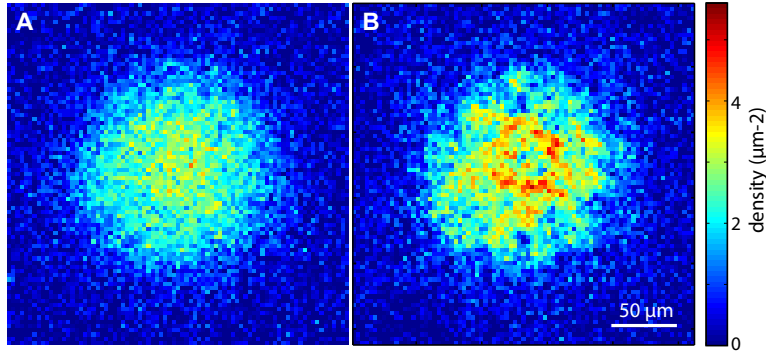


Figure 4.2: **Short time-of-flight imaging** Shown are two images at different temperatures $T_A > T_B$, taken after 4 ms time-of-flight. Here, the initial phase fluctuations become qualitatively visible in the density fluctuations. This leads to randomly distributed clusters in the density distributions. The characteristic size of the density clusters is larger at smaller temperatures (i.e in B), indicating longer wavelength phase fluctuations. However, it is very difficult to obtain quantitative information from this method.

the position-momentum mapping.

We demonstrated a novel method that consists of employing a harmonic potential to act as a matterwave lens [64]. The evolution of the gas in the harmonic potential for a quarter period ($T/4$) brings the far field to the 'focal' plane similar to a gradient index lens in optics. Using this method, we were able to measure for the first time, the momentum distribution of a strongly interacting Fermi gas. The publication in Chapter 2. describes the method and the various operations that can be performed with it.

4.2 The phase diagram of the 2D BEC-BCS crossover

With this $T/4$ -method technique in our toolbox, we set about exploring the state of the system in the strongly interacting regime. In particular, we were interested in mapping out the phase diagram which is defined by two parameters: (i) the 2D interaction strength $\ln(k_F a_{2D})$ and (ii) the ratio of absolute temperature to the Fermi temperature T/T_F .

To investigate the phase diagram, we measured the density distribution of the gas both in momentum and position space. In chapter 3., I discuss the procedure and

4.2. The phase diagram of the 2D BEC-BCS crossover

results in detail. Here, I show some of the qualitative features across the BEC-BCS crossover. As mentioned earlier, the information of the phase fluctuations is lost in the in-situ density profiles. However, the density profiles still contain crucial information of the thermodynamic properties of the system. The evolution of density across the crossover regime is shown in Fig. 4.3 A. On the BEC side $\ln(k_F a_{2D}) < 1$, we observe a smaller cloud with high density whereas the density distribution broadens on the BCS side. The size of the cloud is directly connected to the pressure of the gas which in turn is sensitive to the quantum statistical properties of the system. Therefore, the density profile already shows the evolution from bosonic to fermionic behavior.

As a function of temperature, we observe a smooth trend of increasing density for decreasing temperature. However, we do not observe any qualitative signature of phase transition in these density profiles. This is to be expected because the BKT transition in 2D is after all an infinite order transition, which means that no derivative of the thermodynamic observables exhibits a discontinuity at T_c . Our observation of a smooth evolution of the density profile as a function of temperature is consistent with this argument.

In momentum space, however, the situation seems very different. We observe the rapid apparition of a sharp peak in the low momentum region as the temperature is reduced below some critical value. In fact for the same range of temperatures, the peak density in the in-situ profile ($n(r=0)$) increases only by 10% whereas the momentum space peak density ($n(k=0)$) exhibits an enhancement by almost an order of magnitude. This sharp rise in the zero-momentum density is consistent with a phase transition. Furthermore, this qualitative observation proves that the main signatures of the transition are in the complex phase and not the density. We also observe a clear dependence of the peak momentum density on the interaction strength, which is consistent with the expectation that the pairing gap and critical temperatures on the BCS side drop exponentially with the attraction between fermions.

In the in-situ distribution, it is useful to apply a local density approximation (LDA), wherein even though the overall density varies spatially across the cloud, at short length scales, the density is approximately homogeneous. This of course only works when the size of the cloud is much larger than the confinement length of the trap. For instance, in our experiments, the Thomas-Fermi diameter of the cloud is approximately $100 \mu\text{m}$, whereas the radial confinement length is $\ell_r = \sqrt{\hbar/m\omega_r} \approx$

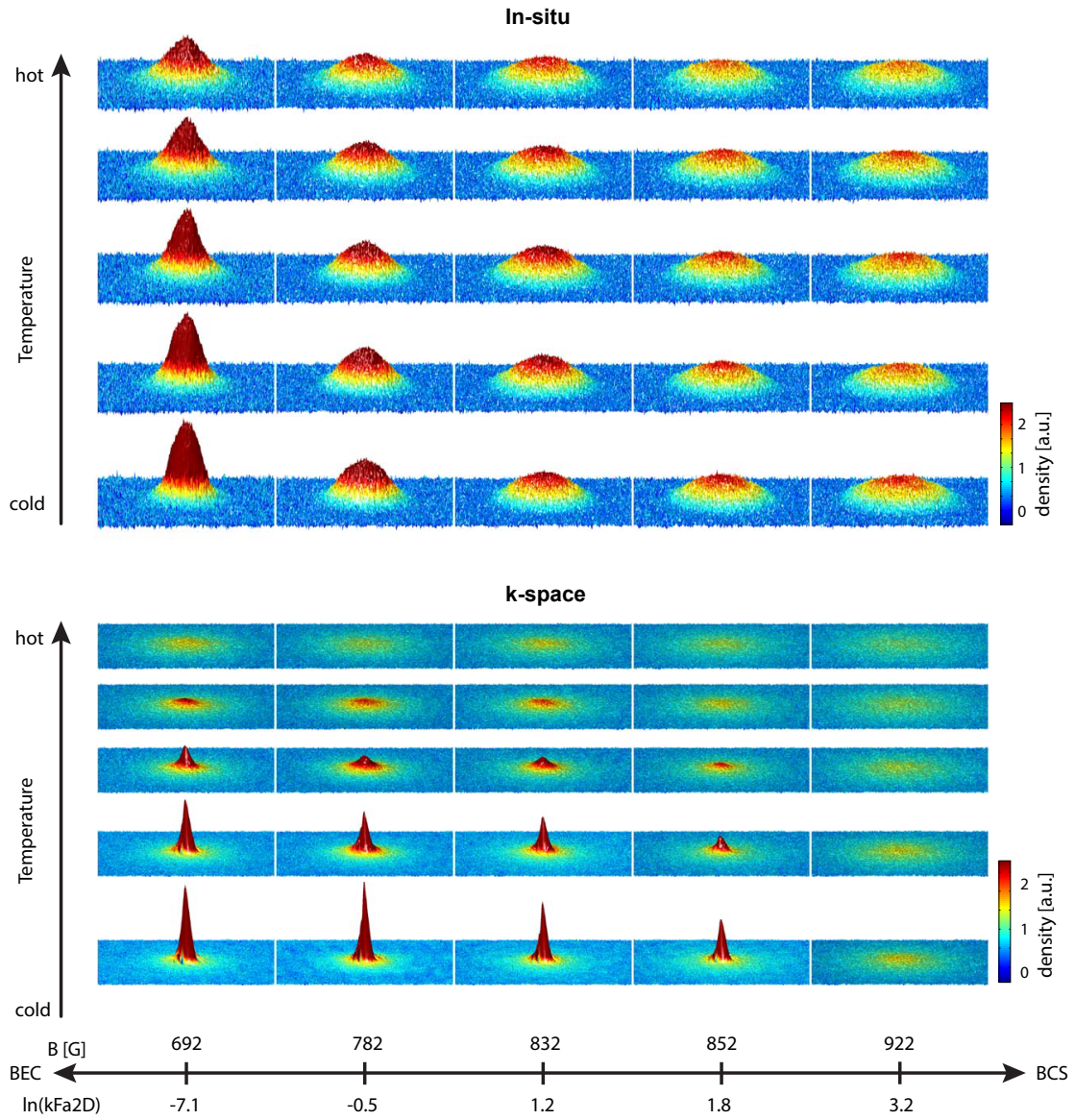


Figure 4.3: The density distributions in position and momentum space.

8 μm . Therefore, we can apply LDA for regions smaller than ℓ_r . In this picture, the inhomogeneous sample can be viewed as a collection of numerous homogeneous systems with their own thermodynamical parameters such as Fermi Energy E_F - and consequently the Fermi temperature T_F and momentum k_F - and chemical potential μ .

From the momentum space distribution, we can extract two quantities: (a) the density of particles at zero momentum which characterizes spatial coherence and signals superfluidity, and (b) the absolute temperature of the gas by fitting a Boltzmann distribution $n(p) = \exp(-p^2/2mk_B T)$ to the high momentum region. Using these observables, we were able to map out, for the first time, the phase diagram of the 2D BEC-BCS crossover. On the BEC side, our results were in good agreement with the expected critical temperature for a 2D Bose gas [65]. In addition, we observed an enhancement of the critical temperature in the strongly correlated regime, which demonstrates the role of strong interactions in determining the critical properties of systems. In our recent experiments, described in Chapter 6, we have uncovered one possible mechanism for the enhanced T_c .

4.3 BKT Superfluidity in a 2D Fermi gas

The measurement of the phase diagram provides insights into the general behavior of the 2D Fermi gas and also allows to extract the critical temperature as function of interaction strengths. However, the nature of the superfluid, particularly the phase correlations, is still an open question.

Previously, the BKT superfluid transition has been studied in bosonic systems, such as superfluid ^4He thin films and 2D ultracold Bose gases. In the latter case, the bosons interact weakly with each other. One question is, whether the BKT predictions hold in the strongly interacting fermionic regime. And if so, how does the existence of the bound state between fermions enter this description? Another question arises regarding the inhomogeneity of the system. The predictions of BKT theory are valid only for homogeneous systems. What happens to phase fluctuations in harmonically trapped systems where the density is necessarily inhomogeneous?

To answer these questions, we again utilized the momentum distribution across the crossover. The quantity of interest is the spectrum of long-wavelength phase fluctuations, or equivalently the decay of the phase correlations. The first-order cor-

relation function $g_1(r)$, which characterizes spatial coherence in many-body systems is directly obtained from the momentum distribution through a Fourier transform.

$$g_1(\mathbf{r}) = \int n(\mathbf{k}) e^{i\mathbf{k}\mathbf{r}} d^2k. \quad (4.1)$$

Studying the BKT transition with a 2D Fermi gas has the key advantage that we can tune the interactions all the way from weakly repulsive (between pairs) to weakly attractive (between fermions) passing through the strongly correlated regime. This allows to quantitatively compare our results on the BEC side to the experiments and computations of 2D Bose gases, which serves as a useful reference for understanding the strongly interacting regime.

In Chapter 4, I describe the measurement and analysis of $g_1(r)$ of a 2D Fermi gas for various interaction strengths across the BEC-BCS crossover. An important aspect of this work was the comparison of our measurements to Quantum Monte Carlo computations performed by Markus Holzmann for a 2D Bose gas. It is quite remarkable that an experiment and computation showed very good agreement in a non-trivial observable such as the correlation function. Importantly, we were able to confirm that the transition observed in the system is consistent with the BKT mechanism. A surprising finding was the observation of algebraic decay of correlations in a trapped inhomogeneous system. In addition, we showed that the decay of correlations in the system can be described by a single power-law exponent which has a critical value that is independent of microscopic interactions. This showed for the first time that measured transitions across the crossover are all in the same universality class.

4.4 Fermion pairing in the normal phase

One of the outstanding problems in many-body physics is to find a description of the normal phase of strongly interacting fermionic systems. In fact, several systems which exhibit unconventional superfluidity have a strongly correlated normal phase which deviates from the Fermi liquid description. Understanding the mechanism of pairing is thought to provide a route to describing high- T_c superconductivity. It has been theoretically predicted that the normal phase supports pairing between fermions which is accompanied by a suppression of the density of states at the Fermi

surface, similar to Cooper pairing. However, unlike BCS pairing (below T_c) which exhibits a complete gap at E_F , the gap in this case is only partial, in the sense that the density of states does not completely vanish but is only suppressed (see Fig. 4.3 A). Hence it is often referred to as a pseudogap. Does this peculiar pairing effect exist in the BEC-BCS crossover?

In the context of degenerate Fermi gases, the description of the normal phase has been extensively debated both theoretically and experimentally. There exist various theoretical predictions for the many-body state above T_c . Experimentally, spectroscopic studies both in 3D [66, 67] and 2D [68] reported the observation of pseudogap behavior.

Here, it is worth discussing the measurements reported in Feld et. al [68]. Using momentum-resolved spectroscopy (similar to ARPES in solid-state physics), the spectral response of a 2D Fermi gas was investigated. The spectral function exhibited a two-branch feature that is expected from pair formation. These signatures were interpreted as a signature of pseudogap pairing. However, due to the time-of-flight used to reach momentum space, the measured functions are averaged over the whole inhomogeneous sample as well as over several layers. While the existence of pairs is clear from the data, the nature of pairs, specifically whether they are trivial dimers or pairs driven by many-body effects (as expected for a pseudogap) remains difficult to discern. In addition, subsequent theory works have shown that the interaction regime explored in Feld et. al [68] falls in the BEC regime where only two-body pairing is relevant [69]. For these reasons, the interpretation of the experiments in [68] have been disputed in subsequent theoretical works [69, 70], and therefore the question of pairing in the normal phase has remained unanswered.

To probe fermion pairing in our 2D Fermi gas, we employed radio-frequency spectroscopy which has been the workhorse spectroscopic technique in the field of cold atoms for several years. The simple idea behind RF spectroscopy is to use the transitions between hyperfine states to reveal the effects of pairing and interactions in the system. We usually perform our experiments with a mixture of atoms in two hyperfine states, say $|1\rangle|2\rangle$. Using a RF pulse, we can transfer atoms from $|2\rangle$ to an unoccupied state $|3\rangle$. For free (non-interacting) atoms, the transition occurs at the well-defined transition energy which is known for a given offset magnetic field. However, when the atoms interact with their surroundings, or when they are paired

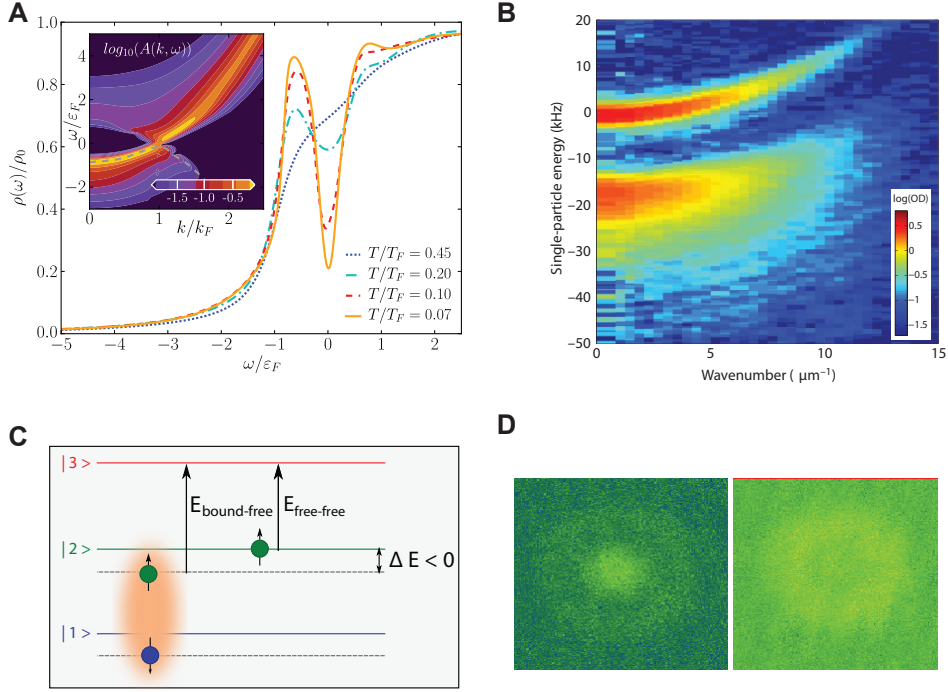


Figure 4.4: Normal phase of a strongly interacting 2D Fermi gas. **A:** The calculated density of states for different temperatures in a strongly interacting Fermi gas ($\ln(k_F a_{2D}) = 0.8$) [71]. The inset corresponds to the single particle spectral function. The apparition of a gap in the density of states is known as a pseudogap. **B:** Experimental measurement of the spectral function in [68] using Angle-resolved radio-frequency spectroscopy. The two branches indicate the presence of pairing. However, the measurement averages over the entire sample which makes it impossible to discern the nature of pairs, i.e. whether they are trivial two-body molecules or many-body pairs. **C:** The scheme of radio-frequency spectroscopy. An atom in hyperfine state $|2\rangle$ is transferred to an unoccupied state $|3\rangle$ using an RF pulse. If the atom is paired with another atom, the energy levels are shifted, which can be spectroscopically measured. **D:** First images from the RF spectroscopy experiment. The two images correspond to different RF frequencies. The appearance of a ring structure at different radii suggests a density-dependent effect. Panels A and B are adapted with permission from the respective publications.

to another fermion their overall energy is shifted. These shifts can be obtained by measuring the response of the system as a function of the frequency of the RF pulse.

Typically, we measure the integrated response of the whole system, i.e. the total fraction of atoms transferred to the third state. However, while performing our experiments, we noticed an interesting feature. For a given frequency, the depletion of atoms occurred at a well-defined radius (or density)! For a different frequency, the radius was different. This meant that the effect we were probing had a dependence on the local density. Therefore, we could use the inhomogeneity of the sample as a feature which allows to study the response for various densities in a single cloud. By Applying the Local Density Approximation (LDA), we were able to study the onset and nature of pairing for various temperatures and interaction strengths.

In Chapter 5, I describe the RF spectroscopy measurements in the normal phase. We performed our measurements in a wider range of interaction strengths than in previous works as well as at lower temperatures. We realized that the dependence of pairing energy on local density is a leading order effect which necessitates the use of a density resolved spectroscopic method. Our experiments revealed a surprising pairing effect in the strongly interacting regime, in particular a crossover from two-body to many-body pairing. In addition, we observed that the density-dependent pairing correlations persist up to remarkably high temperatures. These findings also provide important clues to the behavior of the system in the superfluid phase as will become clear in the next chapter.

4.5 Breaking of scale invariance in the dynamics of a 2D superfluid

Reducing the dimensionality has important consequences for the behavior of many-body systems. In previous sections, we already discussed some examples such as algebraically decaying phase correlations, pseudogap phase at high temperatures etc. Here, we will discuss another crucial effect of scale-invariance violation that arises from the peculiarity of scattering in two dimensions.

Scale-invariance is a fundamental concept in several fields such as high energy physics, cosmology and condensed matter physics. The central idea is that under special circumstances, the properties of the system become invariant under a trans-

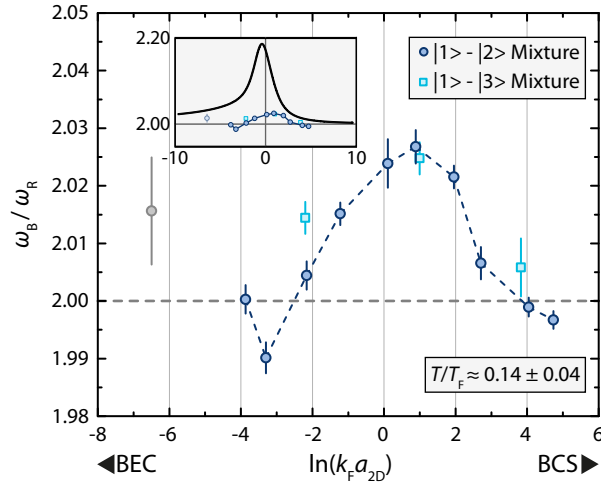


Figure 4.5: **Breathing mode of a 2D Fermi gas.** Our recent measurements of the breathing mode frequency reveal an anomalous shift in the strongly interacting region, which is a signature of the breaking of $SO(2,1)$ symmetry of the harmonically trapped system. Intriguingly, the frequency shifts are almost an order of magnitude smaller than the theoretical expectation [73].

formation of scale. A prominent example of this is a second order transition [72], wherein the correlation length of a system diverges at the critical point and hence the correlation functions exhibit a power law decay with no scale.

In this context, 2D systems are particularly interesting. On the one hand, 2D superfluids exhibit long-range algebraic - and hence scale free - decay of correlations at any temperature below T_c as discussed earlier. On the other hand, scale-invariance is violated at the microscopic level due to the existence of a two-body bound state, as already discussed in Section. 2.3.1. The important question is, how does this quantum anomaly - which is essentially a two-body effect at small scales - manifest in the many-body properties of the system. For example, it would be very interesting to investigate whether transport and critical properties are influenced by this anomaly. If so, this would have broader implications in understanding strongly correlated 2D systems beyond the field of ultracold atoms.

In our group, we addressed the problem of the quantum anomaly in two experimental works. In the first one, we measured how the spectrum of the many-body system is affected by interactions in the BEC-BCS crossover [73]. In harmonically

trapped 2D systems, Pitaevskii and Rosch [74] show the existence of an additional $SO(2, 1)$ scaling symmetry which results the many-body spectrum having equally spaced energy levels. Specifically, this leads to the monopole (or breathing) mode frequency to be fixed to the twice the radial trap frequency. In principle, interactions violate this symmetry and cause a deviation in the breathing mode frequencies $\omega_B \neq 2\omega_r$, which is one manifestation of the quantum anomaly [75, 76, 77]. Previous experiments in the group of M. Köhl had not observed any corrections, which had been attributed to thermal fluctuations [78].

The theory expectation is that, in the strongly interacting regime of a 2D Fermi gas, the thermodynamic equation of state is significantly modified by short-range contact parameter [79, 80, 76, 77], given by

$$I = \langle \psi_{\uparrow}^{\dagger}(\mathbf{r})\psi_{\downarrow}^{\dagger}(\mathbf{r})\psi_{\uparrow}(\mathbf{r})\psi_{\downarrow}(\mathbf{r}) \rangle, \quad (4.2)$$

where ψ_{\uparrow} is the single fermion wavefunction in the spin state \uparrow . Intuitively, the contact is the probability to find two opposite spin fermions close to each other. It is known to play a fundamental role in determining the thermodynamic properties of the system through the universal Tan relations [81, 82]. In the scale-invariant scenario, the pressure of the gas (P) is equal to the internal energy E . However, in the presence of interactions, we get corrections due to the contact parameter of the form:

$$P = E + \frac{I}{4\pi m}. \quad (4.3)$$

This breaks the scaling relation and consequently also modifies the spectrum. For the equation of state of the gas, the effect of the quantum anomaly is represented through a polytropic equation

$$P = n^{2+2\gamma}, \quad (4.4)$$

where γ is known as the polytropic exponent. The value of this exponent across the BEC-BCS crossover has been predicted by QMC calculations of a 2D Fermi gas at $T = 0$ [79], and confirmed with the measurement of thermodynamic equation of state [83, 84, 85]. From these works, we expect the breathing mode frequency to be shifted by maximum value of approximately 10% relative to $2\omega_r$.

We performed the breathing mode frequency measurements at lower temperatures,

with higher accuracy and better control of experimental parameters than previous works. Indeed, we observed, for the first time, an upward shift of the breathing mode frequencies in the strongly interacting regime of the crossover. However, the maximum measured value of the shift relative to the scale-invariant frequency was found to be approximately 1.3 %, which is several times smaller than the theoretical prediction of 10 %. This comes as quite a surprise since the measurement is not only in contradiction with theory but also with experimental works in equilibrium. This means that the non-equilibrium behavior of the system is qualitatively different from the equilibrium one.

The breathing mode frequency shifts are a result of a modification of the thermodynamic equation of state due to interactions. An important question is, how is the BKT physics affected by these strong fermionic correlations that break scale invariance. In Chapter 9, I describe a different set of experiments, where we explored this question by studying the dynamics of a strongly interacting 2D superfluid in the BEC-BCS crossover. This work has an interesting background to it. In May 2017, we set about wanting to measure the dynamical properties of the 2D system in the strongly interacting regime. Simply out of curiosity, we measured the evolution of a driven superfluid both in-situ and in momentum space (i.e. after $T/4$). Almost immediately, we observed interesting features in the dynamics. We found that the momentum-space distribution exhibited a frequency doubling effect compared to the in-situ distribution. In addition, the zero-momentum density evolved in an anomalous manner in the strongly-interacting region. Initially, we interpreted these observations in terms of turbulent cascades, however this turned out to be not the case. Soon after, Nicolás Defenu and Tilman Enss came up with the idea that the observed effects had a deep connection to fermionic correlations. In particular, the momentum-space dynamics were a direct but unexpected manifestation of the violation of the quantum anomaly.

As we investigated this possibility in detail, we uncovered several surprises along the way. We found that whereas the quantum anomaly has a minute effect on the breathing mode frequency, it has a dramatic influence on the spatial coherence properties, in particular the algebraic decay of correlations. In Chapter 6, we provide a detailed explanation of the measurement and results.

4.6. How to take a snapshot of the superfluid order parameter?

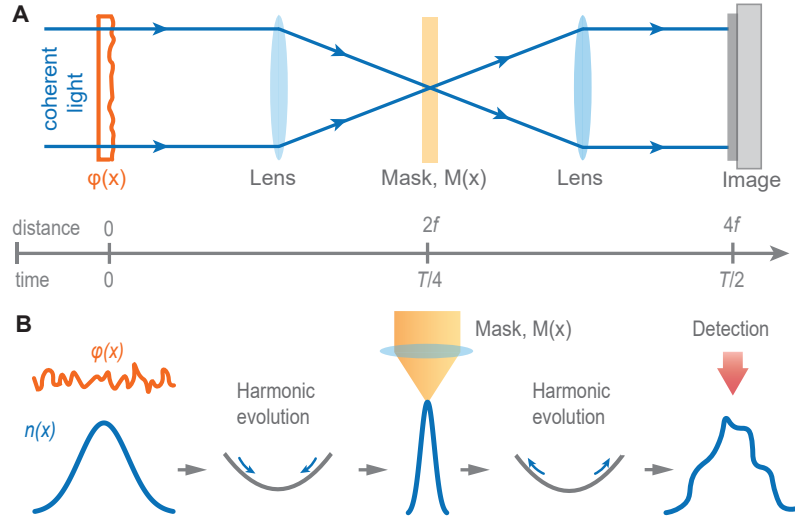


Figure 4.6: **Imaging the superfluid order parameter.** We propose a method which is closely analogous to $4f$ -imaging in optics. By evolving in the harmonic trap for a half period, we return to the position space configuration. The key point is that, specific operations performed in momentum space $T/4$ can reveal important information on the properties of the superfluid, such as superfluid density, complex phase, superfluid velocity and vorticity.

4.6 How to take a snapshot of the superfluid order parameter?

In the works described so far, we employed the $T/4$ technique to measure the momentum distribution and reveal properties of phase fluctuations in the system. The momentum distribution, however, is a trap-averaged quantity which only reveals the statistical properties of the fluctuations. We can ask a curious question: can we take a snapshot of the order parameter of the superfluid?

In Chapter 7, we propose a method which allows to directly image the complex phase, superfluid density and velocity using specific manipulations of the field in momentum-space. Our proposal is inspired by the $4f$ -imaging method in optics of which there are several variants such as Zernike phase contrast imaging, dark-field imaging and schlieren imaging [86]. Here, we applied these methods to the field of a superfluid.

Measuring the momentum distribution of a 2D Fermi gas

5

Publication

PHYSICAL REVIEW A **90**, 043611 (2014)

Matter-wave Fourier optics with a strongly interacting two-dimensional Fermi gas

P. A. Murthy, D. Kedar, T. Lompe, M. Neidig, M. G. Ries, A. N. Wenz, G. Zürn, and S. Jochim

Physikalisches Institut, Ruprecht-Karls-Universität, 69120 Heidelberg, Germany

Abstract

We demonstrate and characterize an experimental technique to directly image the momentum distribution of a strongly interacting two-dimensional quantum gas with high momentum resolution. We apply the principles of Fourier optics to investigate three main operations on the expanding gas: focusing, collimation and magnification. We focus the gas in the radial plane using a harmonic confining potential and thus gain access to the momentum distribution. We pulse a different harmonic potential to stop the rapid axial expansion which allows us to image the momentum distribution with high resolution. Additionally, we propose a method to magnify the mapped momentum distribution to access interesting momentum scales. All these techniques can be applied to a wide range of experiments and in particular to study many-body phases of quantum gases.

DOI: [10.1103/PhysRevA.90.043611](https://doi.org/10.1103/PhysRevA.90.043611)

5.1 Introduction

In a many-body quantum system, the distributions of particles in position and momentum space contain complementary information on the state of the system. In many cases, the change in the characteristic properties of the system at a phase transition is more pronounced in momentum space. Prominent examples for this are Bose-Einstein Condensation [87, 88], the Berezinskii-Kosterlitz-Thouless (BKT) transition [53] and the Superfluid to Mott-Insulator transition [89]. Therefore, it is desirable to not only observe the in situ density distribution of the system but also to access the momentum distribution.

In ultracold quantum gas experiments, this can often be achieved by performing conventional time-of-flight (TOF) imaging, i.e. switching off all trapping potentials and letting the gas expand for a certain time t before imaging [90]. In this process, the particles expand according to their initial momentum and thus the momentum distribution can be obtained from the density distribution after the time-of-flight. There are however several limitations to this technique. First, a direct mapping from momentum to position coordinates is only possible in the so-called far field limit which is reached for $t \rightarrow \infty$. Only then the influence of the initial distribution of the sample vanishes. However, in an experiment the maximum feasible TOF is usually limited by a decreasing signal-to-noise ratio and distortions due to residual potentials.

A second major challenge is that, for a strongly interacting system, interatomic collisions during the expansion can cause a significant redistribution of momentum. For such a non-ballistic expansion, the obtained spatial distribution does not reflect the initial momentum distribution of the sample. Therefore, to access the true momentum distribution of a strongly interacting quantum gas, it is crucial to develop methods that overcome the limitations of this technique. So far the best candidate for weakly interacting systems has been the Bose-gas focusing technique [91, 92, 93, 94, 95] which brings the far field limit to finite TOF. In [95] this is achieved by letting the cloud expand in a weak harmonic potential. However all these methods crucially rely on a ballistic expansion of the sample, which is challenging to achieve for strongly interacting systems.

In this paper, we build upon this work to develop techniques for using Fourier optics of matter waves to perform three different tasks: focusing, collimation and

magnification. In the following sections, we first provide an explanation of the working principle behind the technique and then describe how we use the operations of focusing and collimation to measure the momentum distribution of a strongly interacting 2D Fermi gas. We then propose a magnification scheme which allows to measure the momentum distribution of the system with high resolution.

5.2 Working principle

The ballistic expansion of an ultracold gas can be understood in close analogy with the far field limit in Fourier optics. Using the Fraunhofer diffraction model, the field distribution at a large distance from the source is the Fourier transform of the initial complex field. In the case that a parabolic lens is placed in the optical path, it imprints a quadratic phase shift on the complex field and thus brings the far field distribution to its focal plane [86]. Here, our objective is to implement an equivalent matter wave lens which brings the far field to experimentally accessible time-scales. Note that the far field in this case is defined not in terms of distance from the source, but rather by the time elapsed after releasing the particle from the trap.

Creating a matter wave lens can be accomplished by letting the gas evolve in a harmonic potential $V_{\text{exp}}(x) = \frac{1}{2}m\omega_{\text{exp}}^2 x^2$ instead of a conventional TOF expansion. Here, m is the mass of particles and ω_{exp} is the harmonic oscillator frequency. Without loss of generality, we will only consider a one-dimensional system. This is justified since in a harmonic potential and in the absence of interactions the equations of motion are separable. In a classical picture, each particle starts with some initial momentum and undergoes simple harmonic motion in the potential applied during the expansion. After a quarter of the time period of $V_{\text{exp}}(x)$, i.e. $t = \frac{T_{\text{exp}}}{4} = \frac{1}{4} \frac{2\pi}{\omega_{\text{exp}}}$, the position of each particle is directly proportional to its initial momentum. As illustrated in Fig.5.1, each particle travels along an elliptical trajectory in phase-space and therefore the entire phase-space distribution undergoes a $\pi/2$ rotation after $T_{\text{exp}}/4$.

In the case of a quantum gas, the momentum distribution contains important information about the fluctuations in the system. The classical description using particles and classical fields does not take these into account. Therefore we treat the system in the second quantization formalism using quantum field operators. Let us consider the quantum field operators $\hat{\Psi}(x)$ and $\hat{\Psi}^\dagger(x)$ [96], which respectively

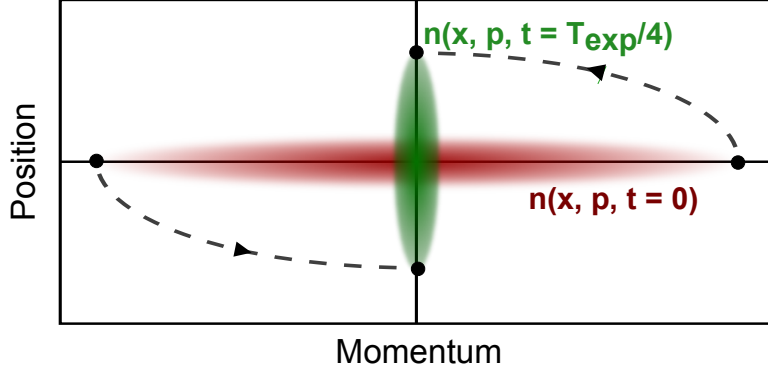


Figure 5.1: Mapping between momentum and position space in phase space representation. The dashed lines illustrate the elliptic phase space trajectories of non-interacting particles in a harmonic potential. The phase space distributions $n(x, p)$ at $t = 0$ and $t = T_{\text{exp}}/4$ are shown in red and green.

annihilate and create a particle in a particular quantum state at a point x ¹. The density distribution of particles in position and momentum space are then given by

$$n(x) = \langle \hat{\Psi}^\dagger(x) \hat{\Psi}(x) \rangle, \quad n(p) = \langle \tilde{\Psi}^\dagger(p) \tilde{\Psi}(p) \rangle. \quad (5.1)$$

In the Heisenberg picture, the evolution of the field operator with a Hamiltonian \hat{H} is governed by

$$i\hbar \partial_t \hat{\Psi}(x, t) = [\hat{\Psi}(x, t), \hat{H}]. \quad (5.2)$$

If we assume a ballistic expansion in a harmonic potential, i.e. without interactions during the expansion, Eq.5.2 reduces to

$$i\hbar \partial_t \hat{\Psi}(x, t) = \left[-\frac{\hbar^2}{2m} \nabla^2 + \frac{1}{2} m \omega_{\text{exp}}^2 x^2 \right] \hat{\Psi}(x, t). \quad (5.3)$$

This time-evolution equation has the form of the Schrödinger equation and is linear in the field. It is in close analogy to the paraxial wave equation in optics which describes the spatial propagation of electromagnetic fields. Solving the field equation, it can be shown that at $T_{\text{exp}}/4$, the spatial field operator reflects the initial field operator

¹Depending on the quantum statistics of the system, the field operators obey certain commutation relations. The statistics does not affect the outcome of the technique.

in momentum space. Therefore, by measuring the spatial density distribution at $t = T_{\text{exp}}/4$, one can infer the momentum distribution at $t = 0$ according to

$$\begin{aligned} n(x, t = T_{\text{exp}}/4) &= \langle \hat{\Psi}^\dagger(x, T_{\text{exp}}/4) \hat{\Psi}(x, T_{\text{exp}}/4) \rangle \\ &= \langle \tilde{\Psi}^\dagger(p, 0) \tilde{\Psi}(p, 0) \rangle = n(p, t = 0), \end{aligned} \quad (5.4)$$

where $p = m\omega x$. A detailed proof can be found in appendix 5.5. From this description, it is apparent that the harmonic potential brings the far field to a single “focal plane” which is realized at an expansion time $t = T_{\text{exp}}/4$.

It is important to note that the mapping between position and momentum space (Eq.5.4) in this method only works because of the quadratic structure of the Hamiltonian (Eq.5.9). This means that interparticle interactions during the expansion would alter the final spatial distribution resulting in a distorted momentum distribution. Hence in an experiment, it is crucial to ensure that interparticle interactions play only a negligible role during the expansion of the gas. In the following section we describe the experimental realization of this technique using a 2D Fermi gas in the BEC-BCS crossover and describe how we overcome the issues arising from strong interactions.

5.3 Experimental realization

For our experiments we use an ultracold Fermi gas of ${}^6\text{Li}$ atoms in the lowest two Zeeman sublevels ($|1\rangle = |F = \frac{1}{2}, m_F = -\frac{1}{2}\rangle$ and $|2\rangle = |\frac{1}{2}, \frac{1}{2}\rangle$). We bring this gas into the 2D regime by loading it into a hybrid trap consisting of an optical standing-wave in z -direction and a weak magnetic confinement in radial direction. The trapping frequencies of this combined potential are $\omega_z = 2\pi \times 5.5$ kHz in axial and $\omega_{x,y} = 2\pi \times 18$ Hz in radial direction. To tune the strength of the interparticle interactions in the gas, we vary the 3D s -wave scattering length a_{3D} . This is achieved by applying magnetic offset fields close to a broad Feshbach resonance centered at 832 G [97]. We probe the system by measuring the atomic density distribution in the x - y plane by performing resonant absorption imaging along the direction of strong confinement (z -axis). The details of the experimental setup and the preparation scheme can be found in [98, 99].

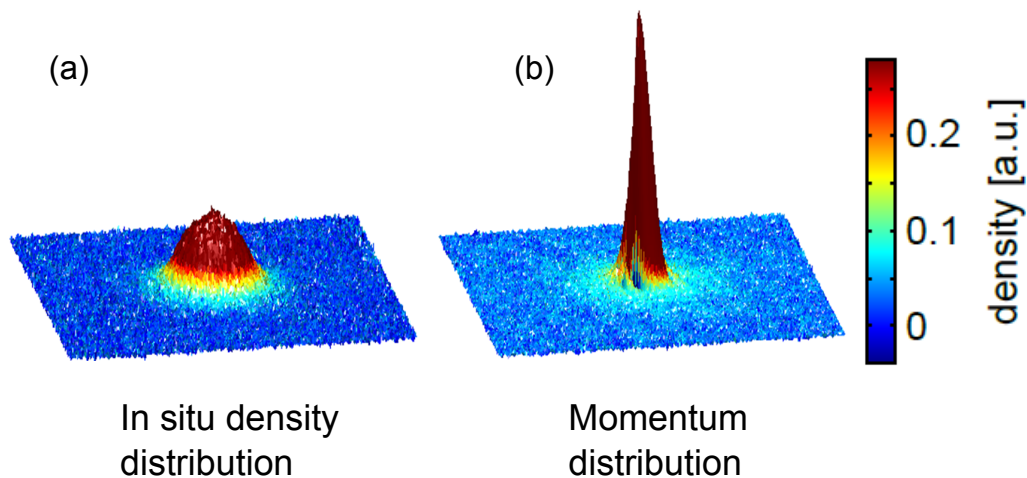


Figure 5.2: Experimentally determined in situ density distribution (a) and the momentum distribution (b) of a 2D gas at a magnetic field of $B = 692$ G where $a_{3D} \simeq 1000 a_{\text{Bohr}}$. The momentum distribution of the gas is obtained from the mapping to a density distribution using the focusing technique described in section 5.3. At sufficiently low temperatures, we observe an enhanced occupation of low momentum states which is not apparent in the in situ density distribution. A detailed investigation of this phenomenon will be reported elsewhere [99].

5.3.1 Focusing

In order to access the momentum distribution we realize the technique theoretically discussed above in a way similar to the one presented in [95] for a 2D Bose gas: we switch off the optical trap and let the gas evolve in the weak magnetic potential, which has a harmonic trapping frequency $\omega_{\text{exp}} = 2\pi \times 10$ Hz in radial direction². As the strong confinement along the z -direction is switched off the sample rapidly expands in z -direction and quickly enters the ballistic regime. After a time-of-flight of $t = T_{\text{exp}}/4 = 25$ ms the x - y momentum distribution at $t = 0$ has been mapped to a density distribution which we observe with absorption imaging. As an example, Fig.5.2 shows images of the in situ density distribution and the corresponding momentum distribution obtained with this focusing technique averaged over about

²Magnetic potentials are well suited for this application since they are usually very smooth and have low anharmonicity, which is equivalent to a matter wave lens which has only minimal aberrations.

30 experimental realizations.

Using the rapid expansion along the z-direction to bring the sample into the ballistic regime works well for weak to intermediate interaction strengths. For example, at a magnetic field of 692 G, we expect less than 0.1 scattering events per particle on average during the expansion (see appendix 5.5). However, in the strongly interacting regime, scattering events during the expansion can significantly distort the mapping of the momentum distribution. We solve this problem by performing a magnetic field ramp with a duration of less than $150 \mu\text{s}$ to a field where the scattering length is smaller, just before release. This ramp converts pairs of atoms into deeply bound molecules, which allows us to measure the pair momentum distribution of the sample [100, 101, 102].

The combination of the interaction quench by the rapid ramp and the quick expansion in z-direction leads to a ballistic expansion of the sample even in the strongly interacting regime. We can therefore use this technique to measure the momentum distribution of our 2D Fermi system across the whole BEC-BCS crossover [58].

5.3.2 Collimation

While the rapid expansion in the axial direction ensures a quick reduction of the density and thus ballistic expansion, it also introduces a limitation for imaging the momentum distribution: During the $T/4$ expansion in the magnetic potential, the axial size of the cloud grows strongly and can exceed the depth of focus of the imaging setup. This limits the optical resolution, and therefore the momentum resolution. After the fast initial expansion, we thus need to limit the axial size of the gas to have sufficient resolution after long TOF.

We achieve this by using the matter wave Fourier optics concept again, this time to collimate the expanding cloud in the axial direction. After the 2D trapping potential is turned off, we switch on an approximately harmonic optical dipole trap potential (ODT). The ODT is switched off when the particles have reached the classical turning point in the potential, i.e. $\Delta t_{\text{col}} = T_{\text{ODT}}/4 = \pi/2\omega_{\text{ODT}}$. This means that once the collimation pulse is turned off, the axial expansion should be stopped and only the radial motion persists (Fig.5.3a). This method is similar to the Delta-Kick Cooling method described in [103].

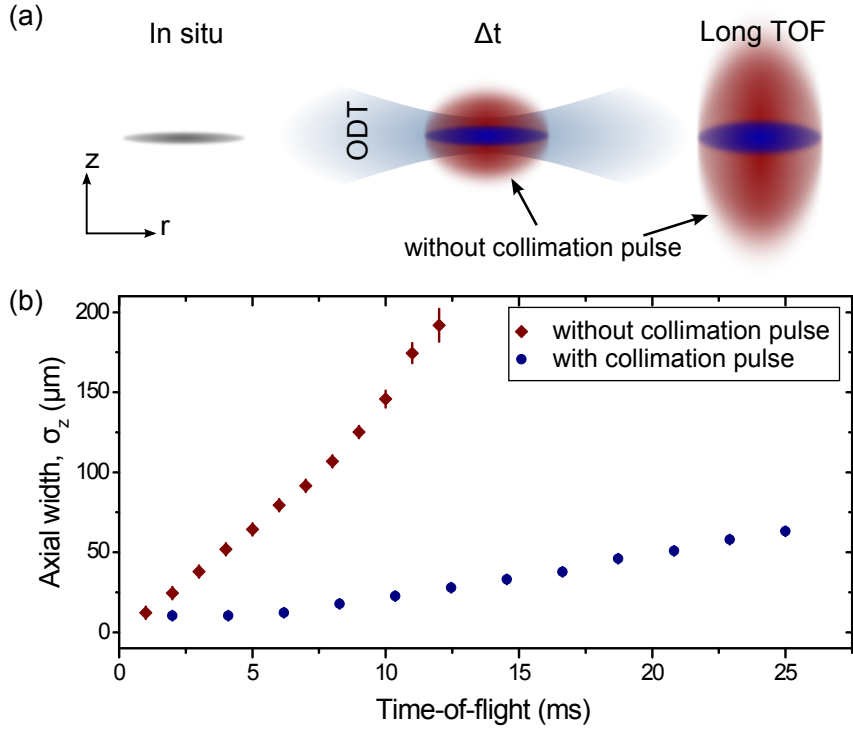


Figure 5.3: (a) Schematic of the axial expansion with and without the collimation pulse. The initial cloud (gray) expands strongly in axial direction when the collimation pulse is not applied (red). With the collimation pulse however, the axial expansion is significantly slowed down (blue). (b) Measurement of axial width as a function of TOF with (blue) and without (red) collimation pulse. In this case the duration of the collimation pulse is $\Delta t_{\text{col}} = 0.5$ ms.

The ODT in our experiment has trapping frequencies of $\omega_{ODT,z} \simeq 2\pi \times 500$ Hz and $\omega_{ODT,r} \simeq 2\pi \times 10$ Hz which means that Δt_{col} for the collimation pulse is only about 0.5 ms. Fig.5.3b shows our measurement of the axial width of the cloud after release as a function of TOF, with and without the collimation pulse. We observe that without the collimation pulse, the axial width exceeds $200 \mu\text{m}$ within a few milliseconds, whereas with the ODT pulse, the axial width is only $70 \mu\text{m}$ even after 25 ms of TOF. Due to the anharmonicity of the ODT potential, the collimation is not perfect and the cloud shows dispersion. Furthermore, the magnetic potential which is anticonfining in the axial direction also contributes to the growth of the

cloud during expansion. However, we still achieve our goal of limiting the axial width after long TOF.

Due to the finite aspect ratio of our ODT, one has to consider the additional radial confinement created by the collimation pulse. Due to the short duration and the relatively weak strength of the radial confinement of the ODT, this effect is expected to be small and it only results in a change of the expansion time needed for focusing. When the collimation pulse is applied, the density of the sample does not decrease as quickly as when there is no collimation pulse (see Fig.5.3). Therefore, scattering events during the expansion are more likely for the same interaction parameter. This issue can be addressed by choosing a magnetic field with even lower scattering length during the expansion with the collimation pulse.

5.3.3 Magnification

When the sample is condensed into low momentum states (Fig.5.2b), the optical density in the momentum space image is concentrated to a small central area. Access to the precise distribution in this region can be hindered by experimental limits to the optical resolution. There are several interesting phenomena, such as the phase coherence near the BKT phase transition, where it would be particularly desirable to resolve this region of interest. We therefore propose a method to magnify the mapped momentum distribution in order to improve momentum resolution without an improvement in optical resolution.

In order to magnify the momentum distribution using only the focusing method, one could decrease ω_{exp} and then perform the focusing for the corresponding longer $T_{\text{exp}}/4$. However, the effectiveness of this method for magnification is limited because the magnification factor has a linear dependence on ω_{exp} . Instead we propose to allow the gas to first expand in an anticonfining potential for a time t_1 and then let it evolve in a confining potential for a time t_2 (see Fig.5.4). In the language of optics, this is equivalent to placing a diverging lens in the optical path before a converging lens. By carefully choosing t_1 and t_2 , it is possible to obtain a magnified momentum distribution. Although a description of the time-evolution in these potentials using field operators is possible, for simplicity we consider only the trajectory of a single particle. This is analogous to using ABCD matrices to trace the path of a ray through different optical components [104, 105]. Using these transfer matrices we

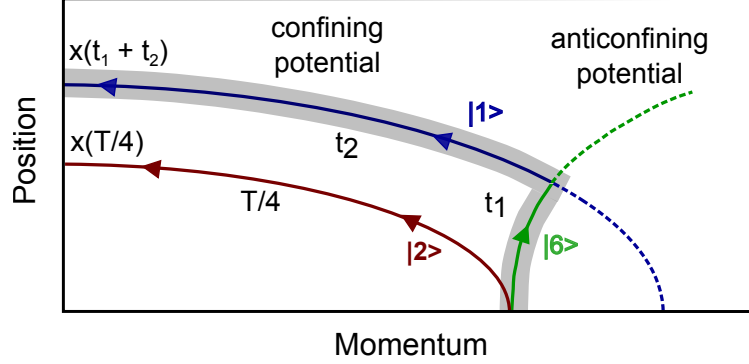


Figure 5.4: Magnifying the momentum distribution. Phase-space trajectory of a particle traveling in a combination of anticonfining and confining potentials (*grey shaded*). By letting the system expand first in a anticonfining potential, a given value of p is mapped to a larger value of x , thus leading to an effective magnification. The colors represent the hyperfine levels of ${}^6\text{Li}$.

can describe the time evolution of the particle in matrix form as

$$\begin{pmatrix} x(t_1 + t_2) \\ p(t_1 + t_2) \end{pmatrix} = \mathbf{T}_c(t_2) \cdot \mathbf{T}_{a.c}(t_1) \cdot \begin{pmatrix} x_0 \\ p_0 \end{pmatrix}, \quad (5.5)$$

where x_0 and p_0 are the initial position and momentum of the particle. \mathbf{T}_c and $\mathbf{T}_{a.c}$ are the transfer matrices obtained by solving the equations of motion in the confining and anticonfining potentials, and are given by

$$\begin{aligned} \mathbf{T}_{a.c}(t_1) &= \begin{bmatrix} \cosh(\omega t_1) & \frac{1}{m\omega} \sinh(\omega t_1) \\ m\omega \sinh(\omega t_1) & \cosh(\omega t_1) \end{bmatrix}, \\ \mathbf{T}_c(t_2) &= \begin{bmatrix} \cos(\omega t_2) & \frac{1}{m\omega} \sin(\omega t_2) \\ -m\omega \sin(\omega t_2) & \cos(\omega t_2) \end{bmatrix}. \end{aligned} \quad (5.6)$$

We solve Eq.5.5 to obtain the final position and momentum of the particle. We tune the parameters t_1 and t_2 such that the final position depends only on the initial momentum. Then, the prefactor of the momentum-dependent term is the magnification factor that we obtain. A unique feature of this method is that for the same lens (fixed ω), it is possible to obtain different magnification factors simply by tuning t_1 and t_2 . This is in contrast to the case of a diverging lens in optics where

the magnification is fixed by the focal length of the lens.

To experimentally realize this technique, one can exploit the hyperfine structure of ${}^6\text{Li}$. Initially the system consists of a mixture of atoms in the high-field seeking states $|1\rangle$ and $|2\rangle$. By applying a microwave π -pulse, one can transfer atoms in state $|1\rangle$ to a hyperfine state $|6\rangle = |F = 3/2, m_F = 3/2\rangle$ just before release. The atoms in state $|6\rangle$ are low-field seeking and thus experience a magnetic potential with opposite sign when released from the optical trap. After a time t_1 in this anticonfining potential, a second π -pulse can be applied to transfer the atoms in state $|6\rangle$ back to state $|1\rangle$. After allowing the gas to evolve in the now confining potential for a time t_2 , one can then image the magnified 2D density distribution of the atoms in state $|1\rangle$.

5.4 Conclusions

In this work we have established a set of methods for performing matter wave Fourier optics with strongly interacting quantum gases. Applying these techniques to a 2D quantum gas of ${}^6\text{Li}$ atoms allowed us to directly observe the 2D momentum distribution of the system. Furthermore, we propose a technique to magnify the momentum distribution by letting the system evolve in a combination of anticonfining and confining potentials. In this way, large magnification factors can be achieved which would allow for detailed studies of the low-momentum region of a momentum distribution.

Moreover, these techniques are not limited to bulk systems but can also be applied to other configurations such as optical lattices. By performing expansion for a time $T_{\text{exp}}/2$ instead of $T_{\text{exp}}/4$, it may be possible to access the topological phase of the sample, similar to 4f-imaging in optics. This will open up possibilities to perform matter wave phase-contrast imaging with quantum gases.

5.5 Appendix

5.5.1 Time-evolution of quantum field operators in a harmonic potential

A quantum gas can be described in the second quantization formalism using quantum field operators $\hat{\Psi}(x)$ which set the occupation number of a particular quantum state in the position basis. For simplicity we only consider a 1D gas here. Due to the

absence of interactions during the ballistic expansion, the expressions factorize and can thus easily be generalized to the 2D and 3D case. We show that for a gas evolving in a harmonic potential, the momentum distribution is mapped to the spatial density distribution after a quarter of the trap period. We construct bosonic field operators which obey the commutation relations

$$[\hat{\Psi}(x, t), \hat{\Psi}^\dagger(y, t)] = \delta(x - y). \quad (5.7)$$

The same can be done for fermionic operators but the obtained results remain unchanged. The time-evolution of the field operators is governed by the Heisenberg equation

$$i\hbar \partial_t \hat{\Psi}(x, t) = [\hat{\Psi}(x, t), \hat{H}(t)]. \quad (5.8)$$

Here, the Hamiltonian $\hat{H}(t)$ is constructed in second-quantization form according to

$$\begin{aligned} \hat{H}(t) &= H(\hat{\Psi}(x, t), \hat{\Psi}^\dagger(x, t)) \\ &= \int dx \hat{\Psi}^\dagger \left[-\frac{\hbar^2}{2m} \nabla^2 + \frac{1}{2} m \omega_{exp}^2 x^2 \right] \hat{\Psi}. \end{aligned} \quad (5.9)$$

Inserting this into Eq.5.8 and using the commutation relation Eq.5.7, we find that

$$i\hbar \partial_t \hat{\Psi}(x, t) = \left[-\frac{\hbar^2}{2m} \nabla^2 + \frac{1}{2} m \omega_{exp}^2 x^2 \right] \hat{\Psi}(x, t). \quad (5.10)$$

This looks like the Schrödinger equation but is the full evolution equation for the field operators. We expand $\hat{\Psi}(x)$ in terms of a time-dependent part and position-dependent Hermite Functions $H_n(\tilde{x})$ by using the ansatz

$$\hat{\Psi}(x, t) = \sum_n \hat{\psi}_n(t) H_n(\tilde{x}), \quad (5.11)$$

where $\tilde{x} = x/l_0$ with oscillator length $l_0 = \sqrt{\hbar/m\omega_{exp}}$. Using this ansatz in the field equation Eq.5.10, we obtain

$$\begin{aligned} i\hbar \frac{\partial}{\partial t} \hat{\psi}_n(t) &= E_n \hat{\psi}_n(t), \\ \hat{\psi}_n(t) &= \hat{\psi}_n(0) e^{-iE_n t/\hbar}. \end{aligned} \quad (5.12)$$

Substituting this in Eq.5.11, we get

$$\hat{\Psi}(x, t) = \sum_n \hat{\psi}_n(0) e^{-iE_n t/\hbar} H_n(\tilde{x}). \quad (5.13)$$

At $t = \frac{T_{\text{exp}}}{4} = \left(\frac{2\pi}{\omega}\right)\frac{1}{4}$, where T_{exp} is the time-period of the oscillator,

$$E_n \cdot T_{\text{exp}}/4 = \hbar\omega_{\text{exp}}\left(n + \frac{1}{2}\right) \cdot \frac{\pi}{2\omega_{\text{exp}}} = \frac{\hbar\pi}{2}\left(n + \frac{1}{2}\right).$$

Since $e^{-i\pi/2} = -i$, Eq.5.13 simplifies to

$$\hat{\Psi}(x, T_{\text{exp}}/4) = \sum_n (-i)^n e^{-i\pi/4} H_n(\tilde{x}) \hat{\psi}_n(0). \quad (5.14)$$

We now use the following rule for the Fourier transform of a Hermite function,

$$\tilde{H}_n(Y) = (-i)^n H_n(Y), \quad (5.15)$$

to arrive at the field operator in momentum space

$$\begin{aligned} \tilde{\Psi}(p, t) &= \frac{1}{l_0} \int dx e^{ipx/\hbar} \hat{\Psi}(x, t) \\ &= \sum_n \hat{\Psi}_n(t) (-i)^n H_n(\tilde{p}) \end{aligned} \quad (5.16)$$

with $\tilde{p} = pl_0/\hbar$. We then find

$$\begin{aligned} &\hat{\Psi}^\dagger(x, T_{\text{exp}}/4) \hat{\Psi}(x, T_{\text{exp}}/4) \\ &= \sum_{n, n'} (i)^n (-i)^{n'} H_n(x) H_{n'}(x) \hat{\psi}_n^\dagger(0) \hat{\psi}_{n'}(0) \\ &= \tilde{\Psi}^\dagger(p = m\omega x, 0) \tilde{\Psi}(p = m\omega x, 0), \end{aligned} \quad (5.17)$$

where we used $\tilde{p} = \tilde{x}$ in Eq.5.16. Therefore, after $T_{\text{exp}}/4$, we obtain the Fourier

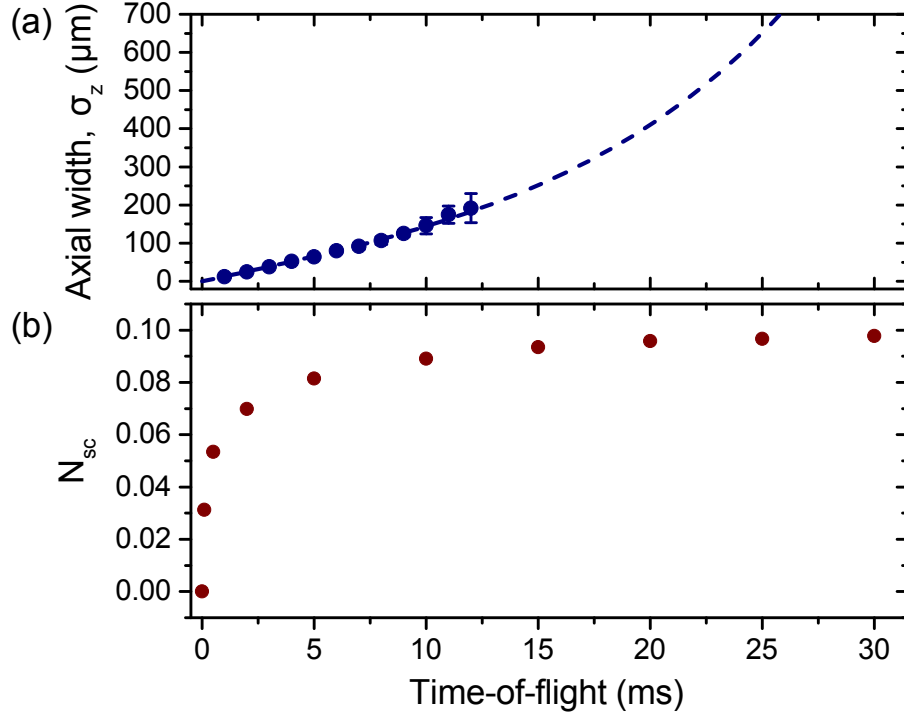


Figure 5.5: (a) Experimentally obtained axial width and the corresponding theoretical prediction for a cloud expanding in the magnetic potential at 692 G. (b) Average number of scattering events per particle in the sample as a function of the elapsed expansion time. After a quick initial rise of N_{sc} , the number of scattering events saturates and reaches about 0.1 for expansion times exceeding 20 ms.

transform of the initial field operator. The corresponding spatial density is given by

$$\begin{aligned}
 n(x, T_{\text{exp}}/4) &= \langle \hat{\Psi}^\dagger(x, T_{\text{exp}}/4) \hat{\Psi}(x, T_{\text{exp}}/4) \rangle \\
 &= \langle \tilde{\Psi}^\dagger(p, 0) \tilde{\Psi}(p, 0) \rangle = n(p, 0),
 \end{aligned} \tag{5.18}$$

with $p = m\omega x$. This proves that the spatial density distribution after $t_{\text{exp}} = T_{\text{exp}}/4$ reflects precisely the initial momentum distribution with a scaling factor $1/m\omega_{\text{exp}}$.

5.5.2 Collisions in an expanding 2D gas

Inter particle collisions during the expansion can distort the mapping between momentum and position space [106]. Therefore, we want to estimate the number of scattering events that occur while the particles are expanding using the expression

$$\Gamma = n\sigma v, \quad (5.19)$$

where n is the density, σ is the scattering cross-section and v is the mean velocity of the particles. In our case, we want to investigate the scattering events for a sample with a temperature of about 60 nK at a magnetic offset field of 692 G, where the images in Fig.5.2 are taken. At this field, the atoms are paired up and form deeply bound bosonic molecules. Their cross-section σ is thus given by $\sigma = 8\pi a_{\text{mol}}^2$, where a_{mol} is the 3D scattering length between molecules which is $a_{\text{mol}}(692 \text{ G}) = 0.6 \times 1463 a_{\text{Bohr}}$ [60, 97]. One thus obtains $\sigma \simeq 5.4 \times 10^{-14} \text{ m}^2$. We assume a Maxwell-Boltzmann distribution of the velocities and obtain the following mean velocity $v = \sqrt{2k_B T / m_{\text{mol}}}$, where k_B is the Boltzmann constant, T is the temperature of the sample and $m_{\text{mol}} = 2 m_{\text{Li}^6}$ is the mass of a bosonic dimer. Hence, for our temperature of about 60 nK we obtain $v \simeq 0.0091 \text{ m/s}$.

To estimate the average scattering rate per particle in our trap, we evaluate the measured in situ density distributions to calculate the average density and obtain $\bar{n}_{3D} \simeq 1.2 \times 10^{12} \text{ cm}^{-3}$. Using these numbers, we obtain an average in situ scattering rate of $\Gamma_0 = \bar{n}_{3D} \sigma v \simeq 580 \text{ Hz}$ per particle.

To calculate the number of scattering events during the expansion, we simulate the evolution of the gas in the weak magnetic potential using the method given in [107, 33]. This yields the axial width of the cloud $\sigma_z(t)$ as a function of the expansion time. The resulting widths together with the corresponding experimental data are shown in Fig.5.5a. Although this method was originally devised to describe the expansion of an anisotropic condensate in the 3D BEC-BCS crossover, the good agreement between the data and the prediction justifies its application to our system³. Neglecting the motion in the radial direction, the density of the cloud is inversely proportional to the axial cloud width σ_z and hence the scattering rate at an expansion

³Since we are in the BEC regime ($1/k_F a_{3D} > 1$), the effective exponent γ in the model described in [107, 33] can be set to 1.

5.5. Appendix

time t is given by

$$\Gamma(t) = \Gamma_0 \cdot \frac{\sigma_z(0)}{\sigma_z(t)}. \quad (5.20)$$

By integrating this quantity over the complete expansion time of 25 ms, we finally obtain the average number of scattering events per particle in our sample during the expansion

$$N_{\text{sc}}(t = 25 \text{ ms}) = \int_0^{t=25 \text{ ms}} \Gamma(t) dt \simeq 0.09. \quad (5.21)$$

Fig.5.5a shows this quantity as a function of the expansion time. One observes that for $t = 25$ ms less than 10 % of all particles undergo collisions during the focusing. It is however interesting to note that while half of the scattering events occur during the first $\simeq 0.5$ ms there are still residual scattering events up to the complete expansion time of 25 ms.

The phase diagram of the BEC-BCS crossover

6

Publication

PHYSICAL REVIEW LETTERS **115**, 010401 (2015)

Observation of Pair Condensation in the Quasi-2D BEC-BCS Crossover

M. G. Ries¹, A. N. Wenz¹, G. Zürn¹, L. Bayha¹, I. Boettcher², D. Kedar¹, P. A. Murthy¹, M. Neidig¹, T. Lompe¹, and S. Jochim¹

¹*Physikalisches Institut, Ruprecht-Karls-Universität Heidelberg*

²*Institut für Theoretische Physik, Ruprecht-Karls-Universität Heidelberg*

Abstract

The condensation of fermion pairs lies at the heart of superfluidity. However, for strongly correlated systems with reduced dimensionality the mechanisms of pairing and condensation are still not fully understood. In our experiment we use ultracold atoms as a generic model system to study the phase transition from a normal to a condensed phase in a strongly interacting quasi-two-dimensional Fermi gas. Using a novel method, we obtain the in-situ pair momentum distribution of the strongly interacting system and observe the emergence of a low-momentum condensate at low temperatures. By tuning temperature and interaction strength we map out the phase diagram of the quasi-2D BEC-BCS crossover.

6.1 Introduction

The characteristics of quantum many-body systems are strongly affected by their dimensionality and the strength of interparticle correlations. In particular, strongly correlated two-dimensional fermionic systems have been of interest because of their

connection to high- T_c superconductivity. Although they have been the subject of intense theoretical studies [44, 108, 58, 109, 110, 79, 71, 111], a complete theoretical framework could not yet be established.

Ultracold quantum gases are an ideal realization to explore strongly interacting 2D Fermi gases, as they offer the possibility to independently tune the dimensionality and the strength of interparticle interactions. Reducing the dimensionality [14] led to the observation of a Berezinskii-Kosterlitz-Thouless (BKT) type phase transition to a superfluid phase in weakly interacting 2D Bose gases [53, 112]. Tuning the strength of interactions in a three-dimensional two-component Fermi gas made it possible to explore the crossover between a molecular BEC and a BCS superfluid [113, 100, 101, 114].

Recently, efforts have been made to combine reduced dimensionality with the tunability of interactions and to experimentally explore ultracold 2D Fermi gases [115, 68, 116, 117, 118, 83]. However, the phase transition to a condensed phase could so far not be observed. Here, we report on the condensation of pairs of fermions in the quasi-2D BEC-BCS crossover.

The BEC-BCS crossover smoothly links a bosonic superfluid of tightly bound diatomic molecules to a fermionic superfluid of Cooper pairs in 2D as well as 3D systems. However, changing the dimensionality leads to some inherent differences. In two dimensions, there is a two-body bound state for all values of the interparticle interaction. Furthermore, due to the enhanced role of fluctuations in 2D, true long-range order is forbidden for homogeneous systems at finite temperature [6, 51]. Still, a low-temperature superfluid phase with quasi long-range order can emerge due to the BKT mechanism [8, 9].

In a 2D gas with contact interactions, the interactions can be described by the 2D scattering length a_{2D} . Using the Fermi wave vector k_F , the dimensionless crossover parameter is given by $\ln(k_F a_{2D})$. The crossover regime is reached for $|\ln(k_F a_{2D})| \lesssim 1$. For $\ln(k_F a_{2D}) \ll -1$, the binding energy is large and the system consists of deeply bound bosonic dimers. For $\ln(k_F a_{2D}) \gg 1$, the dimer binding energy tends to zero. For a thermal energy $k_B T$ significantly larger than the binding energy, the dimers are dissociated due to thermal excitations and the system becomes fermionic.

2D gases are realized by a strongly anisotropic confinement, which leads to a freezing out of the degrees of freedom in one spatial direction. Such a quasi-2D gas

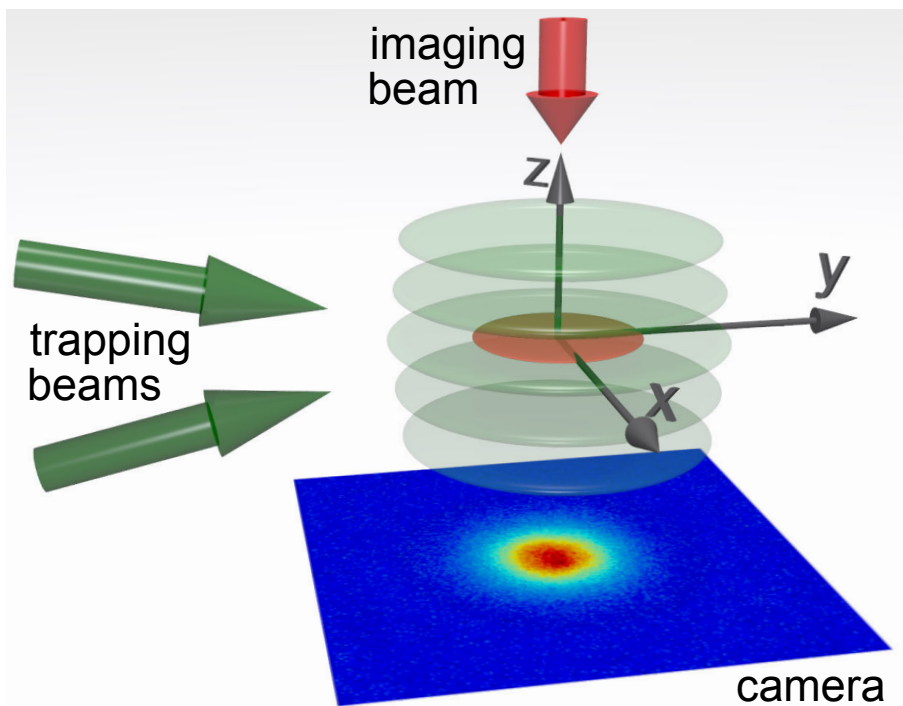


Figure 6.1: **Experimental setup.** A quasi-2D gas (red disk) is created by loading a two-component ultracold Fermi gas of ${}^6\text{Li}$ atoms into a single layer of a standing-wave trap created by two interfering laser beams ($\lambda = 1064$ nm, green arrows) that cross under a small angle (14°). Using absorption imaging along the vertical direction (red arrow) we obtain the column density of the sample.

captures the essential properties of a 2D system. Corrections to the 2D physics may arise from the residual influence of the third dimension (see Appendix 6.5).

6.2 Experimental system

We perform our measurements using a two-component Fermi gas of ${}^6\text{Li}$ atoms in the lowest two Zeeman sublevels, which we denote $|1\rangle$ and $|2\rangle$ [97]. The ultracold gas initially consists of 40 000-50 000 atoms per spin state, which are bound into dimers at a temperature of approximately 50 nK and a magnetic offset field of 795 G ($\ell_z/a_{3D} = 1.08$). It is loaded into a hybrid trap consisting of a single layer of a

6.2. Experimental system

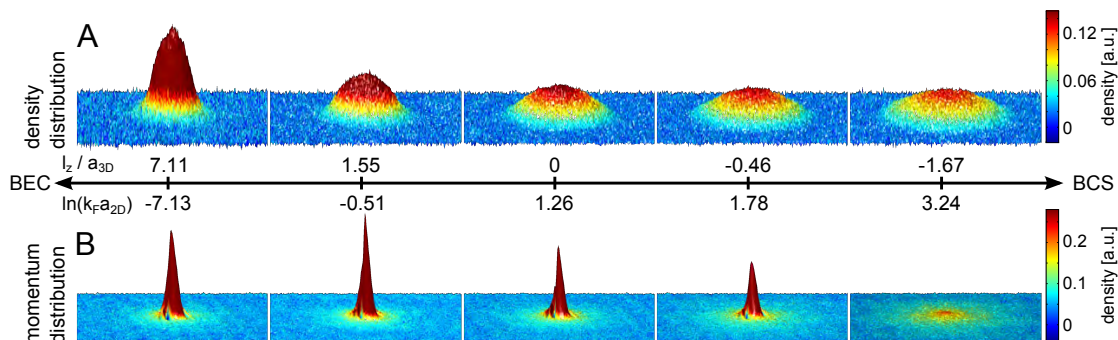


Figure 6.2: **Density distributions at the lowest accessible temperature for different interaction strengths.** (A) In-situ density distribution obtained from absorption imaging along the z -axis. (B) Pair momentum distribution obtained from the $\tau/4$ -method with a pair projection ramp to $\ell_z/a_{3D} = 7.11$ (692 G). The strong enhancement at low momenta in the momentum distribution for $\ln(k_F a_{2D}) < 3.24$ is a clear signature of pair condensation. Each picture is the average of about 30 individual measurements. The temperature of the samples ranges from 64 nK at $\ln(k_F a_{2D}) = -7.13$ to 78 nK at $\ln(k_F a_{2D}) = 3.24$.

standing-wave optical dipole potential and a weak magnetic potential. The combined trapping frequencies are $\omega_x = 2\pi \times 17.88(3)$ Hz and $\omega_y = 2\pi \times 17.82(4)$ Hz in radial, and $\omega_z = 2\pi \times 5.53(3)$ kHz in axial direction. This leads to a pancake-shaped cloud with an aspect ratio of $\frac{\omega_z}{\omega_r} \approx 310$ (see Fig.6.1) and an axial harmonic oscillator length $\ell_z = \sqrt{\hbar/m\omega_z} \approx 551$ nm with the reduced Planck's constant \hbar , the atom mass m , and the axial trapping frequency ω_z . We ensure that there is no significant population of axially excited states by measuring the axial momentum distribution of the gas [116]. Assuming that the internal structure of pairs, i.e. the relative wave function of the fermions inside the pairs, has only negligible effect beyond the two-body sector¹, our system can be described in the 2D framework with the effective 2D scattering length $a_{2D} = \ell_z \sqrt{\pi/A} \exp\left(-\sqrt{\frac{\pi}{2}} \frac{\ell_z}{a_{3D}}\right)$ [119, 115, 58, 120], where $A = 0.905$.

To explore the phase diagram of the quasi-2D BEC-BCS crossover, we tune the

¹For $E_B \gg \hbar\omega_z$, the system consists of tightly bound bosonic molecules whose internal structure is not resolved. For $E_B \ll \hbar\omega_z$ the internal structure of the dimers is well described within the 2D framework. Only for $E_B \approx \hbar\omega_z$, the internal structure is influenced by the third spatial dimension and can deviate from the 2D predictions. This affects the short-range behavior of the system. However, we expect the influence on the long-range behavior to be negligible.

temperature by heating the sample, and the interaction strength by adiabatically ramping the magnetic offset field to values between 692 G ($\ell_z/a_{3D} = 7.11$) and 982 G ($\ell_z/a_{3D} = -2.35$) (Appendix 6.5.4). We probe the 2D density distribution via absorption imaging along the vertical direction (see Fig. 6.1). The density distributions for different interaction strengths are shown in Fig. 6.2A for the coldest accessible temperatures. For growing $\ln(k_F a_{2D})$, the width of the sample increases while its central density decreases from approximately $2.7/\mu\text{m}^2$ at $\ln(k_F a_{2D}) = -7.13$ to approximately $0.76/\mu\text{m}^2$ at $\ln(k_F a_{2D}) = 3.24$. This change of the density distribution illustrates the crossover from a dense condensate of bosonic molecules to a degenerate Fermi gas whose density is reduced by the Fermi pressure. However the phase transition into a condensed phase, which manifests itself in the enhanced density of pairs with vanishing momentum, is not directly visible in the measured density distributions.

We thus conceived a method to probe the in-situ pair momentum distribution of our strongly interacting system by combining a quench of interactions with a matter wave focusing technique, in which the sample expands ballistically in a weakly confining radial harmonic potential [91, 92, 95, 64].

Due to its large aspect ratio, our sample expands rapidly and almost exclusively in the z-direction after the release from the optical trap. Hence, its density suddenly drops and interactions between the expanding particles are quenched. Redistribution of momentum in the radial direction during the expansion is thus negligible at the weakest probed interaction strengths and does not affect the momentum distribution. To minimize interaction effects also in the strongly interacting regime, we perform a fast ramp to the lowest accessible interaction strength on the BEC side ($B = 692$ G, $\ell_z/a_{3D} = 7.11$) on a time scale shorter than $125 \mu\text{s}$ just before the release. This is fast enough that the density and momentum distributions cannot adjust to the new interaction parameter [120, 64]. At the same time, pairs of atoms are projected onto deeply bound molecules whose binding energy E_B significantly exceeds the energy scale given by the axial confinement ($\hbar\omega_z$) and one obtains the pair momentum distribution². A similar technique was already used to explore the three-dimensional BEC-BCS crossover [100, 101, 102]. However, these experiments could not take advantage of the interaction quench and the subsequent ballistic expansion since

²Due to this projection, information about the relative momentum of the paired atoms is lost. We therefore do not observe the Tan contact in the pair momentum distribution [81].

they were lacking the fast expansion in the z-direction.

To obtain the radial momentum distribution, we perform this ballistic expansion in a weakly confining harmonic potential with trap frequency $\omega_{\text{exp}} = 2\pi\nu_{\text{exp}}$ in the radial direction. In a simple picture, the harmonic potential acts as a matter wave lens and brings the far field distribution to finite timescales. After an expansion time of $t_{\text{exp}} = \tau/4$, where $\tau = 1/\nu_{\text{exp}}$ is the period of the harmonic potential, the position of each particle depends only on its initial momentum in the radial plane. Thus $n(\mathbf{x}, t = \tau/4) = \tilde{n}(\hbar\mathbf{k}/(m\omega_{\text{exp}}), t = 0)$ and hence by imaging the density profile after $t_{\text{exp}} = \tau/4$, we gain direct access to the initial 2D momentum distribution [91, 92, 64].

In our case, the radial trap frequency is $\omega_{\text{exp}} \simeq 2\pi \times 10 \text{ Hz}$, which leads to $t_{\text{exp}} = 25 \text{ ms}$ (see Appendix 6.5.4). In contrast to conventional time-of-flight expansion, where the initial spatial distribution of the sample influences the obtained momentum distribution especially at low momenta, distortions are negligible in this method. By combining the interaction quench with the projection onto molecules and the $\tau/4$ momentum-imaging, we are able to access the radial in-situ pair momentum distribution $\tilde{n}(k)$ in the whole crossover regime.

6.3 Condensation of pairs at low momenta

Fig. 6.2B shows the obtained pair momentum distributions for the coldest attainable temperature at different interaction strengths. One observes a dramatic enhancement at low momenta which manifests itself in a sharp central peak. This feature is strongest on the BEC side and persists above $\ln(k_F a_{2D}) = 0$ and the 3D Feshbach resonance, until it vanishes at $\ln(k_F a_{2D}) \approx 3.2$ on the BCS side. Comparing the data at the two largest depicted values of $\ln(k_F a_{2D})$, one observes that the peak momentum density \tilde{n}_0 changes by almost an order of magnitude, whereas the in-situ peak density n_0 changes by less than 10%. As \tilde{n}_0 is a measure for the long-range coherence of the system [121], the observed abrupt change indicates the phase transition to the condensed phase.

For a more quantitative analysis of our data, we azimuthally average the pair momentum distribution. Fig. 6.3A shows the obtained radial distribution for the coldest accessible temperature measured at 782 G, which corresponds to $\ell_z/a_{3D} = 1.55$ ($\ln(k_F a_{2D}) \approx -0.51$). We extract the temperature T of the sample from the high momentum tail of the radial distribution which is well described by a Gaussian. Note

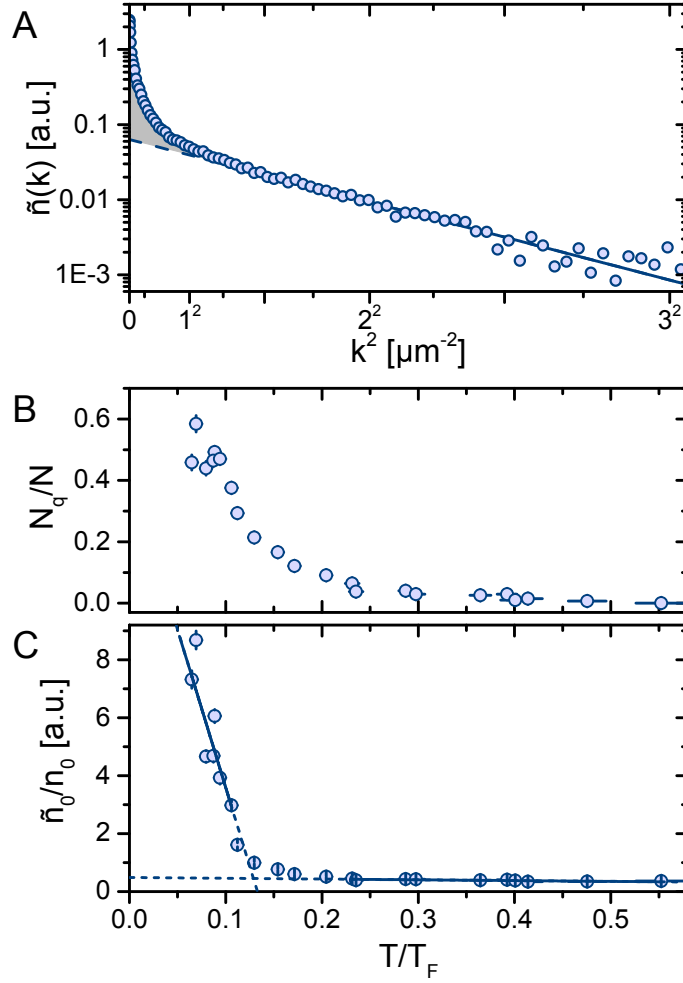


Figure 6.3: **Quantitative analysis of the momentum distribution at $\ell_z/a_{3D} = 1.55$.** (A) Radial momentum distribution $\tilde{n}(k)$ at the coldest accessible temperature. We logarithmically plot $\tilde{n}(k)$ as a function of k^2 . The thermal wing thus appears as a straight line from which we extract the temperature of the sample with a Boltzmann fit (line). The figure is the average of about 30 individual measurements. (B) Non-thermal fraction N_q/N as a function of T/T_F . N_q is indicated by the gray area in panel (A). (C) Normalized peak momentum density \tilde{n}_0/n_0 as a function of T/T_F . The intersection of linear fits to the high and low temperature regime yields the critical temperature T_c/T_F . Each data point in (B) and (C) is the average of about 30 individual measurements, the error bars indicate the standard error of the mean (SEM). Solid lines indicate the fitted data range.

6.3. Condensation of pairs at low momenta

that before the ramp of the interaction strength, the thermal part of the gas consists of molecules for $\ell_z/a_{3D} > 0.55$, free atoms for $\ell_z/a_{3D} < -0.46$, and a mixture of atoms and molecules between these two interaction strengths (see Appendix 6.5.6). For each investigated interaction strength and temperature, we determine the Fermi wave vector and Fermi temperature from the in-situ peak density according to $k_F^2 = 2mk_B T_F/\hbar^2 = 4\pi n_0$. Here, m refers to the mass of a ${}^6\text{Li}$ atom and k_B is Boltzmann's constant. This definition employs the local density approximation at the trap center and allows us to compare the obtained data to predictions for the homogeneous system. Note that $n_0 = n_{0,|1\rangle} = n_{0,|2\rangle}$, where $n_{0,|i\rangle}$ is the peak density of atoms in state $|i\rangle$.

At low momenta, a fraction of the momentum density lies above the Gaussian fit (gray area in Fig. 6.3A). We define this quantity as the non-thermal fraction N_q/N ³ and investigate its behavior as a function of the degeneracy temperature T/T_F (see Fig. 6.3B). While the non-Gaussian fraction vanishes for $T/T_F \gtrsim 0.5$, it slowly grows for decreasing temperatures. For $T/T_F \lesssim 0.2$, the slope increases until we reach $N_q/N \approx 0.6$ for the coldest samples. This is in agreement with theoretical predictions [65, 122, 123] and previous experimental results [121, 95, 124, 56], which find a presuperfluid increase of low momentum states for temperatures above the superfluid transition temperature T_c . This behavior inhibits a precise determination of the transition temperature T_c from N_q/N . To obtain an estimate for the critical temperature, we instead plot the normalized peak momentum density \tilde{n}_0/n_0 as a function of temperature as shown in Fig. 6.3C. This quantity is a measure for the fraction of the sample which exhibits long-range phase coherence [121]. The innermost pixel of the momentum distribution corresponds to a coherence length well above $100\ \mu\text{m}$ which is almost two orders of magnitude larger than the thermal wavelength of the coldest samples. The normalized peak momentum density shows a sudden change of slope which we assume to occur at the phase transition. We estimate T_c/T_F by the intersection of linear fits to the regimes above and below the phase transition. For the example shown in Fig. 6.3, this results in a critical temperature of $T_c/T_F = 0.129$ (35), where the statistical uncertainty is obtained from the standard errors of the two linear fits. The critical phase space density is

³We identify the non-Gaussian fraction N_q/N with the fraction of the cloud which has non-Gaussian fluctuations. In the literature [65, 122], this is referred to as the quasicondensate. Below T_c , the quasicondensate density becomes identical to the superfluid density in mean-field theory.

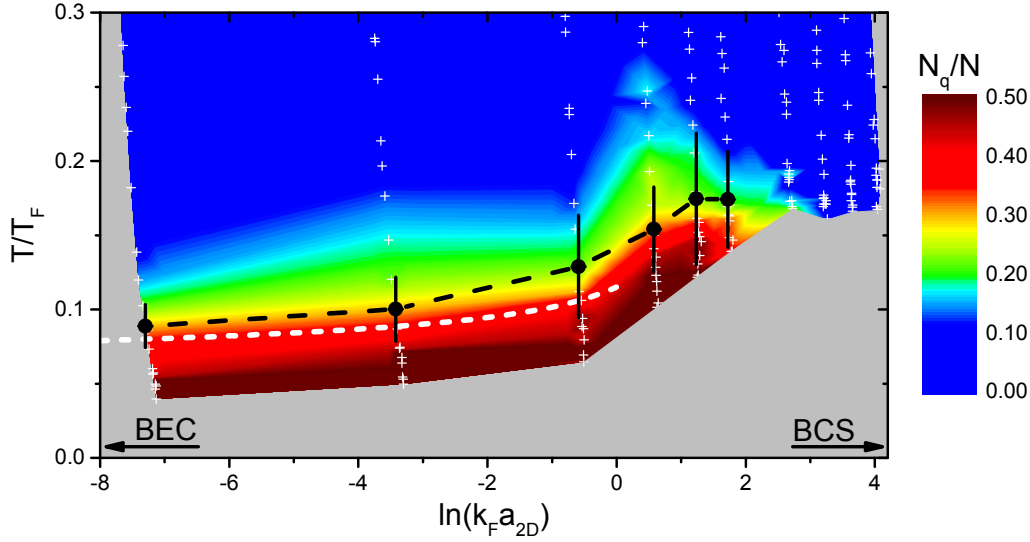


Figure 6.4: **Phase diagram of the strongly interacting 2D Fermi gas.** The experimentally determined critical temperature T_c/T_F is shown as black data points and the error bars indicate the statistical errors. Systematic uncertainties are discussed in detail in [120]. The color scale indicates the non-thermal fraction N_q/N and is linearly interpolated between the measured data points (white crosses). Each data point is the average of about 30 measurements. The dashed white line is the theoretical prediction for the BKT transition temperature given in [125].

$\rho_c = n_{0,c} \lambda_{dB,c}^2 = 3.9(6)$, where $\lambda_{dB,c}$ and $n_{0,c}$ are the thermal de-Broglie wavelength and the peak in-situ density at the critical temperature, respectively.

6.4 The phase diagram

By repeating this analysis for all investigated interaction strengths, we obtain the transition temperature as a function of the interaction parameter $\ln(k_F a_{2D})$. The resulting values are shown as black dots in Fig.6.4 together with the corresponding non-Gaussian fraction N_q/N , which is displayed as a color scale. Comparing the data for T_c/T_F and N_q/N , one finds that the phase transition occurs at a significant non-Gaussian fraction of $N_q/N \approx 0.3$ for all measured interaction strengths.

On the BEC side of the phase diagram, one observes a slow increase of the

measured critical temperature towards the crossover region. Within their statistical uncertainties, the measured values of T_c/T_F are in good agreement with an effective description in terms of 2D bosons [125]. This theoretical prediction describes a BKT transition into a superfluid phase with algebraically decaying phase coherence. Interestingly, the bosonic theory provides a reasonable description of the data up to $\ln(k_F a_{2D}) = 0$, where the 2D scattering amplitude diverges. This indicates that the fermionic nature of the constituents of the bosonic dimers has only little effect on the many-body physics of the system up to this point. The crossover to a fermionic description should thus occur at positive values of $\ln(k_F a_{2D})$. This is in line with recent theoretical predictions [79, 69].

Far on the BCS side, fermionic theories predict an exponential decrease of T_c/T_F [126, 71]. Although we can only give an upper limit for the critical temperature $T_c/T_F \leq 0.16$ for $\ln(k_F a_{2D}) \geq 2$, the observed non-Gaussian fraction is consistent with a decrease towards the BCS limit. However, T_c/T_F is systematically above the theoretical predictions for $\ln(k_F a_{2D}) > 0$ [125, 71, 111]. Part of this deviation might be due to the residual influence of the third dimension. In our system, residual axial excitations grow with increasing $\ln(k_F a_{2D})$. Recently, it was predicted that they lead to an increased critical temperature [127]. Additionally, the three-dimensional internal structure of atom pairs might lead to corrections in the regime where $E_B \approx \hbar\omega_z$, which go beyond the two-body sector. Whether this effect has any influence on the measured phase diagram still needs further experimental and theoretical considerations. Initial steps in this direction have been taken [128].

Our work constitutes a basis for future theoretical and experimental studies of quantum gases in the quasi-2D BEC-BCS crossover. The measured critical temperature suggests the validity of BKT theory on the bosonic side. Superfluidity and the algebraic decay of correlations below the transition remain to be validated. Indeed, our ability to extract the in-situ momentum distribution with negligible distortion offers direct access to the coherence properties of the system. A first analysis of the trap averaged first order correlation function, which we obtain by Fourier-transforming the pair momentum distribution, suggests algebraically decaying phase correlations below the critical temperature. However, due to the inhomogeneity of our system, a careful analysis is required to unambiguously confirm the BKT nature of the observed transition. Additionally, the equation of state can be extracted from the

density distribution in the trap. Finally, the exploration of the dimensional crossover to 3D, in which an increased T_c/T_F is predicted [127], offers new opportunities to understand mechanisms which lead to high critical temperatures.

6.5 Appendix

6.5.1 Preparation of the sample

We start our experimental sequence by transferring a 3D Fermi gas of ${}^6\text{Li}$ atoms in states $|1\rangle$ and $|2\rangle$ [97] from a magneto-optical trap into an optical dipole trap (ODT). This surfboard-shaped trap has an aspect ratio of $\omega_x:\omega_y:\omega_z = 1:8:44$ and is far red detuned ($\lambda = 1064\text{ nm}$) from the optical transition. The gas is then evaporatively cooled into degeneracy at a magnetic offset field of 795 G on the BEC side of the broad Feshbach resonance at 832.2 G [97]. We therefore obtain a 3D molecular Bose-Einstein condensate (mBEC) consisting of about 10^5 molecules with negligible thermal fraction. This sample is finally transferred into a standing-wave optical dipole trap (SWT) as illustrated in Fig. 1A in the main text.

The SWT is created by two elliptical focused 1064 nm Gaussian beams, which intersect under an angle of $\simeq 14^\circ$. This leads to a standing wave interference pattern where the maxima have a distance of $\simeq 4.4\ \mu\text{m}$. The ellipticity of the beams is chosen such that the interference maxima have a circular symmetry in the xy-plane. At the position of the SWT, the magnetic offset field has a saddle point. It leads to an additional weak magnetic confinement (anti-confinement) in radial (axial) direction. The measured trap frequency of the magnetic confinement in radial direction is $\omega_{mag}(B) \approx 2\pi \times 0.39\text{ Hz} \sqrt{B[\text{G}]}$. At a magnetic offset field of 795 G, the combined trapping frequencies for the central layers of the SWT are given in the main text and lead to an aspect ratio of $\omega_x : \omega_y : \omega_z = 1 : 0.997 : 309$.

In order to align the relative position of the atoms in the ODT with one layer of the SWT, we apply a magnetic field gradient in z-direction, which can shift the atoms up or down in the ODT. To optimize the fraction of atoms transferred into this single layer, we furthermore decrease the vertical size of the atoms in the ODT by modulating the position of the ODT in the transverse x-direction on a time scale much faster than all trapping frequencies. This creates a time averaged potential where the width of the trap in x-direction is increased by a factor of approximately

5. In order to further reduce the extension in z-direction of the sample, we ramp to a magnetic offset field of 730 G over 600 ms. This reduces the repulsive interaction and thus the size of the sample. After the transfer into the SWT, we ramp back to 795 G, where we further evaporatively cool the sample by simultaneously applying a magnetic field gradient and lowering the trap depth. This also allows us to control the total number of particles.

In order to access higher temperatures in a controlled fashion, we can then apply a heating procedure. For the lowest three temperatures, we hold the sample in the SWT at 795 G for a variable time (0...1 s) during which it is heated by technical noise. For higher temperatures, we parametrically heat the sample by modulating the depth of the SWT with variable amplitude. After letting the sample equilibrate for 300 ms, we ramp the magnetic offset field to the value we want to investigate, where we wait for an additional 20 ms before probing the system. All magnetic field ramps are performed with ramp speeds $\lesssim 1.9$ G/ms. To ensure adiabaticity of the magnetic field ramps, we compare the temperature of a sample held at an offset field of 732 G to the temperature of a sample which was ramped across the Feshbach resonance to 900 G and back in the same time. We find that for this ramp speed the two temperatures agree within their uncertainties. All magnetic field ramps are thus adiabatic, and we probe the crossover in an isentropic way.

6.5.2 Distribution of particles in the standing-wave trap

In order to probe the distribution in the layers of the SWT, we use a radio-frequency tomography technique. We apply a magnetic field gradient along the z-axis to make the transition frequency $\nu_{|2\rangle|3\rangle}$ between states $|2\rangle$ and $|3\rangle$ spatially dependent on z. The dependence of $\nu_{|2\rangle|3\rangle}$ on the magnetic field is given by $d\nu_{|2\rangle|3\rangle}/dB \simeq 6.3$ kHz/G. We can thus visualize the density distribution by counting the number of transferred atoms as a function of the transition frequency. To minimize the line width of the transition, we need to exclude interaction effects and three-body losses. Hence, we first remove the particles in state $|1\rangle$ by applying a resonant laser pulse for about $10 \mu\text{s}$. To minimize heating and losses, this is done at a magnetic offset field of 1000 G, where the atoms are not bound into molecules at our temperatures and interactions are comparatively weak. Although we still observe significant heating, the thermal energy is small compared to the trap depth and it is therefore not expected that

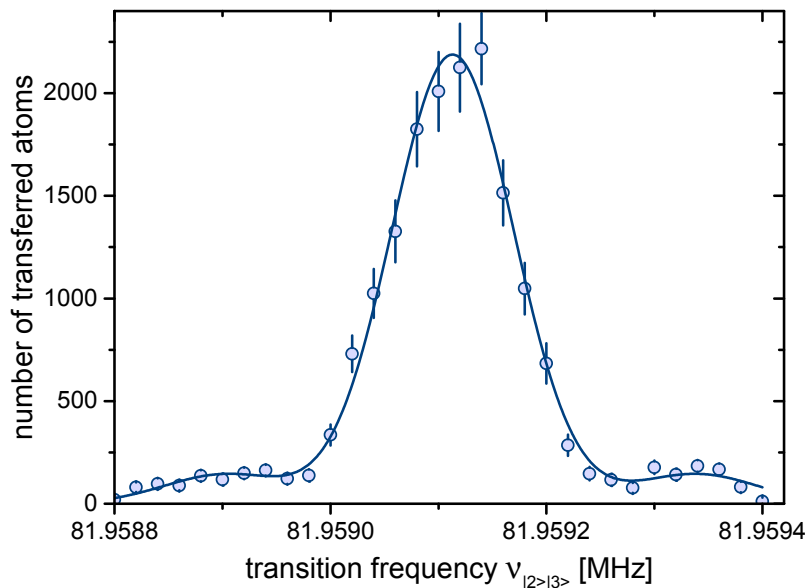


Figure 6.5: **Tomographic measurement of the particle distribution in the standing-wave trap.** Data points represent the number of particles transferred to state $|3\rangle$ as a function of the transition frequency $\nu_{|2\rangle|3\rangle}$. The central maximum at 81.9591 MHz corresponds to atoms in the central layer, the neighboring layers are only slightly populated. The sum of three Gaussian profiles (solid line) is fitted to the data and yields a population of the central layer with approximately 89% of the particles.

particles get transferred between the individual layers. After a ramp back to 795 G, we apply a magnetic field gradient of approximately 70 G/cm along the z-axis. We thus achieve a difference of approximately 200 Hz in transition frequency between atoms in neighboring layers. We then drive the $|2\rangle$ - $|3\rangle$ transition and record the number of transferred particles using state-selective absorption imaging along the y-axis as a function of frequency (see Fig. 6.5).

The large central maximum at 81.9591 MHz in Fig. 6.5 corresponds to atoms in the central layer. Note that only a fraction of atoms is transferred to state $|3\rangle$, and thus the displayed atom number is considerably lower than the total atom number in the trap. The neighboring layers lie at roughly 81.9589 MHz and 81.9593 MHz which was confirmed in previous measurements where several layers were filled. By repeating the tomographic measurement, we can assure that the position of the layers

is stable within a range of $\pi/8$ over time scales of more than a week.

We fit the distribution shown in Fig. 6.5 with three Gaussian profiles of the same width and thus estimate the fraction of atoms in the non-central peaks to be 11%. Note that this value is a conservative upper bound and overestimates the number of atoms in the non-central layer for two reasons: the magnetic field gradient applied during the measurement tilts the trap and thus removes a large percentage (approximately 25%) of all atoms before the transition is driven. Since the central layer is filled with more atoms and to higher energies than the surrounding layers, a greater fraction of atoms will be lost from the central layer. In addition, the atom numbers detected in the non-central peaks are at the detection limit, and are thus influenced by phenomena such as dispersive non-resonant interactions between the imaging light and atoms in state $|2\rangle$.

The phase space density of atoms in the non-central layers is low, and we therefore expect them to follow a thermal distribution. Hence, their influence on the measured condensate fraction, peak condensate density and temperature is negligible. However, the in situ density distribution may be influenced. This is discussed in section ??.

6.5.3 Influence of the finite aspect ratio

In contrast to theory, where the dimensionality of a system can easily be set, experimental realizations of low dimensionality will always remain an approximation. For instance, a two-dimensional system can be realized by strongly confining particles in one of the three spatial dimensions. However, there will always be a residual influence of the third dimension. Its magnitude can be determined by comparing the relevant energy scales of the system (the temperature T , the chemical potential μ and dimer binding energy E_B) to the axial oscillator energy $\hbar\omega_z$. For $T, \mu \gtrsim \hbar\omega_z$, particles populate the axially excited trap levels. We ensure the absence of a significant population of these excited levels by performing a measurement which is explained below. This includes the center-of-mass motion of atom pairs. However, depending on the dimer binding energy E_B the internal structure of atom pairs can be three-dimensional. For $E_B \ll \hbar\omega_z$, the internal structure of the pairs is 2D. For $E_B \gg \hbar\omega_z$, the pairs are deeply bound and their internal 3D structure is not resolved. Hence, only for $E_B \approx \hbar\omega_z$ which in our system occurs at an interaction strength $\ln(k_F a_{2D}) \approx 0.5$, the internal structure of the pairs might affect the behavior of the

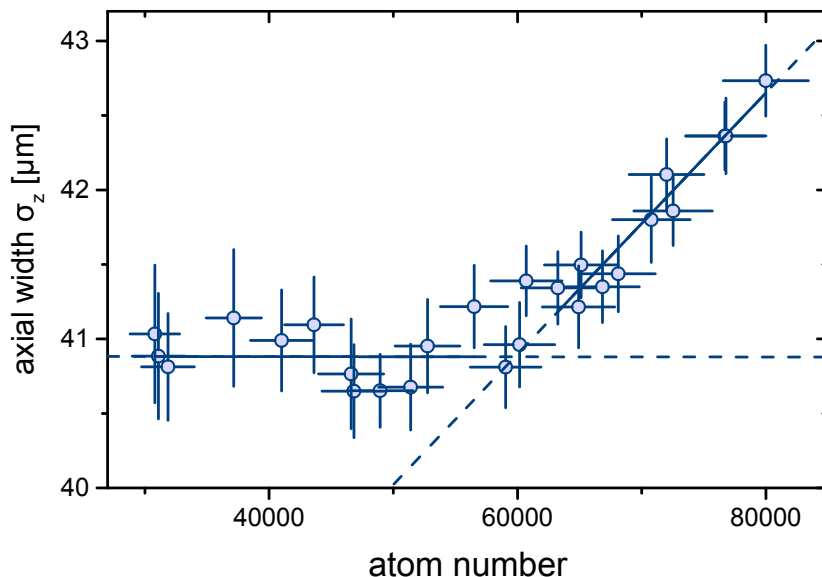


Figure 6.6: **Measurement of axially excited population.** The axial width σ_z is obtained from a Gaussian fit to the density distribution after 3 ms time-of-flight. For atom numbers up to approximately 60 000, only the axial ground state of the trap is occupied and σ_z is constant. For higher atom numbers, axially excited trap levels become populated and σ_z increases. Lines are linear fits to the data, the fit range is indicated by the solid part of each line.

system.

Estimating this effect is complicated: a theoretical treatment beyond the two-body sector is extremely difficult due to strong interactions, and experimental studies would require even larger trap aspect ratios or smaller atom numbers, both of which are currently unfeasible.

We estimate the population of axially excited states due to finite T and μ by investigating the system's momentum distribution in the axial direction. This measurement is performed similar to the technique described in [116] and it relies on the same principles as the previously used band-mapping technique [129].

We release the sample from the SWT, let it expand for a time-of-flight of 3 ms, and measure its vertical extension. In the non-interacting limit, atoms in the axial ground state of the trap have a Gaussian wave function in the axial direction. Their axial expansion can then be described by the dispersion of a Gaussian wave packet, which

is independent of the number of atoms in the axial ground state. Fig. 6.6 shows the axial width σ_z , which is determined from a Gaussian fit to the density distribution, as a function of the number of prepared atoms per spin state N in the weakly interacting Fermi regime at 1400 G and at the coldest attainable temperature. One observes that the axial width is independent of the number of atoms up to approximately $N_{2D} = 60\,000$ atoms per spin state. For $N > N_{2D}$ the axial width starts to increase with growing N . This change in behavior indicates population of the axially excited states, where the atoms have additional momentum in axial direction. The obtained critical atom number N_{2D} is in agreement with the expectations for a trap with the given aspect ratio and anharmonicities. By keeping the atom number below N_{2D} , we can thus ensure that for the investigated temperature only a negligible fraction of atoms populates the axial excited state.

This measurement is performed in the fermionic regime, where due to the Pauli principle multiple occupation of trap levels is suppressed. All other measurements presented here are performed at lower magnetic fields, closer to the bosonic limit ($\ln(k_F a_{2D}) \rightarrow -\infty$). The measurement performed at 1400 G ($\ln(k_F a_{2D}) \gtrsim 6$) thus represents an upper bound on the fraction of particles in the axially excited states as for lower fields the atoms tend to form molecules which occupy lower energy states.

To ensure the absence of a significant amount of axial excitations also for lower magnetic fields and higher temperatures, we make use of the relation between the radial size of a harmonically trapped gas and the energy of the highest occupied oscillator level. We compare the radial size of each sample to that of the measurement at 1400 G, where we have excluded significant population of axially excited states. For this comparison, we estimate the radial Fermi radius r_F by the radius where the particle density reaches the noise floor for a particle number N_{2D} at a magnetic field of 1400 G. Then we integrate the number of particles outside this radius. In this way, we obtain $N_{ex,r}$, an estimate for the number of particles whose energy is larger than $\hbar\omega_z$. Assuming that all degrees of freedom are equally occupied, the number of particles in axially excited states is given by $N_{ex,z} \simeq N_{ex,r}/2$. We find that $N_{ex,z} \lesssim 1.5\%$ for all interaction strengths below $\ln(k_F a_{2D}) = 3$ and temperatures below $T/T_F \simeq 0.3$. Furthermore, for all $T/T_F \lesssim 0.2$, the fraction of axially excited particles is $N_{ex,z} < 1\%$.

Note that this estimate for the axially excited fraction is conservative, as it assumes

constant trap frequencies. It does not take into account that the radial trap frequency decreases by up to about 16% when the magnetic field is decreased to 692 G. This leads to an increase in the corresponding Fermi radius by up to approximately 8%, and to a corresponding overestimation of $N_{ex,z}$.

We have thus measured the phase diagram of a quasi-2D system with small but finite influence of the third dimension. This influence has to be considered when comparing the experimental data to true 2D predictions. Recent theoretical work shows that these effects influence the system and can lead to a higher critical temperature [127].

6.5.4 The rapid ramp of the magnetic field

In order to probe the momentum distribution of the sample, we use the combination of an interaction quench and a matter wave focusing technique described in detail in the main text and in [64]. We turn off the optical SWT, and let the sample expand ballistically in the weak magnetic potential, which is confining in the radial direction. Due to the harmonic shape of this potential, the in-situ momentum distribution of the 2D sample is mapped to a spatial distribution after an expansion time of $t_{\text{exp}} = T/4 = \pi/(2\omega_{\text{exp}})$. In our case, $\omega_{\text{exp}} = \omega_{\text{mag}} \approx 2\pi \times 10$ Hz, which leads to $t_{\text{exp}} = 25$ ms.

To obtain the actual in-situ momentum distribution, it is fundamentally important that interactions are negligible while the gas is expanding, since they would result in a redistribution of momentum. Due to its large aspect ratio, our sample expands rapidly in z -direction. Thus, its density drops rapidly and interactions between the expanding particles are quenched. However, for large interactions strengths there is still residual scattering, which can affect the obtained momentum distribution. We thus minimize the interactions by quickly ramping to the lowest accessible interaction strength on the BEC side (692 G) on a timescale shorter than $125 \mu\text{s}$ just before releasing the sample from the SWT. This procedure leads to a negligible scattering rate during the expansion [64] and projects correlated pairs of atoms onto tightly bound molecules. The measured momentum distribution thus does not contain the relative momentum of the atoms in a pair, but only the center-of-mass momentum of the pair. Thus, fermionic Cooper pairs and bosonic molecules yield the same signature of enhanced low-momentum density in the pair momentum distribution.

As a consequence, information about the Tan contact [81] cannot be obtained from the pair momentum distribution.

We validate that this method does not alter the temperature of the system by comparing the momentum distributions obtained with and without the interaction quench both below (732 G) and above (872 G) the resonance. In both cases the observed temperature are consistent within the experimental uncertainties.

Furthermore, we confirm that the measured non-Gaussian fraction N_q/N remains unchanged for low magnetic fields where pairs are deeply bound. This is achieved by comparing data with and without the magnetic field ramp. For high magnetic fields however, we cannot directly access N_q/N without projecting correlated pairs into molecules. We thus need to make sure that we probe the properties of the interacting system at the original magnetic field, i.e. that the sample does not adapt to the interaction strengths at lower magnetic fields during and after the ramp. To estimate this effect, we prepare a sample at 900 G at a high temperature where we expect $N_q/N = 0$ and perform the rapid ramp without releasing the sample from the trap. We find that it takes more than 11 ms for the momentum distribution to adapt to the interaction strength at the new magnetic field value of 692 G and develop a non-Gaussian fraction. This is two orders of magnitude larger than the timescale of the rapid ramp ($< 125 \mu\text{s}$). Hence, the influence of the rapid ramp technique on the measured quantities can be neglected.

6.5.5 Absorption imaging parameters and calibrations

We use absorption imaging along the z-axis (see Fig.1, main text) to determine the integrated column density $n_{2D}(x, y)$. To obtain a reasonable signal-to-noise ratio we set the imaging intensity to $I \simeq I_{sat}$. Thus, for zero detuning one obtains [130, 131]

$$n_{2D}(x, y) \sigma_0^* = -\ln \frac{I_t(x, y)}{I_0(x, y)} + \frac{I_0(x, y) - I_t(x, y)}{I_{sat}^*} \quad (6.1)$$

$$= OD(x, y) + \frac{I_0(x, y)}{I_{sat}^*} (1 - e^{-OD(x, y)}), \quad (6.2)$$

where I_t is the transmitted intensity after the atomic cloud, I_0 is the initial intensity before the atomic cloud, I_{sat}^* is the effective saturation intensity, σ_0^* is the effective scattering cross section and the optical density OD is defined as $OD = -\ln \frac{I_t}{I_0}$.

Due to the uniform intensity distribution of the imaging beam at the position of the atoms, $I_0(x, y)$ is independent of x and y to a good approximation. In order to calibrate I_0/I_{sat}^* , we take several subsequent data sets of a pure atomic sample at 1400 G both with our regular imaging settings and with a 10 dB attenuated imaging intensity. We then use equation (6.2) and adjust I_0/I_{sat}^* such that the RHS yields the same result both for the regular and the low-intensity setting. Averaging over the data sets then results in $I_0/I_{sat}^* = 0.97_{-0.08}^{+0.13}$. The systematic uncertainties are estimated by the minimum and maximum I_0/I_{sat}^* obtained for the individual data sets. This leads to a systematic uncertainty of $_{-4\%}^{+7\%}$ for the atom number N and the peak density n_{peak} , and a negligible uncertainty for T and N_q/N . In addition, we independently measure the power of the imaging beam and thus determine the imaging intensity to be $I \approx I_{sat}$. This justifies using the literature value σ_0 [132] for σ_0^* .

On the BEC-side, the binding energy of the molecules shifts the resonance frequency which leads to a decreased detection efficiency. Using in-situ images at different fields, we calibrate this factor for our imaging settings. For magnetic fields below 782 G, it deviates from 1 and reaches $N_{at}/N_{mol} = 1.33_{-0.07}^{+0.10}$ at 692 G. This leads to a systematic uncertainty of up to 8% in atom number N and peak density n_{peak} for the affected magnetic fields. More details about the systematic uncertainties can be found in section ??.

The duration of our imaging pulse is $\tau = 8 \mu s$. Due to the small mass of ${}^6\text{Li}$, the atoms are accelerated during the imaging pulse. This results in a Doppler shift of approximately 10 MHz at the end of the imaging pulse. To compensate for this effect, we linearly sweep the imaging laser frequency during the pulse. In order to reduce the shot noise in the absorption images, we use a ten times longer reference pulse. To further improve the quality of the absorption images, we apply a fringe removal algorithm [133].

6.5.6 Temperature determination

We obtain the temperature T of each sample by fitting a Boltzmann distribution given by

$$\tilde{n}(p, t = 0) = n(x, t_{\text{exp}}) = A_0 \exp\left(-\frac{M\omega_{\text{exp}}^2 x^2}{2k_B T}\right) \quad (6.3)$$

to the wing of the radial momentum distribution [64]. Here, M is the mass of the expanding particle, k_B is Boltzmann's constant, A_0 is the amplitude of the fit function, and ω_{exp} is the trapping frequency of the radial magnetic confinement the particles expand in. As evident from Fig. 3A, this function describes the data well over a range of more than 50 pixels. The temperatures used in the main text are the average of approximately 30 realizations. In order to obtain the degeneracy temperature T/T_F , we obtain T_F from the in-situ peak density of the sample as described in the main text.

For magnetic fields ≤ 782 G, the thermal part of the sample has the momentum distribution of molecules. We verified this in a measurement where we prepared the sample at different magnetic fields and let it evolve in time-of-flight for 3 ms before ramping the magnetic field to 527 G, where molecules are deeply bound and are thus not detected in absorption imaging resonant with free atoms. For magnetic fields ≤ 782 G, we observe that all atoms are bound in molecules after this expansion experiment at all investigated temperatures. Thus, they are also bound in the trap. For these magnetic fields, we thus use the molecule mass in equation (6.3). For magnetic fields ≥ 892 G, the binding energy of the quasi-2D dimer is significantly smaller than the thermal energy in our sample. The thermal wing thus has the momentum distribution of atoms and we use the atom mass. For intermediate fields, the thermal part crosses over from the molecular to the atomic momentum distribution. Thus, using the atom and molecule mass one obtains an upper and lower bound on the temperature.

We determine the degeneracy temperature at the intermediate fields from a linear interpolation of T/T_F versus $\ln(k_F a_{2D})$ between 782 G and 892 G for samples where we applied the same heating parameter. This interpolation is depicted in Fig. 6.7 for the lowest attainable temperature. The behavior of the interpolated temperature and of the temperatures obtained using the molecular (red) and atomic (green)

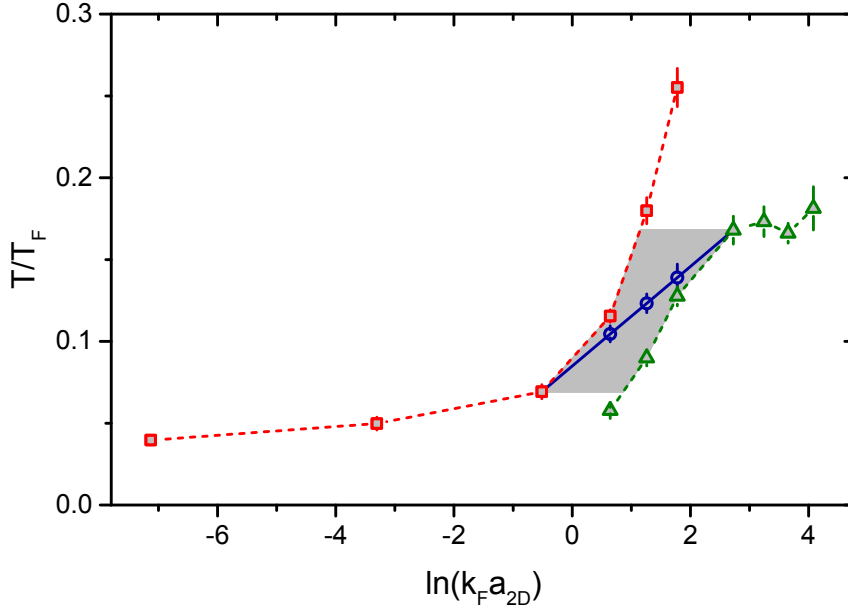


Figure 6.7: **Temperature interpolation in the strongly interacting regime** at the lowest attainable temperature. We obtain the temperature at magnetic fields $782 \text{ G} < B < 892 \text{ G}$, where the thermal part of the gas does not exclusively consist of molecules or atoms, from a linear interpolation between the points at 782 G and 892 G (solid line). The temperatures obtained with the molecule (atom) mass are depicted as red squares (green triangles). The systematic uncertainty of the interpolated temperatures are indicated by the gray area. Dashed lines are guides to the eye. Each data point is the average of approximately 30 individual measurements, the error bars denote the standard error of the mean.

mass justifies the interpolation procedure. The interpolated temperature always lies between the molecular and the atomic limit. It is close to the molecular limit on the BEC side, and crosses over to the atomic limit as $\ln(k_F a_{2D})$ increases. We estimate the systematic error of the interpolated temperature using two assumptions: T/T_F has to be monotonous in $\ln(k_F a_{2D})$, which yields an interval between the T/T_F of the two points between which we interpolate, and T/T_F has to lie between the values obtained from a fit with the molecule mass and the atom mass (red and green data in Fig. 6.7). The overlap of these two intervals is indicated by the gray area in Fig S6.7. It gives an upper bound for the systematic uncertainty of the interpolation result.

6.5. Appendix

B (G)	ℓ_z/a_{3D}	$\ln(k_F a_{2D})_{T_c}$ (stat.)(sys.)	$\ln(k_F \tilde{a}_{2D})_{T_c}$ (stat.)(sys.)	T_c/T_F (stat.)(sys.)	$(T_c/T_F)_{\text{in-situ}}$ (stat.)
692	7.11	7.30 (4) $\begin{pmatrix} +4 \\ -5 \end{pmatrix}$	0.96 (4) $\begin{pmatrix} +2 \\ -3 \end{pmatrix}$	0.089 (15) $\begin{pmatrix} +14 \\ -13 \end{pmatrix}$	0.090 (13)
732	3.98	3.42 (2) $\begin{pmatrix} +4 \\ -6 \end{pmatrix}$	0.45 (2) $\begin{pmatrix} +3 \\ -5 \end{pmatrix}$	0.100 (22) $\begin{pmatrix} +17 \\ -15 \end{pmatrix}$	0.099 (27)
782	1.55	0.59 (1) $\begin{pmatrix} +4 \\ -7 \end{pmatrix}$	0.20 (1) $\begin{pmatrix} +4 \\ -6 \end{pmatrix}$	0.129 (35) $\begin{pmatrix} +24 \\ -18 \end{pmatrix}$	0.112 (44)
812	0.55	0.57 (1) $\begin{pmatrix} +2 \\ -7 \end{pmatrix}$	0.79 (2) $\begin{pmatrix} +2 \\ -7 \end{pmatrix}$	0.146 (25) $\begin{pmatrix} +50 \\ -23 \end{pmatrix}$	0.146 (21)
832	0	1.23 (1) $\begin{pmatrix} +2 \\ -8 \end{pmatrix}$	1.33 (1) $\begin{pmatrix} +2 \\ -8 \end{pmatrix}$	0.167 (39) $\begin{pmatrix} +48 \\ -34 \end{pmatrix}$	0.122 (103)
852	-0.46	1.72 (1) $\begin{pmatrix} +2 \\ -9 \end{pmatrix}$	1.76 (1) $\begin{pmatrix} +2 \\ -9 \end{pmatrix}$	0.167 (27) $\begin{pmatrix} +42 \\ -22 \end{pmatrix}$	0.122 (60)

Table 6.1: **Measured critical temperatures.** The measured critical temperatures T_c/T_F are given with their respective statistical and systematic errors as a function of the magnetic offset field B , ℓ_z/a_{3D} , and the 2D interaction parameter $\ln(k_F a_{2D})$ at T_c/T_F . In addition, also the alternative 2D interaction parameter $\ln(k_F \tilde{a}_{2D})_{T_c}$ obtained with equation (??) and the critical temperature $(T_c/T_F)_{\text{in-situ}}$ obtained from the in-situ temperature fit are given.

The statistical errors of the interpolated T/T_F are obtained from the statistical errors at 782 G and 892 G.

In addition to the temperature determination from the momentum distribution, we also extract the temperature from the in-situ data. Applying the local density approximation to the whole cloud, we plot the in-situ density as a function of the trapping potential $V(r)$ and fit its wing with a Boltzmann distribution, which in this case is given by $n(V) = B_0 \exp\left(-\frac{\alpha V}{k_B T}\right)$, where $1 \leq \alpha \leq 2$ takes into account whether the thermal wing consists of atoms or molecules. For the intermediate magnetic fields, we perform an interpolation similar to the one mentioned above to determine α .

For magnetic fields up to 812 G, the temperatures obtained from both methods agree for low temperatures. For low fields and the highest temperatures, the in-situ fit yields larger temperatures. For larger fields, the temperature from the in-situ data is systematically lower than the temperature obtained from the momentum distribution. The reasons for this deviation are still unclear. Nevertheless, within their errors, the extracted critical temperatures from both methods are still compatible with each other. The values for T_c/T_F obtained with both methods are listed in table 6.1.

Superfluidity in a 2D Fermi gas

7

Publication

PHYSICAL REVIEW LETTERS **115**, 010401 (2015)

Observation of the Berezinskii-Kosterlitz-Thouless Phase Transition in an Ultracold Fermi Gas

P. A. Murthy¹, I. Boettcher², L. Bayha¹, M. Holzmann^{3,4}, D. Kedar¹, M. Neidig¹,
M. G. Ries¹, A. N. Wenz¹, G. Zürn¹, and S. Jochim¹

¹*Physikalisches Institut, Ruprecht-Karls-Universität Heidelberg*

²*Institut für Theoretische Physik, Ruprecht-Karls-Universität Heidelberg*

³*LPTMC, UMR 7600 of CNRS, Université Pierre et Marie Curie*

⁴*Université Grenoble Alpes, CNRS, LPMMC, UMR 5493*

Abstract

We experimentally investigate the first-order correlation function of a trapped Fermi gas in the two-dimensional BEC-BCS crossover. We observe a transition to a low-temperature superfluid phase with algebraically decaying correlations. We show that the spatial coherence of the entire trapped system can be characterized by a single temperature-dependent exponent. We find the exponent at the transition to be constant over a wide range of interaction strengths across the crossover. This suggests that the phase transitions in both the bosonic regime and the strongly interacting crossover regime are of Berezinskii-Kosterlitz-Thouless type and lie within the same universality class. On the bosonic side of the crossover, our data are well-described by the quantum Monte Carlo calculations for a Bose gas. In contrast, in the strongly interacting regime, we observe a superfluid phase which is significantly influenced by the fermionic nature of the constituent particles.

DOI: [10.1103/PhysRevLett.115.010401](https://doi.org/10.1103/PhysRevLett.115.010401)

7.1 Introduction

Long-range coherence is the hallmark of superfluidity and Bose-Einstein condensation [23, 24]. The character of spatial coherence in a system and the properties of the corresponding phase transitions are fundamentally influenced by dimensionality. The two-dimensional case is particularly intriguing as for a homogeneous system, true long-range order cannot persist at any finite temperature due to the dominant role of phase fluctuations with large wavelengths [6, 51, 134]. Although this prevents Bose-Einstein condensation in 2D, a transition to a superfluid phase with quasi-long-range order can still occur, as pointed out by Berezinskii, Kosterlitz, and Thouless (BKT) [8, 9, 10]. A key prediction of this theory is the scale-invariant behavior of the first-order correlation function $g_1(r)$, which, in the low-temperature phase, decays algebraically according to $g_1(r) \propto r^{-\eta}$ for large separations r . Importantly, the BKT theory for homogeneous systems predicts a universal value of $\eta_c = 1/4$ at the critical temperature, accompanied by a universal jump of the superfluid density [135].

Several key signatures of BKT physics have been experimentally observed in a variety of systems such as exciton-polariton condensates [136], layered magnets [137, 138], liquid ^4He films [13], and trapped Bose gases [53, 124, 95, 56, 121, 112, 139]. Particularly in the context of superfluidity, the universal jump in the superfluid density was measured in thin films of liquid ^4He [13]. More recently, in the pioneering interference experiment with a weakly interacting Bose gas [53], the emergence of quasi-long-range order and the proliferation of vortices were shown.

There are still important aspects of superfluidity in two-dimensional systems that remain to be understood, which we aim to elucidate in this work with ultracold atoms. One question is whether the BKT phenomenology can also be extended to systems with nonuniform density. Indeed, if the microscopic symmetries are the same, the general physical picture involving phase fluctuations should be valid also for inhomogeneous systems. However, it is not known if algebraic order persists at all in the presence of inhomogeneity and particularly, whether the correlations in the whole system can still be characterized by a single exponent. Another fundamental issue that arises in the study of superfluidity is the pairing of fermions. While

fermionic superfluidity has been extensively investigated in 3D systems [102, 37, 140], there are open experimental questions in the 2D context. In particular, what is the long-range behavior of spatial coherence of a 2D fermionic superfluid, and can it also be described in the BKT framework like its bosonic counterpart?

In this work, we probe the first-order correlation function $g_1(r)$ of a trapped Fermi gas in the two-dimensional BEC-BCS crossover regime [99, 58]. The correlation function is determined from a measurement of the in situ momentum distribution of the gas. We demonstrate that even in this inhomogeneous system, algebraic order persists in $g_1(r)$ below a critical temperature. Furthermore, a quantitative analysis of the scaling exponents across the crossover reveals the validity of the BKT theory also in the fermionic regime.

7.2 Experimental System

Our measurements are performed with a gas of 10^5 ^6Li atoms confined in a highly anisotropic potential. The axial and radial trapping frequencies are $\omega_z \approx 2\pi \times 5.5$ kHz and $\omega_r \approx 2\pi \times 18$ Hz, leading to an aspect ratio of approximately 300:1. Our experimental system and methodology have been described in detail in Ref. [99]. We perform in situ imaging of the sample as a function of temperature and interaction strength. From the central density, we define the Fermi momentum k_F and Fermi temperature T_F , which constitute the relevant scales in the system. As shown in Ref. [99], for our experimental parameters, all the relevant energy scales are smaller than the axial confinement energy $\hbar\omega_z$. Hence the system is in the quasi-2D regime.

We tune the interparticle interactions using a Feshbach resonance located at 832 G. Using the 3D scattering length a_{3D} [97], the axial oscillator length ℓ_z ¹, and the Fermi momentum, we construct the effective 2D scattering length a_{2D} and crossover parameter $\ln(k_F a_{2D})$ [58]. For $\ln(k_F a_{2D}) \ll -1$ and $\ln(k_F a_{2D}) \gg 1$ we are in the bosonic and fermionic limit of the crossover, respectively.

In addition to the measurements, we perform path-integral quantum Monte Carlo (QMC) computations of a Bose gas [141, 142] in a highly anisotropic 3D trap with parameters similar to those employed in the experiment. In the simulations, the bosons interact via the molecular scattering length $a_{mol} = 0.6 a_{3D}$ [59]. The relevant

¹We define $\ell_z = \sqrt{\hbar/M\omega_z}$, where M is twice the fermion mass.

7.3. The First-order Correlation Function $g_1(r)$

parameters that describe the system in terms of pointlike bosons are the effective bosonic coupling strength $\tilde{g} = \sqrt{8\pi}a_{\text{mol}}/\ell_z$ and the condensation temperature of an ideal 2D Bose gas $T_{\text{BEC}}^0 = \sqrt{6N} \frac{\hbar\omega_r}{\pi k_{\text{B}}} \approx 140 \text{ nK}$, where N is the number of particles. We use these bosonic parameters to compare our measurements to QMC at the lowest magnetic field values, where we have $\tilde{g} = 0.6, 1.07, 2.76, 7.75$. From the QMC computations, we obtain the local density profile and the one-body density matrix $\rho_1(\mathbf{x}, \mathbf{x}') = \langle \hat{\phi}^\dagger(\mathbf{x})\hat{\phi}(\mathbf{x}') \rangle$ for different interaction strengths and temperatures, where $\hat{\phi}(\mathbf{x})$ is the bosonic field operator.

7.3 The First-order Correlation Function $g_1(r)$

The global off-diagonal correlations in the system are encoded in the momentum distribution of particles. To reliably measure the in-plane momentum distribution $\tilde{n}(\mathbf{k})$ of our sample, we employ the matterwave focusing technique described in Refs. [91, 95, 64], where the gas expands freely in the axial direction while being focused by a harmonic potential in the radial plane. After expansion for a quarter of the period of the focusing potential, the initial momentum distribution is mapped to the spatial density profile, which we then image. We combine this focusing method with a rapid magnetic field ramp into the weakly interacting regime. This rapid ramp technique – along with the fast axial expansion due to the large anisotropy of the trap – ensures that inter-particle collisions during the focusing do not cause significant distortions to the measured momentum distribution. From $\tilde{n}(\mathbf{k})$, we extract the absolute temperature T by means of a Boltzmann fit to the high- \mathbf{k} thermal region ².

To quantitatively investigate the spatial coherence in our system, we determine the first-order correlation function $g_1(\mathbf{r})$ by means of a 2D Fourier transform of the measured $\tilde{n}(\mathbf{k})$. It is related to the one-body density matrix $\rho_1(\mathbf{x}, \mathbf{x}')$ by means of

$$\begin{aligned} g_1(\mathbf{r}) &= \int d^2k \tilde{n}(\mathbf{k}) e^{i\mathbf{k}\cdot\mathbf{r}} \\ &= \int d^2R \rho_1(\mathbf{R} - \mathbf{r}/2, \mathbf{R} + \mathbf{r}/2). \end{aligned} \quad (7.1)$$

A derivation of these relations is given in the Appendix 7.5.1. The function $g_1(\mathbf{r})$ is a trap-averaged function, which captures the off-diagonal correlations of all par-

²The temperatures accessed in this work range between 40 nK and 150 nK

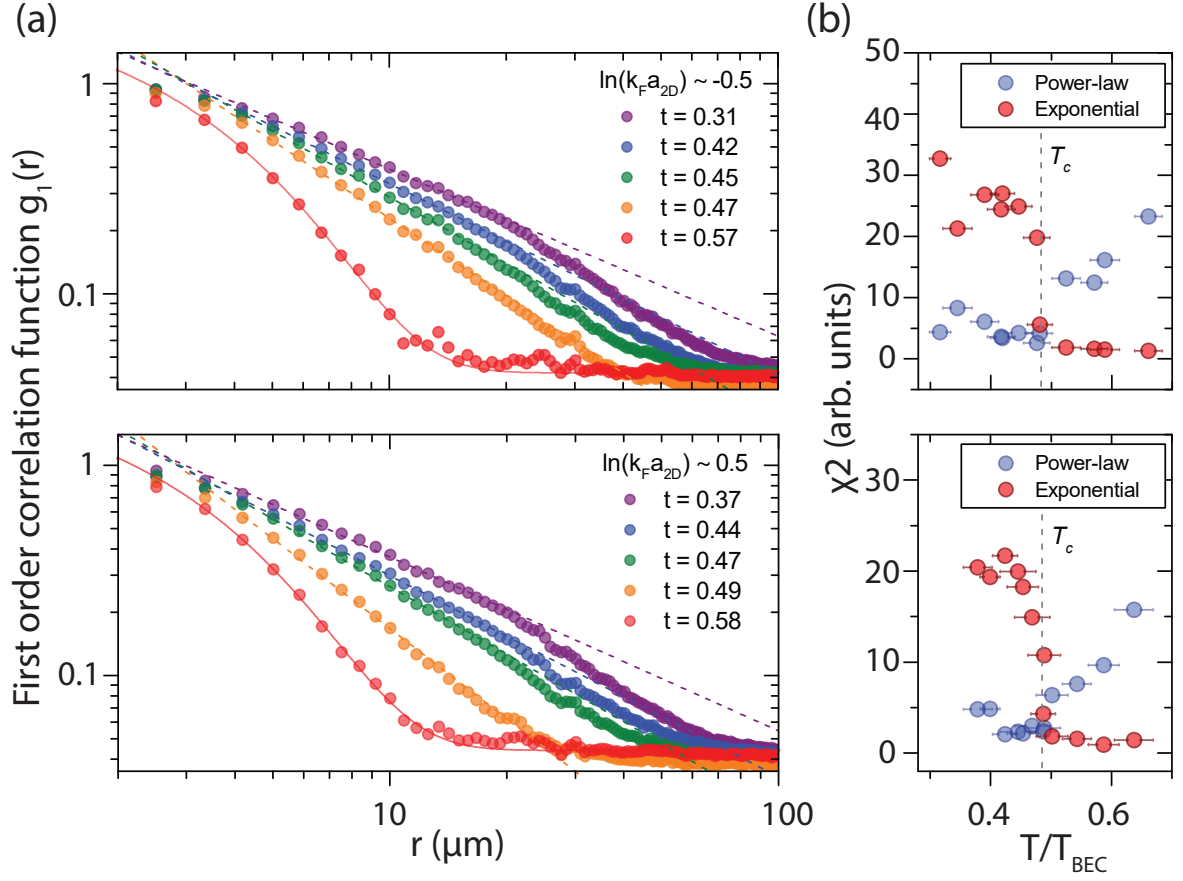


Figure 7.1: First-order correlation function $g_1(r)$ for different temperatures at $\ln(k_F a_{2D}) \simeq -0.5$ (upper left panel) and $\ln(k_F a_{2D}) \simeq 0.5$ (lower left panel). The temperature scale used here is $t = T/T_{\text{BEC}}^0$. At high temperatures correlations decay exponentially as expected for a gas in the normal phase. At low temperatures, we observe algebraic correlations ($g_1(r) \propto r^{-\eta(T)}$) with a temperature-dependent scaling exponent $\eta(T)$. This qualitative change of behavior is clearly visible in the χ^2 for both exponential and algebraic fits (right panel), where a small value signals a good fit. In particular, this allows for an accurate determination of the transition temperature T_c (vertical dashed lines) (see Appendix 7.5.2).

7.3. The First-order Correlation Function $g_1(r)$

ticles in the system. Similarly, one can also define the central correlation function $G_1(\mathbf{r}, 0) = \langle \hat{\phi}^\dagger(\mathbf{r})\hat{\phi}(0) \rangle$, measured in the interference experiments [53, 143], which characterizes the correlations only in the central region of the trap, where the density is approximately uniform. In general, the two functions do not contain the same information and are only equivalent in a translation invariant system (see Appendix 7.5.1). Note that due to the radial symmetry of the trapping and focusing potentials, the correlations only depend on distance and therefore it suffices to consider the azimuthally averaged function $g_1(r)$.

7.3.1 Algebraic decay in $g_1(r)$

Fig. 7.1 shows the experimentally determined $g_1(r)$ for different temperatures in the strongly interacting crossover regime. The correlation functions are normalized such that $g_1(0) = 1$. As expected, at high temperatures $g_1(r)$ decays exponentially with correlation lengths on the order of the thermal wavelength ($\lambda_T \sim 1.5 \mu\text{m}$). As we lower the temperature, we eventually observe the onset of coherence over an extended spatial range that corresponds to several radial oscillator lengths ℓ_r , with $\ell_r \approx 6.8 \mu\text{m}$. This shows that phase fluctuations in the system are non-local and span regions of the sample where the density is not uniform. As pointed out in Refs. [144, 145], such extended spatial coherence in an interacting system is a sufficient condition for superfluidity in two-dimensional systems.

As the temperature is lowered below a critical value, we find that the correlation function in an intermediate range $3\lambda_T < r < 20\lambda_T$ is well-described by a power-law decay, whereas exponential behavior is clearly disfavored. We quantify this by extracting the χ^2 for both fit functions at different temperatures and observe a clear transition from exponential to algebraic decay (see Fig. 7.1 b). This qualitative change in $g_1(r)$ provides an alternative way to determine the phase transition temperature T_c from the kink in $\chi^2(T)$ (see Appendix 7.5.2). We find that the corresponding T_c obtained in this manner agrees with the temperature associated with the onset of pair condensation that was measured in our previous work [99].

7.3.2 Scaling exponents

The power-law decay of $g_1(r)$ means that the spatial coherence of the entire sample is characterized by a single exponent η . Fig. 7.2 shows the experimentally determined

η for all the interaction strengths accessed in this work. We find $\eta(T)$ to increase with temperature until it reaches a maximal value at T_c , indicating a slower fall-off of correlations at lower temperatures. Although such temperature-dependence is qualitatively consistent with BKT theory, we observe the values of the exponents to be in the range $0.6 - 1.4$ for the temperatures accessed in the measurement, which is substantially above the expectation of $\eta \leq 0.25$ for the homogeneous setup.

To confirm the large scaling exponents in the trapped system, we compute the one-body density matrix on the bosonic side using the QMC technique described above. This allows to determine both the trap-averaged correlation function $g_1(r)$ as well as the central correlation function $G_1(r, 0)$. The trap-averaged $g_1(r)$ shows the same behavior as in the experimental case, i.e. a transition from exponential to algebraic decay at low temperatures. The corresponding QMC transition temperatures also agree with the measured values of T_c for $\tilde{g} = 0.60, 1.07$, and 2.76 . Furthermore, the maximal scaling exponent at T_c extracted from the QMC- $g_1(r)$ for $\tilde{g} = 0.6$ is approximately 1.35 , which is close to the experimentally determined $\eta(T_c) \simeq 1.4$. The central correlation function $G_1(r, 0)$ shows a transition to algebraic order as well – with the same T_c as in the experiment – but with a maximal exponent of approximately 0.25 , as expected for a homogeneous system. This finding is also in agreement with the measurement of $G_1(r, 0)$ in the interference experiments [53], and is explained by the nearly uniform density in the center of the trap.

Fig. 7.2a shows the comparison between the experimental and QMC values of $\eta(T)$ for $\tilde{g} = 0.60$ ($\ln(k_F a_{2D}) \simeq -7.3$). Although both show similar dependence on temperature, we find a considerable quantitative deviation between them. As discussed in the Appendix 7.5.3, this discrepancy can mostly be attributed to the effect of the finite imaging resolution in the measurement of $\tilde{n}(\mathbf{k})$, which leads to an apparent broadening at low momenta and thus overestimates the value of η . We show an estimate of this temperature-dependent effect on the exponents (open red triangles) in Fig. 7.2a. There may be other effects in the experiment that contribute additionally to the deviation, such as higher order corrections to the determination of \tilde{g} from the fermionic scattering parameters, and density-dependent inelastic loss processes.

The experimental and simulated data raise the question why correlations in the trapped system decay with a larger scaling exponent than in the homogeneous case.

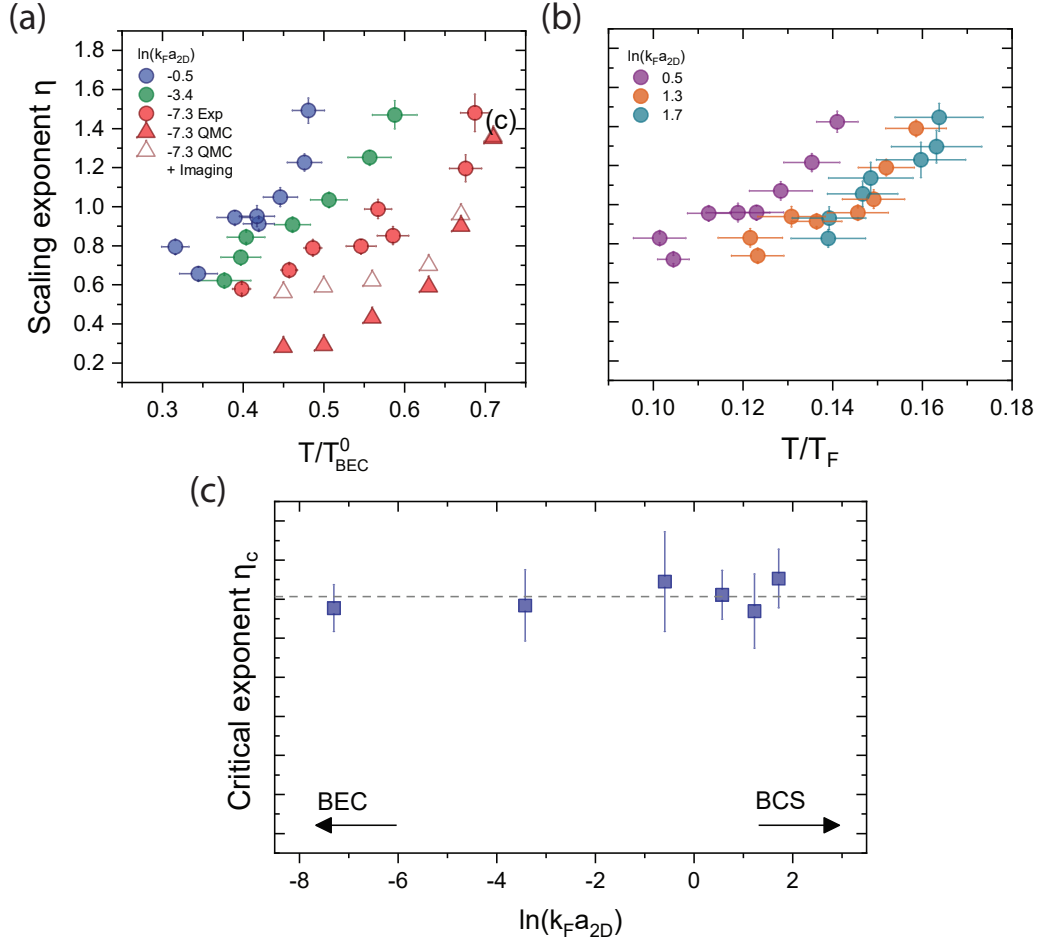


Figure 7.2: Power-law scaling exponents across the two-dimensional BEC-BCS crossover. The temperature-dependent scaling exponent $\eta(T)$ in (a) the bosonic limit and (b) the crossover regime is shown. The relevant temperature scales in these cases are given by T_{BEC}^0 and T_F , respectively. The crossover parameter $\ln(k_F a_{2D})$ is mildly temperature dependent. For reference we display the value at the critical temperature. For $\tilde{g} = 0.60$ ($\ln(k_F a_{2D}) \simeq -7.3$) we show the prediction from QMC calculations for a Bose gas (filled red triangles) and an estimate of the effect of the finite imaging resolution present in the measured data (open red triangles) (see Appendix 7.5.3). We find an exponent which increases with temperature in agreement with BKT-theory. The power-law decay eventually ceases at T_c where a maximal exponent η_c is reached. (c) The value of η_c is approximately constant for all $\ln(k_F a_{2D})$ where we have previously observed condensation of pairs [99]. This strongly suggests that the associated phase transition are within one universality class.

To elucidate the role of inhomogeneity, we consider the bosonic field operator given by $\hat{\phi}(\mathbf{r}) \simeq \sqrt{\rho(\mathbf{r})} \exp(i\hat{\varphi}(\mathbf{r}))$. In this representation, it is clear that one contribution to the decay of $g_1(r)$ in Eq. (7.1) comes from the spatial variation of the superfluid density $\rho(\mathbf{r})$. Using a local density approximation and assuming the superfluid density to have a Thomas–Fermi profile, we estimate a contribution of approximately 0.3 – 0.4 (see Appendix 7.5.4) to the effective exponent. Still, this fails to explain the large exponents observed in the experiment and the QMC simulations close to T_c . This suggests that the increase in the effective exponents is predominantly due to phase fluctuations in the inhomogeneous system, whose spectrum is modified by the discrete level-structure of the harmonic trapping potential and the Thomas–Fermi profile of the superfluid. This inference is further supported by calculations of phase fluctuations in a trapped 2D Bose gas at low temperatures [119], which indicate a trap-induced increase of the effective exponent by up to a factor of three.

Our measurements of $g_1(r)$ and $\eta(T)$ across the two-dimensional BEC-BCS crossover provide a unique opportunity to study BKT physics even in the fermionic regime. Fig. 7.2 displays the measurement of the scaling exponent across the crossover. Remarkably, we find that – despite varying the scattering length by several orders of magnitude – the maximal scaling exponent η_c at the transition shows no dependence on the interaction strength (see Fig. 7.2c). We note that the actual value of $\eta_c \simeq 1.4$ might depend on parameters specific to the experiment, such as particle number and trapping frequencies. Nevertheless, the fact that η_c remains constant across the BEC-BCS crossover unambiguously shows that the long-range properties at the transition are independent of inter-particle interactions. This is evidence that all the observed transitions for different interaction strengths lie in the same universality class. In particular, it shows that, even as we cross over to the fermionic side ($\ln(k_F a_{2D}) > 0$), the observed transitions are of BKT-type.

7.4 Local properties of the superfluid

We now turn to a quantitative investigation of local properties of the system. This allows to benchmark our measurements with (i) the QMC results for point-like bosons in the same quasi-2D trapping potential as realized in the experiment and (ii) QMC calculations of the homogenous 2D Bose gas [65, 122]. For this we investigate the

phase space density (PSD)

$$\mathcal{D} = n\lambda_T^2. \quad (7.2)$$

Herein, n is the 2D density of atoms in a single hyperfine state and $\lambda_T^2 = 2\pi\hbar^2/Mk_B T$ is the thermal wavelength of bosons with M being twice the fermion mass. Note that n coincides with the density of dimers in the bosonic limit.

We first consider coupling strengths $\tilde{g} = 0.60, 1.07$, and 2.76 on the bosonic side of the crossover. Fig. 7.3a shows the comparison between the experimentally measured and QMC-computed values of the PSD in the trap-center for $\tilde{g} = 2.76$. We find excellent agreement between the two data sets. In particular, at T_c , the central PSD for all three \tilde{g} are found to agree very well with $\mathcal{D}_c = \ln(380/\tilde{g})$ derived for a homogeneous 2D Bose gas with weak interactions (horizontal dashed line) [65, 122]. This shows that the onset of algebraic correlations in the trapped system coincides with the local PSD in the center of the trap crossing the critical value of the homogeneous system [141].

As we further increase $\ln(k_F a_{2D})$, the effective boson coupling strength \tilde{g} becomes very large. For $\tilde{g} = 7.75$ ($\ln(k_F a_{2D}) \simeq 0.5$), we find substantial deviations between the experimental and QMC data for the PSD at low temperatures (see Fig. 7.3b). Moreover, our QMC calculations show that the associated 2D Bose gas is in its normal phase for all temperatures accessed in the experiment. In contrast, the measurements show a clear superfluid phase transition at this interaction strength, as shown in Fig. 7.1 (lower panel). This provides evidence for the crossover to a superfluid phase whose properties are not captured by a description that assumes point-like dimers.

Both experimental and simulated data in the bosonic limit are obtained in a highly anisotropic 3D trapping potential. Still, local observables such as the central PSD and the central correlation function $G_1(r, 0)$ agree excellently in their critical properties with the theory of a homogenous 2D Bose gas and the corresponding BKT phenomena. In the case of global correlations, we showed that the inhomogeneity leads to significant deviations from the homogeneous case, most importantly an increase in the exponent of the power-law decay. However, the general features in the off-diagonal correlations – such as the temperature-dependence of $\eta(T)$ and the independence of η_c from $\ln(k_F a_{2D})$ – suggest that the long-range physics are still

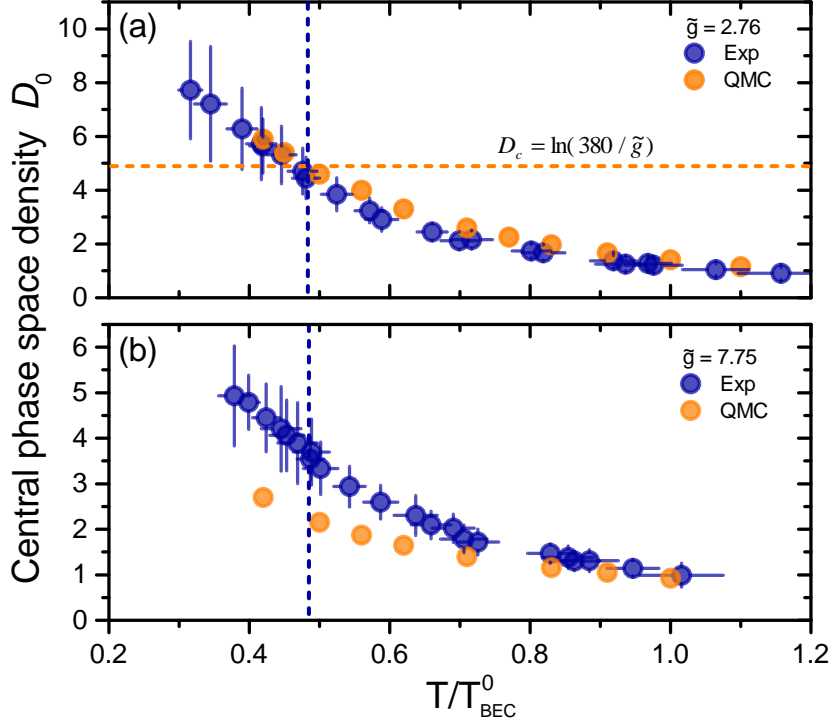


Figure 7.3: Peak phase space density $\mathcal{D}_0 = n_0 \lambda_T^2$ obtained from the central density n_0 . The panels (a) and (b) show experimental and simulated data (for bosons) for the coupling strengths $\tilde{g} = 2.76$ and $\tilde{g} = 7.75$, respectively. The vertical dashed lines indicate the corresponding critical temperatures obtained from the measured onset of algebraic order. (a) We find excellent agreement between experiment and QMC for $\tilde{g} = 2.76$, providing evidence that we realize a strongly interacting 2D Bose gas. We verify the applicability of $\mathcal{D}_c = \ln(380/\tilde{g})$ [65] at this interaction strength (horizontal dashed line). (b) For the stronger coupling $\tilde{g} = 7.75$, however, we find the bosonic simulations to deviate from the measured results, indicating fermionic superfluidity.

captured by the ideas underlying BKT-theory for the two-dimensional XY model.

In conclusion, we investigated the nature of the phase transition of a trapped 2D ultracold Fermi gas. We measured for the first time the first-order correlation function of the entire system and extracted its long-range behavior. We showed that it is consistent with a description by a single power-law exponent for large distances. The transition temperature for onset of algebraic order coincides with the one obtained from the onset of pair condensation in [99]. By comparing the experimental data to QMC calculations on the bosonic side, we found the system to realize a strongly interacting 2D Bose gas. The measured phase space densities and correlations on the fermionic side, instead, are not captured by a description in terms of point-like bosons, which indicates the crossover to a fermionic superfluid.

Our measurements show that the spatial coherence even in trapped systems can be characterized by a single scaling exponent. However, understanding the underlying mechanism remains a challenge for future explorations, and may lead to a deeper understanding of phase transitions in inhomogeneous systems.

7.5 Appendix

7.5.1 Extracting the first-order correlation function

From the matterwave focussing technique we obtain the momentum distribution

$$\tilde{n}(\mathbf{k}) = \langle \hat{a}_{\mathbf{k}}^\dagger \hat{a}_{\mathbf{k}} \rangle \quad (7.3)$$

of the trapped gas. Herein, $\hat{a}_{\mathbf{k}}^\dagger$ is the creation operator for a particle with wave vector \mathbf{k} . Note that $\tilde{n}(\mathbf{k})$ involves an average over all particles in the trap.

We now show that the Fourier transform of this function coincides with $g_1(\mathbf{r})$ in Eq. (1). For this we recall that $\hat{a}_{\mathbf{k}}$ is obtained from $\hat{\phi}(\mathbf{x})$ by means of

$$\hat{\phi}(\mathbf{x}) = \int \frac{d^2k}{(2\pi)^2} e^{i\mathbf{k}\cdot\mathbf{x}} \hat{a}_{\mathbf{k}}. \quad (7.4)$$

Inserting this definition into (1) with the substitution $\mathbf{s} = \mathbf{R} + \mathbf{r}/2$ we arrive at

$$\begin{aligned}
 g_1(\mathbf{r}) &= \int d^2s \rho_1(\mathbf{s}, \mathbf{r} + \mathbf{s}) \\
 &= \int d^2s \langle \hat{\phi}^\dagger(\mathbf{s}) \hat{\phi}(\mathbf{r} + \mathbf{s}) \rangle \\
 &= \int d^2s \frac{d^2k}{(2\pi)^2} \frac{d^2k'}{(2\pi)^2} e^{-i(\mathbf{k}-\mathbf{k}')\cdot\mathbf{s}} e^{i\mathbf{k}'\cdot\mathbf{r}} \langle \hat{a}_{\mathbf{k}}^\dagger \hat{a}_{\mathbf{k}'} \rangle \\
 &= \int \frac{d^2k}{(2\pi)^2} \frac{d^2k'}{(2\pi)^2} (2\pi)^2 \delta^{(2)}(\mathbf{k} - \mathbf{k}') e^{i\mathbf{k}'\cdot\mathbf{r}} \langle \hat{a}_{\mathbf{k}}^\dagger \hat{a}_{\mathbf{k}'} \rangle \\
 &= \int \frac{d^2k}{(2\pi)^2} e^{i\mathbf{k}\cdot\mathbf{r}} \langle \hat{a}_{\mathbf{k}}^\dagger \hat{a}_{\mathbf{k}} \rangle. \tag{7.5}
 \end{aligned}$$

The expression in the last line is the Fourier transform of $\tilde{n}(\mathbf{k})$.

In a translation invariant situation, the one-body density matrix can be written as $\rho_1(\mathbf{x}, \mathbf{x}') = f(\mathbf{x} - \mathbf{x}')$, with some function f . In this case we have $g_1(\mathbf{r}) = \int d^2s \rho_1(0, \mathbf{r}) \propto G_1(0, \mathbf{r})$. The difference between the trap-averaged correlation function, $g_1(\mathbf{r})$, and the central correlation function, $G_1(0, \mathbf{r})$, then consists of an overall (volume) factor, which vanishes in the normalization procedure.

Momentum resolution and coherence length: The matterwave focusing lens used for the measurement of $\tilde{n}(\mathbf{k})$ has a magnification factor $M\omega_{lens}$, where $\omega_{lens} = 2\pi \times 10$ Hz is the trap frequency of the focusing potential and M is the molecular mass. From this, the effective momentum space resolution can be obtained according to $\Delta k = M\omega_{lens}\Delta x/\hbar \simeq 0.035 \mu\text{m}^{-1}$, with $\Delta x \sim 5 \mu\text{m}$ being the spatial imaging resolution. This means that the largest coherence length that is accessible in $g_1(r)$ is approximately $L = 2\pi/\Delta k \sim 105 \mu\text{m}$.

7.5.2 Extracting critical temperature and critical scaling exponent

The qualitative change of the decay of correlations when lowering the temperature allows for a determination of the critical temperature T_c for each value of a_{2D} . For this purpose we fit both an exponential ($g_1(r) = ae^{-r/\xi}$) and algebraic ($g_1(r) = ar^{-\eta}$) model function to the intermediate length scales of $g_1(r)$ and extract the associated χ^2 -value. A smaller value of χ^2 corresponds to a better fit. In Fig. S7.4 (upper panel) we display $\chi^2(T)$ for 812 G ($\tilde{g} = 7.75$). A sharp transition in the behavior of correlations is visible at a certain temperature, which we associate with the critical

temperature T_c . To determine T_c we piecewise linearly interpolate $\chi^2(T)$ according to

$$\chi_{alg}^2(T) = c_1\theta(T_c^{(1)} - T) + c_2(T - T_c^{(1)})\theta(T - T_c^{(1)}), \quad (7.6)$$

$$\chi_{exp}^2(T) = c_3(T_c^{(2)} - T)\theta(T_c^{(2)} - T) + c_4\theta(T - T_c^{(2)}) \quad (7.7)$$

for the algebraic (alg) and exponential (exp) fits, respectively. Here $\theta(x)$ is the Heaviside step function. We generically find c_1 and c_4 to be small, which justifies the choice of a power law fit at low temperatures, and an exponential fit at large temperatures. Furthermore, the temperatures $T_c^{(1)}$ and $T_c^{(2)}$ coincide within a few percent. We set $T_c = (T_c^{(1)} + T_c^{(2)})/2$ to obtain the transition temperature.

Using the critical temperature T_c found in this manner, we extract the scaling exponent η_c at the transition. For this purpose we extrapolate the experimental data points for $\eta(T)$ by means of a quadratic polynomial fit, see Fig. S 7.4 (lower panel) and extract the value of $\eta(T_c)$. We list the measured critical temperatures and scaling exponents in Table 6.1.

Errors: The method described above to extract the critical exponents contains some uncertainties. The statistical errors on the measured exponents are quite small and the error on η_c as shown in Fig. 2.c is mainly due to the uncertainty in the extrapolation of $\eta(T)$. The error bars are obtained according to $\delta\eta_c = |\eta(T_c^{(1)}) - \eta(T_c^{(2)})|/2$.

7.5.3 Systematic Effects

The errors on experimental quantities shown in the main text are statistical uncertainties of our measurements. The systematic effects in our measurements have been discussed in detail in [99]. In this work, we additionally introduce the temperature scale T/T_{BEC}^0 and extract the scaling exponent $\eta(T)$ from $g_1(r)$. These quantities are systematically affected by the following factors:

Uncertainty in particle number

We determine the number of atoms in the cloud from in-situ absorption images. N is affected by the intensity of the imaging beam, magnification of the imaging

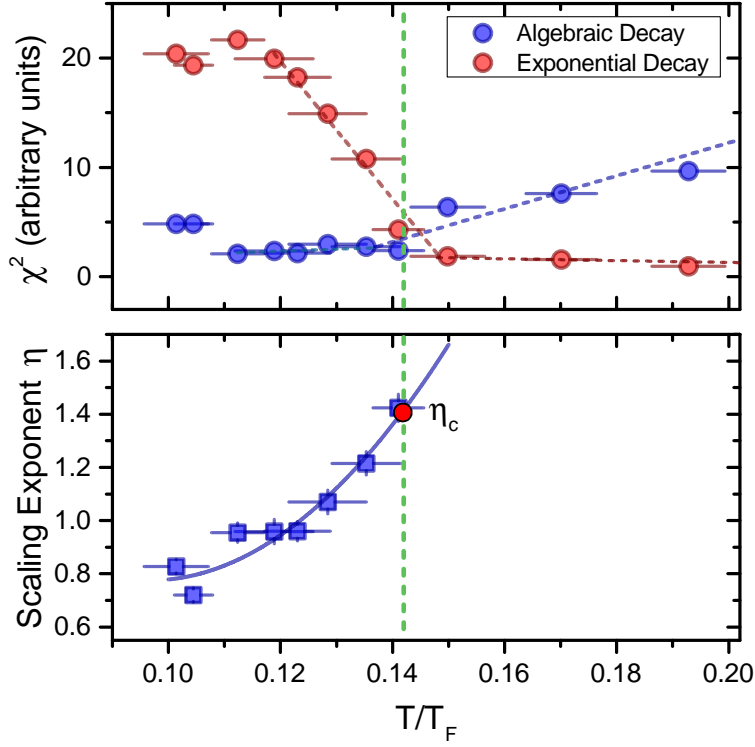


Figure 7.4: Extracting critical temperature T_c and critical exponent η_c at 812 G. The upper panel shows the χ^2 -values for exponential (red) and power law (blue) fits of $g_1(r)$, respectively. Lower values of χ^2 indicate a better description of the data. This allows to determine the critical temperature as the temperature of onset of algebraic decay in $g_1(r)$. The lower panel shows the scaling exponent $\eta(T)$ below T_c . We determine the critical exponent (red circle) by extrapolating $\eta(T)$ using a polynomial fit.

system and the small population of atoms in the non-central pancakes of the trapping potential. The ideal gas condensation temperature depends on the atom number according to $T_{BEC}^0 = \sqrt{6N} \frac{\hbar\omega_r}{\pi k_B}$, and hence it is affected by the uncertainty in N . In addition to experimental uncertainties, the measurements also contain atom number fluctuations of about 10-15%.

Imaging effects

The correlation function $g_1(r)$ is determined by means of a 2D Fourier transform of the in-plane pair momentum distribution $\tilde{n}(\mathbf{k})$. The momentum distribution is obtained using a matterwave focusing technique which consists of a ballistic expansion of the gas in a harmonic potential for a quarter of the trap period ($\tau/4 = 25$ ms) and subsequently imaging the planar density distribution.

The onset of algebraic decay at large distances in $g_1(r)$ corresponds to a peak at low momenta in the measured $\tilde{n}(\mathbf{k})$. Naturally, a peakier $\tilde{n}(\mathbf{k})$ leads to a broader $g_1(r)$ and hence a smaller scaling exponent. This method of determining $g_1(r)$ and $\eta(T)$ from the momentum distribution is limited by two main factors:

a. Vertical expansion during TOF: As shown in [64], the gas expands rapidly in the vertical direction upon release from the trapping potential. After 25 ms, the vertical extent of the cloud is approximately $500 \mu\text{m}$. This can lead to some parts of the sample exceeding the depth of focus of the imaging system, which in turn causes some distortion in the measured density distribution $n(\mathbf{r}, \tau/4)$. In general, it leads to a broadening of the $\tilde{n}(\mathbf{k})$ which has the effect of increasing the measured scaling exponent η .

b. Finite imaging resolution: As we lower the temperature, the momentum distribution becomes narrower. The measured $\tilde{n}(\mathbf{k})$ is the convolution of the actual momentum distribution with the finite resolution of our imaging setup. This convolution leads to a broadening of the momentum distribution for small k and hence a steeper decay of $g_1(r)$ for large r . Moreover, this broadening effect is larger for distributions that are closer in width to the resolution limit. Intuitively, this means that the distortion caused by the imaging resolution is enhanced at lower temperatures. For the extracted scaling exponents, this leads to a temperature-dependent deviation between the actual value and the measured value. The scaling exponent is always overestimated due to the finite imaging resolution.

To estimate the contributions of the vertical extent of the sample and the finite imaging resolution on the extracted scaling exponents, we perform a simulation of the imaging setup which consists of two lenses ($f = 80$ mm) in a 4f-configuration and a CCD camera.

From the QMC-computed $g_1(\mathbf{r})$ at each temperature, we determine $\tilde{n}(\mathbf{k})$ by means of an inverse Fourier transform. This corresponds to a 2D spatial distribution

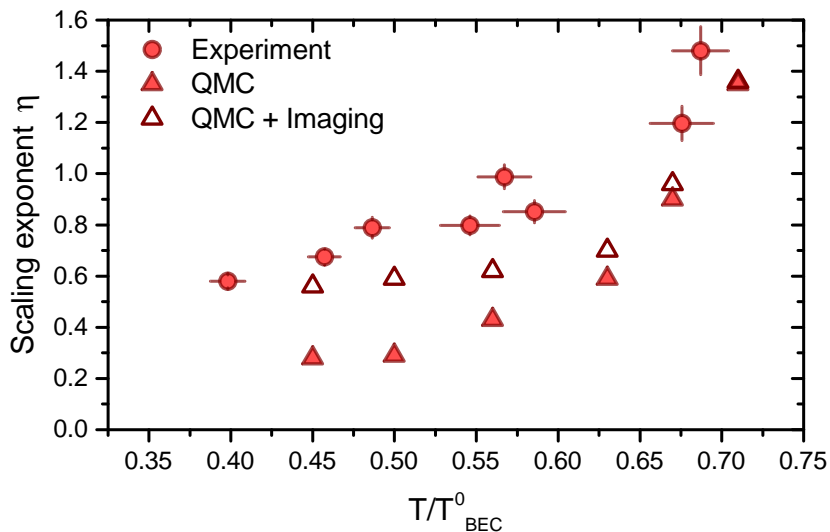


Figure 7.5: Effect of finite imaging resolution on the scaling exponent η for $\tilde{g} = 0.60$. The imaging simulations are performed assuming the $g_1(r)$ and the corresponding exponents η obtained from QMC computations (filled triangles). The open triangles show the exponent extracted after the simulated imaging. We find a substantial temperature-dependent deviation that is qualitatively consistent with the experimentally measured exponents (filled circles).

$\tilde{n}(\mathbf{r})$ of the cloud with $|\mathbf{r}| = \hbar|\mathbf{k}|/M\omega_{lens}$, where ω_{lens} is the trap frequency of the focusing potential. To account for the vertical extent of the cloud after time-of-flight, we construct a 3D density distribution according to $\tilde{n}(x, y, z) = L_z^{-1} \cdot \tilde{n}(x, y)$ for $-L_z/2 < z < L_z/2$, where $L_z \approx 500 \mu\text{m}$ is the vertical size of the cloud. While this is not truly reflective of the actual distribution in the experiment, it is sufficient to capture the essential effect of the vertical size of the gas.

We consider the imaging effect of a thin section of the cloud defocused by a distance z from the focal plane at $z = 0$. Using the paraxial wave equations, we compute the propagation of the imaging beam, approximated as a plane wave, through this section and through the lenses. The resulting intensity distribution contains the effect of the defocus as well as the finite resolution of the lenses. We perform this computation for all $-L_z/2 < z < L_z/2$ and integrate the resulting intensity distributions in the 4f plane according to $I_{4f}(x, y) = \int_{-L_z/2}^{L_z/2} I(x, y, z) dz$. This yields the imaged column density $n'(x, y)$ and hence the imaged momentum distribution $\tilde{n}'(\mathbf{k})$. From this we

obtain the imaged $g_1'(r)$ and the corresponding scaling exponent $\eta'(T)$. Fig. S 7.5 shows the comparison of exponents extracted from the experimental measurement, QMC computations and the imaging simulations, for typical simulation parameters.

From the imaging simulations, it is clear that the finite imaging resolution causes a significant overestimation of the scaling exponent. We find that the main contribution to the deviation is in fact from the finite resolution in the radial plane and the effect of the vertical extension of the cloud is mild. This explains the strong temperature-dependence of the discrepancy between measured and QMC exponents as shown in Fig. S 7.5.

7.5.4 Local density approximation

We estimate the influence of the Thomas–Fermi (TF) profile of the superfluid density on the correlations within a local density approximation. The result of the analysis can be summarized in the following statements: (1) The TF profile results in an additive contribution η_{TF} to the scaling exponent, which is approximately 0.3 at low temperatures; (2) The temperature-dependence of η_{TF} is mild and from the QMC data for the density profiles we estimate the value of η_{TF} at the transition to be approximately 0.4. We conclude that the large scaling exponents observed in the experiment, in particular the value $\eta_c \simeq 1.4$ at the transition, are mostly due to phase fluctuations in the inhomogeneous sample.

We assume that, within a phase-amplitude representation, the bosonic field in the superfluid phase can be written as

$$\hat{\phi}(\mathbf{r}) = \sqrt{\rho(\mathbf{r})} \exp i\hat{\varphi}(\mathbf{r}), \quad (7.8)$$

where $\hat{\phi}$ is an operator, but $\rho(\mathbf{r})$ is a function. We approximate $\rho(\mathbf{r})$ to be given by a TF profile according to $\rho(\mathbf{r}) \simeq \rho_0(1 - r^2/R_{TF}^2)\theta(1 - r^2/R_{TF}^2)$, where $\theta(x)$ is the Heaviside step function, and $R_{TF} = (2\hbar^2\tilde{g}n_0)^{1/2}/M\omega_r$ is the radius of the superfluid core. The particular shape of $\rho(\mathbf{r})$, however, is not essential for the following conclusion. We then find

$$g_1(\mathbf{r}) = \int d^2s \sqrt{\rho(\mathbf{r})\rho(\mathbf{s} + \mathbf{r})} \langle e^{i(\hat{\varphi}_{\mathbf{s}} - \hat{\varphi}_{\mathbf{s}+\mathbf{r}})} \rangle \quad (7.9)$$

for the trap-averaged correlation function. Approximating the phase fluctuations to

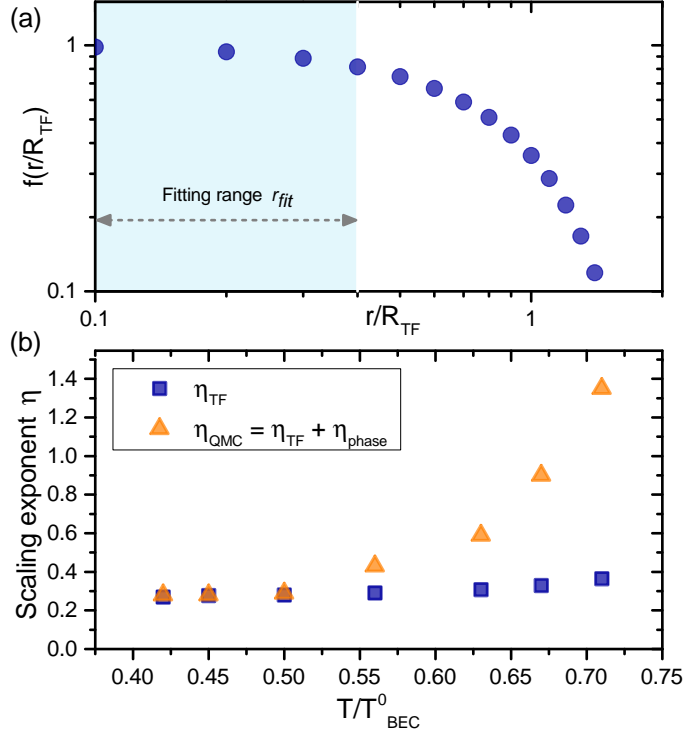


Figure 7.6: Estimated effect of the Thomas–Fermi (TF) profile onto the decay of correlations in a local density approximation. Panel (a) shows the function $f(r/R_{TF})$ from Eq. (7.10) which multiplies the algebraic decay due to phase fluctuations. Our fitting range, highlighted by the blue shaded region, is given by $r/R_{TF} < 0.4$, where the function is rather flat. The fall-off of $f(r/R_{TF})$ leads to an additive contribution η_{TF} to the extracted scaling exponent. The latter is shown in panel (b). At low temperatures, where phase fluctuations are small, we have $\eta \simeq \eta_{TF} \simeq 0.3$. Even at large temperatures, we only have $\eta_{TF} \simeq 0.4$. This effect cannot fully explain the large exponents found from the QMC and experimental data. Hence the associated decay of correlations must be mostly due to phase fluctuations.

be translation invariant we write $\langle e^{i(\hat{\varphi}_s - \hat{\varphi}_{s+r})} \rangle \sim |\mathbf{r} - \mathbf{r}'|^{-\eta_{phase}(T)}$ with a temperature-dependent exponent $\eta_{phase}(T)$, which is assumed to be constant throughout the superfluid region. We arrive at

$$g_1(\mathbf{r}) \sim r^{-\eta_{phase}(T)} f\left(\frac{r}{R_{TF}}\right) \quad (7.10)$$

with the function f being shown in Fig. S 7.6a.

The spatial decay of the function f results in an additive contribution $\delta\eta_{eff} = -d \ln f / d \ln(r/R_{TF}) \simeq 1.97(r/R_{TF})^2$ to the measured scaling exponent. In our experiment, we have $R_{TF} \simeq 100 \mu\text{m}\sqrt{\tilde{g}}$ and typical fitting ranges are $r \leq r_{fit} \simeq 4\ell_r = 30 \mu\text{m}$. Defining the TF contribution as $\eta_{TF} = \delta\eta_{eff}(r_{fit}/R_{TF})$ we have

$$\eta(T) = \eta_{TF}(T) + \eta_{phase}(T) \quad (7.11)$$

for the total scaling exponent extracted from the data. The temperature dependence of the TF contribution results from the temperature dependence of the central density $n_0(T)$. We use the latter from the QMC data for the density profiles to compute $\eta_{TF}(T) = \eta_{TF}(T_0) \frac{n_0(T_0)}{n_0(T)}$, where T_0 is a reference temperature. We choose the latter to be small. The estimated TF contribution $\eta_{TF}(T)$ for $\tilde{g} = 0.60$ is shown in Fig. S 7.6b.

Fermion pairing in the normal phase

8

Publication

SCIENCE **359**, 452-455 (2018)

High-temperature pairing in a strongly interacting two-dimensional Fermi gas

P. A. Murthy¹, M. Neidig¹, R. Klemt¹, L. Bayha¹, I. Boettcher², T. Enss³, M. Holten¹, G. Zürn¹, P. M. Preiss¹, and S. Jochim¹

¹*Physikalisches Institut, Ruprecht-Karls-Universität Heidelberg*

³*Institut für Theoretische Physik, Ruprecht-Karls-Universität Heidelberg*

³*Simon Fraser University, Canada*

Abstract

The nature of the normal phase of strongly correlated fermionic systems is an outstanding question in quantum many-body physics. We use spatially resolved radio-frequency spectroscopy to measure pairing energy of fermions across a wide range of temperatures and interaction strengths in a two-dimensional gas of ultracold fermionic atoms. We observe many-body pairing at temperatures far above the critical temperature for superfluidity. In the strongly interacting regime, the pairing energy in the normal phase significantly exceeds the intrinsic two-body binding energy of the system and shows a clear dependence on local density. This implies that pairing in this regime is driven by many-body correlations, rather than two-body physics. Our findings show that pairing correlations in strongly interacting two-dimensional fermionic systems are remarkably robust against thermal fluctuations.

DOI: [10.1126/science.aan5950](https://doi.org/10.1126/science.aan5950)

8.1 Introduction

Fermion pairing is the key ingredient for superconductivity and superfluidity in fermionic systems [24]. In a system with s-wave interactions, two fundamentally different scenarios can occur: In the first one, as realized for weakly attractive fermions that are described by the theory of Bardeen-Cooper-Schrieffer (BCS), formation and condensation of pairs both take place at the same critical temperature (T_c) [34]. While the mean-field BCS picture successfully describes a large class of superconducting materials, strongly correlated electron systems may follow a different pattern. In this second case, preformed pairs suppress the density of states at the Fermi surface at temperatures exceeding the critical temperature. Finding a description of this so-called 'pseudogap' phase, especially for two-dimensional (2D) systems, is thought to be a promising route to understanding the complex physics of unconventional superconductivity [146, 147]. This is of particular interest in the context of recent ARPES experiments on Iron Chalcogenide films [148, 62], where the combined effect of strong s-wave interactions and reduced dimensionality have been shown to result in preformed pairing and superconductivity at remarkably high temperatures.

The Bose–Einstein Condensation (BEC)-BCS crossover of ultracold atoms constitutes a versatile framework to explore the normal phase of strongly correlated fermions (Fig. 9.1 A). The crossover smoothly connects two distinct regimes of pairing: the BEC regime of tightly bound molecules and the BCS regime of weakly bound Cooper pairs. In 2D (unlike 3D) systems with contact interactions, a two-body bound state with binding energy E_B exists for arbitrarily small attraction between the atoms. The interactions in the many-body system are captured by the dimensionless parameter $\ln(k_F a_{2D})$ where k_F is the Fermi momentum and a_{2D} is the 2D scattering length. As we tune the interaction strength from the BEC (large negative $\ln(k_F a_{2D})$) to the BCS side (large positive $\ln(k_F a_{2D})$), the behavior of the system smoothly changes from bosonic to fermionic character [58]. The fascinating strongly interacting region lies in between these two weakly interacting limits where a_{2D} is on the same order as the inter-particle spacing ($\sim k_F^{-1}$). In our previous works, we used a matterwave focusing method to measure the pair momentum distribution of a 2D Fermi gas across the crossover and observed the Berezinskii–Kosterlitz–Thouless

(BKT) transition to a superfluid phase at low temperatures [99, 54]. An outstanding question concerns the nature of the normal phase above the critical temperature - is it a gapless Fermi Liquid of quasiparticles or a gapped liquid of preformed pairs [70]? While previous cold atom experiments have explored this regime both in 3D [149, 67, 150, 66, 151] and 2D [118, 68] systems, a consensus is yet to emerge.

Here, we address these questions by studying the normal phase of such a 2D ultracold Fermi gas trapped in a harmonic potential. The underlying potential leads to an inhomogeneous density distribution and therefore we can use the local density approximation to directly measure the density dependence of many-body properties. We perform our experiments with a two-component mixture of ${}^6\text{Li}$ atoms with approximately 3×10^4 particles per spin state that are loaded into a single layer of an anisotropic harmonic optical trap. The trap frequencies $\omega_z \approx 2\pi \times 6.95$ kHz and $\omega_\rho \approx 2\pi \times 22$ Hz in the axial and radial directions result in an aspect ratio of about 300:1. We reach the kinematic 2D regime by ensuring that the thermodynamic energy scales, temperature (T) and chemical potential (μ), are smaller than the axial confinement energy. We tune the scattering length a_{2D} by means of a broad magnetic Feshbach resonance [152].

8.2 Experimental System

To investigate fermion pairing in our system, we use radio-frequency (RF) spectroscopy. We perform experiments with the three lowest lying hyperfine states of ${}^6\text{Li}$ which at low magnetic fields are given by: $|1\rangle = |F = \frac{1}{2}mm_F = -\frac{1}{2}\rangle$, $|2\rangle = |\frac{1}{2}, \frac{1}{2}\rangle$, and $|3\rangle = |\frac{3}{2}, -\frac{3}{2}\rangle$. We start with a two-component mixture of atoms in the hyperfine states $|a\rangle|b\rangle \equiv |1\rangle|2\rangle$ or $|a\rangle|b\rangle \equiv |1\rangle|3\rangle$. An RF pulse transfers atoms from state $|b\rangle$ to a third unoccupied hyperfine state $|c\rangle$, and we subsequently image the remaining density distribution in $|b\rangle$. The idea underlying this technique is that the atomic transition frequencies between hyperfine states are shifted by interactions or pairing effects in an ensemble. For example, a state of coexisting pairs and free atoms (Fig. 1B) will lead to two energetically separated branches in the RF spectrum from which we can gain quantitative information on pairing and correlations in the many-body system. Creating initial samples in either 12 or 13 allows us to access a wide range of interaction strengths and minimize final state interaction effects (19).

In our inhomogeneous 2D system, the Fermi energy depends on the local density

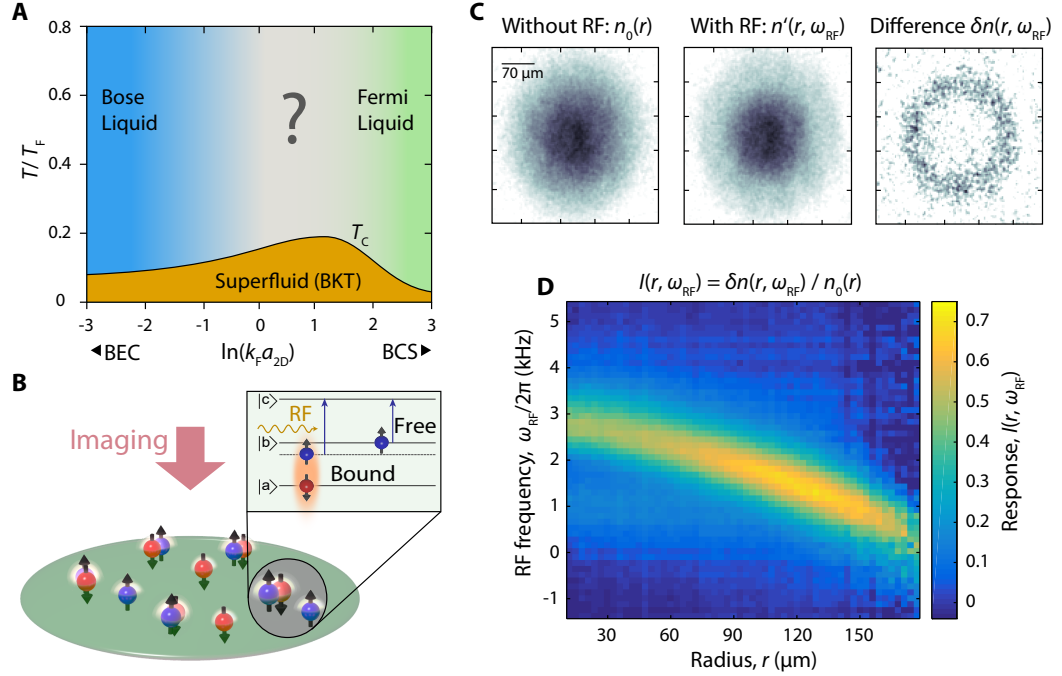


Figure 8.1: **Exploring fermion pairing in a strongly interacting 2D Fermi gas.** **A:** Schematic phase diagram of the BEC – BCS crossover. In this work we investigate the nature of pairing in the normal phase of the crossover regime between the weakly interacting Bose and Fermi liquids. **B:** Illustration of radio-frequency (RF) spectroscopy of a 2D two-component Fermi gas. Pairing and many-body effects shift the atomic transition frequencies between the hyperfine states $|b\rangle - |c\rangle$, which results in observable signatures in the RF response of the system. **C:** Absorption images of the cloud without RF (reference) and with RF at a particular frequency, and the difference between the two images. The ring feature in $\delta n(r)$ reveals the density dependence of the RF response. **D:** Spatially resolved spectral response function reconstructed from absorption images taken at different RF frequencies. At low temperatures in the spin-balanced sample, the occupation of the free particle branch is too low to be observable, which makes it difficult to distinguish between mean-field shifts and pairing effects.

$n(r)$ in each spin state according to $E_F = (2\pi\hbar^2/m)n(r)$, where m is the mass of a ${}^6\text{Li}$ atom. As a consequence, the thermodynamic quantities T/T_F and $\ln(k_F a_{2D})$ also vary spatially across the cloud. We apply the thermometry developed in our previous work [84] to extract these local observables. We measure the local spectral response [153] by choosing a RF pulse duration ($\tau_{\text{RF}} = 4$ ms) that is sufficiently short to prevent significant diffusion of transferred atoms, but also sufficiently long that we obtain an adequate Fourier limited frequency resolution $\delta\omega_{\text{RF}} \approx 2\pi \times 220$ Hz. In Fig. 9.1 C, we show a typical absorption image of the 2D cloud which is used as a reference and one with a RF pulse applied at a particular frequency. The difference between the two images features a spatial ring structure, which qualitatively shows that for a given frequency, the depletion of atoms in initial state $|b\rangle$ occurs at a well-defined density/radius. By performing this measurement for a range of RF frequencies, we can tomographically reconstruct the spatially resolved spectral response function

$$I(r, \omega_{\text{RF}}) = (n_0(r) - n'(r, \omega_{\text{RF}}))/n_0(r), \quad (8.1)$$

where $n_0(r)$ and $n'(r, \omega_{\text{RF}})$ are the density distribution of atoms in state $|b\rangle$ without and with the RF pulse. An example of the tomographically reconstructed spectra is shown in Fig. 9.1 D. The frequency of maximum response depends smoothly on the radius and thereby the local density. Such density dependent shifts may arise from pairing effects - wherein the effective binding energy between fermions is dependent on the density of the medium, or Hartree shifts which are offsets in the spectrum caused by the mean-field interaction energy with no influence on the binding energy between fermions. The position of the RF absorption peak alone (eg. in Fig. 1 D) does not serve as a reliable observable to distinguish between these two effects as it lacks a suitable reference energy that already incorporates Hartree shifts (19). One way to obtain this reference scale is to measure the RF transitions from both bound and free branches to the third unoccupied state (19). However, we find that in the temperature regime ($T/T_F < 1.5$) explored in our experiments, the thermal occupation of the free branch is too small to observe.

8.2.1 Quasi-particle spectroscopy

In order to achieve a sufficient population of the unpaired branch, we apply the quasiparticle spectroscopy method pioneered in [154] for the measurement of the

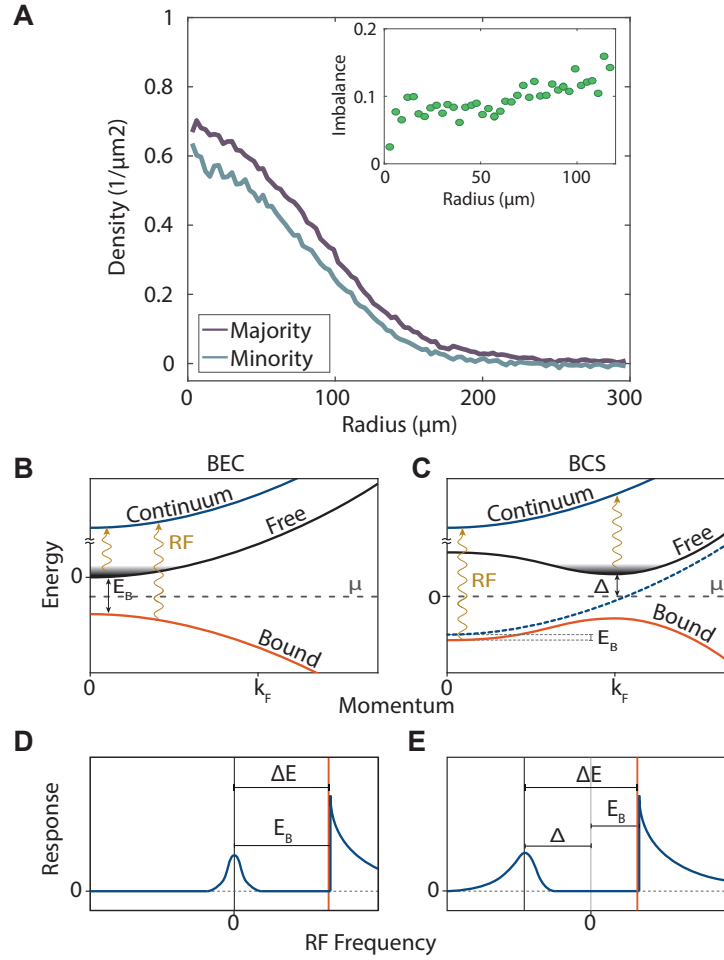


Figure 8.2: **Quasiparticle spectroscopy in the BEC and BCS limits.** **A:** We create a slightly imbalanced mixture of hyperfine states to artificially populate the free particle branch. The density distributions of the majority and minority spins are shown, and the corresponding local imbalance (inset). **B, C:** Schematic illustration of single particle dispersion relations in the BEC and BCS limits at zero temperature. Paired atoms reside in the lowest branch (bound), and are transferred to the continuum of unoccupied states. The excess majority atoms are unpaired and occupy the upper quasiparticle (free) branch in the spectrum at $k \sim 0$ (BEC) and $k \sim k_F$ (BCS). **D, E:** The transition of paired atoms into the continuum yields an asymmetric response with a sharp threshold in the RF spectral function. The quasi-particle transition contributes another peak. Their relative difference yields the pairing energy δE which reveals the distinction between two-body ($\Delta E \sim E_B$) and many-body pairing ($\Delta E > E_B$) in the two limits.

superfluid gap of a 3D Fermi gas. Although our system is in the normal phase, the same technique can be used to determine the pairing gap. The key idea of this method lies in creating a slightly spin-imbalanced mixture so that the excess majority atoms necessarily remain unpaired due to the density mismatch. These unpaired atoms (or dressed quasiparticles) contribute a second absorption maximum in the RF response function besides the one from pairs. Since mean-field interactions shift the whole spectrum, the difference ΔE between the two branches is manifestly independent of it and corresponds only to the pairing energy of the system.

The pairing energy ΔE between the two branches distinguishes between two different pairing scenarios. If ΔE coincides with the two-body bound state E_B , we are in the two-body regime. In contrast, we associate the situation of a density (E_F)-dependent ΔE exceeding E_B with many-body pairing. In Fig. 8.2 B and C, we illustrate these two scenarios using idealized single-particle dispersion relations in the BEC and BCS limits at zero temperature. We provide a brief theoretical account of pairing in these two limits in. The crucial difference between the two cases lies in the occupation of the quasiparticle branch which occurs preferentially at $k \sim 0$ in the BEC [155] and at $k \sim k_F$ in BCS [127] regimes. While the corresponding RF spectra, shown in Fig. 8.2 D and E, appear qualitatively similar, the value of ΔE reveals the fundamental difference in the nature of pairing in the two regimes. We note that the actual dispersion relations at strong interactions and high temperatures – which determine the RF response in the experiment – do not necessarily follow this mean-field description [71, 156]. However, the general criteria to distinguish two-body and many-body pairing scenarios using ΔE remain valid.

8.3 Pairing in the 2D BEC-BCS Crossover

In Fig. 8.3 A and B, we show the measured spectra $I(r, \omega_{\text{RF}})$ for magnetic fields 670 G and 690 G using a $|1\rangle|3\rangle$ mixture, which corresponds to central values of $\ln(k_F a_{2D}) \sim -0.5$ and $\ln(k_F a_{2D}) \sim 1$, respectively. The response from unpaired quasiparticles appears at frequency $\omega_{\text{RF}} \sim 0$, while the pairing branch with an asymmetric lineshape appears at larger frequencies. Examples of spectra at fixed radii are shown in Fig. 8.3 C and D. We fit these local spectra with a combined fit function that includes a symmetric Gaussian (for the quasiparticle peak) and an asymmetric threshold function (for the paired peak) that is convolved with a Gaussian

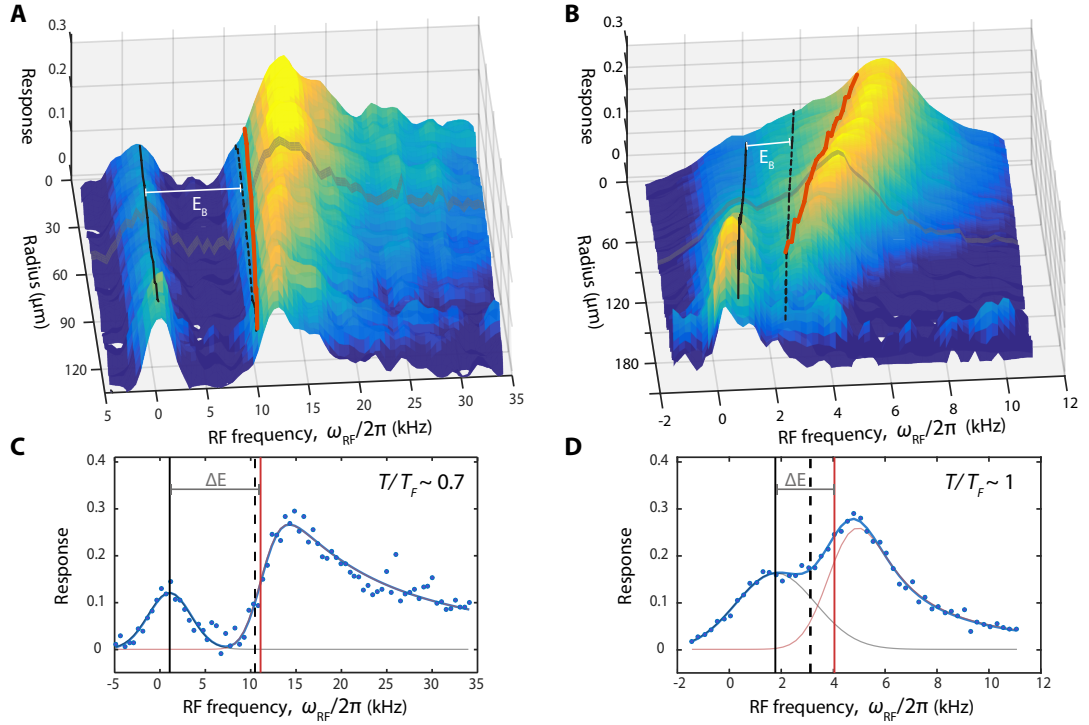


Figure 8.3: From two-body dimers to many-body pairing. The spatially resolved response function $I(r, \omega_{\text{RF}})$ shows qualitatively different behavior for two different scattering lengths. **A, B:** $I(r, \omega_{\text{RF}})$ for central $\ln(k_{\text{F}}a_{2\text{D}}) \sim -0.5$ and 1.0 , respectively. The 3D visualization is obtained using a linear interpolation between 3000 data points each of which is an average of 30 realizations. The black solid line is the peak position of the free branch, the orange line is the threshold position of the bound branch and the black dashed line is displaced from the free peak by the two-body binding energy E_{B} . The energy difference between free and bound branches is the pairing energy ΔE , which is seen to agree with E_{B} in **A** (BEC regime), but significantly exceeds E_{B} in **B** (crossover regime). In addition, ΔE is strongly density dependent in **B**, implying that it originates from many-body correlations. **C, D:** Local spectra at a fixed radius corresponding to a homogeneous system with $T/T_{\text{F}} \sim 0.7$ and 1 respectively (gray region). The solid blue curves are the fits to the data; the black and red curves are gaussian and threshold fits to the two branches.

to account for spectral broadening arising from finite RF frequency resolution and final state effects [157]. The choice of fit function has a systematic effect on the quantitative results presented here, which cannot be eliminated at this point since a reliable theoretical prediction of the shape of the spectral function only exists in the weakly coupled BEC [155] and BCS [127] limits.

At a qualitative level, the main observations from Fig. 8.3 are the following. Both branches in the spectra show density dependence, which can partially be attributed to a mean-field shift. Adding the binding energy E_B to the quasi-particle branch yields the two-body expectation for the threshold position. This picture is applicable to the whole spectrum in Fig 8.3 A, which corresponds to a measurement on the BEC side of the crossover. In contrast, for the spectrum displayed in Fig 8.3 B, corresponding to the crossover regime, we observe $\Delta E \sim E_B$ only in the outer regions of the cloud where the density is low enough that only the two-body bound state plays a role. Towards the center of the cloud, δE begins to significantly exceed E_B and shows a strong dependence on the local density (E_F), indicating that pairing in this regime is a many-body phenomenon. At very low temperatures, the measurement of δE is difficult since the occupation of the free branch is too low, as seen in Fig. 9.1 D. However, we qualitatively observe that the threshold position of the bound branch increases continuously with decreasing temperature, even as we cross the superfluid transition. This indicates that in the crossover regime, a many-body gap opens up far in the normal phase rather than at T_c as expected from BCS theory. This observation is the first main result of this work.

8.4 Crossover from two- to many-body pairing in the normal phase

To quantitatively study the change in the nature of pairing from the BEC to the BCS side, we measure the spectra at different magnetic fields and extract ΔE in units of the two-body binding energy E_B . In Fig. 8.4 A, we plot the temperature dependence of $\Delta E/E_B$ for different interaction strengths, and Fig. 8.4 B shows the variation of $\Delta E/E_B$ as a function of $\ln(k_F a_{2D})$ for a fixed ratio $T/T_F \approx 0.5$. This constitutes an extremely high temperature regime even in the context of ultracold fermion superfluidity, where the largest observed critical temperatures are $T_c/T_F \approx 0.17$

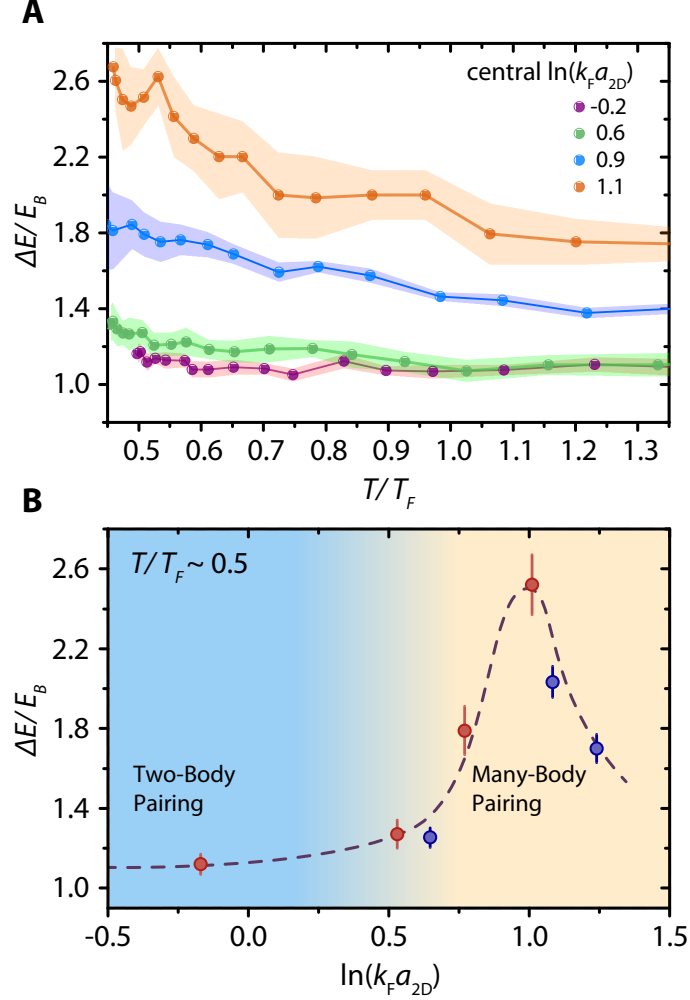


Figure 8.4: **Normal phase in the 2D BEC-BCS crossover regime.** **A:** Pairing energy ΔE in units of E_B plotted as a function of T/T_F for different interaction strengths (central $\ln(k_F a_{2D})$). **B:** Many-body induced high temperature pairing. We plot $\Delta E/E_B$ as a function of $\ln(k_F a_{2D})$ for fixed ratio $T/T_F \sim 0.5$. Red and blue circles correspond to measurements taken with $|1\rangle|3\rangle$ and $|1\rangle|2\rangle$ mixtures. The dashed black line is a guide to the eye. The errors indicated as shaded bands in **A** and bars in **B** are obtained from the fitting procedure. For $\ln(k_F a_{2D}) \leq 0.5$ (strong attraction) we have $\Delta E/E_B \sim 1$ with negligible density-dependence, indicating two-body pairing. For larger $\ln(k_F a_{2D})$ (less attraction), $\Delta E/E_B$ significantly exceeds 1 and reaches a maximum of 2.6 before showing a downward trend. At $\ln(k_F a_{2D}) \sim 1$, we have a critical temperature of $T_c \approx 0.17 T_F$ [99], which indicates the onset of many-body pairing at temperatures several times T_c .

[99, 54]. We perform our measurements with both $|1\rangle|2\rangle$ and $|1\rangle|3\rangle$ mixtures (blue and red points in Fig. 8.4 B) in an overlapping interaction regime. The two mixtures differ vastly in their final state interaction strengths and the fact that we observe consistent behavior with both mixtures demonstrates the robustness of the quantity ΔE against these final state effects.

In Fig. 8.4, we observe that for $\ln(k_F a_{2D}) < 0.5$ the spectra are well-described by two-body physics. In contrast, the pronounced density-dependent gap significantly exceeding E_B for $\ln(k_F a_{2D}) \geq 0.5$ signals the crossover to a many-body pairing regime. In particular, we observe that $\Delta E/E_B$ peaks at $\ln(k_F a_{2D}) \sim 1$, where $\Delta E \approx 2.6E_B$ and is a significant fraction of E_F ($0.6E_F$). The identification of this strongly correlated many-body pairing regime and the observation of many-body induced pairing at temperatures several times the critical temperature is the second main result of this work. For larger $\ln(k_F a_{2D})$, we see a downward trend in $\Delta E/E_B$, and for $\ln(k_F a_{2D}) \geq 1.5$, we observe only a single branch in the spectra near $\omega_{RF} \sim 0$, suggesting the absence of a gap larger than the scale of our experimental resolution. Our qualitative observation of a vanishing gap for weaker attraction is consistent with the picture of the normal phase in the BCS limit being a gapless Fermi liquid [158].

We now turn to a discussion of our results in the context of current theoretical understanding and previous experimental work. In [118], Sommer et al. performed trap-averaged RF spectroscopy in the 3D-2D crossover and found good agreement with mean-field BCS theory in the regime $\ln(k_F a_{2D}) \leq 0.5$. In [68], Feld et al. observed pairing in the normal phase using momentum-resolved (but trap-averaged) spectroscopy also mostly in the regime $\ln(k_F a_{2D}) \leq 0.5$. Beyond this previously explored interaction regime where pairing is purely described by two-body physics [69, 155], our measurements reveal that many-body effects enhance the pairing energy far above the critical temperature. In fact, we show that the most strongly correlated region where many-body pairing occurs in the normal phase lies where $\ln(k_F a_{2D})$ is close to unity rather than zero. With regard to the long-standing question concerning the nature of the normal phase of a strongly interacting Fermi gas [70], our experiments reveal the existence of a large region in the phase diagram where the behavior deviates from both Bose Liquid and Fermi liquid descriptions. Finding a complete description of this strongly correlated phase is an exciting challenge for

both theory and experiment.

8.5 Appendix

8.5.1 Creating a Spin-Imbalanced Mixture

After evaporation we introduce imbalance by a sequence of Landau-Zener passages at $B = 1000$ G where the interaction strength is relatively weak (see Fig. S 8.5 C). In the case of the $|1\rangle|3\rangle$ -mixture, we transfer a small fraction of atoms from state $|1\rangle$ to state $|2\rangle$. The ensuing three-body collisions lead to an imbalance between state $|1\rangle$ and state $|3\rangle$ with a majority of the atoms in state $|3\rangle$. For the $|1\rangle|2\rangle$ -mixture, we transfer atoms from state $|2\rangle$ to state $|3\rangle$ and invert the resulting imbalance with an additional Landau-Zener passage to end up with the majority in state $|2\rangle$.

As we operate in the normal phase, we do not observe a phase separation into a balanced core and a polarized wing as one observes in a superfluid (23, 30) but rather see a local polarization that varies only weakly over the sample. The heat introduced due to the three-body losses in this imbalance scheme limits the achievable temperatures to about $T/T_F > 0.4$.

8.5.2 Radio-Frequency Spectroscopy

Fig. S 8.5 B schematically shows the RF transitions accessed in our experiments. In the case of a $|1\rangle|3\rangle$ -mixture as depicted in the upper panel, we drive the transition from state $|3\rangle$ to $|2\rangle$. Without interactions, the resonance energy for the transition of a free atom is given by $E_{\text{free-free}}$ which is measured in a spin-polarized, non-interacting sample. If the atom in state $|3\rangle$ is paired with an atom in state $|2\rangle$, the energy level is shifted by the binding energy resulting in a reduced resonance energy $E_{\text{bound-free}}$. Thus $E_{\text{bound-free}} < E_{\text{free-free}}$ and the paired branch is at negative frequencies relative to $E_{\text{free-free}}$. For the $|1\rangle|2\rangle$ -mixture as depicted in the lower panel, the situation is similar. However, here $E_{\text{bound-free}} > E_{\text{free-free}}$ and hence the paired branch is at positive RF frequency offsets. For the sake of brevity, we will attribute pairing with positive frequency shifts independent of the mixture throughout this work.

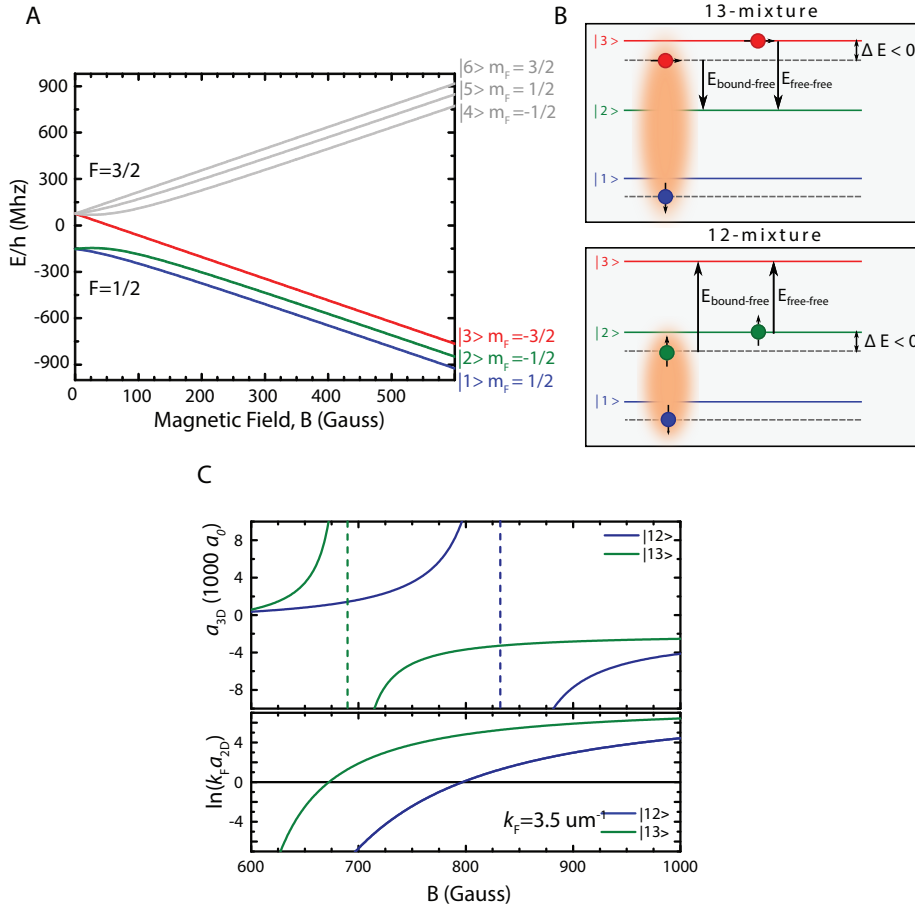


Figure 8.5: **A:** Zeeman sublevels of the ${}^6\text{Li}$ $2^2S_{1/2}$ ground state. Indicated in color are the sublevels experimentally employed. **B:** Schematic illustration of RF spectroscopy in ${}^6\text{Li}$ for both the $|1\rangle|3\rangle$ -mixture in the upper panel and the $|1\rangle|2\rangle$ -mixture in the lower panel. **C:** Upper panel: The 3D scattering length a_{3D} in units of the Bohr radius a_0 is plotted versus magnetic field for the $|1\rangle|2\rangle$ - (blue) and $|1\rangle|3\rangle$ -mixture (green). Lower panel: The corresponding 2D interaction strength $\ln(k_F a_{2D})$ is plotted as a function of magnetic field for a typical Fermi momentum $k_F = 3.5 \mu\text{m}^{-1}$.

Final state effects: In an interacting system, the non-interacting free-free transition is not a suitable reference anymore, as interactions - both in the initial and final state - lead to density-dependent mean-field shifts. We address this question, as explained

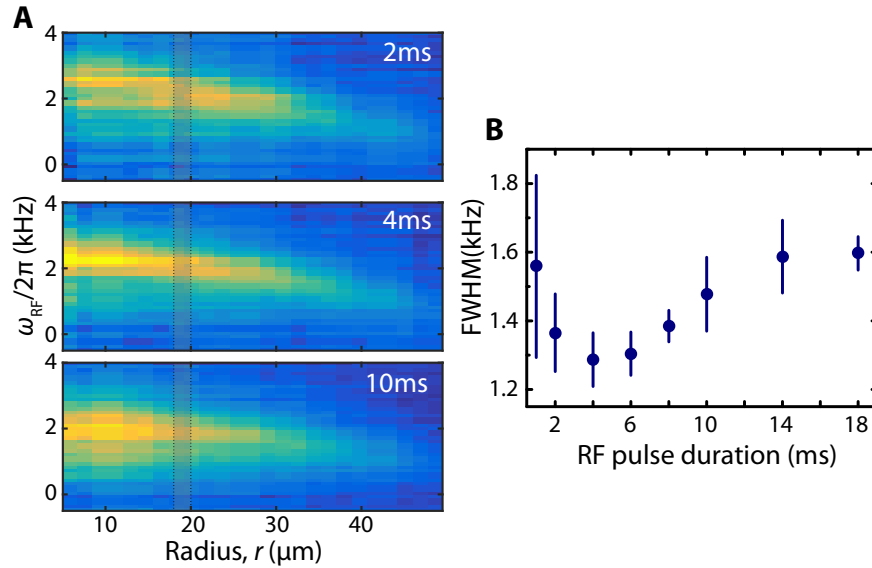


Figure 8.6: Influence of the RF pulse duration on the measured response spectra at 854 G. In **A** the spectra are shown for pulse durations of 2 ms, 4 ms and 10 ms. Along the cuts marked as the shaded area in the spectra, the FWHM is obtained from fits and shown in **B**. A pulse duration of $\tau_{\text{RF}} = 4$ ms gives the optimum trade-off between frequency resolution and the effect of diffusion in the sample.

in the main text, by considering only energy differences. In addition, the final state interactions lead to a broadening of the RF transitions which reduces the resolution. This effect can be significant for the $|1\rangle|3\rangle$ -mixture where the final state is most likely a short-lived repulsive polaron (31). Therefore we make use of the $|1\rangle|3\rangle$ - as well as the $|1\rangle|2\rangle$ -mixture to minimize the effect of final state interactions. A plot of the broad Feshbach resonances which have considerable overlap between the different mixtures can be seen in Fig. S 8.5 C, together with typical values for $\ln(k_{\text{F}}a_{2\text{D}})$. We use the $|1\rangle|3\rangle$ -mixture for magnetic fields below the $|1\rangle|3\rangle$ -resonance where the final state interaction strength has values of $\ln(k_{\text{F}}a_{2\text{D}}) < -7$, and the $|1\rangle|2\rangle$ mixture for larger fields where the final state $\ln(k_{\text{F}}a_{2\text{D}}) > 4.5$. The pairing energies measured with both mixtures in the crossover regime show consistent behaviour independent of the mixture used as shown in Fig. 4 B in the main text.

Spatially resolved spectroscopy: To avoid diffusion of the transferred density, we have to use RF pulses which are short compared to the trapping period and

image the sample directly after the pulse application. However, short RF pulses lead to a Fourier limited frequency resolution and therefore we have to find the optimum trade-off. To investigate this experimentally, we prepare a $|1\rangle|2\rangle$ -mixture at $B = 854$ G and record the RF spectrum for different pulse durations τ_{RF} as can be seen exemplarily in Fig. S 8.6 A. We apply rectangular RF pulses which lead to a Fourier limited width $\Delta\nu \geq 0.886/\Delta t$. For all applied RF pulse durations, the density dependence of the bound-free transition is readily visible. For each pulse duration we adjust the RF power such that a similar fraction of atoms is transferred. This leads to Rabi frequencies between 60 Hz for the longest and 240 Hz for the shortest pulse durations and hence the effect of power broadening is small compared to the Fourier limit. Binning the spectra over two pixels and taking a cut at a fixed radius, we can then compare the measured widths of the bound-free transition. This is shown in Fig. S 8.6 B for the FWHM of the peak. For short RF pulses on the order of 1 ms, the width increases as the Fourier limit there is on the order of 1 kHz. Although the Fourier limit decreases for longer pulse durations, the FWHM increases which we attribute to diffusion of particles during the application of the RF pulse. At around $\tau_{\text{RF}} \approx 4$ ms the minimal FWHM occurs, which is the pulse length we used throughout this paper. This results in a Fourier limited RF resolution of $\Delta\nu = 222$ Hz with a typical Rabi frequency on the order of $\Omega = 150$ Hz.

8.5.3 Theoretical Background on BEC and BCS Limits in 2D

In this section, we provide a brief account of the theoretical aspects of pairing in the well-understood BEC and BCS limits. The treatment presented here has been described in detail in the references (24,25).

Zero temperature BCS theory

The BCS quasiparticle dispersion for an attractive Fermi gas is $E_k = \sqrt{\Delta^2 + \xi_k^2}$, where Δ denotes the superconducting gap, and $\xi_k = \varepsilon_k - \mu$ is the free dispersion relation $\varepsilon_k = \hbar^2 k^2 / 2m$ measured from the chemical potential μ . The spectral function has the form

$$A_{\text{BCS}}(k, E) = \underbrace{v_k^2 \delta(E + E_k - \mu)}_{\text{bound}} + \underbrace{u_k^2 \delta(E - E_k - \mu)}_{\text{free}} \quad (8.2)$$

for the bound and the free branches, with coherence factors $v_k^2 = (1 - \xi_k/E_k)/2$ and $u_k^2 = (1 + \xi_k/E_k)/2$. Within 2D BCS theory the chemical potential at zero temperature $\mu = E_F - E_B/2$ and the gap $\Delta = \sqrt{2E_F E_B} = 2E_F e^{-\ln(k_F a_{2D})}$, while $T_c = e^\gamma \Delta/\pi = 1.13 E_F e^{-\ln(k_F a_{2D})}$.

On the BCS side $E_B \ll E_F$, $\mu > 0$ and the dispersion reaches a minimum gap $\Delta = E_{k_0}$ at wavevector $k_0 = \sqrt{2m\mu}/\hbar \approx k_F$, cf. Fig. 2C. In the BEC limit $E_B \gg E_F$ one has $\mu \rightarrow -E_B/2$, and the coherence factor $v_k^2 \rightarrow Z_k = k_F^2 a_{2D}^2 / (1 + k^2 a_{2D}^2)^2$ approaches the square of the bound-state wave function; thus the BCS spectral function asymptotically crosses over into BEC spectral function (24)

$$A_{\text{BEC}}(k, E) = \underbrace{Z_k \delta(E + \xi_k - \mu)}_{\text{bound}} + \underbrace{(1 - Z_k) \delta(E - \xi_k - \mu)}_{\text{free}}, \quad (8.3)$$

for the bound and the free branch. The two branches bend outwards in Fig. 2B, with a minimal distance E_B at $k = 0$.

The RF response in the absence of final-state interactions involving species $|c\rangle$ takes the form (25)

$$\Gamma_{\text{BCS}}(\omega) = \pi \Omega^2 \sum_k A_{\text{BCS}}(k, E_k - \omega) f(\xi_k - \omega) = \frac{\pi \Omega^2 N_b}{2E_F} f(\xi(\omega) - \omega) \frac{\Delta^2}{\omega^2} \Theta(\xi(\omega) + \mu), \quad (8.4)$$

where Ω is the Rabi frequency, $f(E)$ the Fermi function, and $\xi(\omega) = (\omega^2 - \Delta^2)/2\omega$. N_b denotes the number of particles in state $|b\rangle$, and we have used the constant density of states $\rho(E) = m/(2\pi\hbar^2)$ in 2D. The Θ step function constrains the response to two branches: first, bound-free transitions from the lower branch occur only above a threshold frequency $\omega > \omega_{\text{th}} = \sqrt{\mu^2 + \Delta^2} - \mu = E_B > 0$. Second, free-free transitions from the thermally excited upper branch appear at $\omega < 0$, but are too weak to be observed at low temperature, cf. Fig. 1D. Instead, for small spin imbalance a region around the minimum of the upper quasiparticle branch becomes occupied, and a new RF peak appears at $E_{\text{free}} = -\Delta$ (23), cf. Fig. 2 C,E. Furthermore, interaction-induced Hartree shifts $U < 0$ can also affect the spectra. They are usually incorporated in terms of an effective shift to the chemical potential $\mu_{\text{eff}} = \mu - U$ (23) which, to leading order, results in an overall shift to the spectrum such that $E_{\text{th}} = E_B - U$ and $E_{\text{free}} = -\Delta - U$. At zero temperature we thus obtain

$$\Gamma_{\text{BCS}}(\omega) = \frac{\pi\Omega^2 N_b}{2E_F} \frac{\Delta^2}{\omega^2} [\Theta(\omega - E_B + U) + \delta_{\text{free}}(\omega + \Delta + U)]. \quad (8.5)$$

It is a remarkable consequence of pairing in 2D that, within the BCS theory, the RF threshold remains $\mathbf{E}_{\text{th}} = \mathbf{E}_B - \mathbf{U}$ throughout the crossover. Hence, one cannot distinguish between two-body and many-body pairing by measuring the bound-free transition alone. Only by occupying the upper branch and measuring the free peak at $E_{\text{free}} = -\Delta - U$ can one determine the pairing energy $\Delta E = E_{\text{th}} - E_{\text{free}} = E_B + \Delta$ in a way that requires no knowledge of the mean-field shift U and quantifies the many-body gap Δ .

Finite-temperature BCS theory

Our measurements of a non-monotonous behavior of $\Delta E/E_B$ as a function of $\ln(k_F a_{2D})$ are purely observational and model independent. However, we can gain phenomenological understanding of pairing in this crossover region by evaluating the expectations of BCS theory at finite temperatures. We emphasize that the application of finite temperature BCS theory to the strongly interacting regime is subtle and must be done with care because (i) the BCS prediction for T_c does not account for quantum fluctuations which reduces T_c as has been experimentally verified (8), (ii) BCS theory explicitly ignores the presence of interactions (and therefore the two-body bound state) in the normal phase, which precludes the existence of pairing above T_c , and (iii) BCS theory incorrectly predicts the zero crossing of the chemical potential at $\ln(k_F a_{2D}) = 0$ (7). Even though BCS theory fails in these respects, it has been suggested that it may provide reasonable estimates of the pairing energy in the system at finite temperature (33). In the following section, we only assume that the dispersion relation contains two separated branches and follows the BCS form as shown in Fig. 2 C of the main text. Then, the pairing energy in the RF response (see Fig. 2 of the main text) is given by

$$\Delta E = \begin{cases} 2\sqrt{\mu(T)^2 + \Delta(T)^2} & \text{if } \mu(T) \leq 0 \\ -\mu(T) + \sqrt{\mu(T)^2 + \Delta(T)^2} + \Delta(T) & \text{if } \mu(T) > 0. \end{cases}$$

Here, $\mu(T)$ and $\Delta(T) \leq \Delta(T = 0)$ are the self-consistent solutions of the number and gap equations.

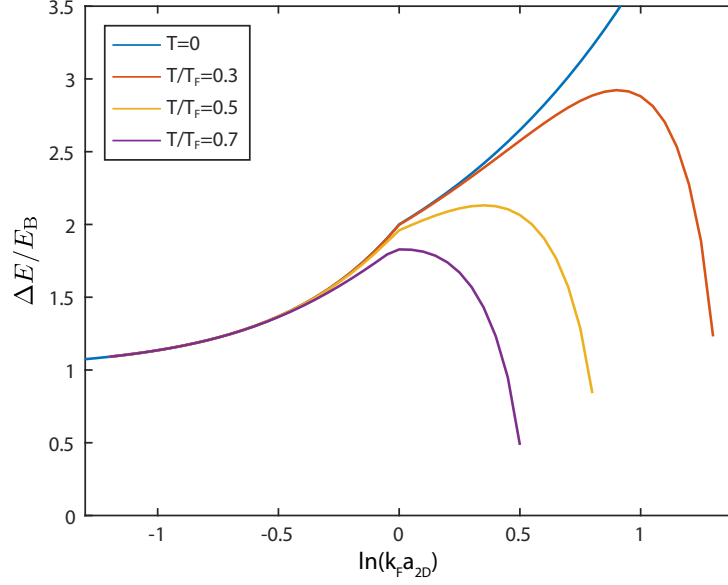


Figure 8.7: Prediction for $\Delta E/E_B$ from finite-temperature BCS theory for $T < T_c$. At zero temperature, pairs evolve from local dimers on the BEC side to many-body pairs on the BCS side. Finite temperatures up to $T/T_F \sim 1$ have little effect on the BEC side, where the binding energy is large, but destroy weakly bound BCS pairs. The qualitative behavior of the pairing energy observed in the experiment is reproduced by BCS theory in the superfluid phase.

Fig. S 8.7 shows the predictions for $\Delta E/E_B$ at various temperatures, which we obtain by solving for μ and Δ numerically. At zero temperature, BCS theory predicts a fully paired state with a smooth crossover from deeply bound dimers with $\Delta E = E_B$ at $\ln(k_F a_{2D}) \ll 0$ to Cooper pairs with $\Delta E \sim \Delta \gg E_B$ at $\ln(k_F a_{2D}) \gg 0$. On the BEC side (large negative $\ln(k_F a_{2D})$), the temperatures in our experiments $0.2 < T/T_F < 1$ are much smaller than the BCS gap Δ , so the gap parameter $\Delta(T)$ and the RF response are essentially unchanged from their zero temperature values. Towards the BCS side (large positive $\ln(k_F a_{2D})$), the gap decreases in absolute terms and is reduced to $\Delta(T) < \Delta_0$ due to nonzero temperature. Cooper pairs cannot form and BCS theory predicts $\Delta E/E_B \rightarrow 0$ in the weakly attractive BCS limit. We note that this prediction of $\Delta E/E_B \rightarrow 0$ at higher temperatures is not physically reasonable in the strongly interacting regime since the two-body bound state is

always present. A modification to the BCS theory that includes the vacuum bound state is required to make a more accurate comparison to experiment.

This BCS calculation qualitatively reproduces the behavior of the pairing energy ΔE in the crossover, including the enhancement of $\Delta E/E_B$ to ~ 2 at $T/T_F = 0.5$ observed in the experiment. Compared to the data, the peak in the BCS prediction is shifted to smaller values in $\ln(k_F a_{2D})$ by about 0.5, similar to the reported shift in the zero crossing of the chemical potential (7). While we do not expect finite-temperature BCS theory to be valid in the strongly correlated region, the qualitative picture of pairing modified by many-body correlations up to $T \approx T_F$ seems to hold.

8.5.4 Axial Excitations

An important consideration in the experimental study of two-dimensional Fermi gases is the role of axial excitations. Since these experiments are always performed in anisotropic three-dimensional potentials (with one strong confinement axis), the effect of axial excitations due to interactions is in principle always present. In this section, we use comparisons to previous experimental and theoretical work to argue that the many-body pairing effect reported in this work is, to leading order, not significantly affected by axial excitations in the system.

In (32), Dyke et. al measure the axial width of the gas in time of flight as a function of interaction strength and particle number and find deviations from pure 2D kinematics in the regime where $E_B > \hbar\omega_z$ and $k_B T > \hbar\omega_z$. We first note that in the regime of many-body pairing, the axially excited fraction in the system is of the order of 0.1 (or smaller) and hence cannot explain the large effect observed in our work. In Fig. S 8.8 we plot the measured pairing energy ΔE as a function of the local $E_F/\hbar\omega_z$ for an interaction parameter $\ell_z/a_{3D} \sim -0.5$, where ℓ_z is the axial harmonic oscillator length and a_{3D} is the 3D scattering length. The vertical gray line is the 'elbow' position in the axial width ($E_F/\hbar\omega_z \sim 0.6$) extracted from Fig. 3 of (32), which denotes approximately the point where the deviation from 2D kinematics occurs for that interaction strength. We find that already in the regime $E_F/\hbar\omega_z < 0.6$, the quantity $\Delta E/E_B$ exceeds unity significantly which shows that the many-body pairing effect is already present in the 2D kinematic regime and is not significantly affected by axial excitations.

The effect of axial excitations and finite temperature on the RF spectra of quasi-

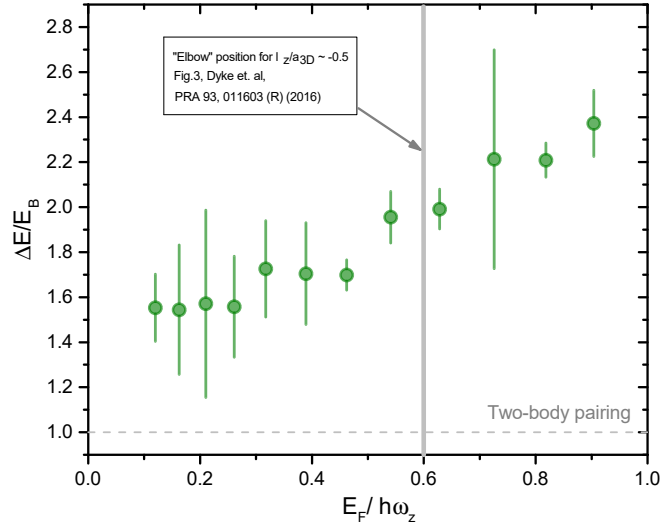


Figure 8.8: Measured pairing energy $\Delta E/E_B$ as a function of the local $E_F/\hbar\omega_z$ at a magnetic offset field of 854 G corresponding to $l_z/a_{3D} \sim -0.5$. The vertical gray line corresponds to the elbow position of the axial width extracted from (32), that sets one possible criterion for 2D kinematics. The fact that we observe the many-body pairing effect to be significant already before this limit suggests that the role of axial excitations is not significant in causing this effect.

two-dimensional Fermi gases has been theoretically worked out in (25). In the presence of axial excitations, the RF spectra are expected to feature additional peaks offset by E_B and occurring at multiples of $\hbar\omega_z$ (as shown in Fig. 4 of (25)), i.e. at E_B , $E_B + \hbar\omega_z$, $E_B + 2\hbar\omega_z$ and so on. In our work, we always observe only one strong pairing peak. Moreover in the strongly interacting regime, the position of the pairing peak is always seen to be consistently and significantly smaller than $\hbar\omega_z$. The scenario presented in (25) is therefore not realized in our experiment suggesting that the role of axial excitations in the many-body pairing regime is not significant.

Scale-invariance breaking in a 2D superfluid

9

Preprint

Quantum scale anomaly and spatial coherence in a 2D Fermi superfluid

P. A. Murthy¹, N. Defenu², L. Bayha¹, M. Holten¹, P. M. Preiss¹, T. Enss², and S. Jochim¹

¹*Physikalisches Institut, Ruprecht-Karls-Universität Heidelberg*

²*Institut für Theoretische Physik, Ruprecht-Karls-Universität Heidelberg*

Abstract

The interplay of strong interactions and reduced dimensionality often leads to peculiar effects in many-body systems. The quantum anomaly is one such effect which occurs when a scaling symmetry that exists in classical systems is violated by quantum fluctuations. Here, we discovered a striking and unexpected manifestation of a quantum anomaly in the momentum-space dynamics of a 2D Fermi superfluid. We measured the position and momentum space distribution of the superfluid during a breathing mode cycle for different interaction strengths across the BEC-BCS crossover. Whereas in the weakly interacting BEC and BCS regimes, the system exhibits self-similar evolution, we find a strong violation in the strongly interacting crossover regime. Moreover, the signature of scale-invariance breaking are dramatically enhanced in the first-order coherence function. In particular the power-law exponents that characterize long-range phase correlations in the system are significantly modified due to this effect. This implies that the quantum anomaly deeply influences the critical properties of 2D superfluids.

9.1 Introduction

Many-body systems are generally characterized by an interplay of several scales, for eg. thermal, interaction and lattice length scales, which often complicates their description. Under special circumstances however, some properties of systems become invariant under a change of scale, hence the term scale-invariance. For instance, rescaling the coordinates of a scale-invariant Hamiltonian by some factor λ leaves it unchanged up to a multiplicative factor: $\hat{H}(\lambda\mathbf{x}) = \lambda^\alpha \hat{H}(\mathbf{x})$, where α is a real constant. Such a concept naturally simplifies the description of systems by making their microscopic details irrelevant. It is for this reason that scale invariance has applications in such a variety of situations such as critical phenomena [159], fluid dynamics [72], complex networks [160], and even in economic systems [161]. Understanding how scale invariance occurs and also how it is violated is therefore of fundamental importance, particularly when the violations are caused by quantum fluctuations in the system.

In this work we explore the question of scale invariance breaking in a two-dimensional Fermi superfluid. 2D systems are particularly interesting to study scaling behavior due to certain intrinsic properties. A classical 2D gas with contact interactions ($V(\mathbf{x}) = g\delta^2(\mathbf{x})$) is fundamentally scale invariant as the δ^2 -potential exhibits no characteristic scale. Therefore, a transformation $\mathbf{x} \rightarrow \lambda\mathbf{x}$ rescales the interaction potential as $V(\lambda\mathbf{x}) = \lambda^{-2}V(\mathbf{x})$ exactly the same way as the kinetic energy [55]. However at the quantum mechanical level, this is no longer true. For two particles scattering via the δ^2 -potential, a two-body bound state always exists for arbitrarily weak attraction. The new energy scale E_B and the associated scattering length scale a_{2D} effectively break the scaling relation between interaction and kinetic energy. This is known as the quantum anomaly.

An important question is whether and how the quantum anomaly influences the behavior of 2D systems at macroscopic scales. This is particularly relevant for 2D superfluids which exhibit algebraic - hence scale-free - decay of phase correlations [54, 53] as described by the Berezinskii–Kosterlitz–Thouless (BKT) mechanism. In this case, how does the introduction of a short-distance scale (a_{2D}) affect the long-range phenomenology such as spatial coherence and transport properties in 2D superfluids? These questions are at the heart of the many-body physics of 2D systems and answering them may provide insights into the general behavior of other

lower dimensional systems such as superfluid films, exciton-polariton condensates and graphene [41].

In the field of ultracold atomic gases, the issue of scale invariance breaking has been explored extensively. 2D Bose gases in the weakly interacting limit are demonstrably scale invariant to a very good approximation [56, 162, 74], suggesting that a_{2D} plays a negligible role in these systems. However, in 2D Fermi gases, particularly in the strongly interacting regime, the effect of a_{2D} becomes appreciable, for instance in the thermodynamic equation of state [83, 84, 85, 79, 80]. On this basis, various theoretical works have predicted a quantitatively pronounced effect of the quantum anomaly in this regime [76, 163, 77]. A notable manifestation of the quantum anomaly specific to harmonically trapped gases is an interaction-induced correction to the collective monopole frequency with respect to the non-interacting value [75, 76, 163, 77, 164]. Although previous studies on monopole modes found no evidence of such a correction [78], recent experiments have, for the first time, reported the observation of an anomalous frequency shift at low temperatures [73]. However, the relative magnitude of these shifts ($\sim 1 - 2\%$) is several times smaller than the theoretical prediction ($\sim 10\%$), raising questions on the physical relevance of the quantum anomaly on the dynamical properties of 2D Fermi gases.

Here, we discovered that fermionic correlations which lead to the quantum anomaly in fact have a remarkably pronounced influence on the large scale behavior of the 2D system. Rather than the breathing mode frequencies, we explore the spatial coherence properties in momentum space, which reveals a dramatic signature of scale invariance breaking that is almost absent in the position space density profiles. Even though the existence of the quantum anomaly in this system has been theoretically predicted, such a striking manifestation as reported in this work comes as a surprise.

9.2 Experimental protocol

In our experiments, we prepared a gas of approximately 2×10^4 ^6Li atoms in the lowest two hyperfine states, trapped in a highly anisotropic potential and cooled to low temperatures $T/T_F \sim 0.05$ deep in the superfluid phase. The radial and axial trap frequencies of the harmonic potential were $\omega_r = 2\pi \times 23$ Hz and $\omega_z = 2\pi \times 7.1$ kHz respectively, corresponding to an aspect ratio $\omega_z/\omega_r \approx 300$. With the relevant thermodynamic scales kept smaller than the axial confinement energy, we ensure

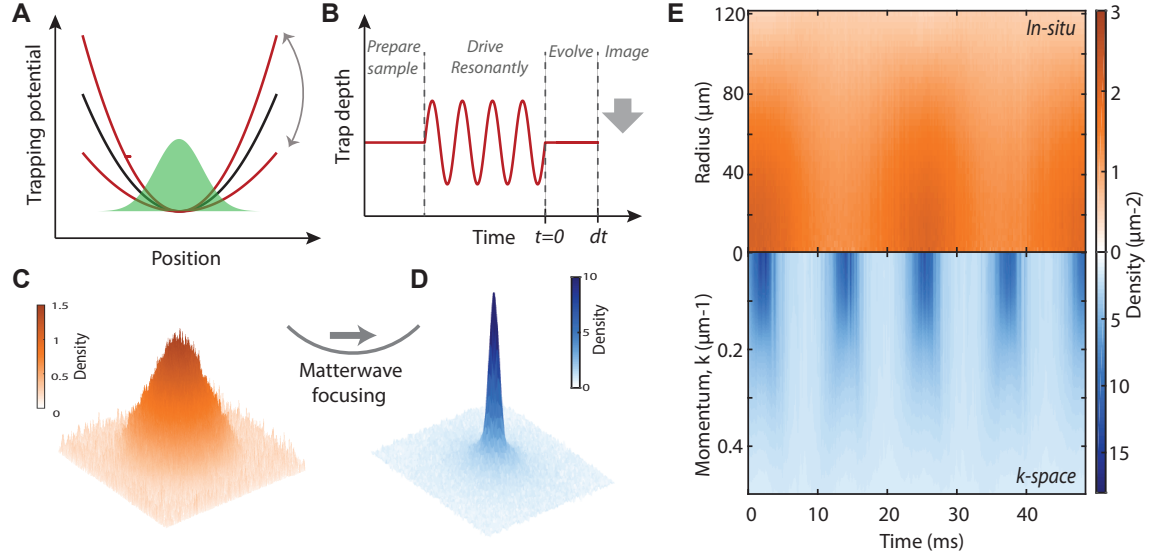


Figure 9.1: **Dynamics of a 2D Fermionic superfluid in position and momentum space.** **A, B** We prepare a 2D Fermi gas and cool it well below the superfluid critical temperature. By resonantly modulating the trap potential, we excite the isotropic breathing mode. Once the drive is stopped, the breathing oscillations continue for a variable time t , after which we measure **(C)** the in-situ density distribution $\rho(r, t)$, and **(D)** the pair momentum distribution $n(k, t)$ using a matterwave focusing technique. **E** Example of azimuthally averaged $\rho(r, t)$ (orange) and $n(k, t)$ (blue) taken at interaction strength $\ln(k_F a_{2D}) \approx 1$. The in-situ density oscillates at twice the trap frequency as expected. The momentum distribution exhibits sharp revivals at twice the rate of the in-situ oscillation. The frequency doubling arises from the sinusoidal oscillation of the hydrodynamic velocity field, which vanishes at the inner and outer turning points of the breathing cycle.

the system is in the kinematically 2D regime. By tuning the interactions between fermions around a Feshbach resonance, we access the 2D BEC-BCS crossover region. The interactions in the 2D many-body system are described by a dimensionless parameter $\ln(k_F a_{2D})$, where k_F is the Fermi momentum and a_{2D} is the 2D scattering length obtained from the 3D scattering length [57, 128]. For $\ln(k_F a_{2D}) < -1$, we are in the BEC regime whereas $\ln(k_F a_{2D}) > 1$ corresponds to the BCS regime. The strongly correlated regime located between these limits occurs when $k_F \sim a_{2D}$. In our previous works, we observed that the crossover region exhibits several special features such as enhanced critical temperature T_c [99] and a large pseudogap region above T_c where pairing is strongly density-dependent [165].

We investigate the interplay between quantum anomaly and phase correlations by measuring the dynamical evolution of the gas both in position space (in-situ) and in momentum space. Measuring the momentum distribution is particularly important as it encodes information of phase fluctuations in the superfluid. First, we brought the system out of its equilibrium configuration by resonantly driving the harmonic trapping potential at twice the trap frequency $2\omega_r$ as illustrated in Fig. 9.1 **A**, **B**. This protocol excites the 2D isotropic breathing mode whereby the gas undergoes periodic cycles of compression and expansion. After a fixed duration (10 cycles), the drive was stopped and the cloud evolved in the original potential for a variable time t . In contrast to previous works which investigated the frequency of the breathing mode, we focus on how the form of the in-situ and momentum distributions change within a single breathing cycle. Since the damping rate of the breathing modes is very small ($\sim 0.01\omega_r$), the motion is essentially isentropic which allows to directly probe scale invariant behavior, ignoring spurious contributions due to finite temperature.

To measure $n(k)$, we employed a matterwave focusing technique that has been previously demonstrated for 2D gases [64]. First, we rapidly ramped the offset magnetic field to the weakly interacting limit of strongly bound dimers. Immediately following the ramp, we switched off the trapping potential and released the sample to ballistically expand in a shallow harmonic potential for a quarter period $T_{\text{exp}}/4 = \pi/2\omega_{\text{exp}} = 21.8$ ms, where ω_{exp} is the shallow trap frequency. The $T_{\text{exp}}/4$ evolution maps the initial momentum distribution of particles to the spatial distribution. As the time scale of the magnetic field ramp ($\tau_{\text{ramp}} \sim 100 \mu\text{s}$) is shorter than the intrinsic timescales of the system, the measured spatial distribution at $t = T_{\text{exp}}/4$ reflects

9.3. Scale-invariance breaking in momentum space

to a very good approximation the initial momentum distribution of pairs. The strong enhancement of the low-momentum modes in $n(k)$ as seen in Fig. 9.1 **D** signals superfluidity in the system as it is related to long-range spatial coherence in the system [54, 99].

In Fig. 9.1 **E**, we show an example of the measured time-evolution of the in-situ $\rho(r, t)$ (orange) and momentum distributions $n(k, t)$ (blue) taken at the interaction parameter $\ln(k_F a_{2D}) \approx 1$. The in-situ distribution exhibits periodic compression and expansion at approximately twice the trap frequency ($\omega_B \approx 2\omega_r$), as expected. In contrast, $n(k, t)$ undergoes sharp revivals at twice the rate of $\rho(r)$, i.e. when the cloud size is maximum (outer turning point, $t = t_o$) as well as minimum (inner turning point, $t = t_i$). At intermediate time scales between the turning points, $n(k)$ is broadened. At a qualitative level, this peculiar effect can be understood to occur due to the oscillation of the hydrodynamic velocity field, $\mathbf{v}_B \propto \cos(\omega_B t)[x\hat{\mathbf{e}}_x + y\hat{\mathbf{e}}_y]$. During the breathing cycle, v_B vanishes at the two turning points. At the intermediate points, the non-zero value of \mathbf{v}_B manifests in a broadened momentum distribution with no visible effects in the in-situ profile. We provide a more detailed description of the effect using variational Gross-Pitaevskii computations in the Appendix 9.5.3. Such an effect has been previously predicted for the 1D Bose gas in Tonks-Girardeau regime using scale invariant dynamics [166] and also experimentally observed in the weakly interacting regime [167].

9.3 Scale-invariance breaking in momentum space

From these dynamical measurements, the occurrence and violation of scale invariance can be confirmed by comparing the in-situ and momentum-space distributions at different points in time. To illustrate this point, let us consider the time-evolution of a scale invariant gas in a harmonic potential. In Ref. [74], Pitaevskii and Rosch showed that, even though the presence of a trapping potential naturally introduces an oscillator length scale and thus explicitly breaks scale invariance, for the special case of a 2D harmonic potential, an additional $SO(2, 1)$ symmetry restores scaling behavior. Due to this dynamical symmetry, the system displays quasi-integrable dynamics with the dynamical many-body wavefunction being given in terms of the

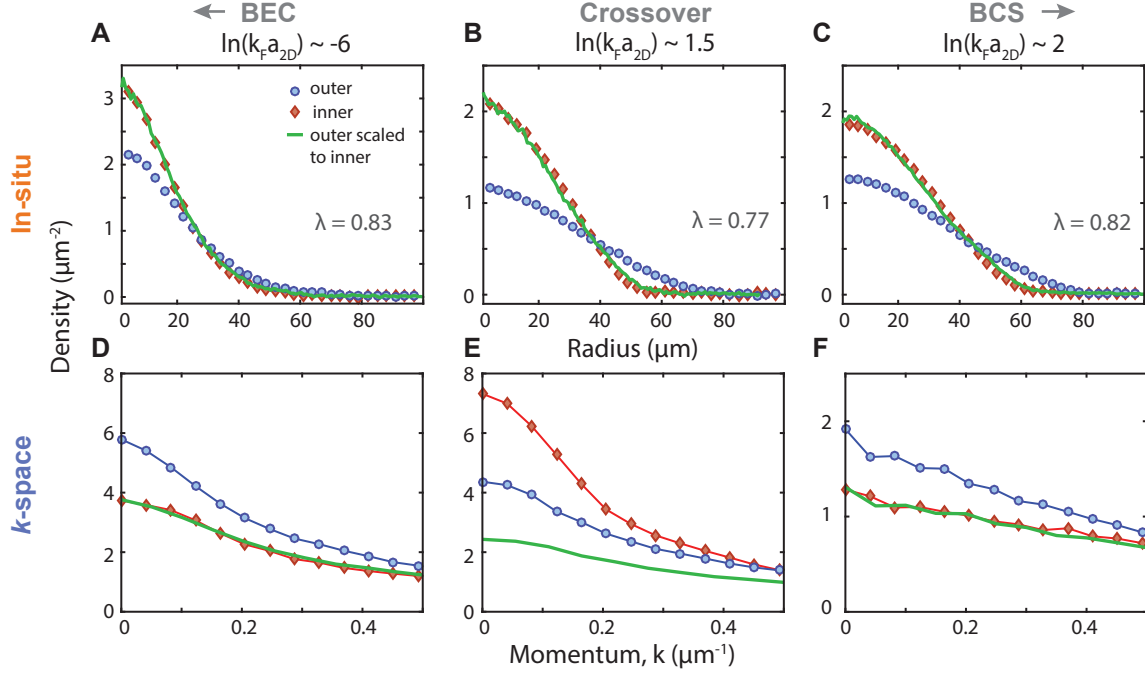


Figure 9.2: **Scale invariance breaking in momentum space.** The in-situ (upper panels) and momentum distributions (lower panels) at the inner and outer turning points for interaction strengths $\ln(k_F a_{2D}) \approx -6$ (**A**, **D**), 1 (**B**, **E**) and 2 (**C**, **F**). For a scale invariant system, the in-situ density profiles at t_o (red diamonds) and t_i (blue circles) should be scalable with a single scaling factor λ , as well as the momentum distributions ($n(k, t_o) \rightarrow n(k, t_i)$) with the inverse factor λ^{-1} . Such scaling behavior is observed both in the weakly interacting BEC and BCS regimes. However in the strongly interacting crossover regime, we find a clear departure from scale invariance. While the evolution of the $\rho(r)$ is still self-similar (**B**), the momentum distribution (**E**) shows a significant discrepancy from the expected result (green). Moreover, the largest deviation (between red and green curves) occurs at low-momenta which are responsible for long-range coherence of the superfluid. This scaling violation at strong interactions is attributed to the quantum anomaly. Since total particle number is conserved, enhancement of density at low- k is compensated by reduction at high- k (not shown).

equilibrium one according to

$$\psi(X, t) = \frac{1}{\lambda^N} \psi(X/\lambda, t = 0) \exp\left(i \frac{m\dot{\lambda}}{2\hbar\lambda} X^2\right) \exp(i\theta(t)), \quad (9.1)$$

where $X = (\mathbf{x}_1, \mathbf{x}_2, \dots, \mathbf{x}_N)$ are the $2N$ position coordinates of many-body system, m is the particle mass, $\theta(t)$ is an overall phase, and $\lambda(t)$ is the time-dependent scale factor which obeys the Ermakov-Milne equation. From the full wave-function Eq. (9.1), one obtains the evolution of the in-situ density and the momentum distribution.

$$\rho(r, t) = \frac{1}{\lambda^2} \rho\left(\frac{r}{\lambda}, t = 0\right) \quad (9.2)$$

$$n(k, t) = \lambda^2 \int n\left(\lambda k + 2m \frac{\dot{\lambda}}{\lambda} r, r, t = 0\right) d^2 r, \quad (9.3)$$

in terms of the Wigner function $n(k, r, t)$. Clearly, the in-situ density is completely self-similar (Eq. 9.2), i.e. the density at any time t can be rescaled to its initial form using a single scaling factor $\lambda(t)$. The momentum distribution $n(k, t)$ displays self-similar scaling with the inverse factor $\lambda_k = \lambda^{-1}$, but only when $\dot{\lambda} = 0$. For the breathing modes, this occurs at the two turning points. Therefore, a comparison of the in-situ and momentum distributions at the inner and outer turning points can be used as a proxy to study scale invariance.

We measured the dynamically evolving in-situ and momentum distributions for various interaction parameters across the BEC-BCS crossover. In Fig. 9.2, we show $\rho(r)$ (upper panels: A, B, C) and $n(k)$ (lower panels: D, E, F) at the inner and outer turning points for three interaction strengths $\ln(k_F a_{2D}) = -6, 1, \text{ and } 2$. In the in-situ distributions, we can collapse the $\rho(r, t_o)$ (blue) onto $\rho(r, t_i)$ using a global scaling factor $0 < \lambda < 1$. This rescaling is represented by the green curves in panels **A-F** ($\rho_{\text{sc}}(r) = \lambda^{-2} \rho(r/\lambda, t_o)$ and $n_{\text{sc}}(k) = \lambda^2 n(\lambda k, t_o)$). The relative deviations from perfect scaling are found to be in the range of 1 – 2%.

In momentum space, the inverse scaling factor λ^{-1} should collapse the inner and outer turning point distributions if the system were scaling invariant. This condition is satisfied to a good approximation both in the BEC ($\ln(k_F a_{2D}) \sim -6$) and BCS ($\ln(k_F a_{2D}) \sim 2$) regimes (Fig. 9.2 **D, F**). However, in the crossover region $\ln(k_F a_{2D}) \sim 1$, we find a striking discrepancy between the measured $n(k, t_i)$ at the inner turning point and the rescaled expectation $n_{\text{sc}}(k)$. In fact, while we

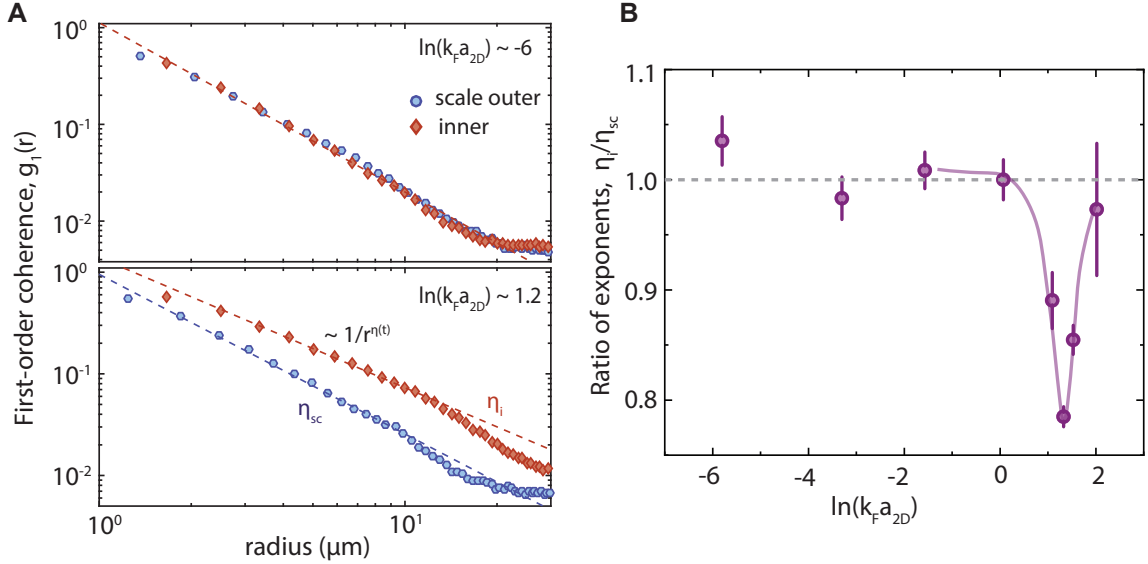


Figure 9.3: The quantum anomaly and spatial coherence. **A** The first-order correlation function $g_1(r, t_i)$ at inner point (red) and rescaled correlation function $g_1(\lambda r, t_o)$ at the outer points (blue), for $\ln(k_F a_{2D}) \sim -6$ (upper panel, BEC) and $\ln(k_F a_{2D}) \sim 1.2$ (lower panel, crossover). In BEC regime, $g_1(r, t_i)$ and $g_1(\lambda r, t_o)$ coincide, whereas in the crossover regime, the two curves are conspicuously different. From the power-law decay of $g_1(r) \sim r^{-\eta}$, we extract the exponent η . **B** The ratio η_i/η_o across the BEC-BCS crossover. The scale-invariant expectation $\eta_i/\eta_o = 1$ is reproduced in the BEC regime. In the crossover regime, we observe a sharp dip in the ratio signaling the scaling violation in the long-range phase correlations. The minimum ratio is at $\ln(k_F a_{2D}) \sim 1$ which coincides with the regime of many-body pairing observed in Murthy2018.

expect $n(k, t_i)$ to be always broader than $n(k, t_o)$ (see Fig. 9.2 **D,F**), the measured momentum distribution at $\ln(k_F a_{2D}) \sim 1.5$ shows the opposite effect. Here, the occupation of the low- k region of $n(k)$ is significantly enhanced not only with respect to the expectation, but also compared to $n(k, t_o)$. This discrepancy evidences that scale invariance is violated due to strong interactions, with an unmistakable signature in momentum-space that is absent in position space! Crucially, we observe the largest discrepancy to be in the low- k region of $n(k)$, indicating that phase correlations in the superfluid may be influenced by the scaling violation.

9.4 Quantum anomaly and phase correlations

The phase correlations in the superfluid are characterized by the first-order correlation function $g_1(r)$ which is directly obtained from the $n(k)$ through a Fourier transform. In our previous work [54], we observed the transition from exponential to algebraic decay in $g_1(r)$, in agreement with BKT theory [168] and Quantum Monte Carlo computations. Here, we use the same procedure described in [54] to extract $g_1(r)$ at the inner and outer turning points, which are shown in for Fig. 9.3 **A**, for two interaction parameters corresponding to the BEC and crossover regimes. To account for the change in cloud size while comparing the two correlation functions, we plot $g_1(r_{sc}, t_o)$ in rescaled coordinates $r_{sc} = \lambda^2 r$. In addition, we extract the exponent η by fitting a power-law ($f(r) \sim r^{-\eta(t)}$) to $g_1(r)$. Even though the exponents we measure are larger than the homogeneous BKT predictions, they have the same qualitative behavior [168], in particular a smaller exponent correspond to a larger superfluid phase space density $D_s = \rho_s \lambda_T^2$, where ρ_s is the superfluid density and λ_T the thermal de Broglie wavelength.

In the BEC regime, the two curves ($g_1(r)$ and $g_1(r_{sc}, t_o)$) collapse onto each other (see Fig. 9.3 **A**), whereas in the crossover regime, the correlation functions are substantially different with the inner $g_1(r)$ decaying slower than expected. In Fig. 9.3 **B**, we show the ration η_i/η_o for different interaction strengths across the BEC-BCS crossover. For scale invariant systems $\eta_i = \eta_o$, i.e the spectrum of phase fluctuations is unaffected by a change in the density. Indeed, we find $\eta_i/\eta_o \approx 1$ in the BEC regime but the ratio dips dramatically in the crossover regime to a value of approximately 0.8, before rising up again in the weakly interacting BCS regime. This quantitative deviation proves that the quantum scale anomaly that originates

in the short-distance fermionic correlations has a striking influence on the long-range phase correlations in the superfluid.

What is the origin of these unexpected effects? First, we remark that the interaction region ($\ln(k_F a_{2D}) \sim 1$) where we see the largest scaling violation in the phase correlations coincides extremely well with the regions of a) maximum critical temperature [99], b) largest density-dependent pairing (pseudogap) [165] and c) the maximum breathing mode frequency shift [73]. This is strongly suggestive that all these effects may have a common mechanism. One possible explanation comes from the density-dependent pairing effect observed in our previous work [165]. Specifically in the crossover region, a change in density during the breathing cycle corresponds to a change in the total pairing energy in the system. Since the total energy of the system is conserved, the enhancement of pairing energy is compensated by the depletion of the pair kinetic energy. We have analyzed the kinetic energy scaling during the evolution and indeed found a violation consistent with this argument (see Appendix 9.5.2).

The observations in Fig. 9.3 may also provide clues towards explaining the enhanced critical temperatures in this region. We recall that the power law exponents are an indicator of superfluid stiffness and phase space density: a smaller η corresponds to more coherence and larger D_s . For scale invariant systems, D_s necessarily remains constant throughout the breathing cycle leading to $\eta_i/\eta_o = 1$. However in the crossover regime, the observation of $\eta_i/\eta_o < 1$ implies that the density-dependent pair correlations in fact enhance the phase space density for the same absolute temperature. In other words, the critical D_s required for the superfluid transition can be attained at higher T_c/T_F , as seen in [99].

In conclusion we have measured the scaling dynamics of a 2D fermi superfluid in the BEC-BCS crossover. In the whole interaction range, the density profile did not exhibit any visible effects of scale invariance breaking and satisfied the prediction of dynamical $SO(2,1)$ symmetry [164]. This is consistent with the significantly low shifts in the breathing mode frequency recently reported in [73], but in clear contradiction with the polytropic equation of state predictions of Refs. [76, 77]. The same discrepancy in fact exists between the dynamical measurements of the nearly invariant breathing mode and the experimentally measured equation of state in equilibrium [83, 84] which depends on scale. Understanding its origin remains an

open question for the future.

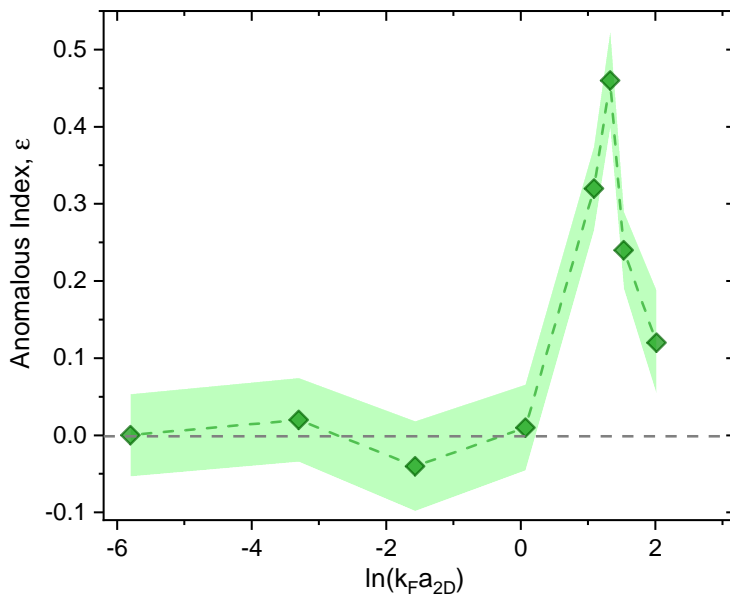
In momentum space, we found a remarkable signature of scale-invariance breaking that was not previously predicted. It is particularly surprising that the short-distance fermionic correlations which break scale invariance have the largest impact on the low momentum modes, which correspond to the long-wavelength phase fluctuations in the superfluid [99, 54, 52]. This implies that the quantum anomaly also has an influence on transport properties which are fundamentally connected to superfluid phase fluctuations. An interesting question is if other scaling phenomena such as turbulent cascades in superfluids are affected by such quantum anomalies.

Acknowledgements We are grateful to I. Boettcher, T. Lompe, J. Hofmann, S. Moroz and K. V. Kheruntsyan for insightful discussions. This work has been supported by the ERC consolidator grant 725636, the Heidelberg Center for Quantum Dynamics and is part of the DFG Collaborative Research Centre SFB 1225 (ISOQUANT). P.M.P. acknowledges funding from European Union Horizon 2020 programme under the Marie Skłodowska-Curie grant agreement No. 706487. Supporting data can be found in the Supplementary Material. Raw data is available upon request.

9.5 Appendix

9.5.1 Preparing the sample

We start our experiments with a molecular Bose–Einstein condensate of approximately 50,000 atoms in the two lowest hyperfine states of ^6Li , which are prepared after a sequence of optical evaporative cooling at a magnetic offset field of 795 G. Thereafter, we transfer the atoms into an optical standing wave trap (SWT) that is created by interference between two cylindrically shaped far detuned laser beams (1064 nm) at a shallow angle of 14° . The spacing between the interference fringes is approximately $4\ \mu\text{m}$ which allows us to load more than 95% of the atoms into a single layer. In the SWT, we perform additional evaporative cooling which results in a gas of $\sim 2 \times 10^4$ atoms at a temperature of 60 nK ($T/T_F \approx 0.05$). The experimental system and protocol for preparing the sample have been discussed in detail in our previous work [99].

Figure 9.4: **Anomalous index.**

9.5.2 Kinetic energy scaling

Here, we estimate the extent of scale invariance breaking in the system by considering the evolution of the pair kinetic energy (T), which is obtained from the instantaneous momentum distributions according to $T(t) = (\hbar^2/2m) \int n(k, t) k^2 d^2k / (2\pi)^2$, where m is the dimer mass. Specifically, we define the dimensionless parameter, which we refer to as the anomalous index

$$\varepsilon = \frac{\log(T_o/\lambda^2 T_i)}{\log(\lambda^2)}, \quad (9.4)$$

where T_i and T_o are the kinetic energies at the inner and outer points. The logarithmic derivative allows to quantitatively estimate the scaling violation in the kinetic energy, independent of the absolute energy scale in the system. In the scale invariant case, $T_i = T_o/\lambda^2$ and hence $\varepsilon = 0$, whereas $\varepsilon \neq 0$ in the presence of quantum anomalous corrections which modify the scaling of kinetic energy, i.e $T_i = T_o/\lambda^2 \rightarrow T_o/\lambda^{2-2\varepsilon}$.

The measured values of ε across the BEC-BCS crossover are shown in Fig. 9.3. We find $\varepsilon \approx 0$ in the BEC regime upto $\ln(k_F a_{2D}) \approx -0.5$. In the crossover regime, the inner kinetic energy is observed to be significantly smaller than expected (i.e

$T_i < T_o/\lambda^2$), and therefore ε is positive with a peak value of $\varepsilon \approx 0.4$ at $\ln(k_F a_{2D}) \sim 1.2$. For weaker interaction strengths in the BCS regime (larger $\ln(k_F a_{2D})$), ε shows a declining trend towards the scale invariant value. Intriguingly, this regime of scaling violation ($\ln(k_F a_{2D}) \approx 1$) coincides very closely to region where we previously observed the many-body pairing in the system [165] as well as the maximum shift in the breathing mode frequency [73].

9.5.3 Frequency doubling in k -space

The observation of the breathing dynamics in momentum space reveals a frequency doubling effect between the in-situ and momentum space distributions, with the $n(k)$ showing sharp revivals both at the inner and the outer turning points of the breathing dynamics. Similar behavior was previously predicted in the oscillatory motion of a 1D Bose gas in the Tonks-Girardeau (TG) limit [166]. In this limit the one dimensional system is actually scale invariant and the dynamics could be computed exactly, while in our case it is convenient to rely on a variational approach, based on Ritz's optimization procedure, to analyze the time-dependent GPE [169].

In the BEC limit $\ln(k_F a_{2D}) \ll -1$ the system can be effectively represented by a weakly interacting 2D Bose-Gas. Ignoring finite temperature effects the system can be described by the celebrated Gross-Pitaevskii equation (GPE)

$$i\hbar\partial_t\psi = -\frac{\hbar^2}{2m}\nabla^2\psi + V(\mathbf{r})\psi + g|\psi|^2\psi \quad (9.5)$$

where $m = 2M$ is the Bosonic molecule mass and $g = 4\pi\hbar^2 a_{3D}/m$. This nonlinear equation describes the evolution of the macroscopic wave function of the condensate ψ . We employ the variational solution to compute the evolution of the ground state wave-function [170]. It is convenient to consider a Gaussian trial wavefunction

$$\psi(r) = A(t) \prod_{\mu=x,y,z} \left(e^{-\frac{(\mu-\mu_0(t))^2}{2w_\mu(t)^2} + i(\mu-\mu_0(t))\alpha_\mu(t)} \cdot e^{i(\mu-\mu_0(t))^2\beta_\mu(t)} \right). \quad (9.6)$$

At a given time t , this function defines a Gaussian distribution centered at the position (x_0, y_0, z_0) . The other variational parameters are A (amplitude), w_μ (width),

α_μ (slope), and β_μ , where $\mu \in \{x, y, z\}$. All these parameters are real numbers. The normalization condition for the wave-function should be satisfied for all times and thus fix the $A(t)$ values unambiguously

$$A(t) = \sqrt{\pi^{3/2} w_x(t) w_y(t) w_z(t)}^{-1} \quad (9.7)$$

The imaginary terms appearing in the exponent of Eq. (9.6) are essential for the dynamical evolution of the system. We aim to find the equations describing the evolution of all these variational parameters [170]. The motion of the center of mass is completely harmonic

$$\ddot{\mu}_0 + m\lambda_\mu^2 \omega^2 \mu_0 = 0 \quad (9.8)$$

$$\alpha_\mu = m\dot{\mu}_0 \quad (9.9)$$

The flow equations for the amplitude are

$$\beta_\mu = -\frac{m}{2} \frac{\dot{w}_\mu}{w_\mu} \quad (9.10)$$

$$\ddot{w}_\mu + \lambda_\mu^2 \omega^2 w_\mu = \frac{1}{m^2} \frac{1}{w_\mu^3} + \frac{P}{w_\mu \prod_\alpha w_\alpha} \quad (9.11)$$

where $P = g/m\pi$.

Thanks to the analytic form of the variational ansatz (9.6) it is possible to obtain analytic expression for the most important experimental quantities. Indeed the *in situ* density at point \mathbf{r} is given by

$$n(\mathbf{r}) = |\psi(\mathbf{r})|^2 = \pi^{-3/2} \prod_{\mu=x,y,z} \frac{e^{-\frac{(\mu-\mu_0(t))^2}{w_\mu(t)^2}}}{w_\mu(t)}, \quad (9.12)$$

and the spectral density at momentum k is

$$n_{\mathbf{k}} = (4\pi)^{\frac{3}{2}} \prod_{\mu=x,y,z} \frac{w_\mu e^{-\frac{w_\mu(t)^2(\alpha_\mu(t)-k)^2}{1+4\beta_\mu(t)^2 w_\mu(t)^2}}}{\sqrt{1+4\beta_\mu(t)^2 w_\mu(t)^4}} \quad (9.13)$$

The motion equation for the width displacement in the planar mode is the one of a simple harmonic oscillator. Since the quench dynamics under consideration

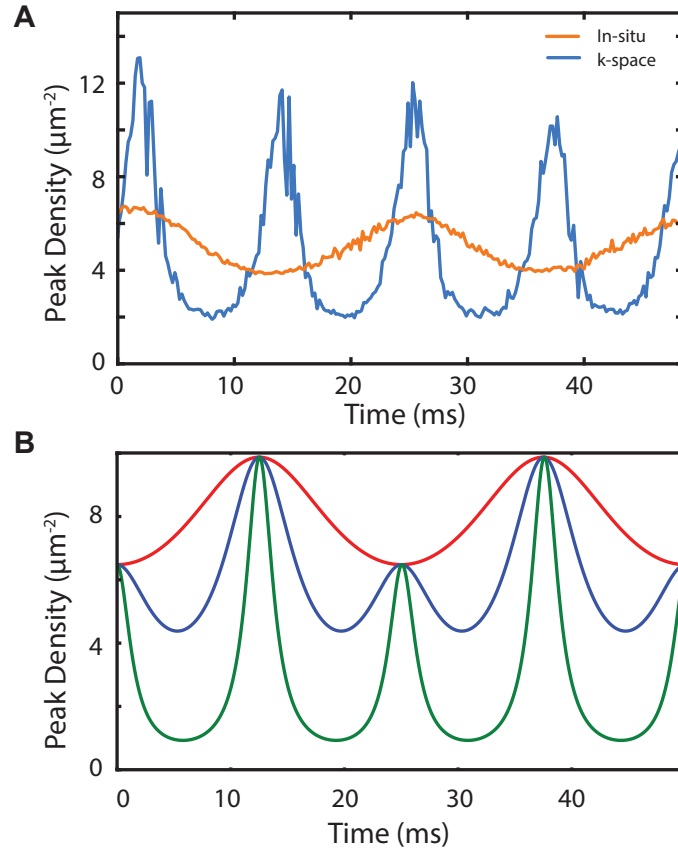


Figure 9.5: Deviation from the equilibrium zero momentum density as a function of time in a single trap period for increasing interaction strength with $\delta_0 = -0.01\bar{w}$.

corresponds to a finite initial value of the displacement at $t = 0$ the width evolve according to the simple equation $w(t) = \bar{w} + \delta_0 \cos(\omega_{xy}t)$, for $\delta_0 \ll 1$, consistently with the harmonic approximation. Focusing on the $k = 0$ component of the spectral density substituting the width expression into Eq.(9.13) in the $k = 0$ case we get in the $m = 1$ case

$$n_{k=0} = \frac{(4\pi)^{3/2} \bar{w}_z (\bar{w} + \delta_0 \cos(\omega_{xy}t))^2}{1 + \delta_0^2 \omega_{xy}^2 \sin^2(\omega_{xy}t) (\bar{w} + \delta_0 \cos(\omega_{xy}t))^2}. \quad (9.14)$$

The analysis of latter formula already yields some interesting informations: the numerator has one maxima, for $\omega_{xy}t = 0$ and one minima for $\omega_{xy}t = \pi$, and produces

the expected *density contribution* to the zero momentum component of the spectral density.

Indeed for a large cloud $w(t) > \bar{w}$ the zero momentum density is larger than at equilibrium, conversely for $w(t) < \bar{w}$ we expect it to be lowered. However the simple *density picture* is modified by the denominator in Eq. (9.14), which contains the *phase contribution* to the spectral density, see Eqs. (9.6) and (9.13). The denominator in Eq. (9.14) has two minima, for $\omega_{xy}t = 0, \pi$, one in correspondance to a maxima of the numerator the other to a minima. Thus we may expect a double peak structure for the zero momentum spectral density with two maxima occurring over a single period $T = 2\pi/\omega_{xy}$. Since the equilibrium value of the width \bar{w} increases with P the possibility of having two maxima into one single frequency period is regulated by the strength of the interaction, at least in the harmonic approximation. Indeed in the limit $\delta_0/\bar{w} \ll 1$ only the denominator in (9.14) contributes to the zero momentum density, as it is shown in Fig.9.5. In the case $\delta_0 \leq \bar{w}$ the harmonic approximation is not valid and we cannot employ formula (9.14). However the doubling effect remains even if it appears at smaller interaction strengths.

Let us compare the experimental results for the width and zero-momentum density results, see Fig.9.5. Good agreement of the experimental data with the theoretical curves is obtained for small quenches $\delta_0 \simeq 0.02\bar{w}$ and large interactions strength $P \simeq 500$ consistently with the conjecture of fermionic dynamics being described by GPE on the BEC side of the crossover.

The variational approach depicted above is fully consistent in $d = 2$ with the scale invariance dynamics described in the main text, as long as the position space Gaussian profile (9.6) is replaced with a generic rescaled many body wave-function $\Psi(X/\lambda(t))$, where the time dependent scale parameter λ obeys the Ermakov-Milne equation

$$\ddot{\lambda} + \omega_{xy}^2 \lambda = \frac{\omega_{xy}^2}{\lambda^3} \quad (9.15)$$

which is consistent with Eq.(9.11) in two dimensions with $P = 0$.

How to take a snapshot of the superfluid order parameter?

10

Preprint

Directly imaging the order parameter of an atomic superfluid using matterwave optics

P. A. Murthy¹ and S. Jochim¹

¹*Physikalisches Institut, Ruprecht-Karls-Universität Heidelberg*

Abstract

We propose a method to directly measure the complex phase, the superfluid density and the velocity field in an superfluid ultracold gas. The method consists of bringing the gas to momentum space using matterwave focusing, performing specific momentum-dependent operations, and subsequently focusing the gas back to in-situ position space. We build on close analogies to well-known techniques in microscopy such as Zernike phase contrast, dark field and schlieren imaging. The application of these ideas directly at the level of the macroscopic wavefunction of the superfluid will allow to directly visualize several complex and intriguing phenomena such as phase fluctuations, topological defects, and enable measurement of transport properties.

10.1 Introduction

Superfluidity is one of the most intriguing phenomena in nature which, even a century past its discovery, continues to puzzle physicists. Superfluids belong to a wider class of many-body systems that exhibit emergent quantum effects at macroscopic scales. Paradoxically, such *quantumness* allows a simplified description of the full quantum state in terms of a classical field, also known as the order parameter [171, 24] $\Psi(\mathbf{x}, t) = \sqrt{n_s(\mathbf{x}, t)} \exp(i\phi(\mathbf{x}, t))$ with spatial density n_s and phase ϕ . In principle,

many of the special properties of superfluids – such as frictionless flow, quantized angular momenta, critical velocity, collective excitations etc. – can be linked to this elegant picture [14]. Although the phenomenon of superfluidity has been the subject of extensive theoretical and experimental research, one can ask the curious question: can we directly take a *snapshot* the order parameter?

With the advent of ultracold Bose and Fermi gases, an excellent experimental platform has emerged for studying superfluidity in a variety of settings. The unprecedented level of tunability in these systems has allowed the measurement of physical observables that are difficult to access in condensed matter systems such as ^4He . Interference and time-of-flight experiments in both Bose and Fermi systems have provided striking visualizations of long range coherence [25, 26], topological defects such as vortices [102] and solitons [172], and correlation functions [53, 54, 173]. Currently, a range of fundamental questions are being pursued under the broad themes of lower dimensional systems - such as Berezinskii–Kosterlitz–Thouless transition in 2D; non-equilibrium phenomena such as the Kibble Zurek mechanism [174, 175], superfluid turbulence [176, 177] and non-thermal fixed points [178]. To answer these questions, we need robust experimental tools that allow direct access to the key observables, and consequently simplify the interpretation of experimental data.

In this letter, we propose a method to directly measure the superfluid order parameter of the superfluid by imaging the density n_s , the local phase ϕ and the local gradients of the field of a trapped ultracold atomic gas cooled below the superfluid critical temperature T_c . Our method is analogous to $4f$ -imaging in optical microscopy [86] (see Fig.10.1 A) from which several well known techniques such as dark-field, phase-contrast and schlieren imaging have been derived. In contrast to optical imaging however, we apply the methods directly on the level of the matterwave field.

The crux of the method lies in the fact that the evolution of a quantum state in a harmonic trap for a quarter of its period amounts to performing a Fourier transform (\mathcal{F}) of the initial wavefunction. In cold atom experiments, this has been demonstrated for both 1D [93, 91, 92] and 2D [95, 64] systems using optical and magnetic potentials. We consider a gas of bosons trapped in an external potential and whose state is described by the field $\Psi(\mathbf{x}, t = 0)$. The gas is suddenly released to expand ballistically in a shallow harmonic potential for a quarter period $T/4 = \pi/2\omega$ (Fig.10.1 B). At $t = T/4$, the different momentum components of the initial state

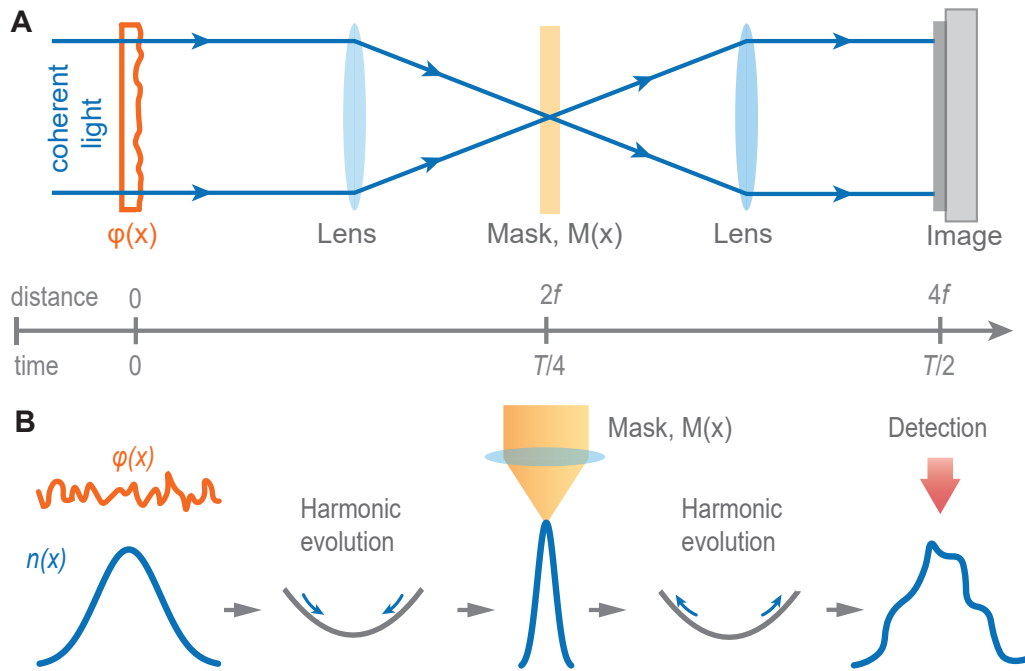


Figure 10.1: Microscopy of the matterwave field. **A** Illustration of the $4f$ imaging setup in optics, which utilizes the Fourier transforming property of a lens. An object modifies an incident coherent light field, which propagates through a series of lenses. At the first Fourier plane at a distance $z = 2f$, a mask function $M(\mathbf{x})$ is imposed on the field followed by propagation through a second lens. **B** An analogous method performed with an ultracold atomic superfluid. Using a matterwave lens that consists of an evolution in a harmonic trap for a quarter period $t = T/4$, the system is brought to Fourier space where a Mask function is applied for a short duration by means of spatially engineered optical potentials. After evolution for another $T/4$, the density of the gas is measured.

separate spatially, and the field and density are given by

$$\Psi(\mathbf{x}, T/4) = \mathcal{F}[\Psi(\mathbf{x}, 0)] \equiv \tilde{\Psi}(\mathbf{p}, 0) \quad (10.1)$$

$$n(\mathbf{x}, T/4) = \tilde{n}(\mathbf{p}, 0), \quad (10.2)$$

with $\mathbf{p} = m\omega\mathbf{x}$. The main requirement for this mapping to work is that the interparticle collisions during the $T/4$ evolution are negligible. This is readily achieved in both 1D and 2D systems, since the interaction energy is released primarily along the tightly confining direction leading to a rapid quench of interactions [64].

At $T/4$, a spatial mask $M(\mathbf{x}) = A_{\text{mask}}(\mathbf{x})e^{i\varphi_{\text{mask}}(\mathbf{x})}$, with amplitude A_{mask} and phase φ_{mask} , is imprinted on the field. The field is subsequently Fourier transformed by yet another $T/4$ evolution which returns it to its original configuration. The modified field at $t = T/2$ is then

$$\Psi(\mathbf{x}, T/2) = \mathcal{F}[M(\mathbf{x})\Psi(\mathbf{x}, T/4)] \quad (10.3)$$

Experimentally, these masks are simply optical patterns generated using spatial light modulators, which have been implemented in several cold atom experiments in recent years [179, 180, 181]. For binary amplitude masks, we propose to use light pulses that are resonant to the atomic hyperfine transitions. By engineering the spatial structure of the resonant beam, atoms at certain positions can be selectively filtered. For masks to purely modify the phase, we propose using optical potentials that are far detuned from the hyperfine transitions, which has been previously employed to create vortices and solitons [172]. For a given spatial potential $V(\mathbf{x})$, the phase imprinted on the field by a far-detuned potential is

$$\varphi_{\text{mask}}(\mathbf{x}) = -\frac{i}{\hbar}V(\mathbf{x})\delta t, \quad (10.4)$$

where δt is the duration of the pulse. By tuning the overall intensity of the optical beam, the required phase shift can be achieved at much shorter time scales than the focusing time $T/4$. We now proceed to describe the operations required to measure the different components of the superfluid order parameter.

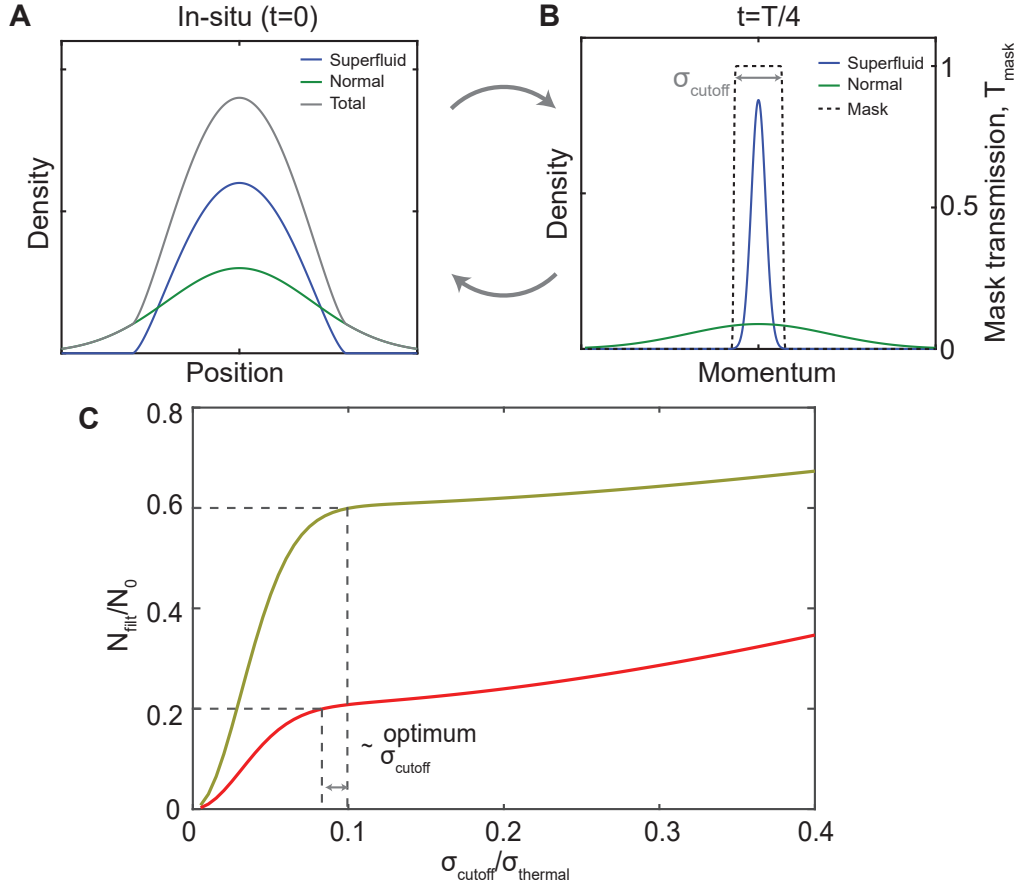


Figure 10.2: Estimating the superfluid density. **A.** Illustration of in-situ density distribution which shows coexisting superfluid (blue) and normal (green) components. **B.** In momentum space ($t = T/4$), the superfluid occupies the low- k modes while the normal gas has a broad distribution. Here, an absorptive mask (dashed line) with a cutoff scale σ_{cutoff} is applied using a resonant laser beam, which removes the normal fraction. At $t = T/2$, the remaining superfluid density is measured. **C** The total fraction of unfiltered atoms N_{filt}/N_0 plotted as a function of σ_{cutoff} scaled by the Boltzmann width σ_n^k for two values of superfluid fraction $\xi = 0.6$ (yellow) and 0.2 (red). The curves show a clear shoulder as they cross the respective values of ξ (dashed lines), which can be used to estimate the optimum σ_{cutoff} .

10.2 Superfluid Density

We start by discussing a scheme to estimate the superfluid density. According to the two-fluid model, a system at a finite temperature below T_c consists of a superfluid component $n_s = |\Psi|^2$ and an incoherent normal component [171]. In space, the two components coexist, as shown in Fig.10.2 A, and hence the in-situ density is given as

$$n(\mathbf{x}, t = 0) = n_s(\mathbf{x}, 0) + n_n(\mathbf{x}, 0) \quad (10.5)$$

Therefore extracting the superfluid density from the total in-situ profile is not a simple task. However, in momentum space the two components have vastly different distributions (see Fig.10.2 B) owing to the large difference in coherence lengths between them. In general, the superfluid component occupies the low-lying momenta with width $\sigma_s^k \sim 1/\min[L, \xi_s]$, where L is the system size and ξ_s is the superfluid coherence length. The thermal component on the other hand follows a broad Boltzmann distribution with width $\sigma_n^k \sim 1/\lambda_T$ determined by the thermal de-Broglie wavelength λ_T . In typical experiments, at low enough temperatures, the ratio of the two k -space widths is of the order of $\sigma_n^k/\sigma_s^k = R_s/\lambda_T \sim 10 - 25$. Such a large separation of scales between the two components makes it possible to apply filtering operations on only one of them. To measure the superfluid density, we use an amplitude mask at $t = T/4$, represented by dashed lines in Fig.10.2 B, that *transmits* only the low- k modes while discarding the thermal fraction. As the system is brought back to position space after another $T/4$ evolution, the measured density mainly consists of the initial superfluid density.

$$n(\mathbf{x}, T/2) \approx n_{\text{SF}}(\mathbf{x}, 0) \quad (10.6)$$

Experimentally, a low-pass filter is implemented using a spatially engineered resonant laser beam that is turned on for a short duration at $T/4$. Although quite simple in principle, the method's efficacy depends to some extent on the choice of the momentum-space cutoff σ_{cutoff} of the filter. At a qualitative level, the measurement will generally be more accurate at lower temperatures where the ratio of the two widths is larger. At a given temperature, however, there exists an optimum cutoff scale which results in the smallest error in estimating the superfluid density. For

a strongly bimodal momentum distribution, the optimum cutoff can be found by analyzing the total particle number as a function of σ_{cutoff} . To illustrate this, we assume that both components follow gaussian distributions with a width factor $\sigma_n^k/\sigma_s^k = 20$. It is quite straightforward to then show that the particle number after filtering N_{filt} has the form,

$$\frac{N_{\text{filt}}}{N_0} = \alpha.\text{erf}^2\left(\frac{\sigma_{\text{cutoff}}}{\sigma_{\text{SF}}^k}\right) + (1 - \alpha).\text{erf}^2\left(\frac{\sigma_{\text{cutoff}}}{\sigma_{\text{T}}^k}\right), \quad (10.7)$$

where N_0 is the total unfiltered particle number, α is the superfluid fraction and erf denotes the Gauss error function. In Fig. 10.2 C, we show the variation of the particle number after filtering as a function of σ_{cutoff} for two different values of superfluid fraction: $\alpha = 0.6, 0.2$. We note that both curves exhibit a clear shoulder feature where the filtered atomic fraction approaches the superfluid fraction and therefore the shoulder position can be used as a reliable proxy to determine the optimum σ_{cutoff} . We note that a similar shoulder should exist for any distribution that has a large enough separation of scales.

10.3 Local Phase

Having detected the superfluid density, we move on to measure the complex phase $\phi(\mathbf{x})$ of the superfluid. The phase is an extremely important quantity in the theory of superfluidity, as it encompasses the elementary excitations of the system such as phase fluctuations and topological defects (vortices and solitons) [14]. Because experiments can only measure the density, information of the phase is typically lost. Interference methods convert phase to density, provided a suitable phase reference is available, either using a separately prepared coherent sample [143, 182, 53] or by beam splitter operations [183]. Here we show that, in analogy to Zernike phase contrast method [184], the *Bose-condensed* component of the system can itself be used as a phase reference, which respect to which the phase fluctuations are defined.

The complex field of the superfluid can be described as $\Psi(\mathbf{x}) = \sqrt{n_0}e^{i(\phi_0 + \phi(\mathbf{x}))} = \Psi_0(\mathbf{x})e^{i\phi(\mathbf{x})}$, where Ψ_0 is the wave-function of the condensate with constant phase

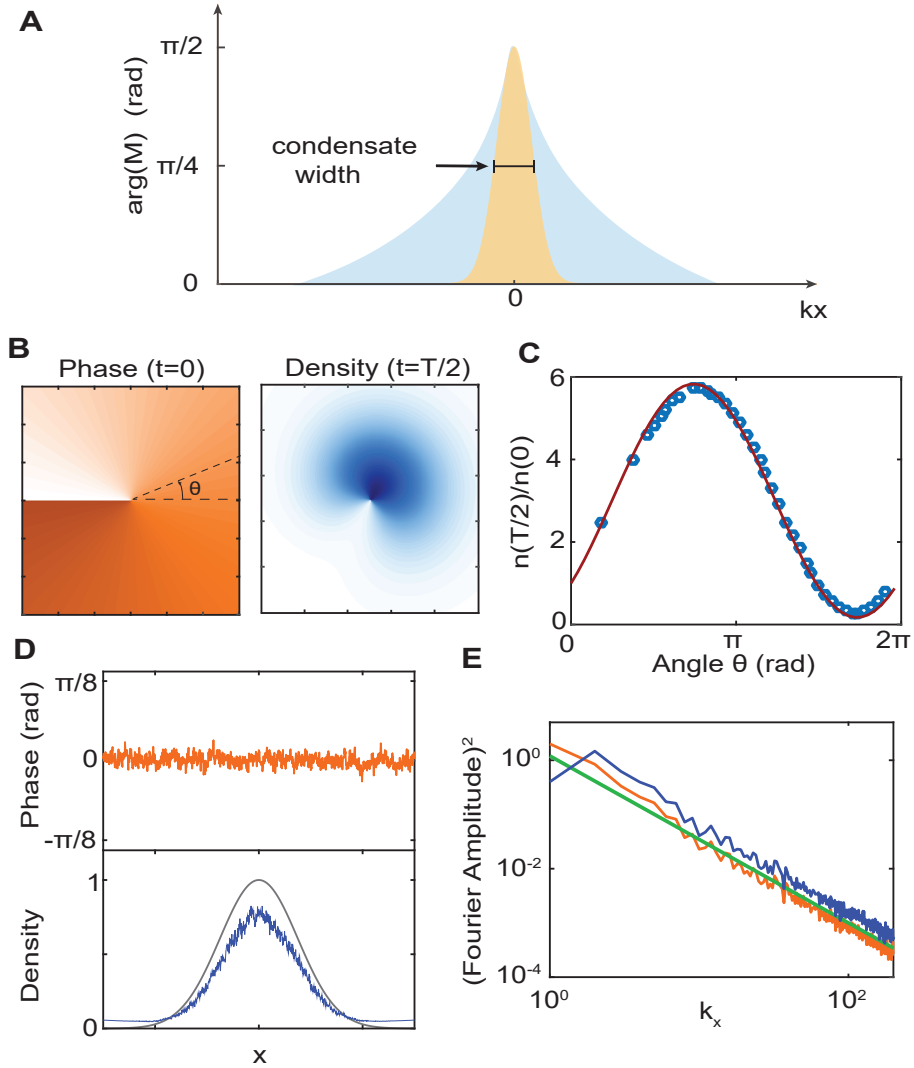


Figure 10.3: Imaging the complex phase. **A** In analogy to Zernike phase contrast microscopy, the mask function selectively imprints a $\pi/2$ phase shift on the $k = 0$ condensate peak (yellow). At $t = T/2$, the density of the cloud then reflects the initial spatial phase $\phi(\mathbf{x})$. **B** The phase of a topological vortex (left panel) becomes visible as a winding of the density (lower panel) at $T/2$. **C** The scaled density $n(x, T/2)/n(x, 0)$ at a fixed radius as a function of θ shows a sinusoidal dependence. **D** Random phase fluctuations with algebraically decaying Fourier spectrum $f(k) \sim k^{-1.5}$ (upper panel), which become measurable as density fluctuations (lower pane, blue line). **E**. The Fourier spectrum of the initial phase fluctuations (orange), the final density fluctuations at $T/2$ (blue) and the reference curve $f \sim k^{-1.5}$, show excellent agreement.

ϕ_0 . The constant and fluctuating components of the field can be written as [90],

$$\Psi = \Psi_0 e^{i\phi(\mathbf{x})} = \Psi_0 + \delta\Psi. \quad (10.8)$$

To image the complex phase $\phi(\mathbf{x})$, we use a mask function that imprints a $\pi/2$ phase shift on the condensate only, as shown in Fig.10.3A. Experimentally, this is achieved by a tightly focused off-resonant laser beam positioned at $k = 0$, and having approximately the same width as the k -space width of the condensate. The field at $t = T/2$ is the given by

$$\Psi(\mathbf{x}, T/2) = \Psi_0 e^{i\pi/2} + \delta\Psi = \Psi_0 [e^{i\pi/2} + e^{i\phi(\mathbf{x})} - 1] \quad (10.9)$$

The corresponding density is $n(\mathbf{x}, T/2) = \Psi^\dagger \Psi = n_0 [3 - 2\sqrt{2} \cos(\phi(\mathbf{x}) - \pi/4)]$, which shows a sinusoidal dependence on the spatial phase. For small phase shifts, we find the approximate density

$$n(\mathbf{x}, T/2) \approx n_0 [1 + 2\phi(\mathbf{x})] \quad (10.10)$$

is directly proportional to the phase. We illustrate this scheme using by simulating two physically relevant examples. The simulation consists of Fourier transforming the initial field, multiplying a factor $e^{i\varphi_{\text{mask}}}$ and Fourier transforming back. In Fig.10.3 B and C, we use the example of a topological vortex $\phi(\mathbf{x}) = m\theta$ (left panel in Fig.10.3B), where $m = \pm 1$ is the winding number. We see that, due to the $\pi/2$ phase shift on the $k = 0$ component, the winding of the initial *phase* at $t = 0$ is converted a winding of the *density* at $t = T/2$. In Fig.10.3 C, we show the scaled density $n(\mathbf{x}, T/2)/n(\mathbf{x}, 0)$ as a function of the azimuthal angle θ for a fixed radius, which shows the expected sinusoidal dependence on the phase.

In Fig.10.3 D and E, we show the example of phase fluctuations in the superfluid. The initial phase chosen here (Fig.10.3 D, upper panel), contains random fluctuations with a Fourier spectrum that decays algebraically according to $f(k) \sim k^{-2+\eta}$, with $\eta = 0.5$. This corresponds to the spatial first order correlation function having the form $g_1(r) = \langle e^{i(\phi(r) - \phi(0))} \rangle \sim r^{-\eta}$. We see that the random fluctuations in the initial phase are converted to density fluctuations at $t = T/2$ (Fig.10.3 D lower panel), which are simple to measure. In Fig.10.3 E, we show the Fourier spectrum

of the scaled density at $T/2$ (blue), the initial phase (orange) and a reference curve $f(k) \sim k^{-1.5}$ (green), which show excellent agreement. Since the spectrum directly relates to the phase coherence function, this implies that density-density correlations at $T/2$ directly relates to $g_1(r)$ at $t = 0$. Power law behavior of phase coherence is found in several phenomena, notably near critical transitions and non-equilibrium systems. Measuring the exponents is therefore relevant for current studies both in lower dimensions [84] and non-equilibrium systems [176].

10.4 Velocity and vorticity

To explore phenomena related to transport, it is essential to extract information that is encoded in the derivatives of the phase. The two relevant quantities in this regard are the superfluid velocity $\mathbf{v}_s(\mathbf{x}) = (\hbar/2m)\nabla\phi(\mathbf{x})$, and the vorticity $\omega = (\hbar/m)\nabla \times \nabla\phi(\mathbf{x})$. The latter characterizes rotationality in superfluids and is non-zero only in the presence of a phase singularity such as a vortex.

To measure v_s and ω , we require a method that converts phase gradient to density. This can be achieved by using a spiral mask $M(\mathbf{x}) = e^{\pm i\theta}$ (see Fig.10.4 A), which has the same form as the phase of a vortex except here it is applied in k -space. The main function of this mask is to imprint a π phase difference between any two diametrically opposite points. In optics, such spiral phase plates have been used to enhance edge features of objects [185, 186, 187, 188]. An important aspect here is that the direction of circulation of the spiral mask impacts the final field at $T/2$, as we will show below. To analyze the effect of the spiral mask, it is simpler to work with polar coordinates $(x, y) \rightarrow (r, \theta)$. The field at $t = T/2$ is given by

$$\Psi(\mathbf{r}, T/2) = \mathcal{F}[e^{\pm i\theta_k} \cdot \mathcal{F}[\Psi(r)]] = \Psi(\mathbf{r}) * \mathcal{F}(e^{\pm i\theta_k})(\mathbf{r}), \quad (10.11)$$

where $*$ is the convolution between functions. The Fourier transform of the phase mask is a radially symmetric function $\mathcal{F}(e^{\pm i\theta})(\mathbf{r}) = 2\pi i e^{\pm i\theta} \int_0^{k_{\max}} dk k J_1(kr)$, where k_{\max} is a cutoff momentum upto which the mask is active. Following the analysis of [188], the final field has the form

$$\Psi_{\pm}(\mathbf{r}, T/2) = C \left[\partial_r \Psi(\mathbf{r}, 0) \pm \frac{i}{r} \partial_{\theta} \Psi^*(\mathbf{r}, 0) \right], \quad (10.12)$$

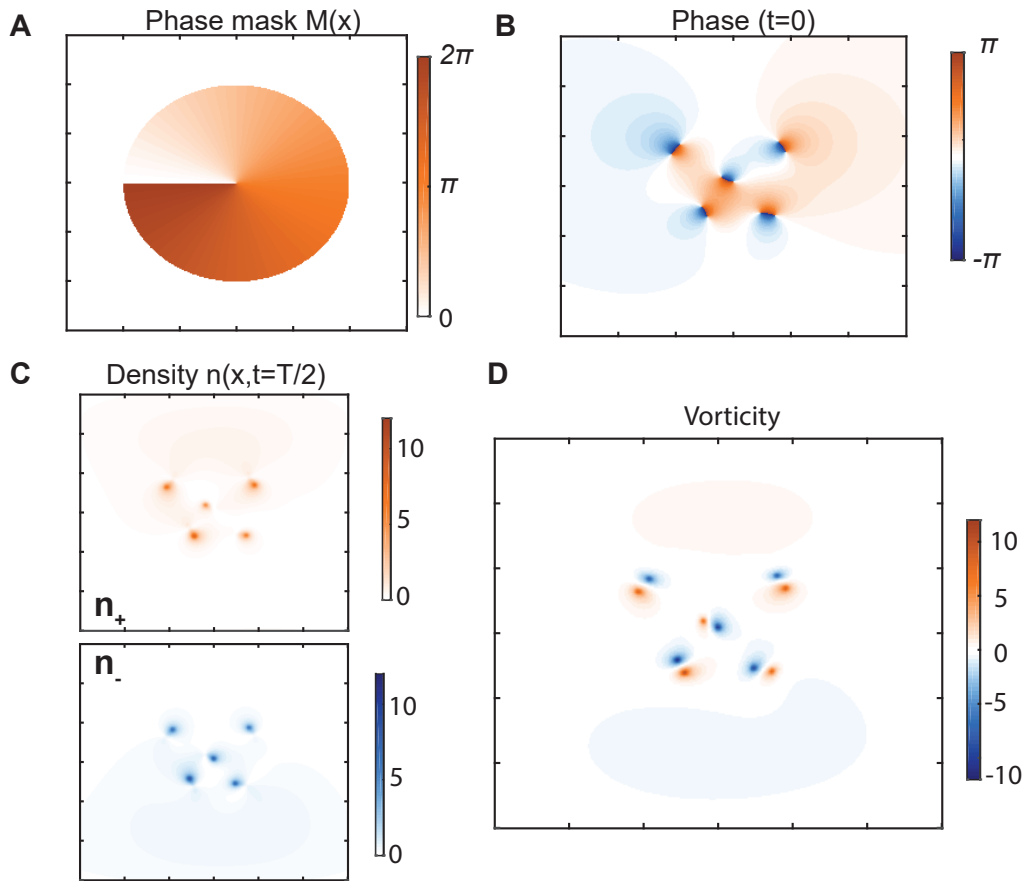


Figure 10.4: Gradient and curl of the phase. **A** We use a spiral phase mask $\arg(M) = \pm\theta$ at $t = T/4$, which leads to two density distributions n^+ and n^- at $t = T/2$ accordingly. **B** Example of a distribution of topological vortex-antivortex pairs. **C** We show n_+ (upper panel) and n_- (lower panel) corresponding to $m = +1$ and $m = -1$. In each of the two images, only the vortices with the circulation parallel to the mask become visible at $t = T/2$. **D** The difference between the two densities $n_+ - n_-$ is directly related to the vorticity of the superfluid.

where $C = \pi e^{i(\theta+\pi)} \int dr' r'^2 \int_0^{k_{\max}} dk k J_1(kr)$ is a normalization factor. It is evident that depending on whether the mask circulation is clockwise or anti-clockwise, we get different expressions for the field. For each of the two cases (Ψ_+, Ψ_-) , we can extract the corresponding density (n_+, n_-) . The velocity and vorticity can be obtained from the sum and difference of the densities of the two components. From the sum of the components,

$$n_+ + n_- = 2C^2 [\partial_r \Psi \partial_r \Psi^* + \frac{1}{r^2} \partial_\theta \Psi \partial_\theta \Psi^*] = 2C^2 |\nabla \Psi|^2, \quad (10.13)$$

we obtain the absolute gradient of the field. For the case of irrotational flow and slowly varying density, we can reduce this further to obtain $n_+ + n_- = 2C^2 n_s(x, 0) |\mathbf{v}_s(\mathbf{x})|^2$, the local superfluid velocity. From the difference between the two components we obtain the local vorticity,

$$\begin{aligned} n_+ - n_- &= \frac{2iC^2}{r} [\partial_r \Psi \partial_\theta \Psi^* - \partial_\theta \Psi \partial_r \Psi^*], \\ &= 2iC^2 (\nabla \times \mathbf{j}), \end{aligned} \quad (10.14)$$

where $\mathbf{j} = (\Psi^* \nabla \Psi - \Psi \nabla \Psi^*)$ is the superfluid current.

In Fig.10.4 B-D, we exemplify this scheme using a phase distribution of vortex-antivortex pairs (upper panel, B), which are predicted to occur in several situations including 2D BKT superfluids. We perform the simulation for both clockwise and anti-clockwise spiral masks and the corresponding densities n_+ and n_- are shown in 10.4 C. An interesting feature of this scheme is that at $t = T/2$, the density becomes concentrated at the vortex core locations where the field gradient is the largest. Furthermore, we see that in each of these images, only the vortices with circulation parallel to the spiral mask become visible. The difference between the images gives us the local vorticity which shows sharp positive and negative peaks shown in Fig.10.4 D.

To realize this experimentally, the main challenge is to simultaneously measure n_+ and n_- in each realization. For this, we propose the following scheme that exploits the availability of hyperfine states in atomic systems. At approximately $t = T/4$, roughly half of the atoms are transferred to a higher lying hyperfine state using a microwave/radio-frequency π -pulse. The light for the phase mask is detuned (in-between the two transitions) such that atoms in one spin component are red-shifted

while those in the other component are blue-shifted with respect to the laser. For the spiral mask, this translates to the two spin components experiencing opposite circulations. Subsequently at $T/2$, the density of each component is measured separately and analyzed.

10.5 Experimental Issues

We now turn to a concrete experimental example where these ideas could be realized. We consider a 2D gas of approximately 5×10^4 ^{87}Rb atoms in the ground state $5S_{1/2}$, trapped in a highly anisotropic harmonic potential, cooled to low temperatures $T \sim 100$ nK and having a radial Thomas–Fermi radius of $R_{\text{TF}} = 50 \mu\text{m}$. The harmonic focusing potential is assumed to have a frequency $\omega = 2\pi \times 5$ Hz and a focusing time $T/4 = 50$ ms. There are three main requirements for the methods proposed above. (i) We need sufficient spatial resolution at $T/4$, such that we can address different k -components using the masks. For the assumed frequency, we find the k -space width of the Bose-condensed component to be $\sigma_s^k = 2\pi\hbar/m\omega R_{\text{TF}} \approx 3 \mu\text{m}$, which is resolvable with an objective (NA ~ 0.2). (ii) The phase imprinting operations should be performed at time scales much shorter than the atomic motion. For a laser beam with wavelength $\lambda = 1064$ nm, we estimate that a pulse with a power of approximately 10 mW focused down to a spot size of radius $3 \mu\text{m}$ and duration $20 \mu\text{s}$ is needed to imprint a $\pi/2$ phase shift, which is feasible. (iii) For the hyperfine state transfer scheme suggested above, we use the manifolds $F = 1$ and $F = 2$, which are energetically separated by 6.8 GHz. Hence an microwave π -pulse can be used to transfer half of the atoms to the higher state in a short time. Additional experimental details are provided in SOM.

In conclusion, we proposed a set of methods that enable direct imaging of the order parameter of an ultracold atomic superfluid. The individual tools suggested in this work rely on already established techniques, such as matterwave focusing, phase imprinting, spatially engineered potentials and hyperfine state transfer. The ideas presented here can be straightforwardly applied to superfluids in a variety of trap geometries such as optical lattices, box traps and annular traps. In the future, it will be exciting to build upon these ideas and develop tools that can be used to measure other fundamental properties of quantum systems related to entanglement and many-particle correlations.

Discussion and Outlook

Understanding the emergent properties of strongly correlated systems is a central goal of many-body physics. The collective behavior of many-body systems is fundamentally influenced by the dimensionality. Our goal has been to explore the interplay between interactions and reduced dimensionality and therefore we started our research program on strongly interacting two-dimensional Fermi gases. In the course of our research over the past four years, we have uncovered several new properties and effects in these remarkable systems. Here, I will discuss some of these in detail.

11.1 Methodological progress

Experimental science is, to a large extent, driven by methods and hence I will first review the methodological progress that was made during the course of this thesis. One of the first achievements in our research on 2D Fermi gases was the development of a robust method to measure the momentum distribution of the sample. Strongly interacting Fermi gases in three dimensions have been studied for more than a decade. However, the conventional time-of-flight method used to measure momentum space properties is always susceptible to interactions between particles during the expansion, which distorts the mapping between momentum and position. In our case, both the reduced dimensionality and the rapid ramp of the magnetic field helped us overcome the problem and ensure a nearly ballistic expansion. The use of a harmonic potential means that a one-to-one mapping between momentum and position occurs exactly at one point in time, which is experimentally accessible. In addition, we were able to solve the problems arising from the expansion in the z -direction by using a collimating pulse. This resulted in the first ever measurement of the full pair momentum distribution of a strongly interacting gas. It is quite remarkable that a concept that is so widely used in optics could be implemented on a strongly correlated system.

In general, accessing the true momentum space is of fundamental interest in many-body physics. To begin with, it allows to measure various properties such as the temperature and non-thermal fraction. More importantly, it enables the measurement of correlation functions that are crucial to characterize many-body phases. Our initial focus was on measuring the first-order correlation function which is a measure of phase correlations in the system. However, our method has been recently extended to the single particle level! In the few-body experiment of our group, the $T/4$ method was combined with a single particle imaging method to measure the positions of each atom in momentum space [189]. This means that any order of correlations functions - two-point, three-point etc. - can be directly measured. Combining this method with single particle detection in position space will enhance our cold atoms toolbox significantly.

In our recent work described in Chapter 10, we took the $T/4$ method one step further. It has always been a matter of curiosity, whether we can get direct access to the superfluid order parameter $\psi(r) = \sqrt{n_0(r)}e^{i\phi(r)}$. The phase $\phi(r)$ is of particular interest since several properties of superfluids such as long-wavelength fluctuations and topological defects are encoded in it. Even several decades after the discovery of the superfluid and its description in terms of classical fields, a direct method to image the phase has not been proposed. We realized that the matterwave optics idea could again be used to image the order parameter. This can be achieved by extending the focusing technique by another $T/4$ evolution which bring us back to position space. By performing certain momentum-dependent operations at $T/4$, we could reveal different properties of the order parameter: superfluid density (n_s), complex phase ($\phi(r)$), local superfluid velocity ($\nabla\phi(r)$) and the vorticity ($\nabla \times \phi(r)$). In particular, this is the first technique that will allow to measure the velocity and vorticity of the superfluid, both of which are important quantities in the study of transport phenomena.

Our proposed method is very simple. In fact, the only requirement of our method is a matterwave lens (harmonic potential) and a means to imprint different masks on the sample in momentum space. This makes it an extremely versatile technique, which could be used not only in 2D Fermi gases but in a variety of cold atom systems such as optical lattices. An exciting prospect is to once again combine this proposal with a single atom imaging technique. This would allow to probe and manipulate

not only the superfluid order parameter but the general many-body wavefunction of different systems.

In our experiments on pairing, we developed a simple method to measure the spatially resolved RF response of the system. Similar techniques had been demonstrated also in 3D Fermi gases, we extended it to 2D systems. The key advantage of 2D system is the measured depletion of the density at a particular radius directly corresponds to the spectral response, without the need for complicated Abel transforms of the distribution which is required in 3D.

During the course of our investigations, we encountered two main technical issues. The first was the fact that the spectral response function only featured a single pairing branch that showed a dependence on density (see Fig. 9.1). The density dependence, although extremely interesting, can arise either from the pair wavefunction being modified by the density (the interesting effect), or the entire spectrum undergoing a mean-field interaction shift (the not-so-interesting effect). Having a single branch does not allow us distinguish between these two. One way to disentangle the two is to subtract the mean-field energy shift. However, the knowledge of the mean-field shift is not reliable in the strongly interacting regime, where it in fact theoretically diverges. Therefore, we implemented the method of quasi-particle spectroscopy that consists of introducing a small spin imbalance. This did the trick, since now we were able to observe two branches and from the difference between them, extract the actual pairing energy.

Another issue was the effect of final state interactions. Ideally in RF spectroscopy, we assume that atoms in the final state do not interact with those in the initial state. However, in ${}^6\text{Li}$, this assumption is not valid and final state interactions are known to cause significant distortions in the spectra. To overcome this problem, we combined the spatially resolved quasiparticle spectroscopy with the ability to create 2D Fermi gases with different spin mixtures, i.e. $|12\rangle$ or $|13\rangle$. Since the initial state is the same but the final state interactions are very different, we were able to establish that the measured pairing energy was independent of final state effects.

11.2 Physical insights

Now I will move on to discuss the physical insights on two-dimensional systems that we gained from the experiments presented in this thesis, and I will particularly try

to highlight the surprises that we uncovered along the way.

The first experiments focused on the phenomenon of superfluidity in the 2D Fermi gas. Prior to this thesis, different experimental groups had explored 2D Fermi gases (although only at high temperatures), and there was a substantial amount of theoretical work as well. Even though we had observed some qualitative signatures of spatial coherence in the short time-of-flight measurements (see Fig. 4.2), the implementation of the $T/4$ technique revealed a remarkably pronounced signature of superfluidity in the momentum distribution, as shown in Chapter 6. This has been the first unambiguous observation of superfluidity in quasi-two-dimensional Fermi gases. On the BEC side, the critical temperature was consistent with the theoretically predicted T_c for a 2D Bose gas. We should note that the theory prediction is expected to be valid only in the weakly interacting perturbative regime that is satisfied only for Bose gases ($\tilde{g} \sim 0.1$). In our experiments, even the weakest interactions on the BEC side ($\tilde{g} \sim 0.6$) correspond to a strongly interacting 2D Bose gas. Therefore, it is quite intriguing that the Bosonic theory should predict the correct critical temperature even in this regime. A crucial insight from this experiment is the significant enhancement of the critical temperature ($T_c/T_F \sim 0.18$) in the strongly interacting regime $\ln(k_F a_{2D}) \sim 1$. This provided the first indication that strong fermionic correlations have an impact on the critical properties of the system.

Following up with this work, we investigated the first-order correlation function of the system as a function of temperature and interactions. This analysis revealed some unexpected effects in the decay of phase correlations. These can be summarized as, (i) Algebraic decay of $g_1(r)$ at distances larger than the thermal de Broglie wavelength. This is also consistent with QMC computations by Markus Holzmann. The algebraic decay is indeed an expectation of BKT theory, but only in homogeneous systems where the effect of density can be neglected. Here, we have an inhomogeneous trapped system, and therefore the measured momentum distribution is averaged over the whole sample. Why should we then observe an algebraic decay in the trap-averaged $g_1(r)$? (ii) The power-law exponents are much larger than the homogeneous expectation. In particular, at the critical temperature, we measure $\eta(T_c \approx 1.4)$, whereas the universal prediction for homogeneous systems is $\eta(T_c \approx 1.4)_{\text{hom}} = 1/4$. (iii) The critical power-law exponents are independent of the interaction strength across the BEC-BCS crossover. This is quite remarkable and possibly the first such

reported observation. Here, the possibility to tune the interactions provides a big advantage. Physically, this means that the long-range physics near the critical point is independent of changes in the microscopic interactions, which formally means that all the transitions belong to the same universality class. This is a subtle point as we saw in the recent measurement of scale invariance breaking.

To understand the large power-law exponents, we estimated the effect of the density variation on the $g_1(r)$ using a local density approximation. We found that even though the density change influences the measurement, it only plays a large role. Most of the contribution to the $g_1(r)$ comes from the phase fluctuations in the system. In fact, this has an interesting implication that the spectrum of long-wavelength phase fluctuations itself is modified by the presence of the harmonic potential. Consequently, the application of Local Density Approximation (LDA) fails in the superfluid phase. This aspect was investigated in more detail by Igor Boettcher and Markus Holzmann [168], who analytically computed the full $g_1(r)$ in a trapped system. They were able to show that the algebraic correlations are indeed due to phase fluctuations which leads to the increased exponents.

In the next set of experiments described in Chapter 8, we studied pairing phenomenon above T_c . As already mentioned in the introduction, pairing is central to fermionic superfluidity. In particular, pairing in the strongly interacting region is not understood. We measured the pairing energy at various interaction strengths and temperatures using a combination of tools as discussed in the previous section. The observations were once again quite surprising. In the BEC regime, we measured the expected two-body pairing energy E_B . However, in the strongly interacting regime, we measured a pairing energy that is substantially higher than E_B and in addition, shows a strong dependence on the local density. In previous theoretical works, the existence of such a phase was qualitatively predicted but the region in which this occurs was not known. The experiments in the group of M. Köhl had explored this question but only explored the BEC regime. In addition, these experiments had technical limitations that prevented them from discerning the nature of pairs. We went beyond these works and in fact found the regime where the pairing wavefunction is significantly modified by the presence of the surrounding medium, very much in the same spirit as Cooper pairing.

These measurements have enhanced our understanding of the normal phase. At a

qualitative level, the many-body pairing regime is consistent with BCS theory to the extent that the spectra have the same features (see Fig. 8.7). However, BCS theory predicts Cooper pairing to occur only below T_c , whereas we observed many-body pairing at extremely high temperatures, of the order of the Fermi temperature. How do we describe this phase? Since, the system is gapped in the strongly interacting region, it is certainly not a Fermi liquid. On the other hand, since the pairing gap is density-dependent, it is also not a liquid of point-like bosons. In this sense, this is a new phase which has not been fully described yet. In the future, it will be interesting to explore the higher order correlations in this regime, possibly by using the single atom momentum-space imaging technique recently developed in our group.

The findings of our work on pairing are immediately relevant for the next experiments. Here, we explored the scaling dynamics of the 2D Fermi gas in the superfluid phase. Scale-invariance is a fundamental concept in several fields and also has special significance in the study of 2D systems, as we have discussed in previous chapters. We observed scale-invariance breaking in the dynamics of the system in momentum space. One of the main experimental aspects of this work is that we used the breathing mode as a novel tool that allows to compare the system at two different points in time (the inner and outer turning points) which correspond to different system size but the same entropy. This means that only the rescaling of coordinates becomes relevant and all other spurious effects such as temperature change drop out. In this picture, the in-situ and momentum space distributions provide complementary information on the equation of state and the spatial coherence properties respectively. Once again, these experiments revealed some surprising effects.

First, we observed that the in-situ density distribution evolved in a nearly self-similar manner across the BEC-BCS crossover. This is in itself quite surprising. The in-situ density distribution directly corresponds to the pressure of the sample, i.e. for the same particle number, a lower peak density indicates higher pressure ($P \propto n^2$). Therefore, from previous theory [79, 80] and equilibrium experiments [83, 84, 85], we would expect that the presence of a polytropic exponent that violates scale-invariance, i.e. $P \propto n^2 \rightarrow n^{2+2\gamma}$, should have an appreciable effect on the time-evolution of the density distribution too. However, this seems to be not the case. Even though our observation is in agreement with the reduced frequency shifts in the breathing mode [73], it is in strong contradiction to the theory expectation as

well as the experimentally measured equation of state. The origin of this discrepancy is not understood currently. It is worth noting that all the theoretical predictions so far are based on the assumption that at any point in its evolution, the gas is always in equilibrium because the scattering rate of particles is much higher than the breathing mode frequency. One hypothesis towards explaining the discrepancy is that the instantaneous thermalization assumption may not be valid. In other words, the thermalization time-scales may be longer than expected and consequently, the breathing motion may not be significantly driven by the equation of state, which may explain the reduced shifts.

The bigger surprise came from the momentum-space measurements. Whereas the in-situ distribution showed nearly no signature of scale-invariance breaking, the momentum distribution showed a dramatic effect. On both the BEC and BCS sides, where the interactions are relatively weak, we observed self-similar evolution in both in-situ and momentum space. However, in the strongly interacting regime, momentum distribution at the inner turning point was narrowed than at the outer turning point, which is exactly the opposite of the expected result. In momentum space, the effect turns out to be very large, which has an intriguing consequence for the first-order correlation function $g_1(r)$ and the power-law exponents. We observed that in the quantum anomalous region, the exponent at the inner turning point is smaller than at the outer, meaning that the system is more coherent at the inner turning point. This has an extremely important implication: that the BKT exponent is modified by the short-range fermionic correlations.

These findings imply that the density-dependent pairing effect that was observed in our RF spectroscopy experiments has a central role to play in the emergent properties of the 2D gas in the strongly interacting regime. In particular, it seems to be the connecting link between the observation of scale-invariance breaking in momentum space and the enhanced critical temperatures found in Chapter 6.

In conclusion, we found that the two-dimensional Fermi gas is a fascinating system which exhibits special emergent effects, such as the BKT phase transition, many-body pairing above T_c and violation of scale invariance. In the future, it will be interesting to find connections between the ultracold gas and other strongly correlated systems such as graphene, Iron pnictides and exciton-polariton condensates.

11.3 A new direction: quantum state assembly

In the experiments presented in the thesis so far, we were interested in the properties of a many-body system with tens of thousands of particles. Of course, in this scenario, we were looking for global effects such as first-order correlations, and did not have full control of the state of the system. What if we could prepare a many-body system with extremely low entropy such that the complete quantum state is within our control? Indeed, this is a very challenging and ambitious goal. However, achieving this can potentially provide a versatile platform to study correlated quantum systems at a deep level.

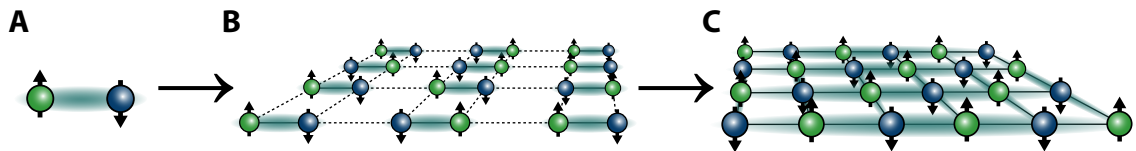


Figure 11.1: **Illustration of Quantum State Assembly.** The example of creating the anti-ferromagnetic ground state of the repulsive Hubbard model. The starting point are individually prepared double wells, which are subsequently merged to form a lattice. The ground state of the building blocks adiabatically connects to that of the final system.

Creating such systems has been discussed in cold atoms literature for several years [190, 191]. There are two main challenges: (i) Creating a low-entropy state, which requires a high degree of control on the trapping potentials and fields, and (ii) Measuring different observables such as correlation functions, which requires the ability to image single atoms. One of the leading experimental candidates in this direction has been the so-called Quantum Gas Microscopes. Here, the approach is to start with a large number of particles in an optical lattice and cool the system down using different techniques. One of the spectacular features of this technique is the ability to image the occupation number of atoms in every lattice site. This approach has had several prominent successes, for example the single-site resolved observation of the Mott Insulator (both Bose and Fermi) and the observation of long-range anti-ferromagnetic ordering in the repulsive Fermi-Hubbard model.

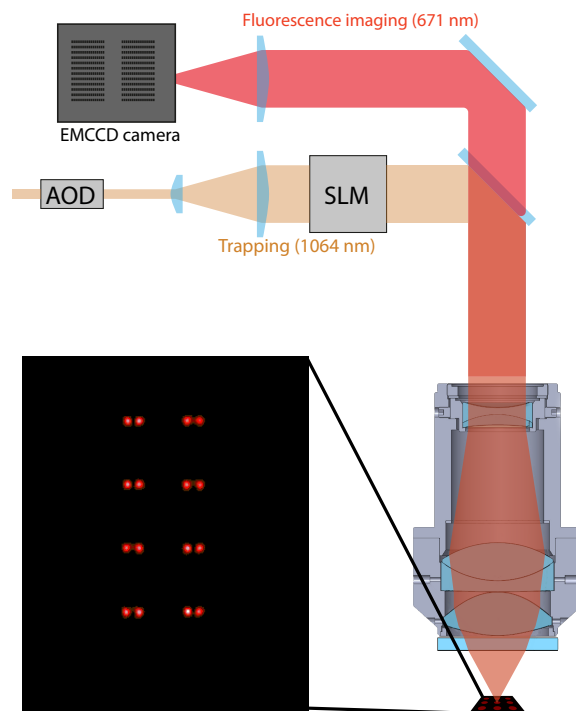


Figure 11.2: **A schematic view of the new experimental upgrade.** Using a combination of an acousto-optical deflector (AOD) and a phase-only Spatial Light Modulator (SLM), we create arbitrary trapping potentials that are beamed through a high-resolution objective. The atoms are imaged using fluorescence imaging through the same objective. The fluorescence photons are collected through the objective and imaged on a single-photon sensitive camera.

In our group, we have started on a different path. Our approach is to start from small systems which have been separately prepared at low entropies and subsequently merge them adiabatically into a larger system. For example, to study the Fermi-Hubbard model at low temperatures, we would start with several double wells in the ground state and merge them to form a lattice. The deterministic preparation of few-particle systems has already been demonstrated in the second experiment in our group [192]. In particular, the preparation of two repulsive fermions in the ground state of a double-well potential has been demonstrated [193]. In addition, the imaging of single atoms in free space has been demonstrated recently.

Now that we have these tools, our goal is to prepare larger systems. We recently implemented a substantial upgrade to the 2D Fermi gas apparatus. The new setup consists of two main components as shown in Fig. 11.2.

(i) Creating arbitrary optical potentials and deterministically prepare the required quantum state. We aim to do this using a Spatial Light Modulator (SLM), which imprints an arbitrary phase distribution on an incoming laser beam. The intensity distribution in the focus of a lens (placed in a $2f$ configuration with the SLM) corresponds to the Fourier transform of the field in the SLM plane. Then, for a desired intensity distribution for trapping, it is possible to calculate the corresponding phase distribution. In practice, calculating the phase is non-trivial and requires the use of iterative algorithms. Details of the phase retrieval can be found in the thesis of Marvin Holten [194].

In our setup, the final intensity distribution using 1064 nm light is beamed on to the atom plane through a high-resolution objective ($NA \sim 0.55$). With this, we can create potential wells with approximately $1.5 \mu\text{m}$ spacing. With a field of view of about $200 \mu\text{m}$, we will be able to project a lattice of size 5×5 . Whether we will be able to prepare low temperature states remains to be seen. Our approach is not only limited to lattice geometries but also continuous systems such as homogeneous box potentials.

(ii) The other crucial component of the setup is high-resolution imaging. For this, we use a single-photon sensitive camera which detects photons collected through the same high resolution objective as used for trapping [195]. In a recent paper, the viability of this method has been demonstrated [189].

As we have seen in this thesis, many-body physics is a wide field with a large number of open questions and several new effects to be discovered. This setup will significantly enhance our toolbox and allow access to several new observables such as higher order correlations functions.

Contributions to publications

1. **Matterwave-fourier optics with a strongly interacting two-dimensional Fermi gas.** *Physical Review A* 90, 043611 (2014). Puneet A. Murthy developed the technique to measure the momentum distribution, together with Selim Jochim, and is the principal author of the manuscript.
2. **Observation of pair-condensation in the quasi-2D BEC-BCS crossover.** *Physical Review Letters* 114, 230401 (2015). Puneet A. Murthy contributed to the experimental measurements, data analysis and interpretation.
3. **Observation of the Berezinskii–Kosterlitz–Thouless phase transition in an ultracold Fermi gas.** *Physical Review Letters* 115, 010401 (2015). Puneet A. Murthy conceptualized the project, performed the data analysis and is the corresponding author of the manuscript. The theoretical interpretation was provided by Igor Boettcher and QMC data by Markus Holzmann.
4. **High-temperature pairing in a strongly interacting two-dimensional Fermi gas.** *Science* 359, 452-455 (2018). Puneet A. Murthy conceptualized the project and implemented the spatially resolved quasi-particle spectroscopy technique for the 2D Fermi gas. In addition, Puneet A. Murthy contributed to the measurements and data analysis, and is the principal author.
5. **Quantum scale anomaly and spatial coherence in a 2D Fermi superfluid.** Preprint (2018). Puneet A. Murthy performed most of the measurements and analysis, and is the principal author. The theoretical interpretation was provided by Nicolás Defenu and Tilman Enss.
6. **Directly imaging the order parameter of an atomic superfluid using matterwave optics.** Preprint (2018). Puneet A. Murthy and Selim Jochim developed the idea for the technique. Puneet A. Murthy prepared the manuscript and is the principal author.

Bibliography

- [1] Piers Coleman. *Introduction to Many-Body Physics*. Cambridge University Press, 2015.
- [2] Philip W Anderson. More is different. *Science*, 177(4047):393–396, 1972.
- [3] Robert B Laughlin and David Pines. From the cover: The theory of everything. *Proceedings of the National Academy of Sciences of the United States of America*, 97(1):28, 2000.
- [4] K. v. Klitzing, G. Dorda, and M. Pepper. New method for high-accuracy determination of the fine-structure constant based on quantized hall resistance. *Phys. Rev. Lett.*, 45:494–497, Aug 1980.
- [5] B. N. Taylor, W. H. Parker, and D. N. Langenberg. Determination of $\frac{e}{h}$, using macroscopic quantum phase coherence in superconductors: Implications for quantum electrodynamics and the fundamental physical constants. *Rev. Mod. Phys.*, 41:375–496, Jul 1969.
- [6] N. D. Mermin and H. Wagner. Absence of Ferromagnetism or Antiferromagnetism in One- or Two-Dimensional Isotropic Heisenberg Models. *Phys. Rev. Lett.*, 17:1133–1136, Nov 1966.
- [7] V. L. Berezinskii. Destruction of long-range order in one-dimensional and two-dimensional systems having a continuous symmetry group I. classical systems. *Sov. Phys. JETP*, 32(3):2–9, 1971.
- [8] V. L. Berezinskii. Destruction of long-range order in one-dimensional and two-dimensional systems possessing a continuous symmetry group. II. quantum systems. *Sov. Phys. JETP*, 34(3):610–616, 1972.

- [9] J. M. Kosterlitz and D. J. Thouless. Ordering, metastability and phase transitions in two-dimensional systems. *J. Phys. C: Solid State Phys.*, 6(7):1181–1203, 1973.
- [10] J. M. Kosterlitz. The critical properties of the two-dimensional xy model. *J. Phys. C: Solid State Phys.*, 7:1046, 1974.
- [11] M. Z. Hasan and C. L. Kane. Colloquium: Topological insulators. *Rev. Mod. Phys.*, 82:3045–3067, Nov 2010.
- [12] Jairo Sinova, Sergio O. Valenzuela, J. Wunderlich, C. H. Back, and T. Jungwirth. Spin hall effects. *Rev. Mod. Phys.*, 87:1213–1260, Oct 2015.
- [13] D. J. Bishop and J. D. Reppy. Study of the Superfluid Transition in Two-Dimensional ^4He Films. *Phys. Rev. Lett.*, 40(26):1727–1730, 1978.
- [14] I. Bloch, J. Dalibard, and W. Zwerger. Many-body physics with ultracold gases. *Rev. Mod. Phys.*, 80:885–964, Jul 2008.
- [15] W.H. Keesom and J.N. van der Ende. *Proc. Roy. Ac. Amsterdam*, 1930.
- [16] J. F. Allen and A. D. Misener. Flow of liquid helium ii. *Nature*, 141(3558):75, 1938.
- [17] P. Kapitza. Viscosity of liquid helium below the λ -point. *Nature*, 141(3558):74, 1938.
- [18] M. J. Buckingham and W. M. Fairbank. The nature of the λ -transition in liquid helium. In *Progress in low temperature physics*, volume 3, pages 80–112. Elsevier, 1961.
- [19] F. London. The λ -phenomenon of liquid helium and the bose-einstein degeneracy. *Nature*, 141(3571):643, 1938.
- [20] L. Landau. Theory of the superfluidity of helium ii. *Phys. Rev.*, 60:356–358, Aug 1941.
- [21] N. N. Bogoliubov. On the theory of superfluidity. *J. Phys (USSR)*, 11(1):23, 1947.

- [22] S Utsunomiya, L Tian, G Roumpos, CW Lai, N Kumada, T Fujisawa, M Kuwata-Gonokami, A Löffler, S Höfling, A Forchel, et al. Observation of bogoliubov excitations in exciton-polariton condensates. *Nature Physics*, 4(9):700, 2008.
- [23] O. Penrose and L. Onsager. Bose-Einstein Condensation and Liquid Helium. *Phys. Rev.*, 104:576–584, Nov 1956.
- [24] C. N. Yang. Concept of Off-Diagonal Long-Range Order and the Quantum Phases of Liquid He and of Superconductors. *Rev. Mod. Phys.*, 34:694–704, Oct 1962.
- [25] I. Bloch, T. Hänsch, and T. Esslinger. Measurement of the spatial coherence of a trapped Bose gas at the phase transition. *Nature*, 403(6766):166–170, 2000.
- [26] M. R. Andrews, C. G. Townsend, H-J. Miesner, D. S. Durfee, D. M. Kurn, and W. Ketterle. Observation of interference between two bose condensates. *Science*, 275(5300):637–641, 1997.
- [27] JR Abo-Shaeer, C Raman, JM Vogels, and Wolfgang Ketterle. Observation of vortex lattices in bose-einstein condensates. *Science*, 292(5516):476–479, 2001.
- [28] R. A. Ogg Jr. Bose-einstein condensation of trapped electron pairs. phase separation and superconductivity of metal-ammonia solutions. *Physical Review*, 69(5-6):243, 1946.
- [29] M. R. Schafroth. Theory of superconductivity. *Physical Review*, 96(5):1442, 1954.
- [30] C. A. Reynolds, B. Serin, W. H. Wright, and L. B. Nesbitt. Superconductivity of isotopes of mercury. *Phys. Rev.*, 78:487–487, May 1950.
- [31] E. Maxwell. Isotope effect in the superconductivity of mercury. *Phys. Rev.*, 78:477–477, May 1950.
- [32] L. N. Cooper. Bound electron pairs in a degenerate fermi gas. *Phys. Rev.*, 104:1189–1190, Nov 1956.

- [33] W. Ketterle and M. W. Zwierlein. Making, probing and understanding ultracold Fermi gases. In *Proc. Int. Sch. Phys. "Enrico Fermi"*, volume CLXIV, Amsterdam, 2008. IOS Press.
- [34] J. Bardeen, L. N. Cooper, and J. R. Schrieffer. Theory of superconductivity. *Phys. Rev.*, 108:1175–1204, Dec 1957.
- [35] I. Giaever and K. Megerle. Study of superconductors by electron tunneling. *Phys. Rev.*, 122:1101–1111, May 1961.
- [36] M. R. Norman, D. Pines, and C. Kallin. The pseudogap: friend or foe of highTc? *Advances in Physics*, 54(8):715–733, dec 2005.
- [37] D. D. Osheroff, R. C. Richardson, and D. M. Lee. Evidence for a New Phase of Solid He³. *Phys. Rev. Lett.*, 28:885–888, Apr 1972.
- [38] F. Steglich, J. Aarts, C. D. Bredl, W. Lieke, D. Meschede, W. Franz, and H. Schäfer. Superconductivity in the presence of strong pauli paramagnetism: CeCu₂Si₂. *Phys. Rev. Lett.*, 43:1892–1896, Dec 1979.
- [39] J. G. Bednorz and K. A. Müller. Possible high Tc superconductivity in the Ba-La-Cu-O system. *Zeitschrift für Physik B Condensed Matter*, 64(2):189–193, Jun 1986.
- [40] Y. Kamihara, T. Watanabe, M. Hirano, and H. Hosono. Iron-Based Layered Superconductor La[O_{1-x}F_x]FeAs ($x = 0.05 - 0.12$) with Tc = 26 K. *Journal of the American Chemical Society*, 130(11):3296–3297, 2008. PMID: 18293989.
- [41] Y. Cao, V. Fatemi, S. Fang, K. Watanabe, T. Taniguchi, E. Kaxiras, and P. Jarillo-Herrero. Unconventional superconductivity in magic-angle graphene superlattices. *Nature*, 2018.
- [42] GR Stewart. Unconventional superconductivity. *Advances in Physics*, 66(2):75–196, 2017.
- [43] M. Sigrist and K. Ueda. Phenomenological theory of unconventional superconductivity. *Rev. Mod. Phys.*, 63:239–311, Apr 1991.

- [44] M. R. Norman. The challenge of unconventional superconductivity. *Science*, 332(6026):196–200, 2011.
- [45] L. V. Keldysh and A. N. Kozlov. Collective properties of excitons in semiconductors. *Sov. Phys. JETP*, 27(3):521, 1968.
- [46] D. M. Eagles. Possible pairing without superconductivity at low carrier concentrations in bulk and thin-film superconducting semiconductors. *Phys. Rev.*, 186:456–463, Oct 1969.
- [47] A. J. Leggett. Diatomic molecules and cooper pairs. In *Modern Trends in the Theory of Condensed Matter*, Proceedings of the XVIth Kapacz Winter School of Theoretical Physics, pages 13–27, 1980.
- [48] J. Dalibard. Collège de France Lectures "Fluides quantiques de basse dimension et transition de Kosterlitz–Thouless", 2017.
- [49] R. E. Peierls. *Helv. Phys. Acta Suppl.*, 7:81, 1934.
- [50] R. E. Peierls. Quelques propriétés typiques des corps solides. *Ann. I. Henri Poincaré*, 5:177–222, 1935.
- [51] P. C. Hohenberg. Existence of long-range order in one and two dimensions. *Phys. Rev.*, 158(2):383–386, 1967.
- [52] Z. Hadzibabic and J. Dalibard. Two-dimensional Bose fluids: An atomic physics perspective. *Riv. del Nuovo Cim.*, 34(389), 2011.
- [53] Z. Hadzibabic, P. Krüger, M. Cheneau, B. Battelier, and J. Dalibard. Berezinskii-Kosterlitz-Thouless crossover in a trapped atomic gas. *Nature*, 441:1118–21, 2006.
- [54] P. A. Murthy, I. Boettcher, L. Bayha, M. Holzmann, D. Kedar, M. Neidig, M. G. Ries, A. N. Wenz, G. Zürn, and S. Jochim. Observation of the berezinskii-kosterlitz-thouless phase transition in an ultracold fermi gas. *Phys. Rev. Lett.*, 115:010401, Jun 2015.
- [55] B. R Holstein. Anomalies for pedestrians. *American journal of physics*, 61(2):142–147, 1993.

- [56] C. L. Hung, X. Zhang, N. Gemelke, and C. Chin. Observation of scale invariance and universality in two-dimensional Bose gases. *Nature*, 470(7333):236–239, 2011.
- [57] D. S. Petrov and G. V. Shlyapnikov. Interatomic collisions in a tightly confined bose gas. *Phys. Rev. A*, 64:012706, Jun 2001.
- [58] J. Levinsen and M. M. Parish. Strongly interacting two-dimensional Fermi gases. *Annu. Rev. Cold Atoms Mol.*, 3(1):71, 2015.
- [59] D. S. Petrov, C. Salomon, and G. V. Shlyapnikov. Weakly Bound Dimers of Fermionic Atoms. *Phys. Rev. Lett.*, 93:090404, Aug 2004.
- [60] D. S. Petrov, C. Salomon, and G. V. Shlyapnikov. Scattering properties of weakly bound dimers of fermionic atoms. *Phys. Rev. A*, 71:012708, 2005.
- [61] Zoran Hadzibabic and Jean Dalibard. Two-dimensional Bose fluids: An atomic physics perspective. *Riv. del Nuovo Cim.*, 34(389), 2011.
- [62] S. Kasahara, T. Yamashita, A. Shi, R. Kobayashi, Y. Shimoyama, T. Watashige, K. Ishida, T. Terashima, T. Wolf, F. Hardy, C. Meingast, H. v. Löhneysen, A. Levchenko, T. Shibauchi, and Y. Matsuda. Giant superconducting fluctuations in the compensated semimetal FeSe at the BCS–BEC crossover. *Nature Communications*, 7:12843, sep 2016.
- [63] V. P. Singh and L. Mathey. Noise correlations of two-dimensional bose gases. *Phys. Rev. A*, 89:053612, May 2014.
- [64] P. A. Murthy, D. Kedar, T. Lompe, M. Neidig, M. G. Ries, A. N. Wenz, G. Zürn, and S. Jochim. Matter wave Fourier optics with a strongly interacting two-dimensional Fermi gas. *Phys. Rev. A*, 90:1–7, 2014.
- [65] N. Prokof'ev, O. Ruebenacker, and B. Svistunov. Critical point of a weakly interacting two-dimensional bose gas. *Phys. Rev. Lett.*, 87:270402, Dec 2001.
- [66] Y. Sagi, T. E. Drake, R. Paudel, R. Chapurin, and Deborah S. Jin. Breakdown of the fermi liquid description for strongly interacting fermions. *Phys. Rev. Lett.*, 114:075301, Feb 2015.

- [67] J. P. Gaebler, J. T. Stewart, T. E. Drake, D. S. Jin, A. Perali, P. Pieri, and G. C. Strinati. Observation of pseudogap behaviour in a strongly interacting fermi gas. *Nature Physics*, 6(8):569–573, jul 2010.
- [68] M. Feld, M. Fröhlich, E. Vogt, M. Koschorreck, and M. Köhl. Observation of a pairing pseudogap in a two-dimensional fermi gas. *Nature*, 480(7375):75–78, nov 2011.
- [69] V. Ngampruetikorn, J. Levinsen, and M. M. Parish. Pair correlations in the two-dimensional fermi gas. *Phys. Rev. Lett.*, 111:265301, Dec 2013.
- [70] P. Törmä. Physics of ultracold fermi gases revealed by spectroscopies. *Physica Scripta*, 91(4):043006, mar 2016.
- [71] M. Bauer, M. M. Parish, and T. Enss. Universal equation of state and pseudogap in the two-dimensional fermi gas. *Phys. Rev. Lett.*, 112:135302, Apr 2014.
- [72] Sidney Coleman. *Aspects of Symmetry: Selected Erice Lectures*, 1988.
- [73] M. Holten, L. Bayha, A. C. Klein, P. A. Murthy, P. M. Preiss, and S. Jochim. Anomalous breaking of scale invariance in a two-dimensional fermi gas.
- [74] L. P. Pitaevskii and A. Rosch. Breathing modes and hidden symmetry of trapped atoms in two dimensions. *Phys. Rev. A*, 55(2):R853–R856, feb 1997.
- [75] M. Olshanii, H. Perrin, and V. Lorent. Example of a Quantum Anomaly in the Physics of Ultracold Gases. *Phys. Rev. Lett.*, 105(9):095302, aug 2010.
- [76] J. Hofmann. Quantum Anomaly, Universal Relations, and Breathing Mode of a Two-Dimensional Fermi Gas. *Phys. Rev. Lett.*, 108(18):185303, may 2012.
- [77] C. Gao and Z. Yu. Breathing mode of two-dimensional atomic fermi gases in harmonic traps. *Phys. Rev. A*, 86:043609, Oct 2012.
- [78] E. Vogt, M. Feld, B. Fröhlich, D. Pertot, M. Koschorreck, and M. Köhl. Scale invariance and viscosity of a two-dimensional fermi gas. *Phys. Rev. Lett.*, 108:070404, Feb 2012.
- [79] G. Bertaina and S. Giorgini. BCS-BEC Crossover in a Two-Dimensional Fermi Gas. *Phys. Rev. Lett.*, 106(11):110403, mar 2011.

- [80] H. Shi, S. Chiesa, and S. Zhang. Ground-state properties of strongly interacting Fermi gases in two dimensions. *Phys. Rev. A*, 92(3):033603, sep 2015.
- [81] Shina Tan. Large momentum part of a strongly correlated fermi gas. *Annals of Physics*, 323(12):2971 – 2986, 2008.
- [82] S. Tan. Large momentum part of a strongly correlated fermi gas. *Annals of Physics*, 323(12):2971 – 2986, 2008.
- [83] V. Makhalov, K. Martiyanov, and A. Turlapov. Ground-State Pressure of Quasi-2D Fermi and Bose Gases. *Phys. Rev. Lett.*, 112(4):045301, jan 2014.
- [84] I. Boettcher, L. Bayha, D. Kedar, P. A. Murthy, M. Neidig, M. G. Ries, A. N. Wenz, G. Zürn, S. Jochim, and T. Enss. Equation of state of ultracold fermions in the 2d bec-bcs crossover region. *Phys. Rev. Lett.*, 116:045303, Jan 2016.
- [85] K. Fenech, P. Dyke, T. Peppler, M. G. Lingham, S. Hoinka, H. Hu, and C. J. Vale. Thermodynamics of an attractive 2d fermi gas. *Phys. Rev. Lett.*, 116:045302, Jan 2016.
- [86] B. EA Saleh and M. C. Teich. *Fundamentals of photonics*, volume 22. Wiley New York, 1991.
- [87] M. H. Anderson, J. R. Ensher, M. R. Matthews, C. E. Wieman, and E. A. Cornell. Observation of bose-einstein condensation in a dilute atomic vapor. *Science (New York, N.Y.)*, 269(5221):198–201, July 1995.
- [88] K. B. Davis, M/ O. M., M. R. Andrews, N. J. van Druten, D. S. Durfee, D. M. Kurn, and W. Ketterle. Bose-einstein condensation in a gas of sodium atoms. *Phys. Rev. Lett.*, 75, 1995.
- [89] M. Greiner, O. Mandel, T. Esslinger, T. W. Hansch, and I. Bloch. Quantum phase transition from a superfluid to a mott insulator in a gas of ultracold atoms. *Nature*, 415(6867):39–44, January 2002.
- [90] W. Ketterle, D. S. Durfee, and D. M. Stamper-Kurn. Making, probing and understanding bose-einstein condensates. *arXiv:cond-mat/9904034*, 1999.

- [91] I. Shvarchuck, Ch. Buggle, D. S. Petrov, K. Dieckmann, M. Zielonkowski, M. Kemmann, T. G. Tiecke, W. von Klitzing, G. V. Shlyapnikov, and J. T. M. Walraven. Bose-Einstein Condensation into Nonequilibrium States Studied by Condensate Focusing. *Phys. Rev. Lett.*, 89:270404, Dec 2002.
- [92] A. H. van Amerongen, J. J. P. van Es, P. Wicke, K. V. Kheruntsyan, and N. J. van Druten. Yang-Yang Thermodynamics on an Atom Chip. *Phys. Rev. Lett.*, 100, 2008.
- [93] T. Jacqmin, B. Fang, T. Berrada, and I. Roscilde, T. and Bouchoule. Momentum distribution of one-dimensional bose gases at the quasicondensation crossover: Theoretical and experimental investigation. *Phys. Rev. A*, 86:043626, Oct 2012.
- [94] J. J. P. van Es, P. Wicke, A. H. van Amerongen, C. Rétif, S. Whitlock, and N. J. van Druten. Box traps on an atom chip for one-dimensional quantum gases. *J. Phys. B: At., Mol. Opt. Phys.*, 43, 2010.
- [95] S. Tung, G. Lamporesi, D. Lobser, L. Xia, and E. A. Cornell. Observation of the Presuperfluid Regime in a Two-Dimensional Bose Gas. *Phys. Rev. Lett.*, 105(23):230408, December 2010.
- [96] J. W. Negele and H. Orland. *Quantum Many Particle Systems*. Advanced Book Classics, 1998.
- [97] G. Zürn, T. Lompe, A. N. Wenz, S. Jochim, P. S. Julienne, and J. M. Hutson. Precise characterization of ^6Li feshbach resonances using trap-sideband-resolved rf spectroscopy of weakly bound molecules. *Phys. Rev. Lett.*, 110:135301, 2013.
- [98] Wenz, A.N. *From Few to Many: Ultracold Atoms in Reduced Dimensions*. PhD thesis, Ruprecht-Karls-Universität Heidelberg, 2013.
- [99] M. G. Ries, A. N. Wenz, G. Zürn, L. Bayha, I. Boettcher, D. Kedar, P. A. Murthy, M. Neidig, T. Lompe, and S. Jochim. Observation of pair condensation in the quasi-2d bec-bcs crossover. *Phys. Rev. Lett.*, 114:230401, Jun 2015.
- [100] C. A. Regal, M. Greiner, and D. S. Jin. Observation of Resonance Condensation of Fermionic Atom Pairs. *Phys. Rev. Lett.*, 92(4):040403–4, 2004.

- [101] M. W. Zwierlein, C. A. Stan, C. H. Schunck, S. M. F. Raupach, A. J. Kerman, and W. Ketterle. Condensation of pairs of fermionic atoms near a feshbach resonance. *Phys. Rev. Lett.*, 92:120403, 2004.
- [102] M W Zwierlein, J R Abo-Shaeer, A Schirotzek, C H Schunck, and W Ketterle. Vortices and superfluidity in a strongly interacting Fermi gas. *Nature*, 435(7045):1047–1051, 2005.
- [103] H. Ammann and N. Christensen. Delta Kick Cooling: A New Method for Cooling Atoms. *Phys. Rev. Lett.*, 78, 1997.
- [104] F. Impens and Ch. J. Bordé. Generalized *abcd* propagation for interacting atomic clouds. *Phys. Rev. A*, 79:043613, Apr 2009.
- [105] J.-F. Riou, Y. Le Coq, F. Impens, W. Guerin, C. J. Bordé, A. Aspect, and P. Bouyer. Theoretical tools for atom-laser-beam propagation. *Phys. Rev. A*, 77:033630, Mar 2008.
- [106] I. Shvarchuck, Ch. Buggle, D. S. Petrov, M. Kemmann, W. von Klitzing, G. V. Shlyapnikov, and J. T. M. Walraven. Hydrodynamic behavior in expanding thermal clouds of ^{87}Rb . *Phys. Rev. A*, 68:063603, Dec 2003.
- [107] H. Hu, A. Minguzzi, X. Liu, and M. P. Tosi. Collective modes and ballistic expansion of a fermi gas in the bcs-bec crossover. *Phys. Rev. Lett.*, 93:190403, Nov 2004.
- [108] Patrick A. Lee, Naoto Nagaosa, and Xiao-Gang Wen. Doping a mott insulator: Physics of high-temperature superconductivity. *Rev. Mod. Phys.*, 78:17–85, Jan 2006.
- [109] Mohit Randeria, Ji-Min Duan, and Lih-Yir Shieh. Bound states, cooper pairing, and bose condensation in two dimensions. *Phys. Rev. Lett.*, 62:981–984, Feb 1989.
- [110] M. Iskin and C. A. R. Sá de Melo. Evolution from bcs to berezinskii-kosterlitz-thouless superfluidity in one-dimensional optical lattices. *Phys. Rev. Lett.*, 103:165301, Oct 2009.

- [111] M. Matsumoto and Y. Ohashi. Pseudogap phenomena in a two-dimensional ultracold Fermi gas near the Berezinskii-Kosterlitz-Thouless transition. *ArXiv e-prints*, July 2014.
- [112] R. Desbuquois, L. Chomaz, T. Yefsah, J. Léonard, J. Beugnon, C. Weitenberg, and J. Dalibard. Superfluid behaviour of a two-dimensional Bose gas. *Nat. Phys.*, 8(9):645–648, 2012.
- [113] M. Bartenstein, A. Altmeyer, S. Riedl, S. Jochim, C. Chin, J. Hecker Denschlag, and R. Grimm. Collective excitations of a degenerate gas at the bec-bcs crossover. *Phys. Rev. Lett.*, 92:203201, 2004.
- [114] T. Bourdel, L. Khaykovich, J. Cubizolles, J. Zhang, F. Chevy, M. Teichmann, L. Tarruell, S. J. J. M. F. Kokkelmans, and C. Salomon. Experimental study of the bec-bcs crossover region in lithium 6. *Phys. Rev. Lett.*, 93:050401, Jul 2004.
- [115] Kirill Martiyanov, Vasiliy Makhalov, and Andrey Turlapov. Observation of a two-dimensional fermi gas of atoms. *Phys. Rev. Lett.*, 105:030404, 2010.
- [116] P. Dyke, E. D. Kuhnle, S. Whitlock, H. Hu, M. Mark, S. Hoinka, M. Lingham, P. Hannaford, and C. J. Vale. Crossover from 2d to 3d in a weakly interacting fermi gas. *Phys. Rev. Lett.*, 106:105304, 2011.
- [117] M. Koschorreck, D. Pertot, E. Vogt, B. Fröhlich, M. Feld, and M. Köhl. Attractive and repulsive fermi polarons in two dimensions. *Nature*, 485(7400):619–622, may 2012.
- [118] A. T. Sommer, L. W. Cheuk, M. J. H. Ku, W. S. Bakr, and M. W. Zwierlein. Evolution of fermion pairing from three to two dimensions. *Phys. Rev. Lett.*, 108:045302, Jan 2012.
- [119] D. S. Petrov, M. Holzmann, and G. V. Shlyapnikov. Bose-Einstein Condensation in Quasi-2D Trapped Gases. *Phys. Rev. Lett.*, 84:2551–2555, Mar 2000.
- [120] See Supplemental Material at <http://link> for a detailed derivation.

- [121] T. Plisson, B. Allard, M. Holzmann, G. Salomon, A. Aspect, P. Bouyer, and T. Bourdel. Coherence properties of a two-dimensional trapped Bose gas around the superfluid transition. *Phys. Rev. A*, 84:061606, Dec 2011.
- [122] N. Prokof'ev and B. Svistunov. Two-Dimensional Weakly Interacting Bose Gas in the Fluctuation Region. *Phys. Rev. A*, 66(043608), 2002.
- [123] R. N. Bisset, M. J. Davis, T. P. Simula, and P. B. Blakie. Quasicondensation and coherence in the quasi-two-dimensional trapped Bose gas. *Phys. Rev. A*, 79:033626, Mar 2009.
- [124] P. Cladé, C. Ryu, a. Ramanathan, K. Helmerson, and W. D. Phillips. Observation of a 2D Bose Gas: From Thermal to Quasicondensate to Superfluid. *Phys. Rev. Lett.*, 102, 2009.
- [125] D. S. Petrov, M. A. Baranov, and G. V. Shlyapnikov. Superfluid transition in quasi-two-dimensional Fermi gases. *Phys. Rev. A*, 67:031601, Mar 2003.
- [126] C. A. R. Sá de Melo, Mohit Randeria, and Jan R. Engelbrecht. Crossover from bcs to bose superconductivity: Transition temperature and time-dependent ginzburg-landau theory. *Phys. Rev. Lett.*, 71:3202–3205, Nov 1993.
- [127] A. M. Fischer and M. M. Parish. Quasi-two-dimensional fermi gases at finite temperatures. *Phys. Rev. B*, 90:214503, Dec 2014.
- [128] P. Dyke, K. Fenech, T. Peppler, M. G. Lingham, S. Hoinka, W. Zhang, S.-G. Peng, B. Mulkerin, H. Hu, X.-J. Liu, and C. J. Vale. Criteria for two-dimensional kinematics in an interacting fermi gas. *Phys. Rev. A*, 93:011603, Jan 2016.
- [129] Bernd Fröhlich, Michael Feld, Enrico Vogt, Marco Koschorreck, Wilhelm Zwerger, and Michael Köhl. Radio-frequency spectroscopy of a strongly interacting two-dimensional fermi gas. *Phys. Rev. Lett.*, 106:105301, 2011.
- [130] G. Reinaudi, T. Lahaye, Z. Wang, and D. Guéry-Odelin. Strong saturation absorption imaging of dense clouds of ultracold atoms. *Opt. Lett.*, 32(21):3143–3145, Nov 2007.

- [131] Tarik Yefsah, Rémi Desbuquois, Lauriane Chomaz, Kenneth J. Günter, and Jean Dalibard. Exploring the thermodynamics of a two-dimensional bose gas. *Phys. Rev. Lett.*, 107:130401, Sep 2011.
- [132] M. E. Gehm. Properties of 6 Li Changed By. 2003.
- [133] C. F. Ockeloen, A. F. Tauschinsky, R. J. C. Spreeuw, and S. Whitlock. Detection of small atom numbers through image processing. *Phys. Rev. A*, 82:061606, Dec 2010.
- [134] J. W. Kane and L. P. Kadanoff. Long-Range Order in Superfluid Helium. *Phys. Rev.*, 155:80–83, Mar 1967.
- [135] David R. Nelson and J. M. Kosterlitz. Universal Jump in the Superfluid Density of Two-Dimensional Superfluids. *Phys. Rev. Lett.*, 39:1201–1205, Nov 1977.
- [136] G. Roumpos, M. Lohse, W. H. Nitsche, J. Keeling, M. H. Szymańska, P. B. Littlewood, A. Löffler, S. Höfling, L. Worschech, A. Forchel, and Y. Yamamoto. Power-law decay of the spatial correlation function in exciton-polariton condensates. *Proc. Natl. Acad. Sci. U.S.A.*, 109(17):6467–6472, 2012.
- [137] W. Dürr, M. Taborelli, O. Paul, R. Germar, W. Gudat, D. Pescia, and M. Landolt. Magnetic Phase Transition in Two-Dimensional Ultrathin Fe Films on Au(100). *Phys. Rev. Lett.*, 62:206–209, Jan 1989.
- [138] C. A. Ballentine, R. L. Fink, J. Araya-Pochet, and J. L. Erskine. Magnetic phase transition in a two-dimensional system: $p(1 \times 1)$ -Ni on Cu(111). *Phys. Rev. B*, 41:2631–2634, Feb 1990.
- [139] J. Choi, S. W. Seo, and Y.-il Shin. Observation of Thermally Activated Vortex Pairs in a Quasi-2D Bose Gas. *Phys. Rev. Lett.*, 110:175302, Apr 2013.
- [140] A. J. Leggett. A theoretical description of the new phases of liquid ^3He . *Rev. Mod. Phys.*, 47:331–414, Apr 1975.
- [141] M. Holzmann and W. Krauth. Kosterlitz-Thouless Transition of the Quasi-Two-Dimensional Trapped Bose Gas. *Phys. Rev. Lett.*, 100:190402, May 2008.

- [142] M. Holzmann, M. Chevallier, and W. Krauth. Universal correlations and coherence in quasi-two-dimensional trapped Bose gases. *Phys. Rev. A*, 81:043622, Apr 2010.
- [143] A. Polkovnikov, E. Altman, and E. Demler. Interference between independent fluctuating condensates. *Proc. Natl. Acad. Sci. U.S.A.*, 103(16):6125–6129, 2006.
- [144] M. Holzmann, G. Baym, J. Blaizot, and F. Laloë. Superfluid transition of homogeneous and trapped two-dimensional Bose gases. *Proc. Natl. Acad. Sci. U.S.A.*, 104(5):1476–1481, 2007.
- [145] M. Holzmann and G. Baym. Condensate superfluidity and infrared structure of the single-particle Green’s function: The Josephson relation. *Phys. Rev. B*, 76:092502, Sep 2007.
- [146] Qijin Chen, Yan He, Chih-Chun Chien, and K Levin. Theory of radio frequency spectroscopy experiments in ultracold fermi gases and their relation to photoemission in the cuprates. *Reports on Progress in Physics*, 72(12):122501, oct 2009.
- [147] Erich J. M. Pseudogaps in strongly interacting fermi gases. 2017.
- [148] J. J. Lee, F. T. Schmitt, R. G. Moore, S. Johnston, Y.-T. Cui, W. Li, M. Yi, Z. K. Liu, M. Hashimoto, Y. Zhang, D. H. Lu, T. P. Devereaux, D.-H. Lee, and Z.-X. Shen. Interfacial mode coupling as the origin of the enhancement of t_c in FeSe films on SrTiO₃. *Nature*, 515(7526):245–248, nov 2014.
- [149] S. Nascimbène, N. Navon, S. Pilati, F. Chevy, S. Giorgini, A. Georges, and C. Salomon. Fermi-liquid behavior of the normal phase of a strongly interacting gas of cold atoms. *Phys. Rev. Lett.*, 106:215303, May 2011.
- [150] A. Perali, F. Palestini, P. Pieri, G. C. Strinati, J. T. Stewart, J. P. Gaebler, T. E. Drake, and D. S. Jin. Evolution of the normal state of a strongly interacting fermi gas from a pseudogap phase to a molecular bose gas. *Phys. Rev. Lett.*, 106:060402, Feb 2011.

- [151] C. H. Schunck, Y. Shin, A. Schirotzek, M. W. Zwierlein, and W. Ketterle. Pairing without superfluidity: The ground state of an imbalanced fermi mixture. *Science*, 316(5826):867–870, may 2007.
- [152] G. Zürn, T. Lompe, A. N. Wenz, S. Jochim, P. S. Julienne, and J. M. Hutson. Precise characterization of ^6Li feshbach resonances using trap-sideband-resolved rf spectroscopy of weakly bound molecules. *Phys. Rev. Lett.*, 110:135301, Mar 2013.
- [153] Y. Shin, C. H. Schunck, A. Schirotzek, and W. Ketterle. Tomographic rf spectroscopy of a trapped fermi gas at unitarity. *Phys. Rev. Lett.*, 99:090403, Aug 2007.
- [154] A. Schirotzek, Y.-il Shin, C. H. Schunck, and W. Ketterle. Determination of the superfluid gap in atomic fermi gases by quasiparticle spectroscopy. *Phys. Rev. Lett.*, 101:140403, Oct 2008.
- [155] M. Barth and J. Hofmann. Pairing effects in the nondegenerate limit of the two-dimensional fermi gas. *Phys. Rev. A*, 89:013614, Jan 2014.
- [156] Ettore Vitali, Hao Shi, Mingpu Qin, and Shiwei Zhang. Visualizing the bec-bcs crossover in a two-dimensional fermi gas: Pairing gaps and dynamical response functions from ab initio computations. *Phys. Rev. A*, 96:061601, Dec 2017.
- [157] C. Langmack, M. Barth, W. Zwerger, and E. Braaten. Clock shift in a strongly interacting two-dimensional fermi gas. *Phys. Rev. Lett.*, 108:060402, Feb 2012.
- [158] B. Fröhlich, M. Feld, E. Vogt, M. Koschorreck, M. Köhl, C. Berthod, and T. Giamarchi. Two-dimensional fermi liquid with attractive interactions. *Phys. Rev. Lett.*, 109:130403, Sep 2012.
- [159] J. Zinn-Justin. *Quantum Field Theory and Critical Phenomena*. 2002.
- [160] A. Barabási and R. Albert. Emergence of scaling in random networks. *Science*, 286(5439):509–512, 1999.
- [161] R. N. Mantegna and H. E. Stanley. Scaling behaviour in the dynamics of an economic index. *Nature*, 376(6535):46, 1995.

- [162] R. Desbuquois, T. Yefsah, L. Chomaz, C. Weitenberg, L. Corman, S. Nascimbène, and J. Dalibard. Determination of scale-invariant equations of state without fitting parameters: Application to the two-dimensional bose gas across the berezinskii-kosterlitz-thouless transition. *Phys. Rev. Lett.*, 113:020404, Jul 2014.
- [163] S. Moroz. Scale-invariant Fermi gas in a time-dependent harmonic potential. *Phys. Rev. A - At. Mol. Opt. Phys.*, 86(1):011601, jul 2012.
- [164] E. Taylor and M. Randeria. Apparent low-energy scale invariance in two-dimensional fermi gases. *Phys. Rev. Lett.*, 109:135301, Sep 2012.
- [165] P. A. Murthy, M. Neidig, R. Klemt, L. Bayha, I. Boettcher, T. Enss, M. Holten, G. Zürn, P. M. Preiss, and S. Jochim. High-temperature pairing in a strongly interacting two-dimensional fermi gas. *Science*, 359(6374):452–455, 2018.
- [166] Y. Y. Atas, I. Bouchoule, D. M. Gangardt, and K. V. Kheruntsyan. Collective many-body bounce in the breathing-mode oscillations of a Tonks-Girardeau gas. *Phys. Rev. A*, 96(4):041605, oct 2017.
- [167] B. Fang, G.e Carleo, A. Johnson, and I. Bouchoule. Quench-induced breathing mode of one-dimensional bose gases. *Phys. Rev. Lett.*, 113:035301, Jul 2014.
- [168] I. Boettcher and M. Holzmann. Quasi-long-range order in trapped two-dimensional bose gases. *Phys. Rev. A*, 94:011602, Jul 2016.
- [169] G. Baym and C. Pethick. Ground-State Properties of Magnetically Trapped Bose-Condensed Rubidium Gas. *Phys. Rev. Lett.*, 76(1):6–9, jan 1996.
- [170] V. M. Pérez-García, H. Michinel, J. I. Cirac, M. Lewenstein, and P. Zoller. Low Energy Excitations of a Bose-Einstein Condensate: A Time-Dependent Variational Analysis. *Phys. Rev. Lett.*, 77(27):5320–5323, dec 1996.
- [171] A. J. Leggett. Bose-einstein condensation in the alkali gases: Some fundamental concepts. *Rev. Mod. Phys.*, 73:307–356, Apr 2001.
- [172] J. Denschlag, J. E. Simsarian, D. L. Feder, Charles W. Clark, L. A. Collins, J. Cubizolles, L. Deng, E. W. Hagley, K. Helmerson, W. P. Reinhardt, S. L.

- Rolston, B. I. Schneider, and W. D. Phillips. Generating solitons by phase engineering of a bose-einstein condensate. *Science*, 287(5450):97–101, 2000.
- [173] T. Langen, R. Geiger, M. Kuhnert, B. Rauer, and J. Schmiedmayer. Local emergence of thermal correlations in an isolated quantum many-body system. *Nat. Phys.*, 9:640–643, 2013.
- [174] N. Navon, A. L. Gaunt, R. P. Smith, and Z. Hadzibabic. Critical dynamics of spontaneous symmetry breaking in a homogeneous Bose gas. *Science*, 347(6218):167–170, 2015.
- [175] M. Aidelsburger, J. L. Ville, R. Saint-Jalm, S. Nascimbène, J. Dalibard, and J. Beugnon. Relaxation dynamics in the merging of n independent condensates. *Phys. Rev. Lett.*, 119:190403, Nov 2017.
- [176] N. Navon, A. L. Gaunt, R. P. Smith, and Z. Hadzibabic. Emergence of a turbulent cascade in a quantum gas. *Nature*, 539(7627):72–75, 2016.
- [177] E. A. L. Henn, J. A. Seman, G. Roati, K. M. F. Magalhães, and V. S. Bagnato. Emergence of turbulence in an oscillating bose-einstein condensate. *Phys. Rev. Lett.*, 103:045301, Jul 2009.
- [178] J. Berges, A. Rothkopf, and J. Schmidt. Nonthermal fixed points: Effective weak coupling for strongly correlated systems far from equilibrium. *Phys. Rev. Lett.*, 101:041603, Jul 2008.
- [179] A. L. Gaunt, T. F. Schmidutz, I. Gotlibovych, R. P. Smith, and Z. Hadzibabic. Bose-einstein condensation of atoms in a uniform potential. *Phys. Rev. Lett.*, 110:200406, May 2013.
- [180] H. Labuhn, D. Barredo, S. Ravets, S. De Léséleuc, T. Macrì, T. Lahaye, and A. Browaeys. Tunable two-dimensional arrays of single rydberg atoms for realizing quantum ising models. *Nature*, 534(7609):667–670, 2016.
- [181] D. Barredo, V. Lienhard, S. de Léséleuc, T. Lahaye, and A. Browaeys. Synthetic three-dimensional atomic structures assembled atom by atom. *arXiv:1712.02727*, 2017.

- [182] Q. Niu, I. Carusotto, and A. B. Kuklov. Imaging of critical correlations in optical lattices and atomic traps. *Phys. Rev. A*, 73:053604, May 2006.
- [183] T. Berrada, S. van Frank, R. Bücke, T. Schumm, J.-F. Schaff, J. Schmiedmayer, B. Julía-Díaz, and A. Polls. Matter-wave recombiners for trapped bose-einstein condensates. *Phys. Rev. A*, 93:063620, Jun 2016.
- [184] F. Zernike. Phase contrast, a new method for the microscopic observation of transparent objects. *Physica*, 9(7):686–698, 1942.
- [185] Serge L. and Yves B. Observation of phase objects by optically processed hilbert transform. *Appl. Phys. Lett.*, 11:49–51, 1967.
- [186] S. Fürhapter, A.r Jesacher, S. Bernet, and M. Ritsch-Marte. Spiral interferometry. *Optics letters*, 30(15):1953–1955, 2005.
- [187] R. Juchtmans, L. Clark, and J. Lubk, A.and Verbeeck. Spiral phase plate contrast in optical and electron microscopy. *Phys. Rev. A*, 94:023838, Aug 2016.
- [188] R. Juchtmans and J. Verbeeck. Local orbital angular momentum revealed by spiral-phase-plate imaging in transmission-electron microscopy. *Phys. Rev. A*, 93:023811, Feb 2016.
- [189] Andrea Bergschneider, Vincent M. Klinkhamer, Jan Hendrik Becher, Ralf Klemt, Gerhard Zürn, Philipp M. Preiss, and Selim Jochim. Spin-resolved single-atom imaging of ${}^6\text{Li}$ in free space. *arXiv*, 2018.
- [190] Dieter Jaksch and Peter Zoller. The cold atom hubbard toolbox. *Annals of physics*, 315(1):52–79, 2005.
- [191] J Ignacio Cirac and Peter Zoller. Goals and opportunities in quantum simulation. *Nature Physics*, 8(4):264, 2012.
- [192] Friedhelm Serwane, Gerhard Zürn, Thomas Lompe, TB Ottenstein, AN Wenz, and S Jochim. Deterministic preparation of a tunable few-fermion system. *Science*, 332(6027):336–338, 2011.

- [193] Simon Murmann, Andrea Bergschneider, Vincent M. Klinkhamer, Gerhard Zürn, Thomas Lompe, and Selim Jochim. Two fermions in a double well: Exploring a fundamental building block of the hubbard model. *Phys. Rev. Lett.*, 114:080402, Feb 2015.
- [194] Marvin Holten. Collective modes and turbulence in two-dimensional fermi gases. Master's thesis, Heidelberg University, 2017.
- [195] Friedhelm Serwane. *Deterministic preparation of a tunable few-fermion system*. PhD thesis, Heidelberg University, 2011.

Acknowledgements

The last few years have been an incredible experience for me. Everything that I have learned and contributed is due to the people around me and the environment they have created.

I am deeply grateful to Selim Jochim for being a terrific mentor during my PhD. Even though I knew almost nothing of cold atom physics when I first met him, he gave me the opportunity to work in his group. He has a natural ability to make people feel comfortable and the friendly atmosphere in our group is, to a large extent, due to him. Along the way, he gave me a lot of freedom to explore and develop my scientific interests and also the support to visit different places which has helped me broaden my perspective. He has an infectious sense of curiosity and enthusiasm for different topics which we have all benefited from.

I am thankful to all my team members with whom I have collaborated over the years. I am grateful to the so-called first generation, a.k.a the "old" guys - Thomas Lompe, Gerhard Zürn, Andre Wenz and Martin Ries -for showing me the ropes in the initial stages of my PhD. Special thanks to Thomas for the helpful advice and discussions, and for providing helpful comments on papers even after he had left the group. Gerhard has been an indispensable part of our group since it started. His "hands-on" approach to problems and his knowledge of electronics has been helpful on so many occasions.

From my generation, I am happy to have had such a wonderful bunch of physicists - Simon Murmann, Andrea Bärschneider, Mathias Neidig and Vincent Klinkhammer - as my contemporaries. I have been friends with Simon since my first day in Heidelberg. It has been great fun to have him as my office-mate and fellow gardener. I am thankful to him for advising me through the difficult times during my PhD. Andrea is one of my closest friends despite me annoying her all the time, and she has played a very important role during my PhD. I thank her immensely for all the moral support when things were not going well and for the Kaffee-zum-mitnehmen walks

to Bellini. I have learned a great deal from our discussions and her experimental skills never fail to amaze me. I am looking forward to working together in Zurich! Vincent and Mathias have been instrumental members of our team. I thank Mathias for all his persistent efforts to improve various aspects of the experiment.

During my PhD I was fortunate to collaborate with extremely talented theoretical physicists: Igor Boettcher, Tilman Enss, Markus Holzmann and Nicolás Defenu. I started working with Igor in the early days of my PhD when we were beginning to study 2D superfluidity. Since then, we have worked together on several projects and it has been a lot of fun along the way. I am particularly grateful to him for the numerous enlightening discussions over Skype and for proofreading our papers.

It has been a privilege to work with Tilman Enss during the course of this thesis. Our experimental work has benefited tremendously from his remarkable theoretical understanding of many-body physics. He is always approachable for physics discussions, from which I have gained a lot of insight over the years. More recently, I had the opportunity to work with Nicolás on the quantum anomaly project, which was a lot of fun.

It has been a great pleasure to work with the newer members of the team. From the 2D Fermi gas experiment, I am grateful to Luca Bayha, Marvin Holten and Antonia Klein, for all the help during the last year and particularly for proofreading the thesis. They have brought in new ideas and perspectives, and I am confident that they will take the group in new exciting directions. Philipp Preiss joined our group as a Postdoc in April 2016 from Harvard and since then, he has become instrumental in all our projects. It is always insightful to discuss physics with him. Many thanks to Jan-Hendrik Becher (the new gardener), Ralf Klemt, Lukas Palm and Keerthan Subramanian from the few-body experiment. I am also thankful to the former members of our group: Tanja Behrle (who helped with the SLM setup), Dhruv Kedar and Sebastian Pres who have contributed to our work over the past years. Thank you all for creating a dynamic atmosphere to work in, without which this thesis would not have been possible.

I thank Prof. Markus Oberthaler for insightful discussions and for agreeing to be my second referee on my committee as well as reading my thesis. I am thankful also to my other committee members, Prof. Peter Bachert and Dr. Tilman Enss.

The non-scientific staff of our institute have supported us immensely. I thank

Ms. Claudia Krämer for the administrative support. Mr. Ralf Ziegler and his amazing team at the workshop helped us significantly by building several mechanical components of our experiment. It is always nice to go to Mr. Ziegler because of his warm personality; he always responds positively to our requests with his signature phrase: "we will do it".

Many thanks to the HGSFP. Prof. Sandra Klevansky and her team have done a terrific job in providing a platform for PhD students in Heidelberg. I have had several positive experiences because of the HGSFP, for eg. the Graduate Days, the winter school, serving as a student representative and the financial support for conferences.

I want to thank my friends who have been a constant source of moral support during my PhD. Many thanks to Andrea Nuila, Simona Wagner, Miguel Ferreira Cao and Alda Arias. Also thanks to Enzo, Katharina and Francesca from Bellini for the numerous coffees and delightful conversations. Thanks to my dear friends from back home: Vena Kapoor, Pavithra Sankaran, M. D. Madhusudhan, Anand Srivastava and Pawan Nandakishore.

I want to thank my family without whom this thesis would not have been possible. Thanks to my parents and my brother for supporting me throughout my education, for encouraging me in my pursuits and for believing in me. Finally, thanks to Sumithra, my partner and best friend, for always being there for me.